



---

# Development and Analysis of a Laser Polishing Strategy to Support the Industrialisation of Additively Manufactured Aluminium Parts

---

BENJAMIN JAY MASON

---

Thesis Submitted November 2023, for the award of Doctor of Philosophy at Cardiff University

*High Value Manufacturing Research Group; Cardiff School of Engineering*

---



## Acknowledgements

There are a series of people who have gone above and beyond with supporting me throughout the production of this thesis. I will be forever indebted to them.

My supervisory team – Prof. R. Setchi, Dr D. Bhaduri, Dr M. Ryan, and Dr A. Kundu – the continued guidance and support throughout has led this project at key points, while also affording an appropriate degree of autonomy to really make it my own. Their diverse range of expertise allowed me to investigate avenues I would not have considered at the outset.

Beyond the direct supervisory group, there have been numerous other academic and research staff that also contributed. Specifically, Dr S. Bigot for the use of the Sensofar Profilometer used extensively in this work. Dr F. Lacan for the operation of and training on the Renishaw AM250 L-PBF machine (however, having to run the machine on your behalf has been one of the more stressful aspects). Prof. E. Brousseau and Dr C. Byrne for entrusting me with undergraduate supervision and teaching roles during the latter stages is an experience I will cherish and hope to resume in the future. On that subject, I must thank the undergraduates that I helped supervise. I learnt a lot through the experience, it made me develop how I communicate technical and non-technical concepts, always hoping to drive you to achieve results you can be proud of.

Cardiff University is staffed by an exemplary technical team, without which this work would not be possible. While too numerous to name, there are some standouts – Mr L Treherne, Mr J. Merridew, and Miss. A. Parnell, thank you for making parts, advising on design, or just taking time to chat, I will miss you all.

Mrs. A. Reid, always available to help with the background university processes, and once again to chat about the world. My time on the student staff panel gave new appreciation for the work you do, and the silent support you give all of us research students.

Lastly from the university, the CUSP and Tribology research groups, past and present, have been a joy to associate with. I hope you all realize the impact you have had, not only on this thesis, but my onwards career. Prof. R. Pullin, your room has always been welcoming and a great environment to work, long may that continue as you support future engineers and researchers. Who would have thought this is where I would now be when I first entered your office all those years ago?

Now that I start a new role, in a new company, I should also thank my new colleagues for believing in my ability. I look forward to continuing my personal development with you and am eager to continue learning from you all.

Finally, my family. I'm not sure you have always understood what I have spent the last four years doing, but the unwavering excitement and interest has fuelled me to push what I thought possible. Mum & Dad, I hope all those radios I broke as a child were worth it. H., I cannot begin to describe the help you have been.

I will remember this time fondly. To my Cardiff University colleagues, this is not the end, I will always be available for a chat and hope to work together again in the future. For now, I embark on a career, with new colleagues, and a whole new challenge to face.

## Abstract

While additive manufacture (AM) is an attractive technology for many areas of engineering, there are substantial barriers to its further industrialisation, one of which is the substandard surface roughness. Literature reviews showed there to be much interest in reducing the as built roughness through parameter optimisation, and various post processing options. One such post-processing technique is laser polishing (LP), sharing many of the benefits of AM (geometric freedom, waste-free operation). The literature reviews also highlighted a series of areas that needed specific attention to facilitate the continued development of LP for AM metal parts, guiding the progress of this thesis. Specific gaps identified were; how to effectively measure the surface roughness of AM parts, how to best laser polish AM aluminium, and what effect the LP has on the material in terms of structure and mechanical properties.

This project started with developing a methodology to reliably and repeatably measure the surface roughness of AM metal parts. The developed methodology was benchmarked using AM aluminium test parts, across a range of measurement devices. It was shown to be robust to changes in measurement device across a wide range of standard roughness parameters. This work also highlights the need for greater understanding regarding the appropriate selection of filter nesting index. Furthermore, the influence of various measurement and post-processing options on the measurement uncertainty have been quantified in terms of pointwise height discrepancies, and the influence on calculated roughness parameters.

Following that, this project developed a novel LP strategy for AM aluminium, utilising multiple steps designed to sequentially ablate and smooth the surface. This was shown to significantly reduce the surface roughness, with a dependency on the initial surface roughness. Minimum roughness values measured were  $1.95 \mu\text{m Sa}$ ,  $18.83 \mu\text{m Sp}$ ,  $14.11 \mu\text{m Sv}$ , and  $25.07 \mu\text{m S10z}$ . Maximum reductions found were 87.4%, 87.4%, 81.7%, and 81.4% for the roughness parameters in turn. The LP strategy resulted in an increase in microhardness in the remelted region, with an associated increase in porosity just below this remelted layer. The maximum hardness after the final polishing step was measured to be  $142 \text{ Hv}_{0.005}$  ( $120 \text{ Hv}_{0.005}$  bulk), while the near surface porosity was estimated to have risen from 0.9% (bulk) to 4.5%.

Evaluating the tensile properties showed mixed results, with LP giving increased, decreased, or no change in values, and different effects depending on whether the samples had been stress relieved, or T6 tempered (peak hardened) prior to polishing. As built samples were found to have increased  $E$  and decreased  $\epsilon_{Fail}$  after LP, with the effect negated through the application of heat treatment. No change in UTS was found due to LP in any condition.

Finally, the fatigue strength was evaluated under both high and low cycle conditions. This showed no significant change in fatigue strength due to the application of either LP or T6 tempering. Showing any benefit of the reduced surface roughness was offset by the increased surface hardness and porosity arising from the LP strategy used.

It is hoped that these results will facilitate the further industrialisation of AM aluminium through the improved understanding of how to evaluate the surface roughness, with the smoothing potential of the LP strategy opening avenues for high value, aesthetic components. Furthermore, the additional data presented regarding the tensile and fatigue properties show there are no significant detrimental effects of the LP strategy.

## Nomenclature

<b>Symbol</b>	<b>Term</b>	<b>Unit</b>
$A$	Indent Area	$\mu\text{m}^2$
$A_{Bulk}$	Apparent solid material area	$\mu\text{m}^2$
$A_o$	Focussed Spot Area	$\mu\text{m}^2$
$A_{Pore}$	Apparent pore area	$\mu\text{m}^2$
$A_{Total}$	Total image area	$\mu\text{m}^2$
$D$	Indent Diameter / diagonal length	$\mu\text{m}$
$dE$	Local Young's Modulus	Pa
$d_o$	Focussed Spot Diameter	$\mu\text{m}$
$dR$	Radius change	mm
$d_z$	Defocussed Spot Diameter	$\mu\text{m}$
$E$	Youngs Modulus	Pa
$E_p$	Pulse Energy	mJ
$F$	Fluence	$\text{J}/\text{cm}^2$
$f$	Pulse Frequency	kHz
$h$	Hatch spacing	$\mu\text{m}$
Hv	Vickers Hardnes	<i>none</i>
$m$	mass	g
$M^2$	Beam Quality	<i>none</i>
$N_{Fail}$	Cycles to failure	<i>none</i>
$N_{Life}$	Desired Fatigue Life	<i>none</i>
$O_X$	Pulse Overlap (X)	%
$O_Y$	Pulse Overlap (Y)	%
$P$	Load	kg
$\rho$	Significance	<i>none</i>
$P_{av}$	Average Power	W
$P_d$	Pulse Distance	$\mu\text{m}$
$P_{Incident}$	Incident (incoming) Radiation Pressure	Pa
$P_p$	Peak Power	kW
$P_{Rad}$	Radiation Pressure	Pa
$r$	Correlation Coefficient	<i>none</i>
$R$	Polishing region radius	mm
$R_B$	Build Rate	$\text{mm}^3/\text{s}$
$R_P$	Processing Rate	$\text{mm}^2/\text{s}, \text{min}/\text{cm}^2$
$R_\sigma$	Stress Ratio	<i>none</i>
$t$	Layer thickness	$\mu\text{m}$
$t_d$	Point Delay	ns
$t_e$	Exposure Time	ns
$T_m$	Melting Point	$^\circ\text{C}$

<b>Symbol</b>	<b>Term</b>	<b>Unit</b>
$t_p$	Pulse Duration	ns
UTS	Ultimate Tensile Stress	Pa
$v$	Scan Speed	mm/s
$z$	Focal Offset	mm
$z_i$	Point Height	$\mu\text{m}$
$z_R$	Rayleigh Length	mm
$\alpha$	Absorptivity	%
$\gamma$	Surface Isotropy	%
$\Delta\sigma$	Stress increment	MPa
$\varepsilon$	Engineering Strain	<i>none</i>
$\varepsilon_{Fail}$	Failure Strain	<i>none</i>
$\varepsilon_{Yield}$	Yield Strain	<i>none</i>
$\kappa$	Thermal Conductivity	W/m °K
$\lambda$	Wavelength	nm
$\xi$	Relative Difference	%
$\rho$	Density	g/cm <sup>3</sup>
$\sigma$	Engineering Stress	Pa
$\sigma_e$	Fatigue Strength (endurance limit)	MPa
$\sigma_0$	Maximum fatigue loading sustained	MPa
$\sigma_{Yield}$	Yield Stress	Pa
$\phi$	Porosity	%
$\psi$	Energy Density	J/mm <sup>3</sup>

## Table of Contents

1	Introduction .....	1
1.1	Motivation.....	1
1.2	Aim and Objectives .....	2
1.3	Thesis Structure .....	2
2	Technical Background and Literature Review.....	4
2.1	Introduction .....	4
2.2	Additive Manufacturing .....	4
2.2.1	Post-processing of AM Parts .....	6
2.2.2	Surface Characteristics.....	7
2.2.3	Surface Roughness Improvements .....	7
2.3	Surface Roughness.....	8
2.3.1	Roughness Components .....	8
2.3.2	Filtration.....	9
2.3.3	Roughness Parameters .....	10
2.3.4	Measurement Techniques .....	13
2.4	Laser Polishing.....	16
2.4.1	Mechanism.....	16
2.4.2	Laser Polishing of Additively Manufactured Surfaces.....	18
2.4.3	Simulations.....	19
2.5	Mechanical Testing of Additively Manufactured Components .....	20
2.5.1	Hardness .....	20
2.5.2	Quasi-Static (Tension, Bending) .....	21
2.5.3	Fatigue.....	22
2.6	Technical Literature Review .....	24
2.6.1	Surface Metrology.....	24
2.6.2	Laser Polishing.....	26
2.6.3	Thermal Post-Processing.....	28
2.6.4	Fatigue.....	29
2.7	Identified Knowledge Gaps .....	33
2.7.1	Surface metrology.....	33
2.7.2	LP Literature Summary.....	33
2.7.3	Fatigue.....	34
3	Methods and Equipment .....	35
3.1	Additive Manufacture of AlSi10Mg Parts .....	35

3.2	Laser Polishing.....	36
3.3	Surface Metrology.....	38
3.3.1	Measurement Systems .....	38
3.3.2	Measurement Stitching.....	39
3.4	Material Testing.....	39
3.4.1	Cross-Section Mounting and Preparation.....	39
3.4.2	Vickers Microhardness.....	40
3.4.3	Etching and Microstructural Evaluation.....	41
3.4.4	Porosity Evaluation .....	41
3.4.5	Quasi-Static Tensile Testing .....	43
3.4.6	Fatigue Testing .....	44
4	A Method for Surface Roughness Measurement of AM PBF Surfaces.....	46
4.1	Introduction .....	46
4.2	Methodology.....	47
4.2.1	Samples .....	47
4.2.2	Measurement Procedure .....	48
4.2.3	Aligning Measurements .....	50
4.2.4	Roughness Parameters of Interest.....	50
4.2.5	Data Post-Processing.....	51
4.2.6	Surface Lay and Isotropy.....	51
4.2.7	Measurement Resolution .....	52
4.2.8	Uncertainty Quantification .....	53
4.3	Results and Discussion .....	55
4.3.1	Visual Inspection of Surfaces .....	55
4.3.2	Qualitative Comparison of Surface Measurements.....	55
4.3.3	Filter Selection .....	58
4.3.4	Roughness Values .....	60
4.3.5	Analysis of Surface Lay and Isotropy.....	65
4.3.6	Resolution .....	66
4.3.7	Uncertainty .....	68
4.4	Final Methodology .....	73
4.5	Surface Roughness Measurement Summary.....	73
5	Development and Evaluation of a LP Strategy for AM Aluminium Parts.....	75
5.1	Introduction .....	75
5.2	Purpose .....	75
5.3	Test Plan.....	75

5.3.1	Samples .....	75
5.3.2	Strategy .....	76
5.3.3	Surface and Material Characterisation .....	77
5.4	Results and Discussion .....	79
5.4.1	Determined LP Settings.....	79
5.4.2	Initial Trials.....	80
5.4.3	Processing Rate Refinement .....	82
5.4.4	Effects of LP Using the Final Strategy.....	83
5.5	Thermal Simulations of Final LP Strategy.....	94
5.5.1	Simulation Setup .....	94
5.5.2	Simulation Results and Discussion .....	96
5.6	Laser Polishing Strategy Development and Analysis Summary .....	100
6	Assessment of the Tensile Properties of AM Aluminium .....	101
6.1	Purpose .....	101
6.2	Test Plan.....	101
6.3	Methods.....	102
6.3.1	Sample Manufacture.....	102
6.3.2	Heat Treatment.....	103
6.3.3	Sample Polishing .....	103
6.3.4	FEA Validation of Miniaturisation and LP Geometry .....	104
6.3.5	Sample Preparation.....	106
6.3.6	Surface Roughness Measurement .....	106
6.3.7	Material Properties.....	106
6.4	Results.....	107
6.4.1	T <sub>M</sub> (Machining) Trial .....	107
6.4.2	T <sub>H</sub> (Heat Treatment) Trial.....	110
6.4.3	Comparisons Between Sample Sets.....	115
6.4.4	Bulk Hardness.....	116
6.5	Discussion.....	117
6.5.1	Comparisons to Datasheet Values .....	117
6.5.2	Comparisons to Literature Values.....	117
6.5.3	Effect of Laser Polishing on Tensile Properties .....	118
6.5.4	Yield Strain Variability .....	119
6.6	Tensile Testing Summary .....	119
7	Assessment of the Fatigue Strength of AM Aluminium.....	121
7.1	Introduction .....	121

7.2	Purpose .....	121
7.3	Test Plan.....	121
7.4	Sample Preparation .....	122
7.5	Results and Discussion .....	125
7.5.1	Low Cycle Fatigue Tests .....	125
7.5.2	High Cycle Fatigue Tests.....	128
7.6	Fatigue Testing Summary.....	132
8	Overarching Conclusions and Future Work. ....	133
8.1	Conclusions .....	133
8.2	Contributions .....	134
8.3	Novelty Statement .....	134
8.4	Future Work.....	135
	References .....	137
I.	Appendix – MATLAB Localisation script.....	152
II.	Appendix – LP initial development test matrix.....	156
III.	Appendix – MATLAB script for determining elastic region and calculating mechanical properties.....	158

## List of Abbreviations

<b>Acronym</b>	<b>Term</b>
μ-CT	Micro-Computed Tomography
2D	Two Dimensional
3D	Three Dimensional
AA	Artificial Ageing
AM	Additive Manufacture
BIPM	International Bureau of Weights and Measures
CFD	Computational Fluid Dynamics
CMOS	Complimentary Metal-Oxide-Semiconductor
CNC	Computer Numeric Control
CW	Continuous Wave Laser
DED	Directed Energy Deposition
DPSS	Diode Pumped Solid State (Laser)
EB-PBF	Electron Beam Powder Bed Fusion
EDX	Electron Dispersive X-ray
EM	Electro-magnetic
FDM	Fused Deposition Modelling
FEA	Finite Element Analysis
FoV	Field of View
FV	Focus Variation
HAZ	Heat Affected Zone
HCF	High-cycle Fatigue
HT	Heat Treatment
HVM	High Value Manufacturing
IBA	Inverse Bremsstrahlung Absorption
IPA	Isopropyl Alcohol
IR	Infra-Red
LCF	Low-cycle Fatigue
LIGO	Laser Interferometer Gravitational-Wave Observatory
LP	Laser Polishing
L-PBF	Laser Powder Bed Fusion
LSP	Laser Shot Peening
MOPA	Master Oscillator Power Amplifier (Laser)
NM	Non-Measured (points)
NPL	National Physical Laboratory
OAS	Optical with Automated Stitching
OMS	Optical with Manual Stitching
PBF	Powder Bed Fusion
ppm	Parts per million
PRF <sub>0</sub>	Fundamental Pulse Frequency
PTFE	Polytetrafluoroethylene
PW	Pulsed Wave (laser source)
RBV	Reduced Build Volume
RMS	Root Mean Squared
SEM	Scanning Electron Microscopy
SHT	Solution Heat Treatment
SLA	Stereo Lithography

<b>Acronym</b>	<b>Term</b>
SM	Subtractive Manufacture
SMaRT	Swansea Materials Research & Testing Ltd.
SP	Shot Peening
SR	Stress Relief
T2D	Tactile 2D
T3D	Tactile 3D
T <sub>H</sub>	Heat Treatment trial Tensile samples
T <sub>M</sub>	Machining trial Tensile samples
UV	Ultraviolet
VG	Video Gauge
W-EDM	Wire EDM
WFM	Waveform

## List of Figures

Figure 2.1: Additively manufactured polymer boat hull produced by University of Maine [18], similar in concept and execution as the device described by Leinster [16].	4
Figure 2.2: Common metal AM processes. Adapted from [21].	5
Figure 2.3: Different forms of blasting media. Top) Steel grit, and Bottom) Steel shot. From [33].	8
Figure 2.4: Example surface showing how different scale wavelengths combine (Roughness, Waviness, and Form), adapted from [41].	9
Figure 2.5: Filter characteristics around the three cut-offs (from ISO 1134 [42]).	10
Figure 2.6: Graphical representation of (A) Skewness and (B) Kurtosis terms. Adapted from [47], [48].	12
Figure 2.7: Example of a surface roughness comparator set. From [49].	13
Figure 2.8: Schematic showing how focus variation is used to resolve surface heights. Left - Microscope optical components. Right - Using contrast to determine focus. From [54].	14
Figure 2.9: Schematic of the working principle behind Confocal Microscopy, from [56].	15
Figure 2.10: Schematic of how interferometry works to detect a change in length. Adapted from [58].	15
Figure 2.11: Schematic of the laser polishing (A) and laser ablation (B) processes [63].	16
Figure 2.12: Example of AM prosthetic knee joint, in the as built condition (Left) and after laser polishing (right). From [66].	18
Figure 2.13: Example of CFD prediction of melt-pool dynamics and residual surface texture resulting from (a-c) pulsed wave, or (d-f) continuous wave laser sources. From [78].	20
Figure 2.14: Common Hardness test methods. Adapted from [80].	21
Figure 2.15: Typical stress-strain curve with main features identified. From [81].	22
Figure 2.16: Australian Olympic cycling team AM Titanium component failure, attributed in part to improperly defined loading conditions during design, accelerating the onset of fatigue cracking. From [85].	23
Figure 2.17: Typical surfaces from AM Aluminium.	24
Figure 2.18: The same surface roughness measurement with different filters applied ( $\lambda_c = 2.5$ mm, 0.8 mm, 0.25 mm, and 0.08 mm) and the resulting roughness (black lines) and waviness (red lines, marked with *) profiles obtained [evaluation length = 17.5 mm, tip radius = 5 $\mu$ m]. From [75, p. 348].	25
Figure 2.19: Representative surface roughness measurement of an AM aluminium part.	26
Figure 2.20: The fatigue samples and build orientations used by Beretta et al., from [134].	31
Figure 2.21: Schematic of laser peening. From [144].	32
Figure 3.1: Renishaw Reduced Build Volume (RBV) system, from [151].	35
Figure 3.2: Depiction of different scanning elements, adapted from [152].	36
Figure 3.3: Laser pulse amplitude profile over time. From [153].	37
Figure 3.4: General relationship between pulse energy (solid line, left), average laser power (dashed line, right) and pulse frequency, showing PRF <sub>0</sub> frequency (dot-dash line). Adapted from [153].	38
Figure 3.5: Schematic of how image stitching can be used to composite multiple images to extend the overall field of view.	39
Figure 3.6: Buehler EcoMet 30 grinder polisher machine, from [156].	40
Figure 3.7: Mitutoyo HM-220 microhardness testing machine and control computer. From [157].	41
Figure 3.8: Example greyscale micrograph (left) and processed imaged (right) from the ImageJ software. Pores are shown in black while the bulk material is white. The insert shows number of areas measured (pores), total area and average size of pores (unknown units), and the % area coverage (porosity, $\phi$ ).	42

Figure 3.9: Schematic of Archimedes' density measurement procedure, from [158]. Where (a) shows measuring the dry mass ( $m_{Air}$ ), and (b) the mass when submerged ( $m_{Water}$ ). .....	43
Figure 3.10: Example of a Video Gauge output. At the top are instantaneous values, on the right a live video feed with the virtual strain gauge marked, and on the left graphs of load against strain and displacement.....	44
Figure 4.1: Example of simulation using measured surface data to assess fluid flow velocities. From [164].....	46
Figure 4.2: Optical micrographs of three of the surfaces analysed with the (A) best, (B) medium, and (C) worst surface condition.....	48
Figure 4.3: Distribution of the line profiles taken across the sample surface. Sample outline shown by the dashed line, all dimensions in mm. ....	49
Figure 4.4: Schematic of the localisation process, a) identify matching features on the surfaces – denoted by with red circles, b) rigid transformations (translation, rotation) of the surfaces so the matched features align, c) crop the surfaces to leave only the corresponding areas (grey shaded area).....	50
Figure 4.5: Two theoretical surfaces with the same Ra.....	50
Figure 4.6: Processing flow for 3D surface measurements. Dotted lines indicate step not required for all instances.....	51
Figure 4.7: Schematic representation of how lay can affect a profile measurement (the predominant lay is across the page) from [42].....	51
Figure 4.8: Example of the MountainsMap "texture direction" output. ....	52
Figure 4.9: Example of a positioning Jig used. ....	54
Figure 4.10: Arrangement of measurements to evaluate uncertainty due to Localisation errors.....	54
Figure 4.11: Process for comparing stitched measurement with direct measurement.....	55
Figure 4.12: Surface measurements of top surface of sample S1 with matching asperities highlighted. The measurement systems used were (a) T3D, (b) OAS, and (c) OMS.....	56
Figure 4.13: Surface Measurements of top surface of sample S3 with matching surface depressions highlighted. The measurement systems used were T3D (a), OAS (b), and OMS (c).....	56
Figure 4.14: OMS result from the top surface of S3, showing stitching artifacts (indicated by dashed lines).....	57
Figure 4.15: (A) OAS result showing erroneous points (black region in inset), and (B) the same surface and region from T3D without the erroneous results.....	57
Figure 4.16: Effect of changing nesting index (0.8 mm and 2.5 mm) on (A) calculated roughness parameters, and (B) overall effect on each examined surface.....	59
Figure 4.17: Arithmetic Mean Roughness values calculated from different measurement systems, after filtering with a (A) 0.8 mm nesting index, and (B) 2.5 mm nesting index.....	61
Figure 4.18: RMS Roughness values calculated from different measurement systems, after filtering with a (A) 0.8 mm nesting index, and (B) 2.5 mm nesting index.....	62
Figure 4.19: Skewness values calculated from different measurement systems, after filtering with a (A) 0.8 mm nesting index, and (B) 2.5 mm nesting index.....	63
Figure 4.20: Kurtosis values calculated from different measurement systems, after filtering with a (A) 0.8 mm nesting index, and (B) 2.5 mm nesting index. ....	64
Figure 4.21: 10-point height ( $S_{10z}$ ) values calculated from different measurement systems, after filtering with a (A) 0.8 mm nesting index, and (B) 2.5 mm nesting index. ....	65
Figure 4.22: Isotropy values ( $\gamma$ ) calculated by MountainsMap (areal measurements) and using PSm (profile measurements). ....	66

Figure 4.23: Effect of Y-spacing on different roughness parameters (A, C) Sa, Sq, Ssk, Sku, and (B, D) Sp, Sv, Sz, and S10z, when processed with different nesting indices (A, B) 0.8 mm, and (C, D) 2.5 mm. ....	67
Figure 4.24: Effect of optical magnification on different roughness parameters (A) Sa, Sq, Ssk, Sku, and (B) Sp, Sv, Sz, and S10z. ....	68
Figure 4.25: Probability density function of calculation deviations from mean surface of measurements taken without moving sample between measurements. ....	69
Figure 4.26: (A) Average heights of measured points (the mean surface) from an examined surface, (B) maximum absolute deviation of measured points from mean surface. Note, colour scale for (B) is logarithmic. ....	69
Figure 4.27: Polar plot of positioning error of measurements when using an alignment jig. The radial distance shows the translational error while the angle shows the rotational difference (both compared to an arbitrary baseline measurement). ....	70
Figure 4.28: (A) Average heights of measured points (the mean surface) from an example surface, (B) maximum absolute deviation of measured points from mean surface. Note, colour scale for (B) is logarithmic. ....	71
Figure 4.29: Average errors calculated comparing direct measurements with matching stitched measurements. ....	71
Figure 4.30: Cumulative probability curves for height errors resulting from different sources. ....	72
Figure 5.1: Schematic of different hatch strategies used. ....	76
Figure 5.2: Surface measurement data post-processing flow used. ....	78
Figure 5.3: Indentation layout used to evaluate the sub surface hardness profiles. ....	79
Figure 5.4: 3D view of surface roughness measurement (normalised axes) rendered with greyscale optical image showing characteristic laser ablated surface texture. ....	80
Figure 5.5: Resultant surfaces after 2-step trials (A) 2/16 passes, and (B) 8/8 passes. ....	81
Figure 5.6: (A) optical micrograph, and (B) false-colour height map of surface processed with four step LP strategy (8/8/4/16 passes). ....	82
Figure 5.7: Roughness reductions ( $\pm 1$ standard deviation range) compared to number of passes for final smoothing step. ....	83
Figure 5.8: Optical micrographs of a surface (A) as built, and (B) after processing with the final LP strategy. ....	84
Figure 5.9: False colour height maps of a surface (A) before, and (B) after processing with the final LP strategy, note the different colour (height) scales. ....	85
Figure 5.10: (A) Total roughness reduction after each step of final strategy, and (B) Sa values after each processing step showing range measured from different samples and areas, mean average shown by dashed line. ....	86
Figure 5.11: (A) Sp, (B) Sv, and (C) S10z Roughness values after each processing step, mean average shown by dashed red line. ....	86
Figure 5.12: (top) Surface height maps, and (bottom) Optical Micrographs. Showing initial surface, and surface after each processing step. ....	87
Figure 5.13: Cross-sectional micrographs of (A) the as-built surface and (B-E) after each LP processing step in turn. (B, D) ablated surfaces, (C, E) smoothed surfaces. ....	88
Figure 5.14: How the relative porosity in the HAZ compares to the bulk porosity throughout the LP process. ....	89
Figure 5.15: Microstructure at the processed surface after each processing step (A-D sequentially). ....	90
Figure 5.16: Near-surface microhardness profiles in the LP region after each processing step. ....	91
Figure 5.17: Optical micrograph of various aluminium samples after applying the final LP strategy. ....	92
Figure 5.18: Range of reduction of different roughness parameters. ....	93

Figure 5.19: Plot of % reduction in Sa against the initial roughness value. ....	94
Figure 5.20: Measured beam spatial profile. ....	95
Figure 5.21: Result probe locations used in simulations (shown by axes). Also shown is full body (green) and region of refined mesh (brown). ....	96
Figure 5.22: Simulated temperature fields just prior to (top) and immediately following (bottom) the mid-point pulse. ....	97
Figure 5.23: Surface temperatures simulated for different laser waveforms. ....	98
Figure 5.24: Simulated temperatures at various depths below scan track mid-point during processing with different laser waveforms. (n.b., Y-scale is different between graphs for clarity). ....	99
Figure 6.1: $T_M$ trial tensile test specimen, based on ASTM E8-E8M. All dimensions in mm. ....	102
Figure 6.2: Miniaturised tensile sample. ....	103
Figure 6.3: Dimensions of the polished region (shaded) overlaid on the sample outline. Geometry of (A) Initial, and (B) Miniaturised specimen. Dimensions in mm. ....	104
Figure 6.4: Image of the FEA model used (initial trial sample), showing the areas where the frictionless support (A – Blue) and load (B – Red) were applied. ....	104
Figure 6.5: Structural FEA model of (top) initial, and (bottom) miniaturized sample geometries, showing von-mises stress. ....	105
Figure 6.6: Structural FEA model of (top) initial, and (bottom) miniaturized sample geometries with ablated volume removed, showing von-mises stress. ....	106
Figure 6.7: Example stress strain curve (solid line) showing the estimated elastic region (dashed line), along with yield (dot-dash line) and failure (dotted line) stress and strains. ....	107
Figure 6.8: Mechanical property results from $T_M$ tests. ....	108
Figure 6.9: Correlation coefficients for the influence of the machining operation, Sample bulk hardness, and surface roughness on mechanical tensile properties. Only coefficients with significance <0.05 are shown. ....	109
Figure 6.10: Correlation coefficients for the influence of Laser Polishing, Sample bulk hardness, and surface roughness on mechanical tensile properties. Only coefficients with significance <0.05 are shown. ....	110
Figure 6.11: Example of sample failure (top) within the gauge length, and (bottom) failure at edge of polished region. ....	111
Figure 6.12: Scatter plot of results comparing initial and final, optimized LP process. ....	112
Figure 6.13: Scatter plot of results comparing initial and miniaturized geometry. ....	113
Figure 6.14: Scatter plots of test data (blue cross) and average values (red bar) for calculated tensile properties for samples showing effect of LP and heat treatment. ....	114
Figure 6.15: Correlation coefficients for the effect of LP on samples in various states of heat treatment. ....	114
Figure 6.16: Correlation coefficients for the effect of SR/T6 heat treatment on samples with and without LP. ....	115
Figure 6.17: Scatter plot of results from matching samples manufactured as part of the $T_M$ and $T_H$ trials. ....	116
Figure 6.18: Plot of maximum, minimum, and average bulk hardness from measurements, datasheets, and reported literature. ....	117
Figure 7.1: Fatigue sample geometry, from ASTM E466 (all dimensions in mm). ....	122
Figure 7.2: Von Mises stress plot of fatigue sample, showing location and magnitude of maximum stress. ....	123
Figure 7.3: Terraced LP geometry used for fatigue sampels. ....	124
Figure 7.4: top) FEA model geometry (section plane on right end), and bottom) von Mises stress plot of finalised LP fatigue geometry (C4: R = 30 mm, dR = 1 mm, 0.5 mm chamfer). ....	125

Figure 7.5: Example profile measurement from LP fatigue sample transition region, where (A) is the unpolished region and (B-E) after each LP step in turn. (E) is the fully polished region. ....	125
Figure 7.6: LCF results showing cycles to failure against maximum tensile stress. R = 0.1, tension-tension. ....	126
Figure 7.7: Examples of LCF crack initiation sites (arrows), where the dashed lines show the extent of the propagation regions. Sample conditions are: (A) As Built, (B) LP, (C) T6, and (D) T6 + LP. ....	127
Figure 7.8: EDX composition map from As Built condition LCF sample.....	128
Figure 7.9: Endurance limit of HCF samples as calculated using Equation 3.1.....	129
Figure 7.10: HCF crack propagation region for As Built sample. Initiation shown by the white arrow. ....	130
Figure 7.11: HCF Crack propagation region for LP sample, with detail of the killer notch at initiation site.....	130
Figure 7.12: EDX composition layered image from LP HCF sample.....	131
Figure 7.13: Optical micrograph showing etched cross section of T6 + LP sample. ....	132

## List of Tables

Table 2.1: Brief description of roughness components, and potential sources of errors. Information from [40].	9
Table 2.2: Types of filters applied to measured data before computing parameter values.	10
Table 2.3: Common surface roughness parameters. From ISO 4287 [45] and ISO 25178-2 [46].	12
Table 2.4: Times and temperatures used to achieve a T6 temper in AM AlSi10Mg.	29
Table 3.1: Renishaw AlSi10Mg powder nominal composition [69].	35
Table 3.2: Standard Renishaw settings for AlSi10Mg powder using the AM250 machine.	36
Table 3.3: Lasertec 40 system specifications	37
Table 3.4: Laser specifications for SPI G3.1 source, as installed in the DMG Lasertec 40 laser milling centre. Data from [153].	37
Table 3.5: Basic setup used for surface roughness measurements taken throughout this project.	38
Table 3.6: Example microstructural sample preparation procedure.	40
Table 3.7: Nominal composition of Keller's Etchant.	41
Table 4.1: Variable manufacturing parameters used for samples in this test.	47
Table 4.2: Details of the different surface measurement techniques used.	48
Table 4.3: Y-resolution levels investigated for T3D system.	53
Table 4.4: Specification of different magnification objectives and resulting measurement size for the OMS system.	53
Table 4.5: Estimates for the time required to measure an 8 mm × 8 mm area using the different systems.	58
Table 4.6: Maximum variability for common roughness parameters from different data post-processing operations.	73
Table 5.1: Parameter ranges used for processing rate optimisation trials.	77
Table 5.2: Initial laser parameters for the ablation and smoothing processes.	80
Table 5.3: Iterations for number of polishing passes used for two-step trials, showing % reduction and surface parameter values achieved with determined number of passes (shown in <b>bold</b> ).	81
Table 5.4: Iterations for number of polishing passes used for four-step strategy trials, showing reduction and value achieved with determined number of passes (shown in <b>bold</b> ) various roughness parameters.	81
Table 5.5: Final determined laser polishing parameters.	83
Table 5.6: Average roughness values measured from the initial surface, and after each processing step.	86
Table 5.7: Thermal conductivity and melting point for AlSi10Mg and two conventionally manufactured alloys.	92
Table 5.8: Range of roughness reductions, and minimum achieved roughness.	93
Table 5.9: Simulation setup details.	96
Table 6.1: Post processing applied to $T_M$ (machining trial) tensile samples.	101
Table 6.2: Post processing applied to $T_H$ tensile samples (HT trial).	102
Table 6.3: Average value for range of outputs for each $T_M$ sample type. Change with respect to the "Net Shape – As Built" condition given in brackets, where positive values indicate an increase, while negative indicate a reduction.	109
Table 6.4: Values for UTS, $\epsilon_{Fail}$ , $\sigma_{Yield}$ , and $E$ , from various literature. Heat treatment conditions reported from each of the following conditions: AB – As Built, SR – Stress Relief, T6 – T6 Temper.	118
Table 6.5: Comparing Failure Strain results in various states of heat treatment found in this work and by Mertens et al. [136].	118
Table 6.6: Summary of the influence of LP on Tensile properties.	120

Table 7.1: Fatigue sample conditions. ....	122
Table 7.2: Test conditions for LCF samples.....	122
Table 7.3: Material removal per LP step.....	123
Table 7.4: Variations in R, dR, and chamfer geometry trialled for terraced LP geometries, along with maximum part stress as a percentage of maximum stress in unpolished geometry (scaled to minimum cross section), and maximum root stress as percentage of maximum part stress.....	124
Table 7.5: Peak stress, Peak Force, and cycle count for each HCF sample at each load-step used. ...	128



# 1 Introduction

While Additive Manufacture (AM) is well established in research and high-value manufacturing (HVM) settings, uptake is significantly slower in more mass-market sectors. Some of the reasons behind this are the high capital and labour costs of industrial-scale machines, safety concerns regarding the machines and raw materials [1], and issues with the resultant part quality such as geometrical accuracy and roughness.

For AM to become practical for end use parts, all of these need addressing. High-value industries will be less concerned by the cost than the part quality, and as AM gains market penetration the capital investments will reduce. Therefore, the most promising route to mass-market is from improvements to the manufactured parts. Improvements are sought in geometric accuracy [2] (to facilitate multi-component assemblies), surface condition [3], [4] (for aesthetic and functional reasons), and mechanical properties [5], [6] (to achieve strengths comparable to conventionally manufactured parts).

The currently tolerated solutions all involve post-manufacture processing to realise these aims, while research is ongoing to optimize the AM processes. Generally, for geometric accuracy and surface condition, various machining operations are necessary [7]. This is not ideal as it adds to the time required to manufacture a part, additional fixturing and machine setup operations, and the generation of waste material. Furthermore, the capabilities of conventional manufacturing operations are limited with AM components due to tool geometries being unable to process deep features and cutting forces risking fine details possible.

Therefore, alternative solutions are necessary to facilitate post-production machining of AM components. Laser processing is an attractive option due to the ability to process highly complex geometries (nearing the capabilities of AM), no tool-wear, and force free processing not risking damage to parts [8]. Furthermore, with laser optics able to focus energy onto very small areas (down to a few tens of micrometres) very fine details can be added to surfaces, such as to create hydrophobic textures.

Laser processing is facing a similarly slow industrial uptake as AM for similar reasons (high initial costs, safety concerns, low productivity etc.). However, with laser architecture continually evolving (lasing mediums, attainable powers, emission wavelengths) and the capabilities becoming better understood they are becoming a viable option for more industries.

## 1.1 Motivation

While this project has evolved over time, based on continued literature reviews and the knowledge gained through the various work packages undertaken. However, the key motivations were consistent throughout and are thus:

To further the industrialisation of metal AM through laser post-processing.

- Laser processing is commonly utilised for cutting, cleaning, and welding operations [9], [10] in a wide variety of industries, with the required machines continually gaining functionality and reducing cost. The capabilities of laser systems are well known, and it is therefore natural to transfer that knowledge to AM.

To address the mechanical and surface condition issues present with current AM technologies.

- Full realisation of the benefits of AM, in terms of geometric freedom and complexity, requires a good understanding of the underlying mechanical properties, else excessive safety factors

are required negating the materials saving by novel geometries. This work will contribute to the knowledge through additional strength data on which to base such designs. Furthermore, there is a growing trend for high-value individuals to prefer bespoke products, e.g., supercar manufacturers offering factory customisation [11]. AM is a natural partner to this through the organic shapes possible and reduced setup costs compared to conventionally manufactured parts (e.g., casting, machining). However, the surfaces of metal AM parts are typically very rough and show signs of other contamination, making them less desirable.

To contribute to national and international environmental targets by the development of efficient processing operations with minimal waste generation.

- AM is touted as a disruptive technology by eliminating the requirement to stock vast quantities of spare parts for the upkeep of current machines [12], and extending the service life of legacy designs, by manufacturing the exact components only when, and where, they are required. Furthermore, as AM is a net-shape process, there is nearly no waste material generated, unlike the vast quantities of swarf generated by subtractive manufacturing (SM) processes [13].

While not directly referenced in this work, some key industries have the potential to benefit from the outcomes. These include HVM applications such as aerospace, and space exploration, motorsport (especially Formula 1 and other prototypes) and high-value automotive more generally. In addition, electronics, sensors, and micro-electromechanical systems may also find value in the ability to produce defined and accurate textures on AM surfaces.

## 1.2 Aim and Objectives

The aim of this project is to support the industrialisation of AM Aluminium through the development of a novel laser-based post processing strategy. Furthermore, an enhanced understanding of the quasi-static tensile and fatigue properties of the material is to be generated to enhance the ability of designers to make best use of AM Aluminium.

To facilitate this, the following objectives have been set:

- 1) Determine an effective, reliable, repeatable, and rigorous measurement methodology for the assessment of the surface roughness of AM powder-bed fusion parts.
- 2) Develop a novel laser polishing strategy to reduce the surface roughness of as-built AM Aluminium parts. This will support wider the uptake of AM through aesthetic improvements (for example, in luxury consumer goods) while also being applicable to surface texturing and functionalisation.
- 3) Assess the influences of the laser polishing operation near the surface on properties such as microstructure, hardness, and porosity near the remelted region.
- 4) Quantify the effect of laser polishing on the mechanical properties of samples, specifically the quasi-static tension and axial fatigue tests.

## 1.3 Thesis Structure

This thesis is structured with Chapter 2 giving a high-level overview of the key techniques discussed subsequently, background theory, and governing equations. Namely additive manufacture of aluminium, surface roughness, laser polishing, and mechanical testing techniques. Chapter 2 culminates with a targeted literature review covering the key topics covered in chapters 4-7, and a summary of the identified knowledge gaps that guided the subsequent works.

Chapter 3 then follows with the equipment specifications and method of operations for key processes used throughout the thesis. Sample manufacture, laser polishing, surface measurement, and mechanical testing are covered.

The developed surface measurement process is explained in Chapter 4, addressing objective 1, benchmarked using AM Aluminium samples. The chapter includes sections on how the strategy was evaluated and induced errors that need to be considered. A comparison between a series of different measurement devices is presented, showing the procedure is repeatable and robust to changes in measurement setup.

Chapter 5 discusses the development of the novel laser polishing strategy, regarding objective 2. Chapter 5 also covers objective 3 through the evaluation of the surface effects (roughness, microhardness, microstructure).

Objective 4 is the focus of Chapters 6 and 7, which discuss the tensile and fatigue properties of the AM Aluminium respectively.

Finally, Chapter 8 contains an overarching discussion of conclusions from the thesis culminating with recommendations for future works.

## 2 Technical Background and Literature Review

### 2.1 Introduction

This chapter provides a high-level overview and history of the topics covered in subsequent chapters. In particular, additive manufacture, surface roughness, laser polishing, and mechanical testing will be discussed, including the underlying theory and governing equations. An in-depth literature review then follows on the key topics, covering the current research, and highlighting the knowledge gaps this thesis aims to address.

### 2.2 Additive Manufacturing

Some of the earliest experiments around AM occurred in the 1960s, focussing on using twin laser sources to polymerise a liquid resin in order to construct three-dimensional (3D) shapes [14]. While the rate of development being especially rapid in these early days, success was less common. Dr Hideo Kodama published a pair of reports and a patent application in 1980 and 1981 describing a single laser approach [15], and is widely regarded as one of the first practical demonstrations of AM.

However, there are even earlier references to what we would now know as AM in various literature, one of the earliest being in *“Things Pass By”* by Murray Leinster (1945) where a device known as a “plastic constructor” is used [16]. This plastic constructor deposits molten plastic from a robotic arm which is then allowed to harden, bearing more than a passing resemblance to the current Fused Deposition Modelling (FDM) technique<sup>1</sup>. Figure 2.1 shows a polymer boat hull produced by the University of Maine using a bespoke (and very large) FDM system, in a remarkably similar way to how Leinster envisioned. Another early reference was in Raymond F. Jones’ short story *“Tools of the Trade”*, published in *Astounding Science Fiction* in November 1950, with a technology referred to as “Molecular Spray” [17] which resembles a modern powder deposition process, with the added capability of depositing many different materials simultaneously. While the multi-material aspect of Jones’ technology has not yet been realised, the deposition and solidification of materials to build up 3D parts has been realised through a variety of techniques.

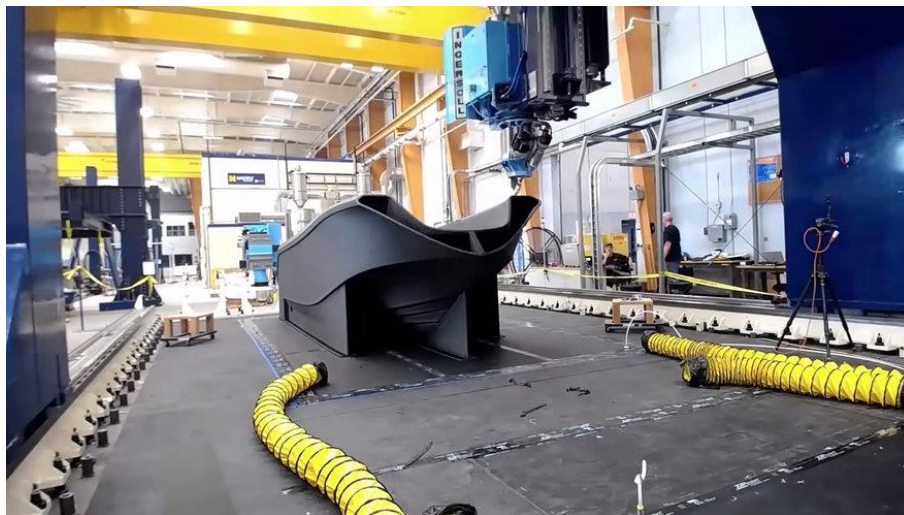


Figure 2.1: Additively manufactured polymer boat hull produced by University of Maine [18], similar in concept and execution as the device described by Leinster [16].

---

<sup>1</sup> While Leinster’s ideas for AM came to be surprisingly accurate, other aspects of the story are less accurate. For example, the story is set in 1992 and mentions a global population of 2 billion when estimates put the historical value at 5.5 billion. Another is a passage stating *“Clumsy, laboring [sic] rockets had barely circled its moon. Only twice had explorers returned from a satellite hardly a quarter-million miles away”* while in reality the Apollo Program landed on the moon 6 times between 1968 and 1972.

In a contemporary context, AM is a very broad field that covers a multitude of different techniques. All take raw material in an easy-to-handle form (powder, wire, sheet, liquid etc.) and assemble these into a final 3D shape. The first stage of the AM process is to turn the 3D model into a series of two-dimensional (2D) layers, or slices. The AM machine then produces each of these slices in turn to build the final model.

One of the more prevalent techniques uses powder as the feedstock, spread evenly across a given build area, with an energy source being directed over the surface to fuse the material. The addition of powder and fusing selected areas repeats sequentially until the part is complete. This is known as powder bed fusion (PBF). Energy sources are typically laser or electron beam, known as L-PBF and EB-PBF respectively. Solidification can be by either sintering, where the powder softens and diffusion causes them to bond at temperatures below the melting point, or full melting. One of the first to market L-PBF was DTM (now part of 3D Systems) in the late 1980s [19], building on previous work at the University of Texas at Austin where L-PBF was first developed [20]. L-PBF has become one of the most common techniques for producing metal parts with AM and is the focus of the work carried out in this thesis.

Other techniques include directed energy deposition (DED) where raw material (powder or wire) is applied only to the locations where it is to be consolidated, stereo lithography (SLA) where a photopolymer resin is exposed to an ultraviolet light source and hardens, binder jetting, FDM, and many others, some of these are shown schematically in Figure 2.2. Each has its own benefits, drawbacks, and target application.

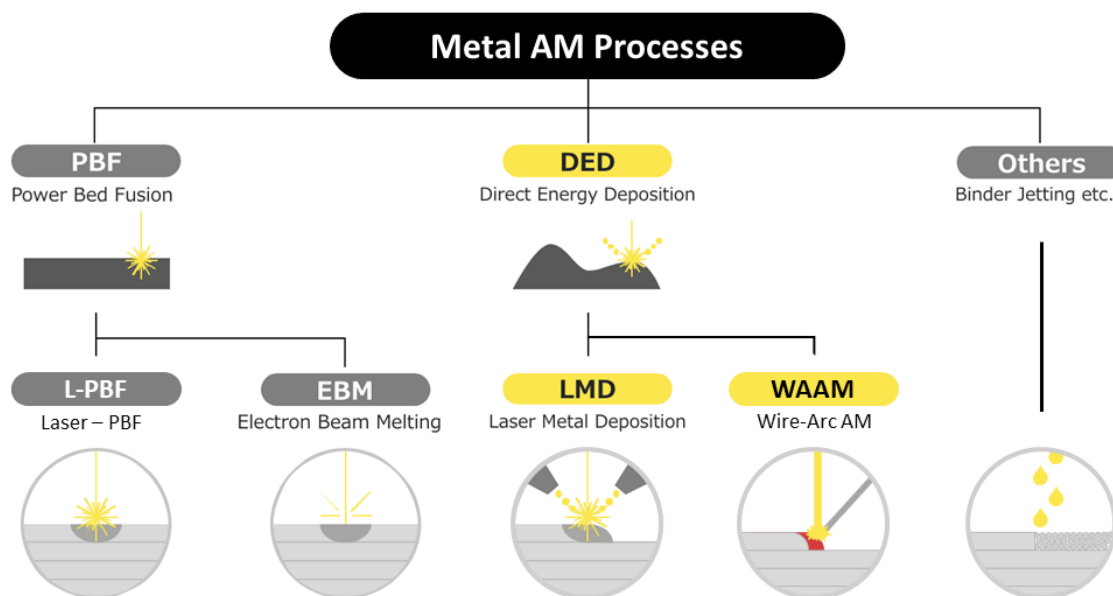


Figure 2.2: Common metal AM processes. Adapted from [21].

For any AM process there are associated parameters that are set, either by the operator or machine manufacturer, that can affect the end part. For the L-PBF process some of the most commonly investigated are layer thickness ( $t$ ), laser power ( $P_{av}$ ), scan speed ( $v$ ), hatch spacing ( $h$ ) – the distance between adjacent laser tracks, and scan strategy – how the laser beam is moved over the surface. In pulsed wave (PW) lasers the scan speed is a function of exposure time ( $t_e$ ), pulse distance ( $P_d$ ), and point delay time ( $t_d$ ), the relationship is given by Equation 2.1. Another important derived parameter is the energy density ( $\psi$ ), either as a volumetric value (as given in Equation 2.2), areal (by omitting the thickness term), or linear (further omitting the hatch spacing). The energy density has

been shown to correlate with many material responses (hardness, roughness, etc.) and can predict if a parameter set is likely to cause phenomena such as keyhole melting.

$$v = \frac{P_d}{t_e + t_d} \text{ [m/s]} \quad \text{Equation 2.1}$$

$$\psi = \frac{P_{av}}{v \cdot h \cdot t} \text{ [J/mm}^3\text{]} \quad \text{Equation 2.2}$$

Other process parameters, such as part position and orientation within the build chamber, chamber temperature, shielding gas type and flow, oxygen content, and many others have also been shown to influence material responses [22].

In industrial settings there is a further consideration, the build rate ( $R_B$ ) which is a measure of how quickly a part will be constructed (shown in Equation 2.3 [23]). This is important as the longer a part takes to build the more it costs (energy use, technician time, shielding gas, etc.) so to minimize the cost, a faster build rate is desirable. However, increasing the scan speed or hatch distance can lead to incomplete melting and excessive porosity in the part, while increasing a layer thickness will result in undesirable artefacts on the surfaces, known as stair-stepping.

$$R_B = v \cdot h \cdot t \text{ [mm}^3\text{/s]} \quad \text{Equation 2.3}$$

Many engineering materials can be processed using AM including polymers, ceramics, and metals, through various AM technologies. Of particular interest here is the use of metals, such as steels (usually stainless steels), and alloys of titanium (e.g., the Ti6Al4V grade), nickel, and aluminium. With respect to aluminium alloys, one of the most common is AlSi10Mg. This alloy has no direct equivalent used in traditional manufacturing, however, the A360 casting alloy [24] and Al 6061 wrought alloy [25] are commonly used for comparisons.

## 2.2.1 Post-processing of AM Parts

### 2.2.1.1 Thermal Stress Relieving and Annealing.

A common post-processing step for AM parts is to anneal the parts after manufacture. This reduces the residual thermal tensile stresses, therefore improving mechanical properties. Some researchers have expanded this to apply treatments equivalent to those available on conventional materials (such as T6 on aluminium). One feature of thermal stress relief is that it does not affect the surface of the part. This may be beneficial when the manufactured dimensions are critical, however in many instances further post-processing is required to reduce surface roughness to acceptable levels. Further discussion on heat treatment of aluminium parts follows in Chapter 6, including different heat treatment options and the material responses.

### 2.2.1.2 Peening

Another prevalent process for modifying the mechanical properties of materials is peening. Peening uses high-energy impacts to plastically deform the surface layer of a part, inducing residual compressive stresses, improving toughness.

Usually, peening is achieved by propelling small beads into the surface (often ceramic), where the impact energy gives the peening effect. Shot peening can result in compressive stresses down to a depth of 0.5 mm [26], requiring no specialist equipment or training to carry out successfully.

An alternative is Laser Shock Peening (LSP), where high-energy laser pulses are used to heat a small volume of material enough to become a plasma. The shockwave produced by the plasma transformation then gives the peening effect. LSP can achieve deeper compressive stresses (> 1 mm [26]) however is uncommon due to the high laser energies required and difficulties in setup and operation.

### 2.2.2 Surface Characteristics

AM surfaces typically have an as-built roughness in the range of 5-15  $\mu\text{m Ra}$ , far greater than is typical from machining operations ( $\text{Ra} < 6 \mu\text{m}$  [27]). Along with this high roughness there are often distinct features present on surfaces, such as partially melted and adhered particles, deep pits, tall peaks, spatter, and so on. These individual features are dispersed across a surface and so are often not reflected in reported roughness values. A more extensive list of flaws can be found in ISO 8785 [28]. A more in-depth discussion on surface roughness, features, and measurement techniques follows in Section 2.3.

### 2.2.3 Surface Roughness Improvements

#### 2.2.3.1 Build Optimisation

The ideal solution to improve substandard surface texture would be to develop a set of build parameters that reduce the roughness to an acceptable level, negating the requirement for remedial work while simultaneously retaining the full geometric freedom afforded by AM. In this regard much progress has been made by the likes of Calignano et al. [29] who found scan speed was especially influential in the as-built top surface roughness of L-PBF Aluminium parts. Simultaneously, Delfs et al. [30] suggested by reorientating parts within the build volume, roughness in critical areas can be reduced by minimizing the “stair-step” effect caused by layer transitions. These results, along with other research, highlights the difficulty in optimizing process parameters with respect to surface roughness.

Even with optimal settings, the intrinsic roughness of the PBF process ( $\approx 5 \mu\text{m} - 30 \mu\text{m Ra}$ ) is significantly higher than that expected by traditional manufacturing methods such as milling ( $1 \mu\text{m} - 6 \mu\text{m Ra}$ ), grinding ( $\approx 1 \mu\text{m Ra}$ ), and even casting ( $\approx 2 \mu\text{m Ra}$  for investment casting) [27]. Compounding this is the influence of surface inclination on roughness, potentially requiring different build parameters for each different surface inclination. A solution not practical, or even possible in many cases. Therefore, supplementary post processing has been investigated to reduce the surface roughness of AM components.

#### 2.2.3.2 Shot / Sand Blasting.

The simplest surface modification technique is blasting. Small grains of a hard material (glass, silica, sand, metallic or ceramic beads etc.) are propelled into a surface by compressed air, where the impact abrades the surface, reducing the roughness. When using some media, a burnishing effect can be realised (plastic deformation of the surface without material removal) which has the added benefit of work-hardening the surface layers, increasing the surface hardness [31]. Examples of some different blasting media are shown in Figure 2.3.

Shot blasting and sand blasting are commonly used due to their low cost and simplicity. All external surfaces can be processed so long as there is line-of-sight between the nozzle and the surface (i.e., not internal structures) [32]. Highly complex geometries can be processed with low material removal and good geometry retention. However, blasting is a highly manual process, with results dependant on operator ability. Blasting is therefore difficult to control at production scales and can lead to inconsistent results. Furthermore, the abrasive action of the media can lead to contamination of the workpiece, especially around complex geometries, requiring extensive cleaning to fully remove.

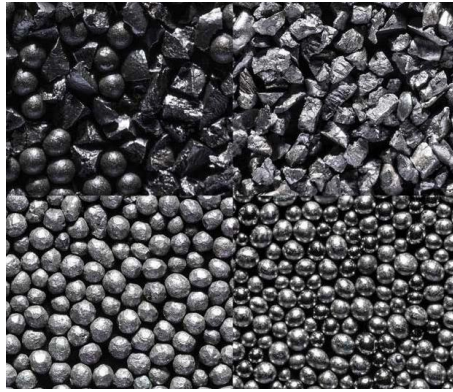


Figure 2.3: Different forms of blasting media. Top) Steel grit, and Bottom) Steel shot. From [33].

### 2.2.3.3 Machining

When the dimensional accuracy of a part or certain features is critical, machining is a go-to manufacturing operation. Machining, such as milling or turning, is a very well understood process, so the alignment, size, and location of features can be realised to very fine tolerances (essential for mating faces etc.). Major drawbacks of machining include the difficulty in fixturing parts [34] (especially with the complex geometries possible with AM) and the requirement to allow tool access to the relevant features.

While machining can achieve roughness values down to  $1 \mu\text{m Ra}$ , usual values are somewhat higher than this. There are many factors that influence the final part roughness, from feed rate and spindle speeds, to cutting tool condition and depth of cut [35]. Therefore, it is common for machining operations to start with “roughing” cuts, that remove a lot of material quickly, and then moving on to “finishing” cuts, where less material is removed, achieving a much lower surface roughness.

### 2.2.3.4 Laser Polishing

Laser polishing (LP) is a technique where a surface is exposed to laser irradiation to melt the surface asperities (peaks on the surface), relocating the molten material through surface tension forces, resulting in a smoothed surface [36], [37]. With additional energy inputs ablation can occur (vaporisation and removal of the material) which can be more effective in smoothing very rough surfaces. By employing different parameters (such as hatch spacing) textures can be imparted to the material, such as on hip implants to improve the tribological performance [38]. LP will be further discussed in Section 2.4.

LP is a developing area of research, with the advantages of low material removal, exceptional geometric freedom, and no waste products that can cause environmental concerns [39]. However, more conventional methods (milling, grinding, blasting etc.) remain popular as they are mature processes, and the required equipment is already common in manufacturing. Laser processing holds some unique benefits compared to machining, despite the typically lower productivity rates ( $1\text{min}/\text{cm}^2$  for LP [36],  $\approx\text{s}/\text{cm}^2$  for milling). For example, laser beams are much narrower than typical rotary tools and can therefore access more challenging areas, and the force-free operation means very high aspect-ratio features can be manufactured without the risk of tool breakage.

## 2.3 Surface Roughness

### 2.3.1 Roughness Components

There are many methods to evaluate the surface condition of a part, either qualitatively or quantitatively. Qualitative methods include the identification of specific features and surface defects, while quantitative methods include roughness measurements, contact angle evaluation, and so on.

All real surfaces are “rough”, they undulate from the desired shape to some degree. For some surfaces this can be microscopic (amplitudes measured in nanometres) while others can be seen visually. It is customary to describe surfaces in terms of *roughness*, *waviness*, and *form*. A description of each, along with potential causes, are presented in Table 2.1, and shown diagrammatically in Figure 2.4.

Table 2.1: Brief description of roughness components, and potential sources of errors. Information from [40].

Component	Description	Sources of error
<b>Roughness</b>	Shortest wavelength generally of interest, and the focus of most surface characterisation work.	Worn cutting teeth or the grit of a grinding wheel
<b>Waviness</b>	Medium wavelength component	Process specific issues, e.g., chatter.
<b>Form</b>	The longest wavelength component. Can be thought of as the desired shape.	Deficiencies in manufacturing equipment, such as worn positional control components.

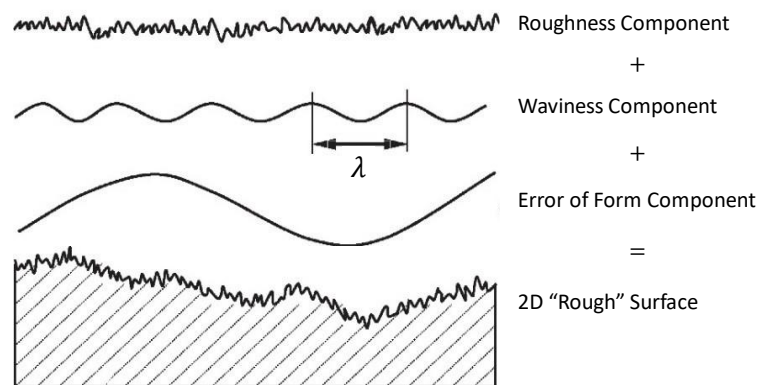


Figure 2.4: Example surface showing how different scale wavelengths combine (Roughness, Waviness, and Form), adapted from [41].

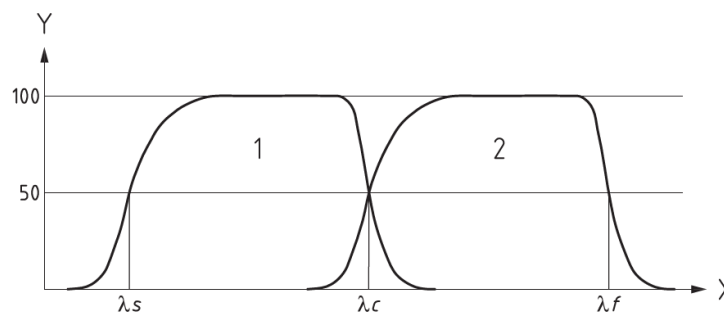
### 2.3.2 Filtration

To separate out these different components a measured surface requires filtering (in terms of the spatial wavelengths). Each filter is described by a cut-off (2D) or nesting index (3D)<sup>2</sup> which is effectively the wavelength at which the filter attenuates (or passes) 50% of the amplitude [42]. An ideal filter would have a step characteristic, where all wavelengths on one side of the cut-off are passed, while all those on the other are removed. In practice, there is a transition period, as demonstrated in Figure 2.5. If a filter is described as “high-pass” it retains (or passes) the higher spatial frequency components (shorter wavelength), while a “low-pass” filter retains lower spatial frequency components [42]. The three filters required for surface roughness measurements are described in Table 2.2. The nomenclature is slightly different depending on if the filter is being applied to 2D or 3D measurements. For 2D the filters are  $\lambda_f$ ,  $\lambda_c$ , and  $\lambda_s$  (decreasing target wavelength) while the corresponding 3D names are F-operator, L-Filter, and S-Filter respectively.

<sup>2</sup> The term nesting index is used throughout this report where the topic concerns both 2D and 3D measurements, or where the dimensionality is not specified.

Table 2.2: Types of filters applied to measured data before computing parameter values.

Filter name	Target wavelength	Description
$\lambda_f$ , F-operator	Form	Removes the effects of form from the measurement. Usually applied as idealised planar, cylindrical, spherical, or polynomial shapes
$\lambda_c$ , L-Filter	Roughness / Waviness	Separates the roughness and waviness components (depending on if applied as a high-pass or low-pass filter respectively).
$\lambda_s$ , S-Filter	Microroughness	Removes the shortest wavelength components, known as microroughness. Microroughness is often due to electrical noise or other interference.



Key

1	Roughness profile	Y	Transmission %
2	Waviness profile	X	Wavelength

Figure 2.5: Filter characteristics around the three cut-offs (from ISO 1134 [42]).

The first filter applied should be a low-pass  $\lambda_s$  filter (S-Filter) to remove microroughness and noise, followed by a high-pass  $\lambda_f$  filter (F-Operator) to remove errors of form [43], this is known as the Primary profile (2D) or S-F surface (3D). By then applying a high-pass  $\lambda_c$  filter (L-Filter) the roughness profile is found (S-L Surface in 3D). Conversely, if a low-pass  $\lambda_c$  filter / L-Filter is applied the waviness profile or L-F surface would result.

In practice, filters act as a moving weighted average of the measurement, and the exact shape of the weighting function can take many forms. The most common uses a gaussian weighting acting over a region equal to the filter cut-off. There are other filters available, with different attributes, however, the gaussian filter remains popular due to the low computation requirements [43].

At the periphery of measurements filters can distort the results significantly. Known as end effects, in essence, these are regions where the weighting function may need to extend beyond the measurement range. The ideal solution to this is to discard a region around the edge of a measurement where the filter cannot act. Alternatively, ISO 16610-28 [44] prescribes a range of methods to artificially extend the effective measured range to enable the filter to act right up to the edge of the measured region. This is important as there are often situations where it is impractical, or not possible, to measure a large enough region of a surface to avoid filter end effects. For example, one key benefit of AM is the geometric freedom possible, but this obviously restricts the size and flatness of areas.

### 2.3.3 Roughness Parameters

As part of the characterisation process there are a range of values that can be calculated from the surface data. Some of the more common roughness values are given in Table 2.3, along with a brief

description and 2D equation. In the equations  $n$  is the number of points evaluated, and  $z_i$  is the height of the point at location  $i$ .

It should be noted, the same equations hold when applied to a surface after any stage of filtering. For 2D results the abbreviation changes to reflect this (e.g., Pq, Wq for root mean squared (RMS) heights on Primary and Waviness profiles respectively).

Table 2.3: Common surface roughness parameters. From ISO 4287 [45] and ISO 25178-2 [46].

Parameters	Abbreviation	Description	2D Equation
<b>Arithmetic mean height</b>	$Ra, Sa$	Arithmetic mean of absolute deviations from the mean line	$Ra = \frac{\sum_{i=1}^n  z_i }{n}$
<b>Root Mean Squared (RMS) height</b>	$Rq, Sq$	RMS value of deviations from the mean line	$Rq = \sqrt{\frac{\sum_{i=1}^n z_i^2}{n}}$
<b>Valley depth</b>	$Rv, Sv$	Maximum depth of the profile below the mean line	
<b>Peak height</b>	$Rp, Sp$	Maximum height of the profile above the mean line	
<b>Total height</b>	$Rz, Sz$	Total height of the profile	$Rz \approx Rp + Rv$
<b>Ten-point height†</b>	$S10z$	Difference between the average height of the five tallest peaks, and average depth of five deepest pits/valleys.	$S10z = S5p + S5v$
<b>Skewness</b>	$Rsk, Ssk$	Measure of the asymmetry in the distribution of peaks and valleys, $Ssk > 0$ generally indicates the existence of some higher peaks away from the mean and while $Ssk < 0$ that of deeper valleys. See Figure 2.6 (a).	$Rsk = \frac{1}{Rq^3} \left( \frac{\sum_{i=1}^n z_i^3}{n} \right)$
<b>Kurtosis</b>	$Rku, Sku$	Describes the shape, specifically the outliers or tails of the distribution of peaks and valleys. Larger values ( $Sku > 3$ ) indicate greater propensity of higher peaks/valleys (outliers), while lower values ( $Sku < 3$ ) indicate otherwise. See Figure 2.6 (b).	$Rku = \frac{1}{Rq^4} \left( \frac{\sum_{i=1}^n z_i^4}{n} \right)$

†Ten-point height is not included in the latest revisions of ISO 4287 and therefore the Equation presented is from ISO 25178-2.

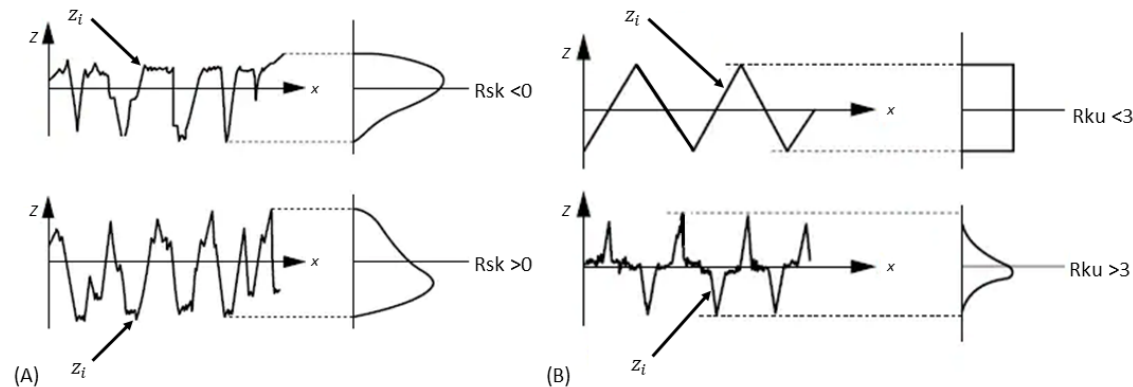


Figure 2.6: Graphical representation of (A) Skewness and (B) Kurtosis terms. Adapted from [47], [48].

### 2.3.4 Measurement Techniques

The simplest method of evaluating surface roughness is to touch the surface and describe how it feels. There are obvious limitations to this method, such as how different operators would interpret “rough” and “smooth”. To overcome this, comparator sets can be used (such as the one shown in Figure 2.7), which give example surfaces to compare against, with associated quantitative values. Notice in the figure that multiple different manufacturing techniques are included, as the shape of the roughness, not just its maximum/minimum/average height will affect the visuotactile experience.

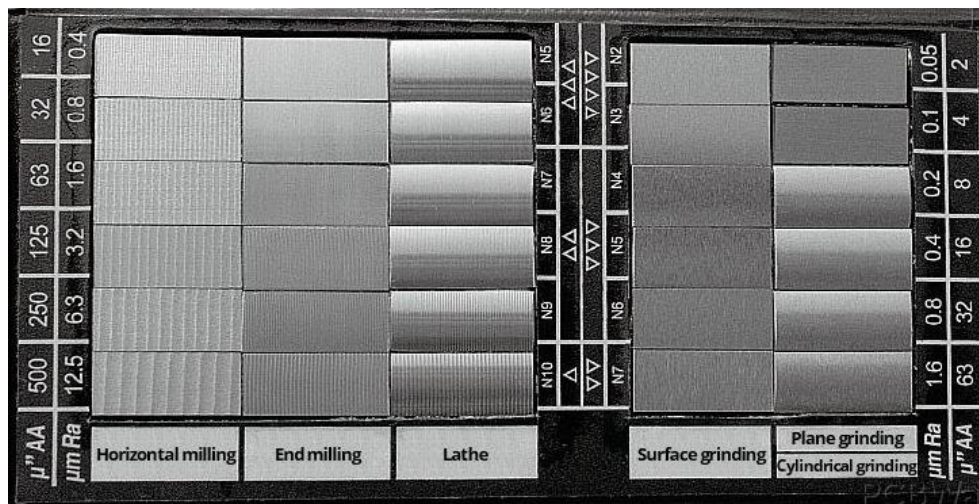


Figure 2.7: Example of a surface roughness comparator set. From [49].

In order to assign numbers to “rough” and “smooth” it is necessary to make a record of the surface shape. Initially, this was simply using levers to amplify the vertical deviations and plot the motions on a strip of graph paper, however, modern machines use electronics to measure and record the surface form with exceptional detail (e.g., quoted vertical resolutions of <10 nm are not uncommon [50], [51]).

Roughness measurements can be evaluated either over a line (profile measurements) or over an area. Areal measurements are generally preferred as they capture much more information about a surface and reduce the likelihood of missing important isolated features common on AM surfaces. However areal methods also suffer from protracted acquisition times making them impractical in many situations. Therefore, profile techniques are still popular due to the speed of acquisition and low technological requirements.

While it is tempting to think of the measurement result as being a record of the “true” surface shape, it depends on how the measurement probe interacts with the surface. For systems that contact the surface, this will be related to tip geometry and contacting forces and is known as the mechanical surface. For non-contact systems (that use light, X-ray radiation, or electrons etc.) the result is a record of the electromagnetic (EM) surface as it relates to how EM radiation interacts with the surface matter.

#### 2.3.4.1 Contact Profilometry

The simplest method of measuring a surface is to physically trace the surface undulations using a stylus that is drawn across a surface to collect 2D profiles of the surface. This is known generally as Contact Profilometry. Vorburger & Raja made an interesting comparison between the operation of stylus profilometers and record players, noting that the performance was surprisingly comparable [52, p. 26].

A series of these 2D profiles, taken at regular intervals perpendicular to the traverse direction, can be assembled into a 3D or areal measurement. There are some inherent drawbacks with contact profilometry, such as the contact forces damaging the surfaces of soft materials (plastics, aluminium etc.) and the limited vertical range available. Due to the sequential nature of taking many 2D profiles to construct a 3D measurement the times taken areas can become prohibitively high depending on the total range and resolution required.

#### 2.3.4.2 Non-Contact Profilometry

The other main class of measurement devices do not contact the surface to be measured and are therefore referred to as non-contact profilometry. Often this is achieved optically, either by image processing (focus variation, fringe projection etc.) that image areas directly, or in a pointwise fashion (e.g., confocal, interferometry) analysing the distance between a sensor and the surface. Overviews of some such technologies are given in the following sub-sections.

Most non-contact techniques are designed to capture areal data as standard, compared to the line-by-line approach of contact systems. This makes them appealing due to the reduced acquisition times compared to contact systems.

##### A. Focus Variation

Focus Variation (FV) profilometry involves imaging a surface with a narrow depth of field at various distances, and algorithmically determining at what distance each pixel is in focus [53]. In practice focus is found by the contrast between a given pixel and those within a certain region around it, low contrast indicates poor focus and vice versa. This is shown schematically in Figure 2.8.

FV is a popular technique for measuring surfaces with high roughness due to the reduced acquisition times compared to other optical measurement techniques. FV is not suitable for surfaces with low roughness as there is a limit to how narrow the focal distance of optics can be, in effect making a finite vertical range of the surface being in focus at once.

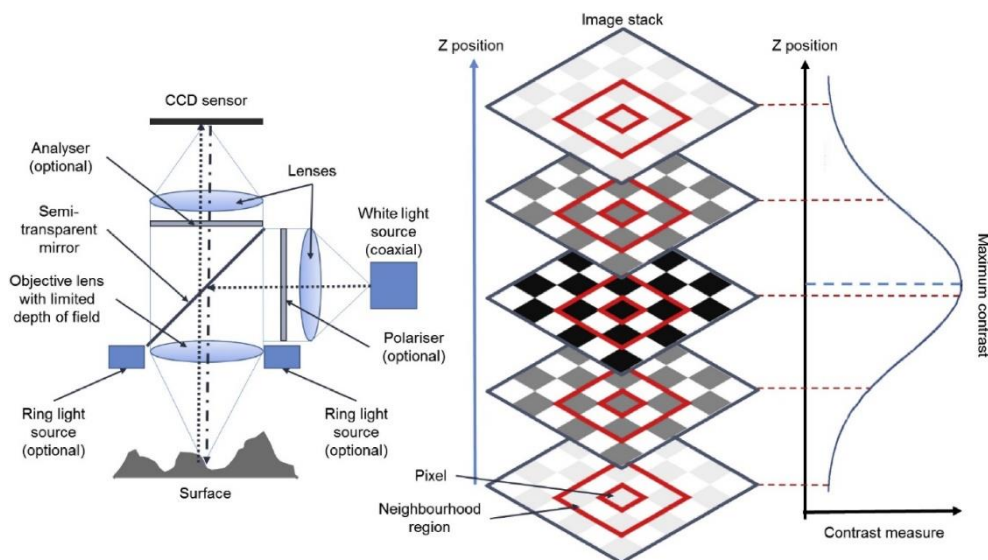


Figure 2.8: Schematic showing how focus variation is used to resolve surface heights. Left - Microscope optical components. Right - Using contrast to determine focus. From [54].

##### B. Confocal

Confocal microscopy operates on a similar principle to a pinhole camera. Light is passed through a small aperture, reflects off the surface, and back through an aperture onto a detector. When the surface point is in focus the detected intensity is greatest, reducing rapidly if the surface is above or

below the focal point. This is demonstrated in Figure 2.9. By modulating the distance between the optical system and the sample the height can be found for any point on the surface. Combined with X-Y motion surface height maps can be generated [55]. Confocal is better suited to smooth surfaces than FV and is less affected by surface reflectivity, at the expense of increased acquisition times.

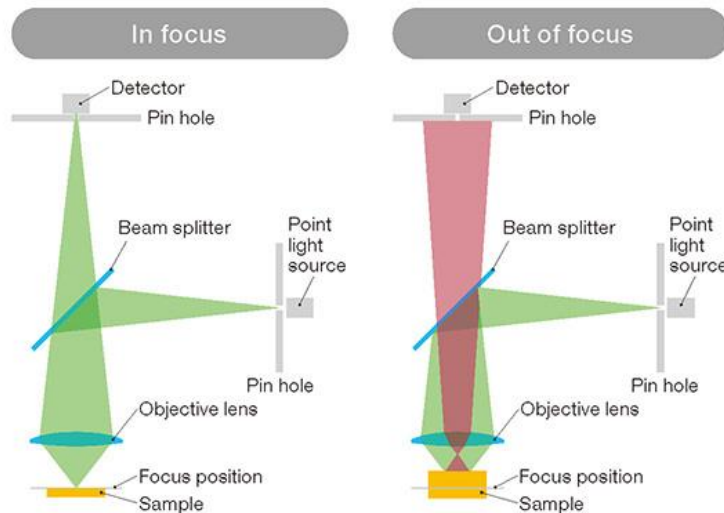


Figure 2.9: Schematic of the working principle behind Confocal Microscopy, from [56].

### C. Interferometry

Interferometry uses laser light to measure the difference in lengths between two beam paths, this is achieved by splitting the incident laser beam along two paths, the reference length and the test length (distance to the sample surface). The beams are recombined and directed to a detector, the phase shift between them is then used to calculate the difference in length, and therefore the height of a point [27]. This is shown schematically in Figure 2.10. Much like with Confocal, surface height maps are generated by combining this with X-Y translations. Interferometry represents an even greater level of precision than Confocal; however, the required equipment tends to be much more expensive due to the accuracy required. One of the most well-known examples of Interferometry is the Laser Interferometer Gravitational-Wave Observatory (LIGO) experiment that can detect differences of less than the width of a proton, over multi-km distances [57].

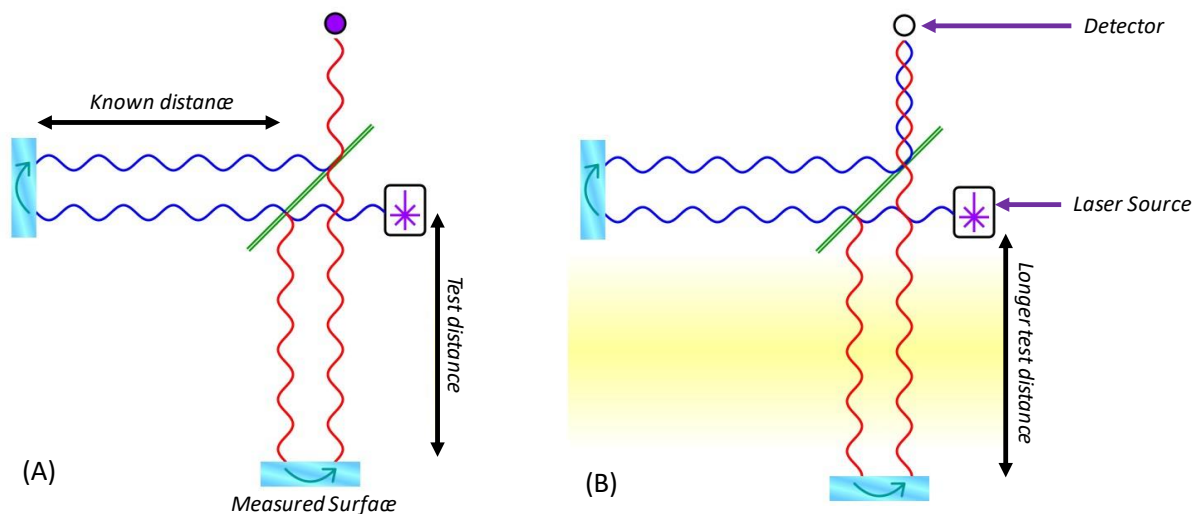


Figure 2.10: Schematic of how interferometry works to detect a change in length. Adapted from [58].

It is clear that each of FV, confocal, and interferometry have their own specific benefits and considerations, and each are best suited to different applications. Based on the reduced acquisition times and improved performance on rough surfaces, FV was selected for use throughout this thesis.

## 2.4 Laser Polishing

### 2.4.1 Mechanism

The basic principle behind LP is to expose a material to laser irradiation, the energy heats the material causing it to melt. Heating is not achieved by thermal energy directly, but rather by photon energy being absorbed by atoms causing electrons to raise orbital levels [59]. This is why many different laser wavelengths ( $\lambda$ ) can be used to heat materials, from far infra-red (IR) from CO<sub>2</sub> lasers ( $\lambda = 10.6 \mu m$ ) [60] to ultraviolet (UV) from Excimer lasers ( $\lambda \leq 350 nm$ ) [61]. The most efficient wavelength to use therefore depends on the absorptivity of the target material.

While molten the material can flow, due to effects such as surface tension and radiation pressure<sup>3</sup>, before solidifying into a new shape. Material from the surface peaks is redistributed into the pits/valleys, resulting in a smoother surface. This is shown schematically in Figure 2.11 (A).

With higher energy inputs the material can vaporise, after which it is removed by an extraction system, known as ablation, shown in Figure 2.11 (B). At sufficient energy levels the vaporised material can become a plasma (charged particles) at which point the laser energy transferred to the surface rapidly decreases due to the inverse bremsstrahlung absorption (IBA) effect (also known as plasma shielding) [62].

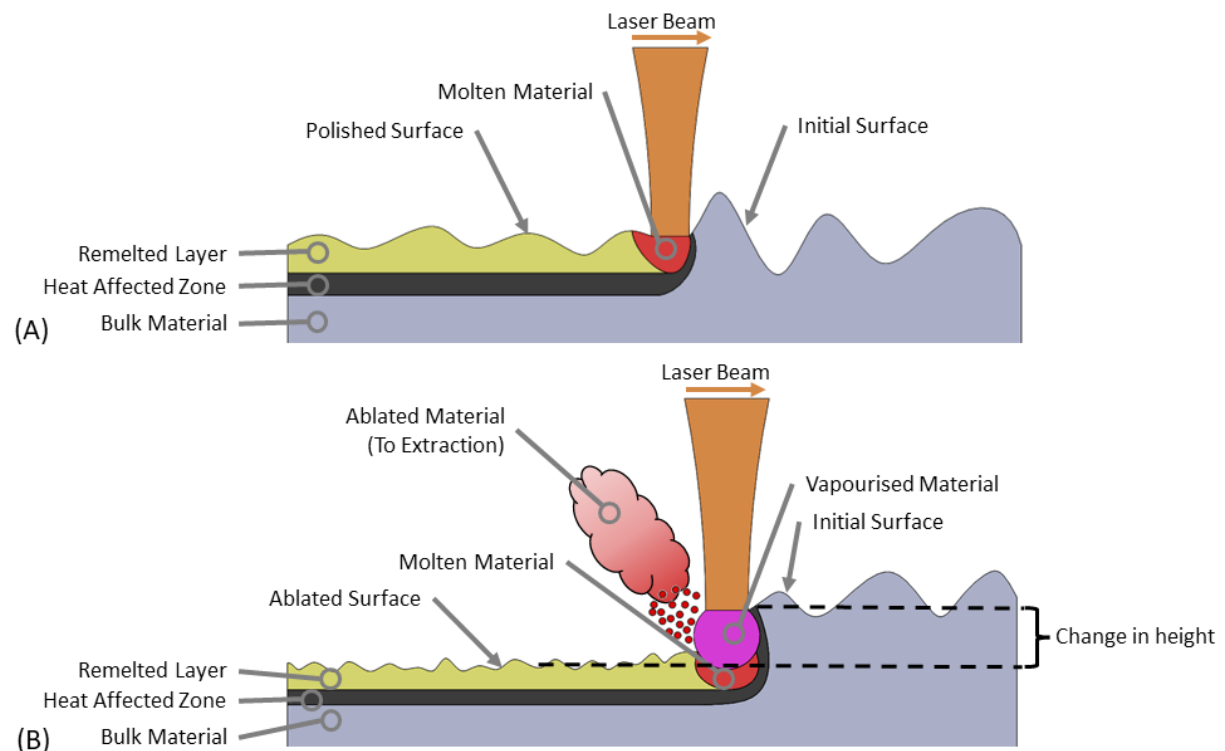


Figure 2.11: Schematic of the laser polishing (A) and laser ablation (B) processes [63].

<sup>3</sup> Radiation Pressure,  $P_{Rad}$ , due to momentum change of incident and reflected photons. For a black body (zero reflectance), and using equipment specification used later in this thesis:

$$P_{Incident} = Intensity [W/m^2] / Speed\ of\ Light [m/s] = (20 W / \pi * 16 \mu m^2) / 3 * 10^8 m/s = 83 Pa.$$

For a perfect reflector the contribution of reflected photons is equal and opposite to the incident pressure ( $P_{Rad} = 2 * P_{Incident}$ ) however for partial reflectors the emitted pressure is multiplied by the reflectivity, i.e.  $P_{Rad} = P_{Incident} * (1 + Reflectivity) = 83 Pa * 1.85 = 153 Pa$  [200].

A comprehensive review put together by Bordatchev et al. [64] noted that results can differ greatly even when LP settings are preserved between studies. While this review primarily focussed on LP of conventionally manufactured materials, this observation highlights the necessity to optimize the process for the specific laser system to be used.

The laser sources used are often in the infra-red range ( $\lambda \approx 1000$  nm), but other frequencies are also used, such as ultra-violet ( $\lambda \approx 250$  nm). Furthermore, lasers can either be continuous wave (CW) or pulsed wave (PW). PW sources can have a relatively low average power rating (e.g., 10s of Watts) but due to this being applied over short durations have equivalent, or higher, peak energies than CW sources. Both PW and CW systems have been used extensively in research for processing a wide range of materials.

There are a number of key equations used to describe the operation of a laser source, for example, the pulse energy ( $E_p$ ) and peak power ( $P_p$ ) of a pulse are calculated by Equation 2.4 and Equation 2.5. Where  $P_{av}$  is the average laser power,  $f$  is the pulse frequency, and  $t_p$  is the pulse duration. The factor of 0.94 in Equation 2.5 relates to the intensity profile in time of the pulse.

$$E_p = P_{av} / f \quad \text{Equation 2.4}$$

$$P_p = 0.94 \cdot E_p / t_p \quad \text{Equation 2.5}$$

Meanwhile, the Rayleigh Range ( $z_R$ ) is at what distance from focus the laser spot has twice the area of the focussed spot ( $A_o$ ) and comes from Equation 2.6. This is then used to calculate the spot diameter ( $d_z$ ) at a given offset ( $z$ ), using Equation 2.7. At focus Equation 2.7 reduces to simply  $d_o$  (the focused spot diameter) as expected.

$$z_R = \frac{\pi \cdot d_o^2}{4 \cdot \lambda} \quad \text{Equation 2.6}$$

$$d_z = d_o \cdot \sqrt{\left(1 + \left[\frac{z}{z_R}\right]^2\right)} \quad \text{Equation 2.7}$$

When using a PW system, such as the Lasertec 40, the distance between successive laser pulses, the pulse distance ( $P_d$ ), is directly related to the scan speed as shown by Equation 2.8.

$$P_d = v / f \quad \text{Equation 2.8}$$

Arguably the most influential parameters are Fluence ( $F$ ), a measure of the laser beam energy density, and overlap factors in x and y ( $O_x$ ,  $O_y$ ) which represent how much successive pulses or scan paths irradiate the same area. Fluence and the overlap factors are calculated using Equation 2.9, Equation 2.10, and Equation 2.11 in turn. When calculating Fluence, it is clear that the spatial energy distribution of a laser beam will impact the energy density, in the case of this work the beam is near-gaussian, and therefore the factor 2 is required.

$$F = 2 \cdot E_p / A_z \quad \text{Equation 2.9}$$

$$O_x = 1 - \frac{P_d}{d_z + (v \cdot t_e)} \quad \text{Equation 2.10}$$

$$O_y = 1 - \frac{h}{d_z} \quad \text{Equation 2.11}$$

By using  $F$ ,  $O_x$ , and  $O_y$ , it is possible to translate settings used on one laser machine to another (being mindful of the findings in [64]), provided  $\lambda$ ,  $f$ , and  $t_e$  are the same on both systems. This is due to these parameters accounting for differences in spot size and average power, and therefore a very powerful tool for evaluating the performance of a given LP strategy.

#### 2.4.2 Laser Polishing of Additively Manufactured Surfaces

LP is an attractive post-processing technique for AM surfaces as it is non-contact, only requiring line-of-sight between the laser optics and the workpiece, therefore retaining much of the geometric freedom possible with AM, while avoiding the environmental concerns associated with electro-chemical processes. Furthermore, as LP is a thermal process (at short-to-long pulse durations<sup>4</sup>), some degree of microstructural modification occurs during processing allowing for material properties to be varied in different locations. Finally, LP can be combined with laser texturing or laser machining for surface functionalization to enhance properties such as corrosion resistance [65] or tribological performance [38]. An example of an LP processed part is shown in Figure 2.12, clearly showing the difference compared to the unprocessed part (left).



Figure 2.12: Example of AM prosthetic knee joint, in the as built condition (Left) and after laser polishing (right). From [66].

Along with these advantages, there are some specific challenges associated with LP adoption. Namely, the highly specialised equipment required requiring large capital expenditure, heightened safety concerns associated with lasers [67], and low productivity rates. Furthermore, there are uncertain material effects of LP, such as microstructure, microhardness, and composition within the heat affected zone (HAZ). Research is being undertaken globally to understand these material effects, improve the productivity (and process control), and find new applications for laser processing generally.

Much like with AM, LP of Aluminium presents specific challenges due to the high reflectivity (low absorptivity,  $\alpha$ ), low melting point ( $T_m$ ), and high thermal conductivity ( $\kappa$ ). These combine to make the processing window relatively narrow, requiring sufficient energy input to overcome the high reflectivity (>85% [68]) and thermal conductivity ( $\kappa$ ,  $\approx 160$  W/mK [69]) in order to melt the material, while the low melting temperature (580°C [69]) can lead to excessive ablation and other thermal damage.

Current research into LP of AM surfaces is trending towards achieving the smoothest residual surface (with the aim of LP replacing conventional post-processing operations), improving the

---

<sup>4</sup> At ultra-short pulse durations (ps, fs) there is not time for thermal effects to occur, and instead the laser-material interaction is limited to the molecular scale [201].

processing rates, or performing LP in situ on AM machines. Both CW sources [70] and PW sources have been used (most often operating in the nanosecond range [71]) with various degrees of success. Furthermore, system architectures can either use multi-axis motion control (e.g. [4]), or a single optical axis with an orthogonal mechanical axis (e.g., optical motion along the length of a cylindrical part with rotation provided by a mechanical axis, in [72]).

A major complication when understanding the reported results is the processes used to evaluate the surface roughness. In some instances, different filter cut-off values are used [73], [74], artificially increasing the apparent effectiveness (demonstrated in [75, p. 348]). Others use a baseline roughness for the part as a whole, taken from an unprocessed region, and compare that to the measured roughness after processing [70]. This may be necessary when the research objective is to use the same equipment for the sample manufacture and subsequent LP (in-situ post processing or hybrid manufacture, such as in [76]). However, due to the highly variable nature of AM surfaces (as will be discussed in Chapter 4) this may not give a true reflection of the process effectiveness. Ideally the same area would be measured before and after processing to ensure an accurate effectiveness is being reported. Measuring matching regions also allows qualitative evaluation of the process by observing if any distinct features persist after polishing (e.g., specific tall peaks, adhered particles etc.) that a numeric roughness measure cannot account for. Chapter 4 discusses a method for measuring AM surfaces in a repeatable manner. The current state of LP of AM Aluminium will be further discussed in Chapter 5, with regard to the LP procedure developed as part of this project.

Overall, laser processing has the potential to be a key enabler for the continued industrialisation of AM. Lasers offer key benefits compared to conventional, subtractive techniques thanks to being non-contact and force free. This means that deep or high aspect-ratio features that are traditionally challenging (heightened risk of tool or part breakage) can be processed by lasers with much lower risks. Furthermore, being able to control the surface chemistry, hardness, or microstructure may negate the need for further surface finishing techniques (e.g., anodizing). This work will focus on improving the effectiveness of LP, while also understanding the material response to LP.

### 2.4.3 Simulations

With the transition to “Industry 4.0” there is an ever-greater emphasis, and reliance, on computational simulations. One of the main obstacles for research, especially around AM, is the cost of materials and time taken to undertake experiments, making simulations the preferred option in many cases.

LP simulation has followed a similar trajectory to simulating AM processes, that is to say, efforts tend to focus on micro-scale simulations, utilising Computational Fluid Dynamics (CFD) to model the melt-pool dynamics and residual textures [77], [78]. An example of this sort of prediction is provided in Figure 2.13. While micro-scale predictions are useful in explaining why certain laser types and operating modes have different effects on the surface topology, there has been a relative lack of interest in macro-scale simulations looking at how part bulk temperatures evolve during processing and how this in turn feeds back into the polishing effectiveness.

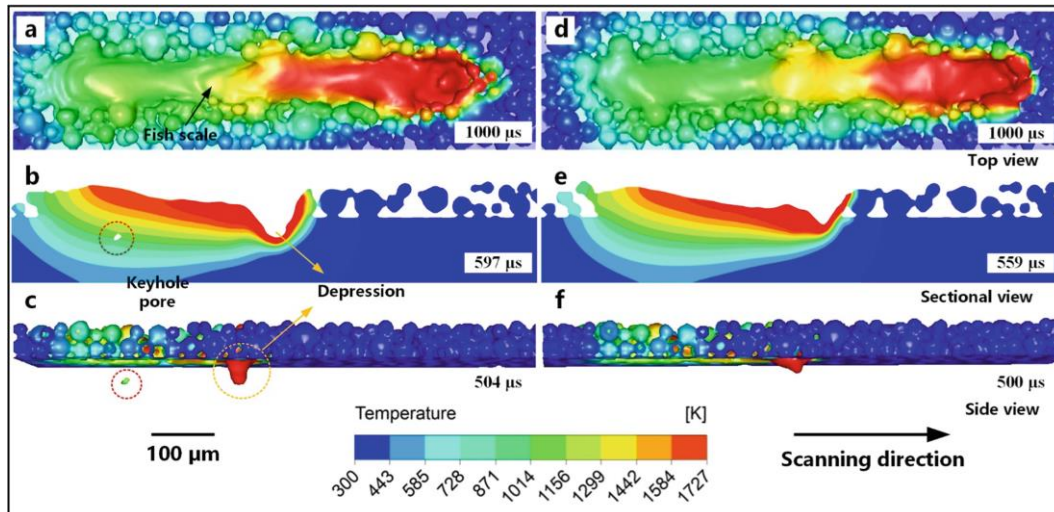


Figure 2.13: Example of CFD prediction of melt-pool dynamics and residual surface texture resulting from (a-c) pulsed wave, or (d-f) continuous wave laser sources. From [78].

## 2.5 Mechanical Testing of Additively Manufactured Components

In order for AM parts to be widely accepted in industrial applications designers need to be certain of the mechanical properties of the components to specify them appropriately. Traditional manufacturing methods have centuries of data to rely on to determine the various properties, such as Young's Modulus ( $E$ ), tensile strength, strain limits, fatigue life predictions, and so on. AM does not have this luxury. With the high cost of materials, machines, and manufacturing time, there are significant challenges to amassing similar quantities of data at the required quality.

Furthermore, the relative instability of the AM process, in terms of part properties when compared to conventionally manufactured materials, is often referenced as a reason for the slow industrialization of the process. In aerospace, there are strict requirements to prove the capabilities of a design before it is allowed to fly. For conventionally manufactured materials the expected mechanical properties do not vary much, to the extent that usually only a single value is presented in material datasheets. This gives great confidence in a designed part having the same properties irrespective of manufacturing specifics (time and date, exact machine/location, speeds/feeds etc.). This is not true for AM, for a part to be flight-approved in a safety-critical location, not just the design needs to be qualified, but all aspects of the manufacturing process. The build parameters are fixed, along with the design and any post-processing applied, unless the part is to be re-qualified [79]. The problem is even more acute in healthcare, where AM is enjoying relatively widespread adoption, as the part traceability is so stringent that for modern multi-laser systems, the exact laser module used to manufacture the part must be recorded and repeatable<sup>5</sup>. Adding to the challenge of amassing a comprehensive database of material properties for use in design.

What follows is an overview of some common mechanical testing options.

### 2.5.1 Hardness

There are many different techniques for measuring the hardness of materials, but all operate on similar principles. A load ( $P$ ) is applied to the surface through an accurately shaped indenter, then the hardness is calculated proportional to the contact area (indent width), or depth of penetration. Examples of common indenter geometries are shown in Figure 2.14.

<sup>5</sup> Private communication as part of an AM machine manufacturer factory tour.

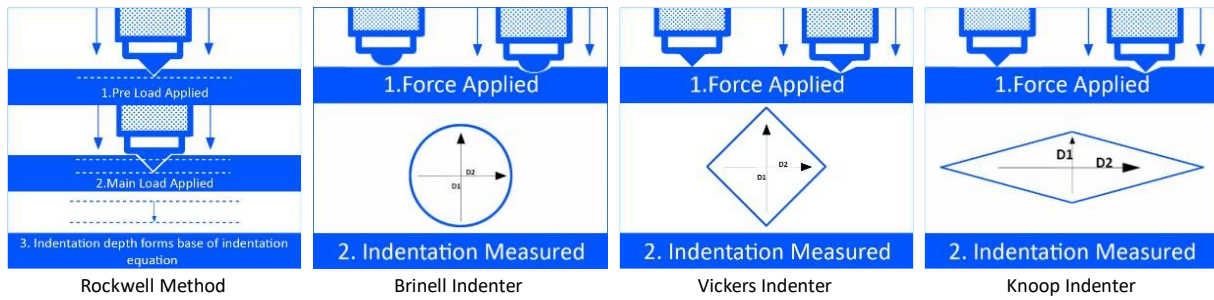


Figure 2.14: Common Hardness test methods. Adapted from [80].

One of the most common methods is the Vickers hardness scale which utilises a pyramidal indenter with a face angle of  $136^\circ$ . The two diagonals ( $D_1$ ,  $D_2$ ) of the square indent are measured and averaged ( $D$ , Equation 2.12) from which the contact area ( $A$ ) can be found (Equation 2.13). In practice, the hardness ( $Hv$ ) is calculated directly using Equation 2.14.

$$D = \frac{D_1 + D_2}{2} \quad \text{Equation 2.12}$$

$$A = \frac{D^2}{2 * \sin(136/2)} \quad \text{Equation 2.13}$$

$$Hv = P/A \cong \frac{P}{0.5393 \cdot D^2} \quad \text{Equation 2.14}$$

Hardness is a useful metric as it allows indirect insight into the microstructure of a material. For example, in steels higher hardness is associated with the formation of martensite grain structures. And for Aluminium, it has been reported, that the micro-hardness at the surface is increased after laser polishing, corresponding to regions of differing microstructure to the unpolished areas [71].

The reason why hardness can imply the size of grains present is that smaller grains inhibit dislocation movement and therefore reduce the ductility of metals, while in larger grains dislocations can travel uninterrupted for relatively long distances reducing the hardness.

### 2.5.2 Quasi-Static (Tension, Bending)

Quasi-static mechanical testing – such as tension, bending, and compression – forms the backbone of many engineering analyses. The term quasi-static refers to testing at a sufficiently slow strain rate that it can be assumed dynamic effects are not present, in contrast to impact toughness where dynamic effects dominate. Quasi-static testing permits the determination of fundamental properties such as ultimate and yield strength and elongations and Young's Modulus by interrogation of the stress-strain (force-displacement) curves generated. An example is shown in Figure 2.15.

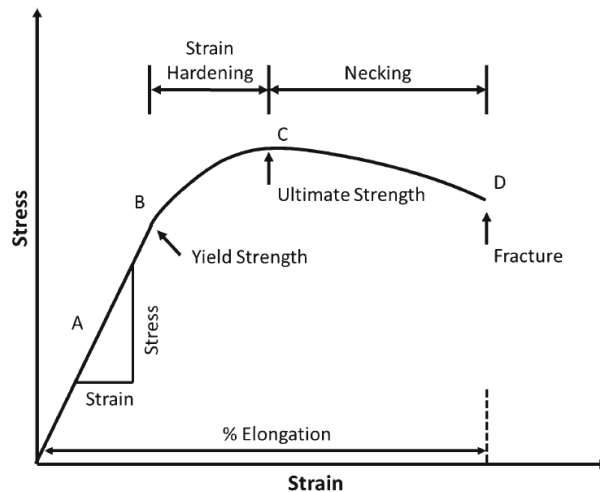


Figure 2.15: Typical stress-strain curve with main features identified. From [81].

Tensile testing is one of the simplest quasi-static tests to perform and interpret. A test coupon is subjected to a steadily increasing displacement at one end and the required load is recorded. Strain rates used depend on the ductility of a sample but generally are in the region of a few millimetres per second ( $mm/s$ ). Tensile testing is widely standardized for both test method and coupon design, such as in ASTM E8 and ISO 6892-1, to facilitate easy and direct comparisons of results between tests and laboratories. Tensile testing will be further discussed in Chapter 6.

Traditionally testing is conducted on standardised sample geometries, but this assumes isotropic / quasi-isotropic mechanical properties, and the coupon size will not affect the results. For AM it is well known that the materials are not isotropic and therefore the number of test specimen required to characterise the material would be prohibitive. Combined with this, AM affords unparalleled geometric freedom, facilitating new design methodologies (such as topology optimisation or generative design). All of this has led to a movement within AM to move away from coupon testing (both static and fatigue), and rather focus on testing of representative geometries<sup>6</sup>, reducing the testing burden and properly accounting for the manufactured geometries and conditions.

### 2.5.3 Fatigue

In most practical applications parts are limited not by their ultimate failure strengths, but by their performance under fatigue loading. Fatigue was first identified in the 19<sup>th</sup> century, often attributed to Wilhelm Albert and their observations of failures of mine conveyor chains, and subsequent part testing. The first documented use of the term fatigue was by F. Braithwaite (who in turn attributed it to a Mr Field) in 1854, describing numerous incidents where fatigue was involved [82]. In the subsequent 150 years engineers have been constantly battling to better understand fatigue, while pushing the limits of designs to create ever more material efficient designs. Every so often the limits are pushed too far, often with disastrous consequences.

The aerospace industry is especially conscious of the effects of fatigue as structural failures of aircraft typically result in total aircraft loss<sup>7</sup>. One infamous example of structural fatigue in aircraft was the De Havilland DH106 Comet of the 1950s. The first jet-powered passenger airliner flew faster

<sup>6</sup> Discussed during a panel session between L. Pambaguain; F. Montredon; D. Wells; and A. Andreaco. "Additive Verification and Qualification" at 1<sup>st</sup> International Conference on Advanced Manufacturing. 10/03/2022. <https://atpi.eventsair.com/icam22/>

<sup>7</sup> The USA's National Transportation Safety Board [202] and the UK's Air Accidents Investigation Branch [203] each have over 100 investigations/reports available that reference fatigue of aircraft components.

and higher than anything that came before. The increased altitudes required the cabin to be pressurised to allow passengers to travel in comfort and not suffer from oxygen deprivation. Despite extensive pressure testing during development, there were two crashes after only three years of operational service. The root cause was determined to be stress concentrations around various square apertures in the aircraft hull, raising the local stresses far beyond design calculations, leading to fatigue cracking and subsequent failure of the airframe [83]. Since then, much greater attention has been paid to local stresses and the adoption of rounded passenger windows in subsequent jet airliners.

The lessons learned, in part by the Comet, are still relevant today, with high-value industries – such as aerospace – investigating the role of AM with respect to lightweighting of components to reduce costs and improve efficiency. However, as the Australian cycling team found in the 2020 Tokyo Olympics, properly defined loads and appropriate testing are still essential [84].



*Figure 2.16: Australian Olympic cycling team AM Titanium component failure, attributed in part to improperly defined loading conditions during design, accelerating the onset of fatigue cracking. From [85].*

Fatigue testing can come in many forms depending on how the load is applied; tension, compression, bending, torsion, pressurisation, temperature, and combinations thereof. Furthermore, within this, there are considerations as to how the applied stress will change over time. It is customary to report either the maximum or mean stress, along with the “Stress Ratio” ( $R_\sigma$ ) which is simply the maximum stress divided by the minimum stress. Common values of  $R_\sigma$  are 0, when the stress varies between 0 and some other value, -1 where the maximum and minimum stress values are the same magnitude (and the average stress is 0).

A final consideration is what to record and how to interpret the results. As a minimum, the test conditions will be recorded (and assumed constant), along with the number of cycles to a pre-defined stopping condition (failure, cycle count, specified reduction in stiffness). Less common is recording how the load/deformation varies within a cycle (due to the massive amounts of data this would entail for long tests), that may give insight into how the performance changes over time and indicate early warning signs.

It is well known that fatigue performance not only relates to a material's mechanical properties, but also the overall form and surface condition. While AM allows more free-form geometries to be realised - enabling preferential load paths, the aforementioned rough surfaces and differing bulk properties compared to wrought require evaluation of the fatigue performance of AM materials and components. There has therefore been a lot of research into both improving the mechanical properties and surface condition of AM parts through manufacturing parameters, improvements to surface condition (and to a lesser extent the mechanical properties), and post-processing operations to address both material properties and the surface condition.

## 2.6 Technical Literature Review

### 2.6.1 Surface Metrology

The theory behind surface roughness measurement and quantification was discussed in Chapter 2.3, here the specific considerations required for AM surfaces are introduced, along with a review of the current research and best practices.

#### 2.6.1.1 Challenges of Measuring AM Surfaces

While there has been a proliferation of work regarding the surface roughness measurement of AM parts [86], [87], there are still challenges to overcome. Firstly, AM surfaces are unlike those produced by any other manufacturing technique; high roughness values, contamination (e.g., soot), tall/high aspect-ratio features, and a high degree of variability. Examples can be seen in Figure 2.17. This means a suitable measurement device needs to have a large measurement range in all three directions, while also having a fine resolution to ensure even relatively small features, such as adhered particles, are properly captured.

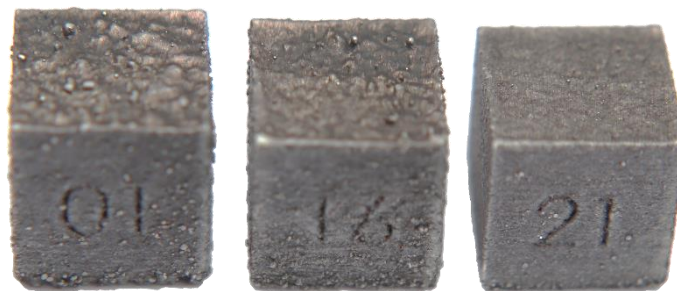


Figure 2.17: Typical surfaces from AM Aluminium.

A secondary consideration, and a by-product of the high variability, is how to appropriately assess the surfaces. It is common to quantify a surface using standardized metrics (such as those listed in Table 2.2) however these cannot describe distinct features.

Even when evaluating the surface as a whole, using standardized metrics, the options are practically endless. However, the array of roughness parameters available can obfuscate any correlations if too many are evaluated, while not selecting enough (or selecting incorrectly) limits the ability to identify correlations at all. It has been shown previously that skewness can distinguish between surfaces built horizontally and vertically on L-PBF polyamide-12 samples. It was found that side surfaces typically had a negative skew (most of the surface “above” mean line, valleys dominate), possibly due to adhered particles, whereas top surfaces typically exhibited a positive skew [87]. When selecting roughness parameters, it is also important to consider the function of a surface, for example, the material ratio (ratio of the bearing length to the evaluation length) is a much better metric than the average height of a surface in tribological applications [40]. It has been suggested by Leach et al., that while standardized parameters are useful due to their prevalence, there may be better options for assessing AM surfaces [2].

Finally, filtering to isolate different surface components (waviness, roughness etc.) is standard practice, and the methods are well established for conventional manufacturing methods. Researchers have attempted to apply the same guidelines to AM surfaces [88], however, the required measurement ranges can become prohibitive (measurement range 5 times than the filter length). The effect of selecting one filter rather than another can be stark, either inflating or suppressing the calculated roughness values by many times, an example of this is shown in Figure 2.18. As Lou et al. succinctly put it, the challenge of how to filter AM surface measurements is further complicated as “it is not clear what roughness and waviness mean to AM processes” [89]. In conventional machining operations (as discussed in Chapter 2.3) waviness can be attributed to chatter while roughness is typically related to the cutting tool geometry and condition, clearly two mechanisms that do not present themselves in most AM processes. Finally, as has been repeatedly noted by others, this highlights the need to clearly report full information about the measurement setup, process, and post processing, along with the roughness values chosen [75], [90].

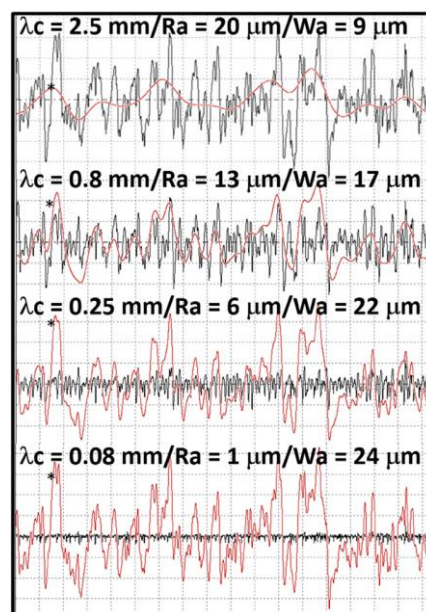


Figure 2.18: The same surface roughness measurement with different filters applied ( $\lambda_c = 2.5$  mm, 0.8 mm, 0.25 mm, and 0.08 mm) and the resulting roughness (black lines) and waviness (red lines, marked with \*) profiles obtained [evaluation length = 17.5 mm, tip radius = 5  $\mu\text{m}$ ]. From [75, p. 348].

### 2.6.1.2 Current Measurement Trends

It was reported by Diaz in 2019 that there were no standards or formal guidelines for how to measure the surface roughness of AM parts [75], and while there has been much activity in the area, there is still limited information available. Some, like Triantaphyllou et al., have undertaken comparative studies to determine an appropriate process for a given material. In that case, they determined a 2.5 mm L-Filter, rather than the ISO 4288 prescribed 8 mm, could effectively capture the main surface characteristics of PBF (both laser and electron-beam) Titanium samples at various build angles [88].

Beyond that, there has been little progress towards identifying, or implementing, good practice for the measurement and reporting of AM surface roughness. There has been greater interest in how to describe these surfaces using alternative techniques. For example, Newton et al. [91] have developed techniques to identify, isolate, and categorize surface features (e.g., adhered particles). They go on to propose applying traditional surface roughness metrics to the surface with these identified features removed [86]. A significant drawback of these alternative methods is the trouble

in relating them to surfaces manufactured by alternative methods, and therefore it is likely that conventional surface roughness parameters will endure.

In general, there are three main ways measurement details are reported. The gold standard are highly detailed accounts, including measurement device capabilities, objective specifications (if appropriate), and all post processing steps applied [87], [88], [89], [92], [93], [94]. Then at the other extreme, there are publications that give minimal detail, e.g., only final roughness values and device type [41], [95], [96], [97], [98], [99]. Finally, there are those that fall somewhere in between, giving adequate information about either the measurement setup, or post-processing, but typically not both [100], [101].

However, there is not a standard “recipe” for how to collect, process, and present surface data from AM samples. This chapter discusses the evaluation of one such recipe, comparing results from three readily available systems with a focus on the effects with respect to part-scale roughness measurements. Following this, a more in-depth study was conducted using one of the systems to evaluate the effect of some measurement setup and data processing options (localisation, stitching) in terms of variance in reported height for each pixel.

## 2.6.2 Laser Polishing

### 2.6.2.1 AM Surfaces

The typical characteristics of AM surfaces are widely reported, exhibiting features such as high roughness, adhered particles, soot contamination, deep pits, and high peaks. A 3D surface measurement is shown in Figure 2.19 of a typical AM aluminium surface (vertical scale amplified for clarity). These are detrimental to the aesthetics of parts but can also influence the functionality. Furthermore, mounting surfaces need to be well defined to ensure components are orientated correctly, often achieved through remedial work, and the high roughness can have adverse impacts on the tribological, fatigue, and corrosion characteristics of a material [102], [103]. In addition to the roughness, AM Aluminium surfaces tend to have a dull appearance due to soot build up from the manufacturing process, which LP can effectively clean from the surface further improving aesthetics [8].

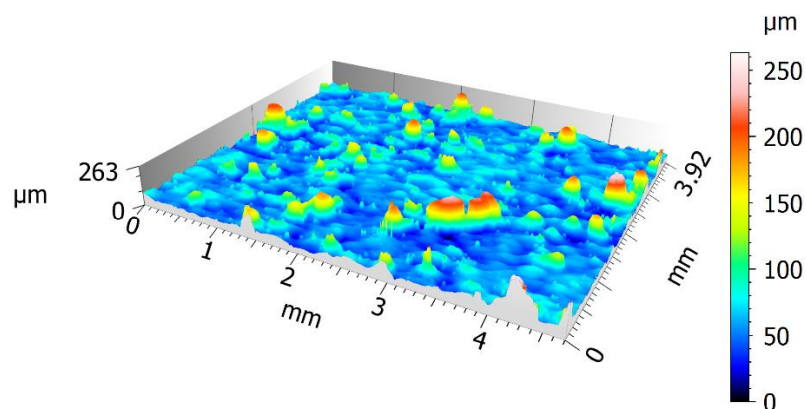


Figure 2.19: Representative surface roughness measurement of an AM aluminium part.

### 2.6.2.2 Laser Polishing of AM Metal Parts.

The laser system used in this work was a *DMG Sauer Lasertec 40* laser milling centre, equipped with a *SPI Lasers G3.1* nanosecond source, details of which are provided in Section 3.2. There has been much interest in LP using CW lasers, and to a lesser extent PW lasers. Hofele et al. found that CW LP had a significantly increased processing rate compared to  $\mu$ s-PW LP (about  $5 \times$  greater) while also having a lower achievable roughness ( $R_a$ ) with a single pass. However, the resultant roughness was

the same when four polishing passes were used for both PW and CW operation [73]. It should be noted that the processing parameters were subtly different between the CW and PW operating modes, albeit both having been optimized separately. Other studies regarding CW LP have found CO<sub>2</sub> sources can achieve roughness of 7.9  $\mu\text{m Sa}$  [104], and single-pass reductions in excess of 70% [105]. Meanwhile, fibre lasers have given resultant roughness below 2.5  $\mu\text{m Ra}$  [106]. When it comes to PW LP, there is little consensus about which pulse frequency range is optimal, with many authors investigating long-pulse LP [73], [107], and few reporting results for ultra-short pulse machining [108], [109].

Nanosecond laser sources are a popular choice for laser machining due to the short pulse durations reducing the damage caused to surrounding material by overheating [110] while being more cost effective than ultra-short pulse duration sources (femtosecond, picosecond). Therefore, developing an effective and repeatable LP strategy using a nanosecond source would enable combined smoothing and texturing processes.

Nüsser et al. [111] investigated different pulse durations and intensity profiles for LP of tool steel, finding that while circular beams gave lower achievable roughness than square beams, and a top-hat intensity profile preferable to a gaussian beam. In general they also found ns pulse durations gave better performance than  $\mu\text{s}$ . Zhihao et al. [112] also used a ns laser source (12 ns – 500 ns) to polish AM Inconel 718 samples, achieving Ra reductions from 7.5  $\mu\text{m}$  to under 0.1  $\mu\text{m}$ , however it is unclear what pulse durations were used, or how the roughness was measured. Reductions of up to 80% have been achieved on AM Ti64 using 270 ns pulse durations [113]. Furthermore, Xu et al. used a ns excimer laser (UV) to polish rolled 6013 Aluminium, finding significant improvements to the fatigue and corrosion resistance of the material [114].

There are two key pieces of previous research that informed the development of the presented strategy. The first by Bhaduri et al. found limiting heat loss from the specimen resulted in greater smoothing of AM Aluminium surfaces. They achieved this by using a ceramic baseplate to insulate the sample from the machine X-Y stage and therefore minimise conductive losses [71]. The mechanism behind this effect is thought to be the increased heat retention in the part reducing the thermal gradients, and therefore cooling rate, giving more time for the melt to flow under the effect of gravity and surface tension. Near-surface temperatures were found to be approximately 30% higher compared to processing without the baseplate. Based on their report, throughout the present work a ceramic baseplate was also utilised in conjunction with a Polytetrafluoroethylene (PTFE) positioning jig.

The second piece of formative research was by Petkov et al. who found for processing AM Titanium parts a three-stage process was desirable. They proposed a strategy starting with a general ablation step, followed by targeted ablation of remaining asperities, and finally a remelting step. While Petkov et al. were unable to determine optimal parameters for the final step, the initial two ablation steps resulted in smoothing from over 6  $\mu\text{m}$  to 1.8  $\mu\text{m Sa}$  [115].

Previous unpublished work at Cardiff University found a 15 ns exposure time at 290 kHz was effective at removing many of the surface asperities. This is likely due to the short pulse durations, and low duty-cycle, minimizing heat transfer to surrounding material [116]. Furthermore, there was no evidence of adhered particles remaining after processing. It did however leave micro-textures on the surface (many regular depressions) and a dull appearance (see Figure 5.4). This strategy was equally effective on both top and side surfaces.

Finally, Bhaduri et al. also found that for the AlSi10Mg aluminium alloy the greatest degree of smoothing was achieved with a fluence of 12 J/cm<sup>2</sup>, with spot overlaps in both X and Y directions of 97%. They achieved this using pulse durations of 220 ns at 100 kHz [71]. It was possible to replicate these laser parameters on the *Lasertec 40* milling centre, and so was used as a baseline for the smoothing steps as presented.

### 2.6.3 Thermal Post-Processing

Traditional thermal post-processing techniques generally involve heating a material to a specific temperature for a certain length of time before cooling it back down again. Depending on the time, temperature, and cooling method the resultant mechanical properties can be tailored for a given application. For Aluminium there are five broad temper designations; O – annealed, W – solution heat treated, T – stable tempers (except O), F – untreated, and H – strain hardened. These are followed by a series of numbers that give more information about the process or resulting properties, for example there are ten main T-codes, T1 to T10, describing the order of operations required [117], [118]. Each different temper has its uses, and some of the more common tempers include O, T4, and T6.

The following sub-sections describe the main HT operations, how they are achieved, and the effects on material properties.

#### 2.6.3.1 Stress Relief

SR has been widely applied to AM parts to reduce the residual tensile stresses left by the high thermal gradients during manufacture. Post-manufacture SR is so ubiquitous that many AM material datasheets specify properties in the as built and stress relieved conditions, for example from Renishaw plc [69] and EOS GmbH [119].

SR involves heating a component to a set temperature, maintaining that temperature for a period of time, and finally allowing it to cool back to ambient temperatures. In aluminium SR is generally achieved between 45% and 60% of the melting temperature [120]. While at the elevated temperature the crystal structure within the material relaxes allowing residual stresses to dissipate. SR is similar to annealing in conventionally manufactured materials.

#### 2.6.3.2 Solution Heat Treatment

Solution Heat Treatment (SHT) is a higher temperature process that causes changes to the crystal/grain structure of a material, and therefore modify the mechanical properties. The part is heated to just below its solidus temperature and held for a period of time (known as heat soak), this allows the soluble alloying elements to fully dissolve and the crystal structure to reform. Ideally this mixture will be a nearly homogeneous solid solution of the various elements present (hence the process name) [117].

Heating is followed by very rapid cooling (quenching) to retain the crystal structure and keep the alloying elements in solution. In most alloys the solubility of alloying elements increases with temperature, and thus an aim of quenching is to maintain those elements in solution in greater proportions than normally possible, known as a supersaturated solution [117].

#### 2.6.3.3 Precipitation Hardening / Artificial Aging

Once in a supersaturated state following SHT, alloying elements can come out of solution over time to form precipitates, called precipitation hardening. Precipitation hardening inhibits dislocation movement through high internal strains present around precipitates that have the same crystal structure as the surrounding alloy. In the case of Aluminium-magnesium-silicon alloys, Mg<sub>2</sub>Si precipitates out of the solid solution and leads to a strengthening effect [117]. The degree of

hardening is dependent on the size and distribution of the precipitates and is therefore sensitive to the time and temperature of the process [121].

Precipitation hardening can happen at room temperature for some alloys (known as natural aging) and for some alloys, stable tempers can be achieved after a matter of days (resulting in T3 and T4 tempers). Achieving precipitation hardening through reheating is known as Artificial Aging (AA) and is used to prevent or limit changes to the mechanical properties over time. The greatest strengthening is achieved in the “Peak Hardened” condition (known as a T6 temper). Under- and over-aging are both a function of temperature and time, and lead to reduced strengths, but may improve other properties. Over-aging Aluminium gives the T7 temper, often desirable due to increased dimensional stability and fatigue resistance compared with other tempers, at the expense of ultimate strengths [117].

Due to the maximum strength generated, the T6 temper is widely used, and many authors have developed processes to achieve the effect for AM parts. The consensus for process times and temperatures is given in Table 2.4, the variation in times and temperatures are also given in the table. Not all authors include a stress relief step prior to the T6 temper.

Table 2.4: Times and temperatures used to achieve a T6 temper in AM AlSi10Mg.

	Temperature	Time	Cooling Method	Temperature range	Time range
<b>Stress Relief</b>	300 °C	2 hours	Air Cool	≥ 230 °C [122]	≤6 hr [123]
<b>Solution Heat Treatment</b>	520 °C	6 hours	Water Quench	450 °C [124] – 560 °C [125]	≥0.5 hr [119], [126]
<b>Artificial Aging</b>	160 °C	6 hours	Air Cool	140 °C [126] – 200 °C [127]	1 hr [127] – 24 hr [128]

## 2.6.4 Fatigue

### 2.6.4.1 Test Methods

The usual methods for fatigue testing involve applying cyclic stresses of a given amplitude, with or without an additional mean load, for a period of time or sample failure. In the LCF regime failure is the usual stopping criterion due to the relatively low cycle counts required. When investigating HCF performance, however, cycle counts of  $10^7$  are not uncommon making exhaustive testing impractical. Therefore, it is customary to define a stopping point prior to failure. When this condition is met the sample is removed from the test and referred to as a run-out. On S-N plots (applied stress against number of cycles) runouts are indicated by arrows to show the cycle count to failure is unknown.

There have been many attempts to devise a test method to expedite the determination of fatigue endurance limits, however these have often been found to be inaccurate or impractical [129]. To this end, in 1999 Maxwell and Nicholas published research into one such method [129] that has become widely accepted and validated, now known as step-load testing. In their test plan, a target endurance limit is set ( $N_{Life}$ ), and the sample is fatigue loaded first at a stress below the assumed endurance limit for  $N_{Life}$  cycles. If the sample survives the applied stress is increased by an amount,  $\Delta\sigma$  (suggested to be no more than 7% the initial stress by the authors) and subjected to another series of  $N_{Life}$  cycles. This repeats until sample failure. The fatigue endurance limit, the maximum stress sustained for  $N_{Life}$  cycles can then be estimated by linear interpolation (Equation 2.15) [129], [130].

$$\sigma_e = \sigma_0 + \Delta\sigma \frac{N_{Fail}}{N_{Life}} \quad \text{Equation 2.15}$$

Where:  $\sigma_e$  is the maximum stress sustained for  $N_{Life}$  cycles (the endurance limit),  $\sigma_0$  is the maximum tested stress sustained for  $N_{Life}$  cycles without failure, and  $N_{Fail}$  is the number of cycles sustained at final stress before failure ( $N_{Fail} < N_{Life}$ ).

There has historically been some concern that step-load testing can lead to a phenomenon known as “coaxing” whereby the gradual increase in stress gives a fatigue strength far higher than would be found through normal, constant amplitude testing. Sinclair found in 1952 that coaxing was present in ferrous metals, but not in brass or aluminium. It was postulated that coaxing was a strain-aging process, and therefore not present on materials with little capacity for strain-aging [131]. Other authors have also found coaxing to not be present in other materials including steels [132] and titanium alloys [130], [133], with step-loading tests giving comparable fatigue strengths to those obtained by other methods and is therefore valid in this case.

#### 2.6.4.2 Fatigue Properties of AM Metals

In literature there has been inevitable interest in the fatigue properties of various AM metals, under different load conditions (e.g., plane bending, rotating bending, axial), and the effect of different post-processing operations. What follows is a broad overview of overview of AM fatigue, with particular attention paid to previous work sharing conditions with the results presented in Chapter 7.6 (i.e.,  $R_\sigma = 0.1$ , tension-tension, Aluminium, and/or LP).

##### A. Directionality

It is widely accepted that AM materials have differing static mechanical properties depending on build orientation, and the same is true for fatigue. Some authors have investigated 3-point bending fatigue of AM AlSi10Mg, using samples such as those shown in Figure 2.20, and have found strong directionality for as-built samples, including a dependence on whether the radii were manufactured on the top or bottom surface of inclined samples. Overall, they found horizontally built samples were slightly stronger than vertically built samples, while angled samples with the radii on the top surface (series E in Figure 2.20) performing similarly to horizontally built. Conversely, samples with the radii on the bottom surface (series D in Figure 2.20) were substantially weaker than all other build orientations [103], [134]. Beretta et al. however found that machining samples could alleviate a lot of this directionality by removing surface defects, likely due to porosity in the bulk of the material being generally spherical in shape [134]. Brandão et al. found build orientation had limited influence on the fatigue properties of AlSi10Mg [102].

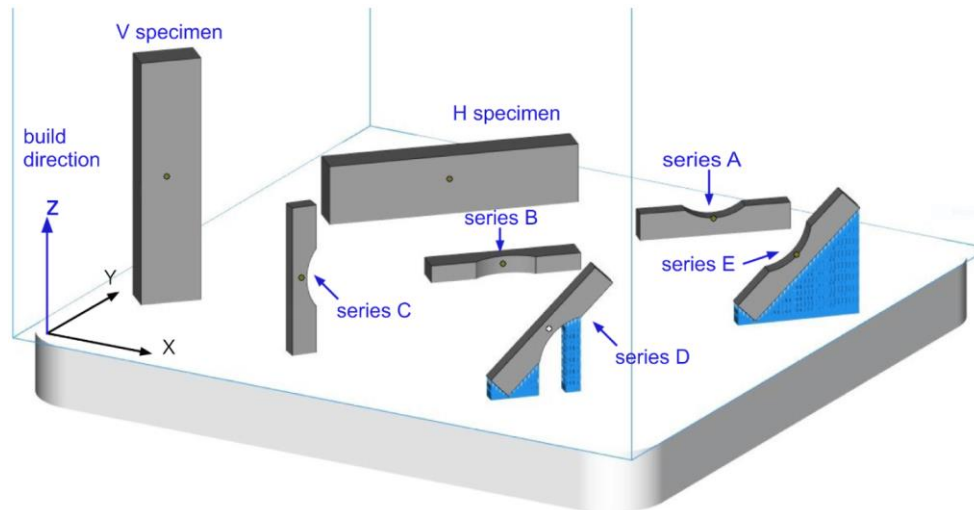


Figure 2.20: The fatigue samples and build orientations used by Beretta et al., from [134].

Mower and Long looked at the rotating bending fatigue strength of two different stainless steels (17-4PH and 316L) and found the horizontal samples performed similarly to wrought ( $\approx 15\%$  lower in the case of 316L) while vertically built samples were significantly worse. They also noted an increased variability in the fatigue strength of AM samples compared to the wrought material [25]. Finally, Brandl et al. also found horizontal samples had higher fatigue strengths than vertical or inclined samples, however, the difference was minimized through build plate heating [135]. While interesting, these findings are not of direct relevance to the following tests as, like the tensile samples, they are all manufactured horizontally.

#### B. Influence of Heat Treatments on Fatigue Properties of AM Metals

As noted by Bagherifard et al., the fatigue performance of AM metals is poor due to the exceptionally low ductility compared to conventionally manufactured equivalents [125]. It is therefore expected that heat treatments may be useful in preparing AM components for use where fatigue loadings are of considerable concern, thanks to the significantly increased ductility afforded (see Chapter 6 and ref. [136]). This logic holds true for tempered samples, with many authors finding substantial increases in fatigue strength after T6-tempering [5], [6], [135] (AlSi10Mg, tension-tension,  $R_\sigma = 0.1$  for each). However, SR appears to have a detrimental influence on fatigue strength compared to as built [137], but may reduce scatter in the results [23].

#### C. Roughness Effects

Correlating fatigue properties to surface roughness is attractive for engineers as roughness is relatively easy to measure compared to, for example, porosity. There are however mixed empirical results, with Spierings et al. finding no significant effect due to different surface treatments (blasting, machining, mechanical polishing) on 316L Stainless Steel [138], whereas Aboulkhair et al. found machining sample surfaces to be beneficial for AlSi10Mg at lower stress levels ( $<150$  MPa) [5], [139], implying increased resistance to crack initiation. Bagehorn et al. found reduced roughness increased fatigue resistance for Ti64 samples [97].

A recurring theme across this area of research is the concept of “killer notches”, locations where fatigue crack initiation occurs. These killer notches can be either surface features, near-surface porosity, or bulk porosity. Wits et al. investigated the effect of pore location on fatigue life for AlSi10Mg. Porosity was induced through different scan strategies (laser power, hatch spacing, etc.) and the surface layers were machined away to isolate the effect. They found defect size strongly correlated to fatigue life, more so than pore location [140]. Mower and Long [25] and Bagehorn et

al. [97] both found by machining surfaces crack initiation moved from the surface to bulk defects, for AlSi10Mg and Ti64 respectively.

Due to this apparent link, there has been great interest in relating fatigue properties to fundamental mechanics to aid in forecasting strengths. Ghiotti et al. applied a linear-elastic fracture mechanics approach to AM Ti64 but found limitations due to inherent manufacturing defects [141]. Gillham et al. took this one step further, using the “theory of critical distances” to predict the fatigue strength of AM Ti64. They were successful when applied to tension-tension samples ( $R_\sigma = 0.1$ ) with sharp notches manufactured into the sides, with reducing accuracy as the notch size approached the scale of surface roughness. The maximum error reported was 16%, which the authors argued was within the 20% often expected for fatigue predictions [142]. A more direct approach was taken by Buchenau et al. who found the surface roughness parameter  $S_k$  (Core height)<sup>8</sup> correlated very well with fatigue strength ( $N_{Life} = 10^5$ , Ti64,  $R_\sigma = 0.1$ , tension-tension) [143].

#### 2.6.4.3 Influence of Laser Processing on Fatigue Performance

Within the literature, there are two methods of laser processing generally employed, LP and LSP. LSP is similar to conventional shot peening (SP) in that the desired outcome is to impart residual compressive stresses in the surface to aid in fatigue resistance. LSP achieves this by directing the incident laser pulse onto a sacrificial layer (e.g., paint, metal tape) generating a shockwave. The shockwave is concentrated into the processed material by a thin layer of water. This is shown schematically in Figure 2.21.

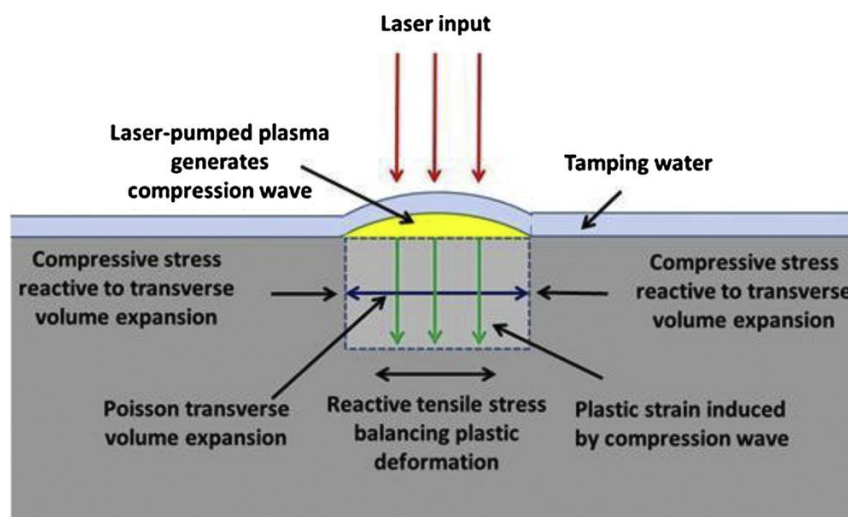


Figure 2.21: Schematic of laser peening. From [144].

LSP has been shown to significantly increase the fatigue strengths of various AM materials, with Hackel et al. finding 316L samples subjected to four-point bending fatigue had the longest lives after LSP compared to as-built or SP [144]. Maleki et al. found, for AlSi10Mg subjected to rotating-bending fatigue, an increase in fatigue life from  $1.3 \times 10^4$  cycles in the as built condition to  $2.2 \times 10^6$  cycles after LSP, with crack initiation a short distance below the surface. Similar increases were achieved with SP and “severe vibratory peening” [145]. Nasab et al. also found substantial increases to the fatigue life (AlSi7Mg, 3-point bending,  $R_\sigma = 0.1$ ), attributing this to the residual compressive stresses and pore closure near the surface [146].

<sup>8</sup> Core height is found from the material ratio curves (Abbott-Firestone curves) by extending the central, nearly linear region (30% to 70% probability) to the probability limits.  $S_k$  is then the difference between where this line intersects 0% and 100% probabilities. See ISO 25178-2, pp. 22 for more detail [46].

LSP does involve some significant limitations, namely, the requirement to coat the part in a sacrificial ablative layer (often PTFE or Aluminium tape), to have a continual covering of laminar water on the surface, and pulse intensities in the GW/cm<sup>2</sup> range [26]. All of these conspire to make LSP labour intensive, time consuming, and difficult to implement. Therefore, it was not considered for further evaluation in this work.

While LSP results in residual compressive stresses through a depth of over 0.5 mm [145], [146], LP does not have this effect. LP is primarily a smoothing process, with associated microstructural changes (e.g., Chapter 5 and ref. [71]). With this in mind, and the high variability in LP strategies employed, it is unsurprising that the effects on fatigue performance are far less clear than for LSP. For example, for Ti64 Kahlin et al. found a reduction in fatigue strength after LP, with an increase in the number of crack initiation locations (tension-tension,  $R_\sigma = 0.1$ ) [147]. Meanwhile, Lee et al. [148] and Ordnung et al. [149] both found LP increased fatigue strength (Axial  $R_\sigma = -1$  and 3-point bending  $R_\sigma = 0.1$  respectively). For steels, Aviles et al. found no significant change in fatigue strength after LP in a nitrogen atmosphere (conventionally manufactured AISI 1045, tension-tension,  $R_\sigma = 0.1$ ) [150], building upon previous work by the same authors that concluded fatigue performance was more closely linked to microstructural changes than to surface roughness effects (same material and test conditions) [72].

## 2.7 Identified Knowledge Gaps

### 2.7.1 Surface metrology

Overall, the literature shows AM PBF surfaces present unique challenges for the measurement and assessment of surface roughness. From the highly varied surface, to high aspect ratio features, and long spatial-wavelength roughness components, the previously accepted methods and standards are not best suited to assessing these surfaces. This is especially true when filtering surfaces to extract roughness or waviness components. Much work exists attempting to empirically determine a suitable nesting index; however, these generally still require very large measurement ranges, and do not factor in the functionality of a surface. There has also been much effort devoted to novel assessment techniques, such as quantification of discrete features. However, these assume a certain level of proficiency when it comes to the measurement of surfaces, and subsequent reporting of results. Currently, there is a significant deficiency in the literature in this regard. Chapter 4, therefore, will evaluate a practical, reliable, and easy to follow “recipe” for the measurement, evaluation, and reporting of roughness data from PBF components.

### 2.7.2 LP Literature Summary

Laser processing has been the topic of many different studies, both from conventionally manufactured and AM parts. Lasers have been shown to be effective for various surface modification processes, including cleaning, texturing, and smoothing. Laser polishing has been shown to be effective across a wide range of laser architectures, with particular interest in CW sources (available with very high powers, and common in large-scale cutting machines). However, nanosecond sources (commonly used for micro-machining processes) have been of lesser interest in the literature, despite their apparent advantages. The development of a laser polishing strategy utilising nanosecond pulse durations is thus the focus of Chapter 5. Nanosecond pulse durations strike a good compromise between cheap, reliable operation, and reduced heat input into the surrounding material. Previous research has shown that multi-step processing has the potential to achieve greater smoothing than single step processing while maximizing the heat retention within a part can also increase the smoothing potential.

### 2.7.3 Fatigue

Due to the very high cycle counts often investigated for fatigue testing, there has been numerous attempts to design reduced-duration tests. One of the more successful and accepted is the step-load testing, where a desired life is set, and only the maximum load sustained for that life is of interest. While there are concerns that the gradually increasing load may artificially inflate the fatigue life, this has not been found for a range of materials including aluminium.

It is natural for the fatigue properties of AM metal to be of great interest to researchers, and there have been many diverse studies conducted over the years. Much like for quasi-static properties, it has been repeatedly found that AM metals exhibit significant anisotropy, in terms of both build direction and the orientation of specific features during manufacture. There have also been many attempts to improve the fatigue resistance of AM metals through various heat treatments (with mixed results) and reducing the surface roughness.

There is comparatively little understanding for how laser processing influences the fatigue strength of materials. Laser shock peening is an emerging technique to increase the fatigue resistance, however, is time consuming to implement and requires highly specialised equipment. It is suggested that laser polishing may improve fatigue resistance by eliminating crack initiation sites, however there are mixed experimental results in the reported literature. The influence of laser polishing on the fatigue performance of AM AlSi10Mg coupons is investigated in Chapter 7.

## 3 Methods and Equipment

### 3.1 Additive Manufacture of AlSi10Mg Parts

Cardiff University has a Renishaw AM250 L-PBF machine, that uses a Ytterbium fibre laser source with a focussed spot diameter of 70  $\mu\text{m}$ . The laser is operated in a PW mode and has a maximum average power of 200 W. The maximum build volume is 250 mm  $\times$  250 mm  $\times$  300 mm. A Reduced Build Volume (RBV) device can be fitted to the build chamber, shown in Figure 3.1, that has maximum dimensions of 78 mm  $\times$  78 mm  $\times$  55 mm. The machine is capable of processing many different metal powders, including titanium alloys, nickel-based alloys, steels, and aluminium alloys. This work focuses on the AlSi10Mg aluminium alloy, whose nominal composition is given in Table 3.1.



Figure 3.1: Renishaw Reduced Build Volume (RBV) system, from [151].

Table 3.1: Renishaw AlSi10Mg powder nominal composition [69].

Element	Symbol	Mass (%)
Aluminium	Al	Balance
Silicon	Si	9.00 – 11.00
Magnesium	Mg	0.25 – 0.45
Iron	Fe	< 0.25
Nitrogen	N	< 0.20
Oxygen	O	< 0.20
Titanium	Ti	< 0.15
Zinc	Zn	< 0.10
Manganese	Mn	< 0.10
Nickel	Ni	< 0.05
Copper	Cu	< 0.05
Lead	Pb	< 0.02
Tin	Sn	< 0.02

To prevent oxidation of parts during processing the AM250 uses an inert Argon atmosphere throughout the manufacturing process. One of the main features of the machine is the low argon consumption as the build chamber is first evacuated (to -950 mBar gauge pressure) before the argon is introduced, the chamber is then held at slightly positive pressure to prevent air (and therefore oxygen) ingress. The residual oxygen content is monitored at two locations within the build chamber and maintained below a set value, measured in parts per million (ppm).

It is possible to change all the main manufacturing parameters on the AM250 and specify them separately for different parts within a build. It is also possible to specify different settings for

different regions of the part - top, bottom, and side surfaces, or the core, to optimize both mechanical properties and surface roughness.

A typical value for  $t_d$  on this machine is 10  $\mu\text{s}$ . The recommended parameters for AlSi10Mg powders on the AM250 machine are given in Table 3.2, and shall be used throughout this work unless otherwise stated. The scan order was: fill hatch, fill contours, and then borders (shown in Figure 3.2) all using the same settings.

Table 3.2: Standard Renishaw settings for AlSi10Mg powder using the AM250 machine.

Parameter	Symbol	Value
Laser Power	$P_{av}$	200 W
Hatch Spacing	$h$	100 $\mu\text{m}$
Pulse Distance	$P_d$	80 $\mu\text{m}$
Exposure time	$t_e$	140 $\mu\text{s}$
Oxygen content		<1000 ppm
Scan Speed †	$v$	533 mm/s
Energy Density †	$\Psi$	187.5 J/mm <sup>3</sup>

† The scan speed and energy density values were calculated using Equations 2.1 and 2.2 from Chapter 2.

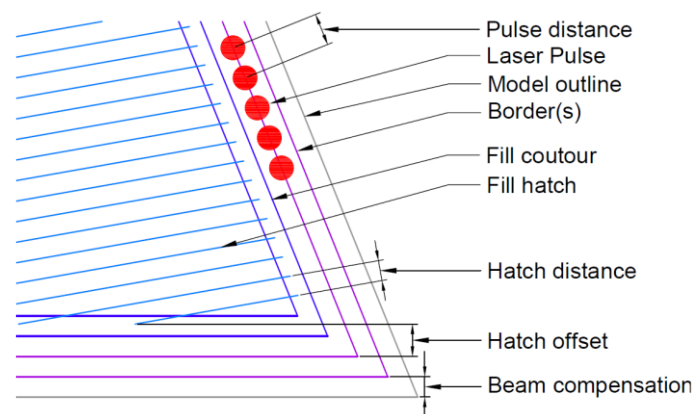


Figure 3.2: Depiction of different scanning elements, adapted from [152].

### 3.2 Laser Polishing

The laser system used throughout this project for LP was a *DMG Sauer Lasertec 40* laser milling centre, equipped with an SPI Lasers G3.1 nanosecond source. The key mechanical specifications are presented in Table 3.3, while the laser specifications are provided in Table 3.4. The pulse durations are selectable within the control software, referred to as *Waveforms* subsequently. Examples of the pulse profiles over time are shown in Figure 3.3, waveforms (WFM) 0 and 5 are used subsequently in this work (WFM 0 - black line, WFM 5 – light blue line in the figure). Unlike the Renishaw AM 250, the Lasertec 40 does not operate in an inert atmosphere. All processing is conducted in air, at ambient conditions, leaving the possibility for oxidation of the workpiece. Any combustion products and spatter removed by an exhaust and filtration system.

Table 3.3: Lasertec 40 system specifications

Parameter	Specification
Mechanical axis travel (x, y, z)	400 mm × 300 mm × 500 mm
Maximum table load	50 kg
Optical head	Galvo Scanner
Laser scanner area (x, y)	60 mm × 60 mm
Maximum scan speed	1000 mm/s
Lens type	100 mm telecentric

Table 3.4: Laser specifications for SPI G3.1 source, as installed in the DMG Lasertec 40 laser milling centre. Data from [153].

Parameter	Symbol	Value
Average Power	$P_{av}$	$\leq 20$ W
Laser Source		Yb-doped fibre laser <sup>9</sup>
Focused Spot Diameter	$d_o$	32 $\mu$ m
Beam Quality		$M^2 \approx 1.2$
Wavelength	$\lambda$	1064 nm
Pulse Frequency	$f$	$\leq 500$ kHz
Pulse Duration	$t_p$	15 – 220 ns (Pre-set)

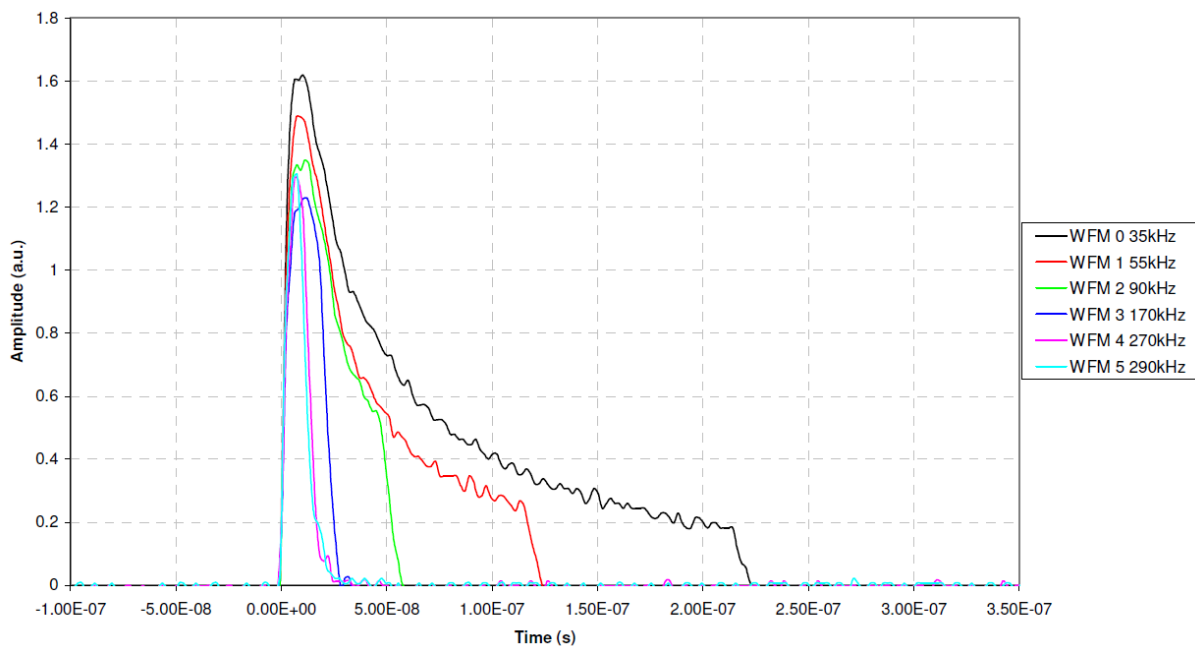


Figure 3.3: Laser pulse amplitude profile over time. From [153].

The laser source is capable of pulse frequencies up to 500 kHz, each waveform has an associated characteristic frequency, known as  $PRF_0$ , above which pulse energy decreases. The relationship between pulse frequency ( $f$ ), pulse energy ( $E_p$ ), and average laser power ( $P_{av}$ ) is shown in Figure 3.4. While the Lasertec 40 is not designed for polishing operations, the average laser power, scan speed, hatch distance, and focus offset can all be adjusted to suitable levels to achieve the polishing effect.

<sup>9</sup> Diode-pumped solid-state (DPSS); Q-switched; master oscillator power amplifier (MOPA) type.

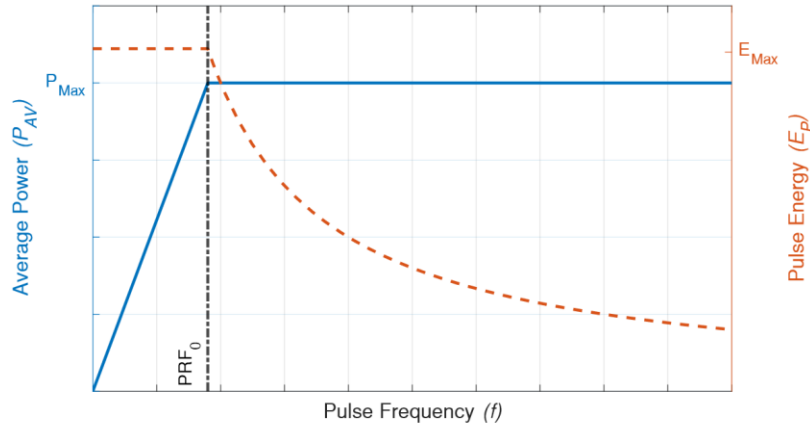


Figure 3.4: General relationship between pulse energy (solid line, left), average laser power (dashed line, right) and pulse frequency, showing  $PRF_0$  frequency (dot-dash line). Adapted from [153].

### 3.3 Surface Metrology

#### 3.3.1 Measurement Systems

Quantifying surface roughness is a core component of this project and a key technique for assessing how effective a given LP strategy is and identifying potential causes for different mechanical properties. Throughout this project, the main method of measuring surface roughness is FV, the method of operation is described in detail in Section 2.3, augmented in some instances by contact profilometry. FV was the selected technique due to its reduced acquisition times and better high-roughness performance compared to alternative techniques. The setup for the key pieces of equipment is described in Table 3.5.

Table 3.5: Basic setup used for surface roughness measurements taken throughout this project.

System	Technique	Notes
Sensofar Smart [51]	Focus Variation	10× Objective Natural Aperture (NA) 0.30 “Medium” Sensitivity* “Medium” Threshold* Ring light and coaxial illumination 1.7 mm × 1.42 mm FoV per image 1.38 μm/px (on surface)
Alicona G5 InfiniteFocus [154]	Focus Variation	20 × Objective Coaxial illumination 0.81 mm × 0.81 mm FoV per image Surfaces down sampled to 1.766 μm/px. Automated stitching
Taylor Hobson Form Talysurf 2 [50]	Contact Profilometry	2 μm radius, 60° diamond conisphere tip Range: X = 50 mm, Y = 100 mm, Z = 1.04 mm Resolution: X = 1 μm, Y = 1 μm, Z = 16 nm Run-up distance 0.3 mm Traverse speed 0.5 mm/s

\* Sensitivity and Threshold are options within machine control software relating to focus determination algorithm.

A more complete evaluation of the measurement systems, and a description of the procedure used, is provided in Chapter 4.

### 3.3.2 Measurement Stitching

To increase the Field of View (FoV) afforded by an optical measurement system it is possible to assemble multiple measurements together as a mosaic. This is referred to as *image stitching* (or just *stitching*) and is shown schematically in Figure 3.5. This has the effect of removing the intrinsic limitations on the measurement X-Y range (vertical limits can arise due to the distance between the objective and the focal plane). Image stitching is often used throughout this work and is realised through the standard *Mountains* software by *Digital surf*; specifically, the *SensoMap* version developed by *Sensofar Metrology* to work with their devices.

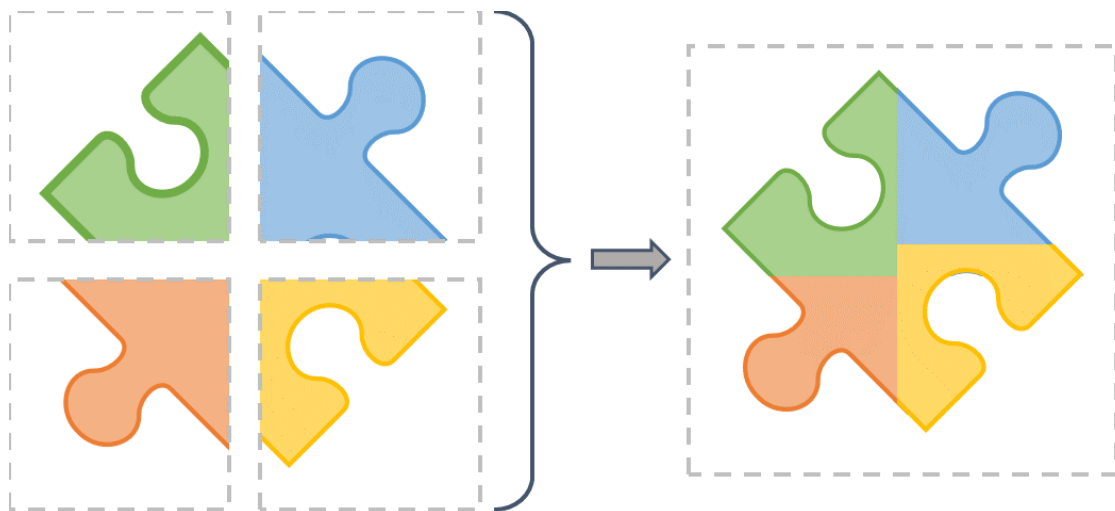


Figure 3.5: Schematic of how image stitching can be used to composite multiple images to extend the overall field of view.

Various sizes of mosaic are employed and are detailed at the relevant point within this report. Wherever stitching is used stepovers of 1.50 mm and 1.25 mm are used in the X and Y directions respectively, giving overlaps between adjacent images of approximately 0.2 mm. This overlap was judged to give a good balance between stitching accuracy and acquisition time (larger overlaps necessitate more images and take longer to stitch). Wherever possible no adjustments were made to measurements prior to stitching, however in some instances (especially on laser polished surfaces) it was necessary to apply a levelling operation first.

## 3.4 Material Testing

### 3.4.1 Cross-Section Mounting and Preparation.

Samples destined for cross-sectional analysis were first sectioned using wire electrical discharge machining (W-EDM). Sectioned samples were then mounted using a castable epoxy resin. The resin was cured at room temperature for 24 hours, followed by tempering at 60°C for 6 hours to fully harden, according to manufacturer specifications [155]. The final preparation step is mechanical polishing according to the process given in Table 3.6, achieved using a Buehler EcoMet30 grinder polisher (shown in Figure 3.6). This mechanical polishing ensures the sample surface is flat and exceptionally smooth, essential when evaluating microstructure or hardness at very low loads.

An alternative mounting option is compression mounting where heat and pressure are used to encapsulate a sample in a thermoplastic resin. Compression mounting is touted as having superior edge retention compared to casting. Another benefit of compression mounting is the availability of electrically conductive resins for when techniques such as scanning electron microscopy (SEM) are required. Compression mounting was not used in this work as the mounting temperatures of approximately 180°C are similar to the stress relieving temperature of AM AlSi10Mg (160°C) and could therefore have an influence on the microstructure of samples.

Table 3.6: Example microstructural sample preparation procedure.

Stage	Process
1	240 grit Silicon Carbide (SiC) paper with water cooling
2	400 grit SiC paper with water cooling
3	6 $\mu\text{m}$ diamond suspension on a polishing cloth
4	3 $\mu\text{m}$ diamond suspension on a polishing cloth
5	0.06 $\mu\text{m}$ Silica suspension on a polishing pad



Figure 3.6: Buehler EcoMet 30 grinder polisher machine, from [156].

#### 3.4.2 Vickers Microhardness

To collect microhardness data a Mitutoyo HM-220B was used (shown in Figure 3.7). The HM-220B can apply loads between 0.05 g and 2 kg, however the lowest practical load on aluminium was found to be 3 g. At loads below 3 g in aluminium, the indentations are too small to resolve optically due to the diffraction limit of light.

Surfaces are imaged by a 3.1-megapixel (2048  $\times$  1536 px) Complimentary Metal-Oxide-Semiconductor (CMOS) sensor, via 20 $\times$  and 100 $\times$  magnification objectives, and displayed on an attached computer. Through software, the indents can be measured automatically, but this was found to be ineffective in areas of high porosity or where multiple indents were visible in the image, therefore manual measurement within the control software was often used.

An alternative option for measuring indentation sizes was a Leica DM LM optical microscope fitted with various magnification objectives between 5 $\times$  and 150 $\times$ , capturing the micrograph with a 3.1-megapixel CMOS sensor (2048  $\times$  1536 px). It was also necessary to use this system when measuring the distance between the surface and a given indent when generating hardness profiles.



Figure 3.7: Mitutoyo HM-220 microhardness testing machine and control computer. From [157].

### 3.4.3 Etching and Microstructural Evaluation

It is well known that L-PBF and LP lead to very distinctive grain structures due to the very rapid cooling rates and high thermal gradients. In order to evaluate this the grain structure needs to be exposed before micrographs can be taken. For aluminium alloys, this is achieved using a mix of acids known as Keller's Etchant (or Keller's reagent). The composition is given in Table 3.7.

Prepared samples are submerged in the etchant for up to one minute and rinsed in water to reveal the microstructure. Micrographs were then taken using the previously described Leica DM LM microscope.

Table 3.7: Nominal composition of Keller's Etchant.

Component	Quantity (% volume)
Distilled Water	95.0
Nitric Acid	2.5
Hydrochloric Acid	1.5
Hydrofluoric Acid	1.0

### 3.4.4 Porosity Evaluation

#### 3.4.4.1 Cross-Section Area Coverage

One method for estimating sample porosity ( $\phi$ ) is to look at cross sections and calculate the pore area present. This is a popular method for the fast acquisition time, highly automated process, and no requirement for specialist training or equipment.

The basic principle involves taking micrographs of prepared cross-sectioned samples and using image processing to find the area of pores present. Prior to imaging samples were cleaned with IPA, followed by water, and dried with a lint-free cloth to remove any contamination. Porosity is found using Equation 3.1, based on either the area of the bulk material or pores compared to the total area imaged.

$$\phi = 1 - \frac{A_{Bulk}}{A_{Total}} = \frac{A_{Pores}}{A_{Total}} \quad \text{Equation 3.1}$$

Through software, it is also possible to measure the dimensions of pores and the area of individual pores. For this work, the ImageJ software was used to estimate all values. Within ImageJ it is first necessary to transform the micrograph to greyscale and then a black and white image. The threshold for what greyscale intensity should be black or white is set such that there is clear distinction between the sample material and any pores present. In this instance, thanks to the high contrast between the aluminium and pores (see Figure 3.8, left) the automatic threshold<sup>10</sup> within ImageJ gave good results. ImageJ can then automatically calculate various metrics such as area coverage (effectively % porosity) and statistics about the areas of individual pores. An example result is shown in Figure 3.8. While this method clearly is only an estimate of the sample porosity due to the cross sections potentially being through areas of unusually high or low porosity.

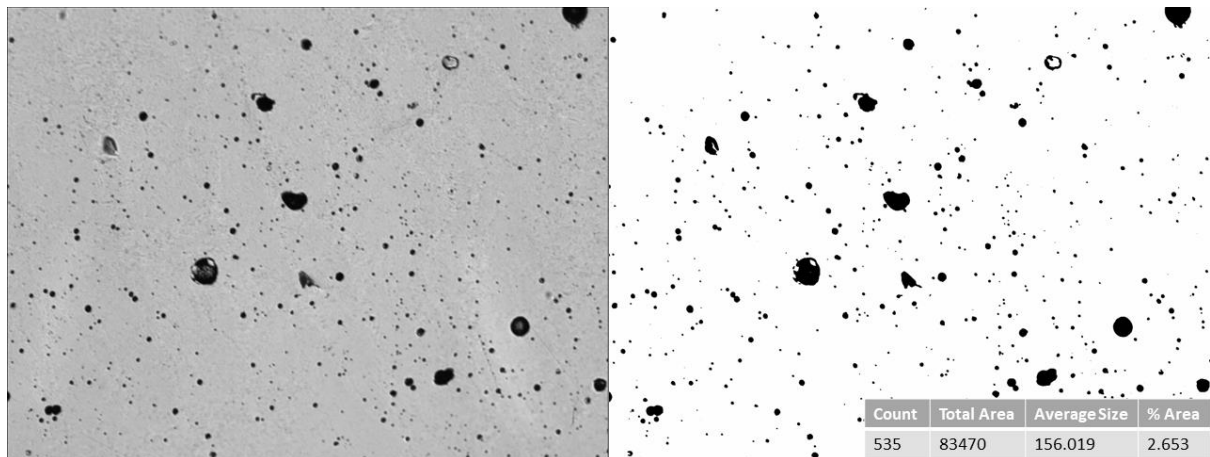


Figure 3.8: Example greyscale micrograph (left) and processed image (right) from the ImageJ software. Pores are shown in black while the bulk material is white. The insert shows number of areas measured (pores), total area and average size of pores (unknown units), and the % area coverage (porosity,  $\phi$ ).

#### 3.4.4.2 Volumetric

To assess the bulk porosity of samples there are two methods available: Archimedes' method and micro-computer tomography ( $\mu$ -CT). Archimedes' method relies on Archimedes' principle of buoyancy to determine the density of a specimen. The goal is to find the difference in mass ( $m$ ) of a specimen in air and when immersed in water, as shown in Figure 3.9. Equation 3.2 is then used to find the part density ( $\rho_{Part}$ ), and in turn the porosity from Equation 3.3, where  $\rho$  is density and  $m$  is mass, and the subscripts denote what material it is referring to.

$$\rho_{Part} = \frac{m_{Air} \cdot (\rho_{Water} - \rho_{Air})}{m_{Air} - m_{Water}} + \rho_{Air} \quad \text{Equation 3.2}$$

$$\phi = 1 - (\rho_{Part} / \rho_{Nominal}) \quad \text{Equation 3.3}$$

<sup>10</sup> Default based on the IsoData algorithm (<https://doi.org/10.1109/TSMC.1978.4310039>). More information about the thresholding options can be found at: <https://imagej.net/plugins/auto-threshold>.

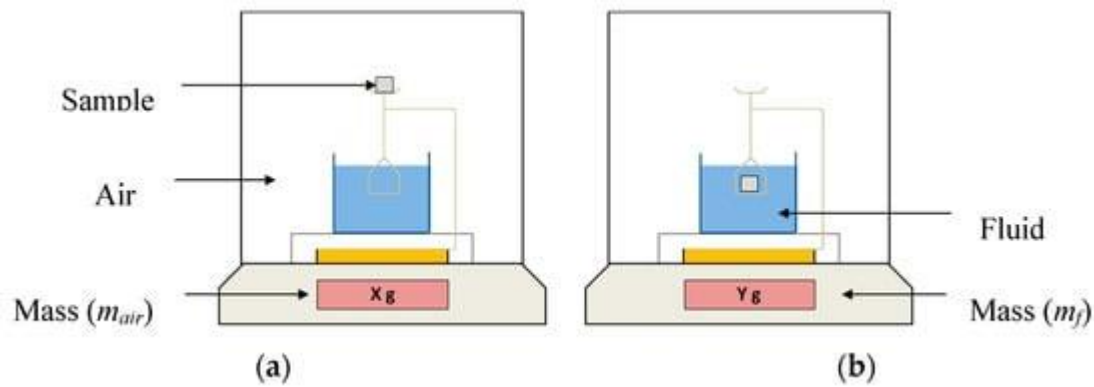


Figure 3.9: Schematic of Archimedes' density measurement procedure, from [158]. Where (a) shows measuring the dry mass ( $m_{Air}$ ), and (b) the mass when submerged ( $m_{Water}$ ).

$\mu$ -CT, on the other hand, uses X-rays to take multiple 2D images of a part that are then assembled in software to give a 3D model showing internal and external features. The porosity can be calculated directly from this along with the volume and dimensions of individual pores within the material.  $\mu$ -CT has the inherent advantage of giving much greater detail about the internal characteristics of a part, at the expense of increased time requirements and the necessity to access highly specialized equipment.

It has previously been shown that trends measured by different techniques (cross section area/volumetric) are comparable even though exact values are somewhat different [159]. This is likely due to the resolutions of the different methods and un-melted powder present within some pores.

Despite the many advantages of volumetric porosity measurements, they have not been utilised in this thesis. This is due to the requirement for specialist equipment and high cost (in the case of  $\mu$ -CT). Furthermore, cross-sectional measurements allow for quantification of both the porosity and assessment of pore attributes (distribution, size, aspect ratio etc.), making it the preferred method for this application.

### 3.4.5 Quasi-Static Tensile Testing

#### 3.4.5.1 Load Machine

For this work tensile testing was performed using a *Zwick-Roell Z050 universal testing frame*. Displacements are applied by a screw-thread mechanism and loads are measured using a 50 kN load cell. Due to the geometry of test samples used in this work sample fixturing was achieved using parallel jaw "Wedge Grips" and a displacement rate of 2 mm/s.

#### 3.4.5.2 Video Strain Gauge

The traditional method for measuring strain in a test sample is to attach a strain gauge to the surface and log the changes in resistance (proportional to the deformation) from which the strain in that location can be calculated. There are some significant drawbacks to this approach, namely, it only gives a strain value for that exact location, and the very presence of the sensor can affect the results. For large sample sets it is impractical to attach and calibrate a strain gauge to each sample before testing and so many researchers will rely on the test machine outputs. However, even the best designed load machines will have some compliance and deformation under load (adding to the sample deformation) and cannot account for any slip of the sample in the fixtures while the system settles.

One way of getting around these issues is to use a non-contact technique, such as the Video Gauge (VG) from *Imetrum*, which takes a video input of the surface and calculates strain between

landmarks on the surface. Landmarks, often a dot of paint to give strong contrast to the sample surface, can either be pairs of points applied to the surface, or an array of points (speckle pattern) from which a strain map can be calculated. To ensure good results from the VG, samples were first painted black to eliminate glare from the surface and further increase contrast. The gauge length was marked with a small amount of white paint, these were used as reference points by the VG to determine the sample strain. An example of the VG output display is provided in Figure 3.10.

Understanding the accuracy of these systems is a non-trivial task, being strongly dependent on the physical arrangement of the sample and camera, optics used, illumination, landmark clarity, and many other factors. Liu, Yuan, and Zhang presented an evaluation of the uncertainty associated with the Imentrum VG system, highlighting the interrelation between the various setup options (optics, physical arrangement etc.) while also noting the system can be thought of as a reliable method for measuring displacements especially in laboratory settings [160].

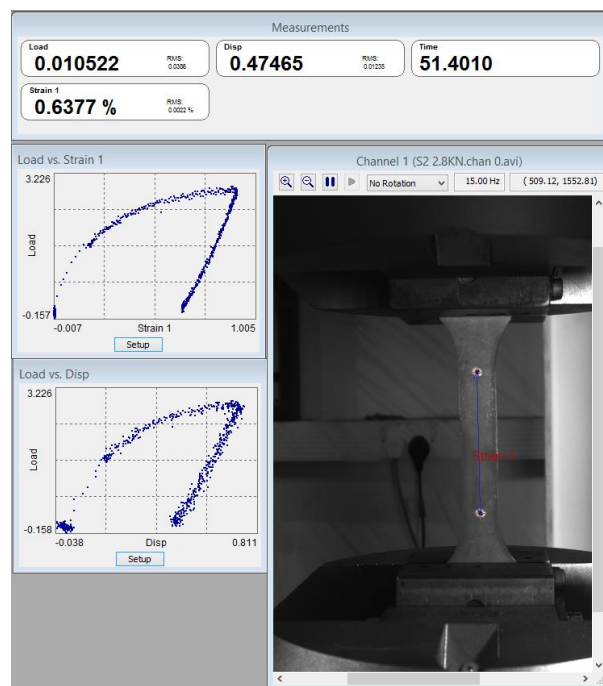


Figure 3.10: Example of a Video Gauge output. At the top are instantaneous values, on the right a live video feed with the virtual strain gauge marked, and on the left graphs of load against strain and displacement.

### 3.4.6 Fatigue Testing

All fatigue tests were performed at room temperature in tension-tension with  $R_\sigma = 0.1$ , in a sinusoidal pattern. Fatigue loadings that are not reversed are seen as more severe than those that have periods of zero stress as there is no crack closure during the cycles [138]. Furthermore, by maintaining the samples in tension throughout there is no risk of buckling.

#### 3.4.6.1 Low Cycle Fatigue

Low Cycle Fatigue (LCF) was performed using an *MTS 858 Mini Bionix II* servohydraulic test system. The machine is capable of 25 kN axial load and 250 Nm torsion over maximum displacements of 100 mm and 270° respectively. Further details about the test system can be found in the reference [161]. Sample fixturing was achieved using the same wedge grips as used for tensile testing as the grip geometry is inherently self-tightening and transfers loads in a more uniform way than other fixture mechanisms (e.g., pinned). Further discussion of the loads and loading profile used is provided in Chapter 7.

#### 3.4.6.2 High Cycle Fatigue

High Cycle Fatigue (HCF) testing was conducted by *Swansea Materials Research & Testing Ltd (SMaRT)* using a 100 kN *Amsler Vibrophore* equipped with a *Servocon* digital controller. Fixturing was achieved using MTS Hydraulic wedge grips. Further details about the loads applied and achieved frequencies will be presented in Chapter 7.

Vibrophores operate by statically loading a sample to the mean stress value and exploiting resonance to apply the dynamic loads. Loading frequency is determined by various factors including the specimen stiffness and is therefore not a selectable parameter. Two of the main benefits of vibrophores are the achievable frequencies (>200 Hz) and low energy requirements compared to servohydraulic systems [162], however, full data logging is rarely achieved - usually only cycle count and environmental conditions are monitored.

## 4 A Method for Surface Roughness Measurement of AM PBF Surfaces

### 4.1 Introduction

There is an often-paraphrased quote from Lord Kelvin that resonates across many fields of science:

*“I often say that when you can measure what you are speaking about, and express it in numbers, you know something about it; but when you cannot measure it, when you cannot express it in numbers, your knowledge is of a meagre and unsatisfactory kind; it may be the beginning of knowledge, but you have scarcely, in your thoughts, advanced to the stage of science, whatever the matter may be”<sup>11</sup>*

- William Thompson, 1<sup>st</sup> Baron Kelvin (1883) [163]

While the message may seem intuitive at first glance, it underscores just how important high-quality measurements are to science, known broadly as metrology. Institutions like the International Bureau of Weights and Measures (BIPM) exist solely to ensure measurements are presented in a consistent manner regardless of where they are made. Meanwhile, national bodies such as the National Physical Laboratory (NPL) in the UK are then tasked with ensuring the same value will be found when measuring with different apparatus (within a margin of uncertainty).

This logic permeates every aspect of science and is of particular interest in this work regarding the surface roughness measurement of AM parts. And while there are standards specifying different roughness metrics (e.g., ISO 4287), and the required data post processing for conventionally manufactured surfaces (ISO 4288), there is less guidance for the evaluation of AM surface roughness.

Surface roughness of AM parts has been the focus of many studies as it not only affects the aesthetics of parts, but also potentially functional properties such as tribology, fatigue, and corrosion resistance [102], [103]. Furthermore, the same techniques/processes can be used to measure surfaces more generally, such as evaluating surface texturing/functionalisation, where the accurate measurement of features is required to confirm the accuracy of manufacture and effectively model the downstream effects. For example, Escudero-Ornelas et al. [164] simulated the flow velocities over “real” (as measured) surfaces and the idealised (designed) surfaces, as shown in Figure 4.1.

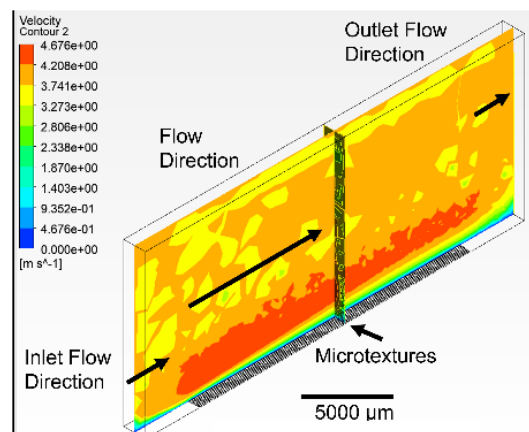


Figure 4.1: Example of simulation using measured surface data to assess fluid flow velocities. From [164].

<sup>11</sup> The quote is often reduced to “If you cannot measure it, you cannot improve it.”

There has been much work to improve the surface condition of AM parts through both build process optimisation [100], [165] and post-processing [8], [97]. However, as much of the surface roughness data reported is not prepared by metrologists, the ability to interpret results can be limited due to missing information about how exactly the measurements were made and what post-processing is applied (e.g., filters) [90]. This makes comparisons between datasets challenging, while also adversely affecting the uptake of AM in large-scale manufacturing and other commercial applications [166]. It has been recommended by multiple authors [30] that details about the measurement system and data processing should be provided along with the results.

Another difficulty when assessing the surfaces of AM components is the relative lack of experience when compared to traditional manufacturing methods. The surfaces produced by subtractive manufacturing (milling, turning), casting, and forging are very well understood, and industrial standards are available to guide the process of collecting and interpreting the data.

The following chapter therefore evaluates three different measurement devices, developing a workflow for the reliable and repeatable acquisition and analysis of surface roughness measurements. It is positioned as a practical guide for practitioners and technicians, rather than metrologists, with the goal of facilitating industrialisation of AM through improved understanding of the manufactured surfaces.

## 4.2 Methodology

### 4.2.1 Samples

For the following testing, a series of AlSi10Mg cubic samples (10 mm × 10 mm × 10 mm) were manufactured using a Renishaw AM250 L-PBF machine (described in Chapter 3.1). From a wider sample set three were selected for this work, representing a range of surface conditions and features. The variable manufacturing settings for these samples are given in Table 4.1. Laser power and layer height were kept constant at 200 W and 25 µm respectively.

Table 4.1: Variable manufacturing parameters used for samples in this test.

Parameter	Symbol	Unit	S1	S2	S3
Pulse Distance	$P_d$	µm	64	80	96
Exposure Time	$t_e$	µs	112	168	112
Hatch Spacing	$h$	µm	64	64	96
Scan Speed†	$v$	mm/s	524.6	449.4	786.9
Energy Density†	$\Psi$	J/mm <sup>3</sup>	238.3	278.1	105.9

† Scan Speed and Energy Density values calculated from Equations 3.1 and 3.2.

Samples were mechanically removed from the build plate and cleaned using compressed air. No other physical post-processing was applied to maintain the as-built surface condition. Micrographs of three of the surfaces are provided in Figure 4.2. A total of five surfaces were measured for this work including both horizontally and vertically built surfaces.

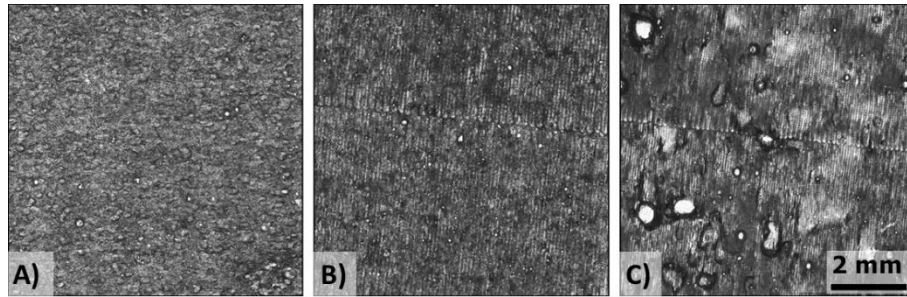


Figure 4.2: Optical micrographs of three of the surfaces analysed with the (A) best, (B) medium, and (C) worst surface condition.

#### 4.2.2 Measurement Procedure

Four techniques were used to measure the surface topography of the samples. Two optical systems and a tactile system collected 3D (areal) measurements. 2D (line) measurements were also conducted using the same tactile system, due to their continued widespread use, prevalence of appropriate measurement systems, and very rapid acquisition times. To measure an adequate area of the test surfaces, the optical systems both required measurement stitching (as previously described in Chapter 3.3.2). The Alicona G5 Infinite Focus had automated stitching capability, while the Sensofar Smart required manual stitching through software (MountainsMap). Both optical systems used the FV technique to resolve the surface heights. The same device was used for all tactile measurements, a Taylor Hobson Form Talysurf 2, equipped with a motorized Y-stage to enable areal measurements to be taken. Details of the measurement systems are given in Table 4.2, further details about the systems were previously presented in Table 3.4.

Table 4.2: Details of the different surface measurement techniques used.

Measurement type	Measurement system	Settings	Identifier
Optical profilometry	Alicona G5 InfiniteFocus [154] (Areal measurements using Focus Variation)	0.81 mm × 0.81 mm FoV per image Total FoV 8.1 mm × 8.1 mm Surfaces down sampled to 1.766 μm/px. Automated stitching	OAS
Optical profilometry	Sensofar Smart [51] (Areal measurements using Focus Variation)	5 × 6 array of measurements Total FoV 7.7 mm × 7.65 mm Manual stitching	OMS
Tactile profilometry	Taylor Hobson Form Talysurf 2 [50] (Areal measurements)	Evaluation length 8 mm Data points (X) 12000 Y-Spacing 0.01 mm Number of lines 801	T3D
Tactile profilometry	Taylor Hobson Form Talysurf 2 [50] (Profile measurements)	Evaluation length 8 mm Data points (X) 12000	T2D

For the areal measurements an 8 mm × 8 mm area was measured (approximately) to cover nearly the whole surface without encountering distortions around the surface periphery, as noted by Yasa et al. [167]. While the Alicona captured data at a surface resolution of approximately 0.9 μm/px, the results were down sampled to 1.766 μm/px. This is similar to the surface resolution of the Sensofar (1.38 μm/px). To further reduce the influence of different measurement resolutions, a 2.5 μm S-filter was applied prior to any other filtering.

#### 4.2.2.1 Optical Measurements with Automated Stitching

The measurement process using the Alicona G5 (OAS) involved placing the sample on the X-Y stage, with the imaged region at one corner of the desired measurement range. This location was stored, and offsets were applied to give the limits of the total FoV. The Z-range of the measurements was set by moving the focus above and below the surface, storing both. The range was checked by traversing to several locations over the surface to ensure no part came into focus at the vertical limits. The measurements were then taken with the machine measuring each FoV before moving on to the next, and finally assembling the individual measurements into a single result file.

#### 4.2.2.2 Optical Measurements with Manual Stitching

The procedure when using the Sensofar Smart (OMS) was much the same, but with manual repositioning between each measurement (including checking the Z-range) and importing these into Mountains for stitching. To stitch the measurements the grid of measurements is set by the user and an algorithm searches for appropriate overlaps over which neighbouring measurements are of the same area. To achieve the desired total measurement range, an array of  $5 \times 6$  images was required.

#### 4.2.2.3 Tactile Areal Measurements

Tactile area measurements (T3D) necessitated the samples to be secured to the Y-stage to prevent movement during the measurement. Once this was set the stylus was located at each corner of the measurement range to ensure the stylus would remain in contact with the surface at all times. Once satisfied the probe was brought into contact with the surface. Due to the limited Z-range possible with the fitted stylus, it was necessary to check that any extreme features (e.g., very tall peaks) did not extend past this possible range as it would lead to a failed measurement and possible device damage.

With all this in place, the measurement was commenced, with the machine taking a series of 2D measurements, at regular distances apart in the Y-direction, which were assembled into a single result by the measurement system.

#### 4.2.2.4 Tactile Profile Measurements

Tactile profile measurements (T2D) followed a similar process to the area measurements, but with manual repositioning between each measurement. Individual profiles were distributed across the surface as shown in Figure 4.3. Ten measurements were taken from each surface, and the maximum calculated value for each roughness parameter was used for further analysis, as specified in ISO 1134 [42], with the different directions to minimise the effect of any directionality, or lay, of the surfaces. To facilitate this a jig was manufactured to ensure consistent alignment of the samples with respect to the profile directions.

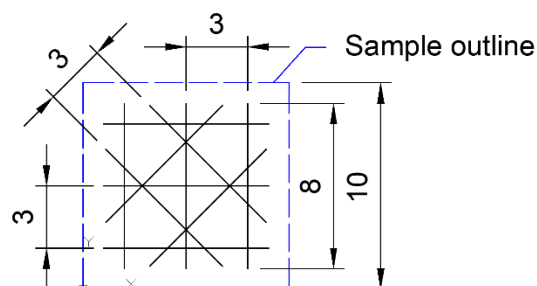


Figure 4.3: Distribution of the line profiles taken across the sample surface. Sample outline shown by the dashed line, all dimensions in mm.

### 4.2.3 Aligning Measurements

To ensure accurate comparisons between measurements it is important to ensure the measured areas are the same. This applies not just when comparing measurement techniques, as is the case here, but after any surface modifications such as wear testing or polishing (as will be of interest later in this thesis, Chapter 5). To achieve this there is a function within Mountains to “localise” measurements. The basic premise is to identify matching features present in two different measurements and apply translations and rotations to one of the datasets to overlay these matching features. The area that is not shared between the two measurements can then be removed (cropped), leaving only the matching area. This is shown schematically in Figure 4.4. In this case, where there are three areal measurements to be compared this process was repeated three times, with different pairings of measurement systems, using previously extracted areas.

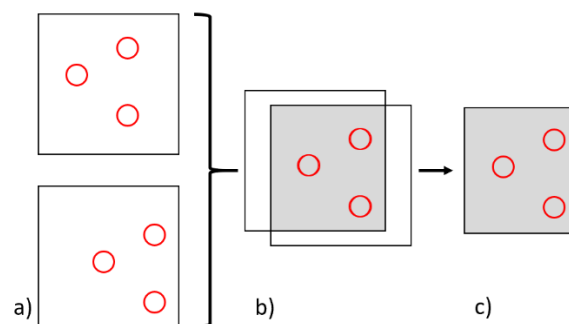


Figure 4.4: Schematic of the localisation process, a) identify matching features on the surfaces – denoted by with red circles, b) rigid transformations (translation, rotation) of the surfaces so the matched features align, c) crop the surfaces to leave only the corresponding areas (grey shaded area).

### 4.2.4 Roughness Parameters of Interest

The arithmetic mean height of deviations ( $R_a$ ,  $S_a$ ) are the most commonly quoted parameters when discussing surface roughness [168], however, does not contain enough information to fully assess a surface [165], [169]. A simple example is two surfaces that are the mirror image of each other would have the same  $R_a$ , but very different mechanical properties (e.g., Figure 4.5).

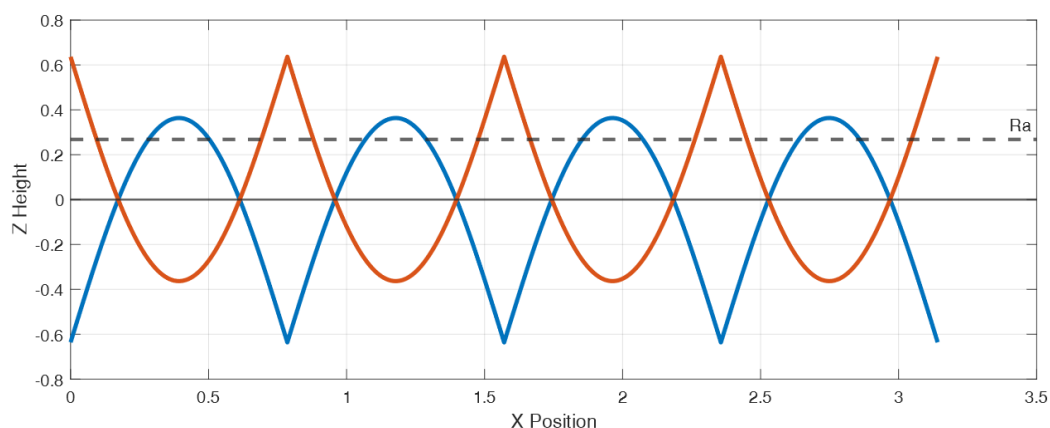


Figure 4.5: Two theoretical surfaces with the same  $R_a$ .

To provide a more complete understanding of how different measuring techniques capture a surface the full range of roughness parameters presented in Table 2.3 were computed and compared. The aim of this chapter was not to fully characterise a surface, only to evaluate measurement methods, therefore no comment is made on the relative merits of different roughness parameters here.

#### 4.2.5 Data Post-Processing

Once captured, the data was imported into the TalyMap version of Digital Surf’s Mountains software [170] for processing. The processing flow for the areal measurements followed the same basic structure, where the data was levelled (least-squared method), matching regions extracted, filtered, and finally roughness values calculated. For the optical systems, it was necessary to interpolate data for regions where the height was not resolved, called non-measured (NM) points, after levelling. The NM point interpolation was achieved using an automatic algorithm within MountainsMap. The algorithm used is proprietary and includes options for how to fill the NM points. Options include adding points at the maximum or minimum measured value, or with a “smooth shape” based on surrounding measured data. For this application, the smooth shape was preferred to estimate what the surface shape was in the regions without measurement information.

Manual stitching of the OMS data was carried out first, before any other processing was applied (using the SensoMap version of MountainsMap). The processing flow is shown schematically in Figure 4.6. The filtering also included a 2.5  $\mu\text{m}$  S-Filter (low-pass) to remove measurement noise. This value was chosen based on a 2  $\mu\text{m}$  stylus tip from ISO 1134 [42], and larger than the apparent pixel size on the surface for both optical systems.

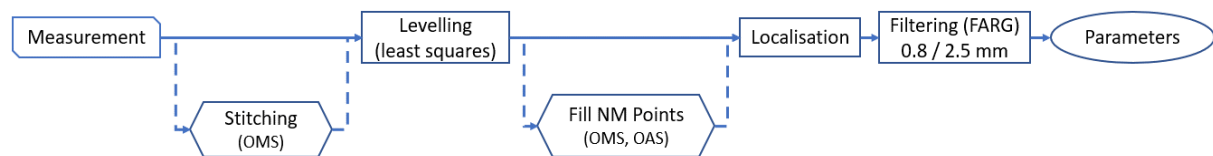


Figure 4.6: Processing flow for 3D surface measurements. Dotted lines indicate step not required for all instances.

Two filters were evaluated to differentiate between the roughness and waviness components of the measured surfaces. One with a nesting index of 2.5 mm, based on the previously referenced work by Triantaphyllou et al. [88]. The other, using a nesting index of 0.8 mm, from the ISO 13565-1 recommendation for stratified surfaces [171], along with the author’s previous experience, and assessing the maximum feature diameter present on the surfaces.

The profile measurements were processed in a similar fashion (levelling, filtering, parameter calculation), however, only the maximum parameter values from each surface were considered moving forward as per ISO 1134 [42]. Similar filters were applied to the profile measurements as the areal measurements.

#### 4.2.6 Surface Lay and Isotropy

It is often discussed in literature that the “stair-step” effect is present on AM surfaces and would therefore contribute to a surface directionality, known as lay. This is important with tactile measurements as the orientation of the measurement with respect to the lay can have a significant effect on the results, shown schematically in Figure 4.7.

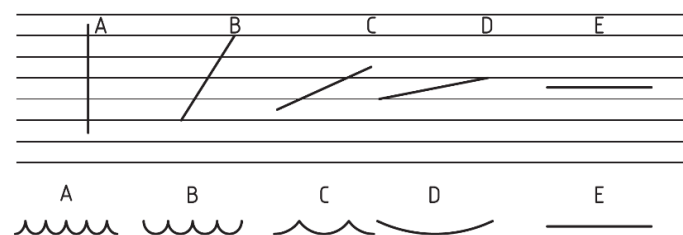


Figure 4.7: Schematic representation of how lay can affect a profile measurement (the predominant lay is across the page) from [42].

To quantify the lay of a given surface two techniques were employed. First, within MountainsMap there is an operator called “Texture Direction” that presents a graph showing the relative strength of texture directions, with large peaks corresponding to dominant lay (see Figure 4.8). The operator also gives a measure of the “Isotropy”, defined as “the higher the percentage value the more the surface resembles itself in every direction [172] ” i.e., high isotropy means low directionality. This was used on the S-F surface (microroughness and form removed) of the areal measurements to eliminate the effect of the L-operator.

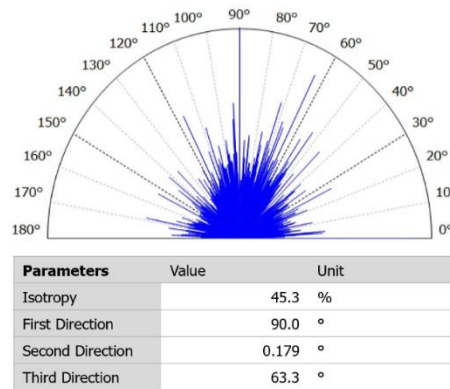


Figure 4.8: Example of the MountainsMap “texture direction” output.

To evaluate the profile measurements the “mean width of profile elements” parameter was calculated from the primary profiles (PSm), and the average of these was taken based on trace direction (from Figure 4.3). The surface “isotropy” ( $\gamma$ ) was then calculated using Equation 4.1. High values of  $\gamma$  indicate the surface is similar in all directions (in terms of PSm only) and therefore absent of a significant lay.

$$\gamma = 1 - \left( \frac{PSm_{Max} - PSm_{Min}}{PSm_{Av}} \right) \quad \text{Equation 4.1}$$

#### 4.2.7 Measurement Resolution

Efficiency is a major motivation in industrial settings, both in terms of financial cost and time requirements. This is relevant to quality control/assurance processes as a reduced process time allows for faster identification of issues, and leaves technicians available to complete other tasks, such as testing or measurement of larger populations. With this in mind, the most accessible option to reduce surface measurement acquisition time is to reduce the measurement resolution. This can be achieved by using a lower magnification objective for optical systems, or fewer individual traces for tactile systems. Reduced measurement resolutions have the additional benefits of smaller file sizes for a given measurement area and thus a reduction in data processing time, both enhancing the efficiency gains.

To evaluate both of these, an operator within MountainsMap is available to down sample a measurement. For the T3D results the resolution in Y was reduced only, as the number of samples along X is much less significant in terms of acquisition time. For OMS the results were down sampled in both X and Y to emulate a lower magnification objective. The levels chosen are given in Table 4.3 and Table 4.4 for the T3D and OMS systems respectively. It should be noted, as shown in Table 4.4, that different magnification objectives also have different capabilities in the Z-direction (height), however, the operator used can only change the Z-resolution to predefined levels that do not match the quoted resolutions for the chosen objectives. Furthermore, the surface roughness of AM parts is

typically many orders-of-magnitude greater than these quoted Z-resolutions and therefore assumed insignificant.

In both cases down sampling was performed on the unfiltered surface measurements, and data processing then followed the same process described previously. Roughness parameters were compared between the full resolution, and down sampled measurements, and the relative difference was used to assess the validity of the reduced resolutions.

Table 4.3: Y-resolution levels investigated for T3D system.

Y-spacing	Number for 7 mm wide area	Relative resolution
10 $\mu\text{m}$	701	100%
20 $\mu\text{m}$	351	50%
25 $\mu\text{m}$	281	40%
40 $\mu\text{m}$	176	25%
50 $\mu\text{m}$	141	20%
100 $\mu\text{m}$	71	10%

Table 4.4: Specification of different magnification objectives and resulting measurement size for the OMS system.

Objective	Field of view <sup>†</sup> ( $\mu\text{m}$ )	Pixel size <sup>†</sup> on surface ( $\mu\text{m}$ )	Z-resolution <sup>†</sup> (nm)	Array size (for 7 mm $\times$ 7 mm area)	Image resolution used (pixels)
10 $\times$	1700 $\times$ 1420	1.38	25	5 $\times$ 6	5586 $\times$ 5553
5 $\times$	3400 $\times$ 2837	2.76	75	3 $\times$ 3	2792 $\times$ 2776
2.5 $\times$	6800 $\times$ 5675	5.52	300	1 $\times$ 2	1396 $\times$ 1388

<sup>†</sup>Values from manufacturer specifications [51].

#### 4.2.8 Uncertainty Quantification

The determination of the measurement uncertainty of optical profilometry techniques is non-trivial and work is ongoing to address this problem [54], [173]. In a practical sense, practitioners are required to somewhat trust the machines at our disposal, be this through calibrations or cross-checking results with alternative machines (as has been done elsewhere in this chapter). While this can be useful for evaluating different devices or techniques, there is still much scope to corrupt results through inappropriate post-processing. It is therefore important to understand the influence of different post-processing operations on the measurements.

To this end, it was decided to solely use the Sensofar Smart optical profiler for this section due to the rapid acquisition time and extensive use throughout. The following sources of errors were identified for evaluation: measurement noise, sample positioning, localisation, and stitching. The method for assessing each is described in the following subsections (A-D) and the common evaluation method is explained.

##### A. Measurement Noise

A series of measurements were taken from the top surface of a new specimen for comparison. The sample was not moved between measurements of the same area. Nine measurements were taken from each of four areas. For one area the measurement setup was not changed, for the remaining sets, the illumination intensity was adjusted. Changes were made to either, the axial illumination (0.25% steps between 0% and 2.5%), the ring light (from 0% to 10% in 2.5% increments), or both. Otherwise, illumination settings were maintained at 1.25% axial light and 5% ring light intensities.

## B. Positioning Repeatability

Throughout this project, comparative measurements were required (e.g., before and after an LP process was applied) and therefore jigs were used to facilitate this. Therefore, a new set of nine measurements were taken from each of three different areas. This time the sample was located by a positioning jig (an example is shown in Figure 4.9). Between each measurement the sample was removed and replaced from the microscope stage. The remaining measurement conditions were maintained throughout.

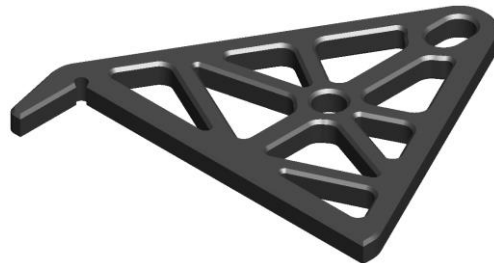


Figure 4.9: Example of a positioning Jig used.

## C. Localisation

To assess the errors induced by the localisation algorithm, a single area was imaged nine times. While more areas would have been preferable, the localisation process is time intensive making further evaluations impractical.

Between each measurement small X-Y translations were applied ( $\approx 0.1$  mm) shown in Figure 4.10. These measurements were localised in SensoMap relative to an arbitrary “base” measurement (as explained in Section 4.2.3) before exporting for further analysis.

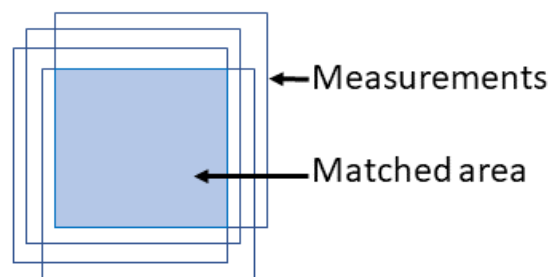


Figure 4.10: Arrangement of measurements to evaluate uncertainty due to Localisation errors.

## D. Measurement Stitching

At four different locations three measurements were taken with an X translation of 0.75 mm between each. The outer two were then stitched in software ( $\approx 0.25$  mm overlap) and the stitched measurement was localised with the central measurement in the usual way, shown in Figure 4.11.

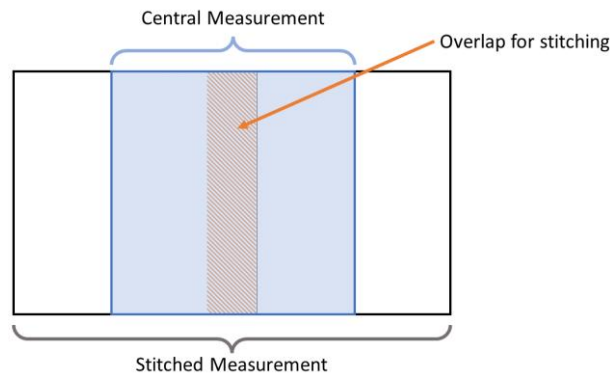


Figure 4.11: Process for comparing stitched measurement with direct measurement.

#### E. Method of Evaluation

Once the measurements were collected, and any necessary processing applied, the files were exported in a text file as an array of Z-heights for analysis. As all measurements were taken with the same microscope, using the same objective lens, the array sizes were consistent (and apparent pixel sizes identical) and therefore knowing the X-Y coordinates was not necessary.

These were then imported into MATLAB where, for each area, the average height at each X-Y location was calculated. From that, the deviation from this average for each individual measurement was calculated. The maximum, minimum, and average heights across a given set of measurements could be visualised. The probability distribution of the height discrepancies were then computed, and variability (errors) compared between each condition to assess the relative contributions.

### 4.3 Results and Discussion

#### 4.3.1 Visual Inspection of Surfaces

Visual inspection of the samples showed the top surfaces (horizontally built) had a shiny appearance, free from soot, but with pronounced waviness components. Furthermore, these surfaces showed evidence of the chessboard scanning strategy used and few distinct peaks present. These peaks were approximately hemi-spherical with diameters and heights of around 0.5 mm. The side surfaces (vertically built), in contrast, had a dull appearance indicating soot contamination, but overall, more uniform in terms of adhered particles and flatness.

These observed differences in surface appearance indicate a divergence of measurement strategy may be warranted (e.g., illumination intensity, measurement range). However, the measurement setup is highly dependent on a multitude of different factors, including surface condition, machine specification, measurement purpose, and time available. This has not been studied as part of this project, but the effect of illumination type has been reported elsewhere [174], among others.

#### 4.3.2 Qualitative Comparison of Surface Measurements

The surface measurements were prepared by levelling and filling NM points, and the colour maps presented with matched Z-scales ( $z=0$  at the bottom of the measurement range) for evaluation. Figure 4.12 shows an example of this. It can be seen that the relative size and shapes of asperities were consistent across measurement systems, however, the T3D system shows distortion in the X-direction as displayed (perpendicular to the trace direction). This is likely due to the relatively low sampling rate in that direction ( $10\ \mu\text{m}$ ) compared to the optical systems ( $\approx 1.5\ \mu\text{m}$ ).

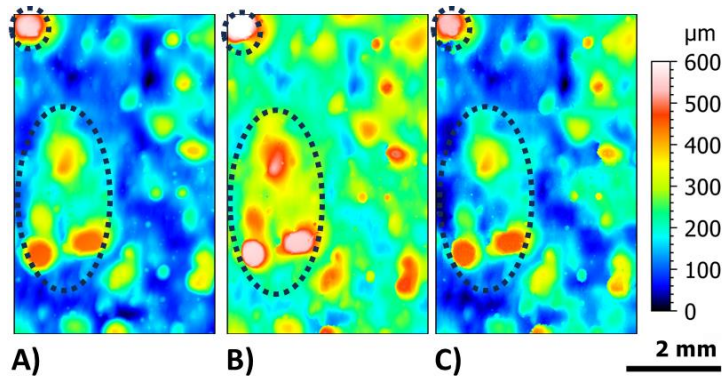


Figure 4.12: Surface measurements of top surface of sample S1 with matching asperities highlighted. The measurement systems used were (a) T3D, (b) OAS, and (c) OMS.

Depressions in the surface (valleys, pits) were assessed in a similar fashion. The top surface results for S3 are presented in Figure 4.13, where greater differentiation between the systems is observable. While all show the main surface depressions, T3D appears to have improved definition around the edges compared to the optical systems. Focusing on the optical systems, OMS has much less definition overall (for this measurement) than the other systems, however, this may be due to the colour scale applied.

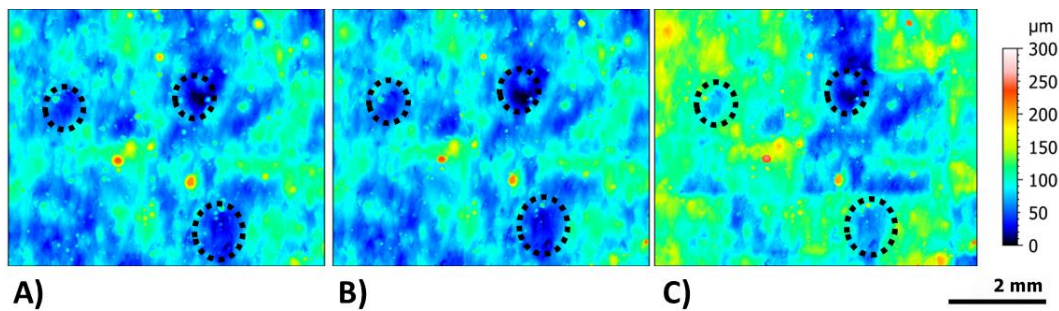


Figure 4.13: Surface Measurements of top surface of sample S3 with matching surface depressions highlighted. The measurement systems used were T3D (a), OAS (b), and OMS (c).

It is well known that tactile profilometers can encounter difficulties with high aspect-ratio features due to the surface contacting the stylus flank rather than the tip, artificially reducing slope angles and in some cases reducing depths of features [92], [175]. Similarly, optical systems can struggle with these features due to inappropriate illumination of the slopes and the excessively small regions in focus at any time at high inclinations. From the results observed here, and assessment of NM points, it is probable these effects are not present on the presented surfaces. The effect of inappropriate illumination has been suitably mitigated through measurement setup, with the agreement between results indicating this has been successful.

Also observable in Figure 4.13(c) is the reduced definition of many asperities, and stitching artefacts. The artefacts manifest as sudden height changes or discontinuities in the image, this is shown in more detail in Figure 4.14. The quantifiable effects of this are discussed in further detail in Section 4.3.7.1D, but it is clear that significant errors can be present at the junction between individual FoVs. It is notable that while the OAS system also uses image stitching to extend the FoV, it does not report the same artefacts, likely due to having a consistent coordinate system to work from, especially the Z-height reference.

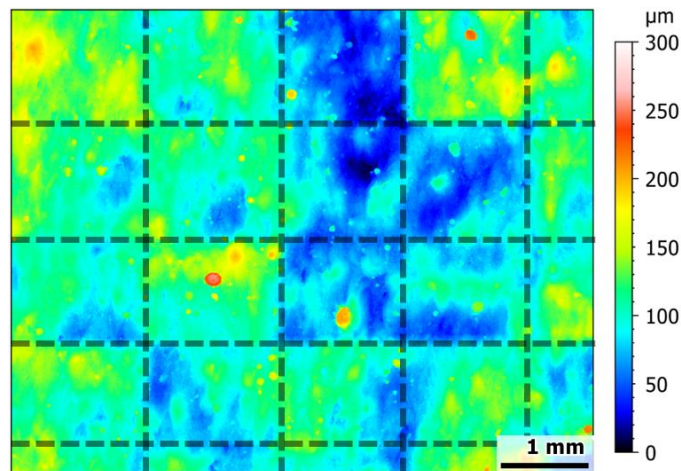


Figure 4.14: OMS result from the top surface of S3, showing stitching artifacts (indicated by dashed lines).

It should be noted that this is present even with relatively large overlaps between measurements (0.25 mm/0.15 mm along X/Y respectively). The stitching algorithm within MountainsMap is also somewhat inconsistent, typically with rougher surfaces stitching with minimal artefacts, while smoother surfaces can fail to stitch at all. There are controls within the algorithm that determine the “search area” between measurements (measurement overlap) and if levelling is applied prior to stitching. In both cases, there is an effect on the time taken to calculate the stitch. For large arrays, such as  $5 \times 6$  used here, the stitching algorithm can take an hour to complete on the available computer, making it impractical to optimize the performance in every case. Section 4.3.4 compares the roughness values calculated from the different measurement processes, and from those results it is assumed that the stitching artefacts are insignificant in terms of the calculated surface roughness ( $S_a$ ,  $S_q$ , etc.).

Another example of measurement errors is unique to the optical systems. Due to their reliance on the optical properties of a surface to take a measurement, the surface condition can have an outsized effect on measurement quality. It has been discussed above how insufficient illumination (e.g., at the bottom of deep features) can result in incorrectly measured heights, excessive illumination can have a similar effect. For example, a very shiny surface can easily over-expose the microscope’s sensor making it impossible to calculate the pixel heights in the affected regions. An alternative effect is where a highly reflective surface can act as a focussing element, leading to the profilometer calculating the height of maximum focus/contrast (and therefore surface height) to be significantly different from where the true surface is. This is shown in Figure 4.15(a). A similar effect can occur with tactile profilometers where the stylus loses contact with the surface (known as skipping), however, this is mitigated through machine/stylus design and traversal speed.

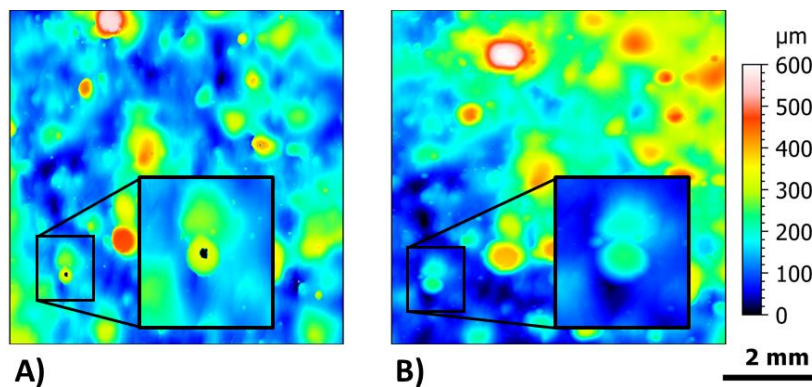


Figure 4.15: (A) OAS result showing erroneous points (black region in inset), and (B) the same surface and region from T3D without the erroneous results.

Mountains contains an operator to remove outliers such as these, however, due to the highly complex nature of AM surfaces (especially those built vertically) care must be taken to ensure only outlier points are removed and not features on the surface (e.g., adhered particles). Therefore, this function was not used for any of the work presented in this thesis.

There was one further, significant, way in which the measurement systems differed, the acquisition times, and the effort required to generate and process the data. Some estimates for the durations of measurements using each system are shown in Table 4.5. The OAS and T3D systems are both “set and forget”, in that they do not need continued attention after the measurement is commenced. On the other hand, the OMS and T2D measurements required constant operator attention. In addition, the OMS system also required extensive operator time in order to stitch the measurements ( $\approx 1$  hr), something the OAS and T3D systems do automatically. Therefore, when measuring large areas such as this, it is advantageous to use a system similar to either OAS or T3D. T2D is also a time-efficient choice, however the low measurement resolution also needs to be accounted for.

Table 4.5: Estimates for the time required to measure an  $8\text{ mm} \times 8\text{ mm}$  area using the different systems.

System	Setup	Measurement time ( $8\text{ mm} \times 8\text{ mm}$ )
OAS	20 min	90 min
OMS	3 min	40 min
T3D	20 min	6 hours
T2D	1 min	15 min (10 profiles)

To summarise the qualitative comparison of the surface measurements, while all systems used were able to resolve the surface features present, each has its own limitations. T3D reports features elongated in the Y-direction, thought to be due to the different sampling rates used in X/Y. The optical systems resolve the shapes of features consistent with each other but have the inherent limitations of optical systems; namely, steep surfaces, high aspect-ratio features, and inconsistent optical properties (reflectance) negatively impacting the FV algorithms used. Finally, the OMS system shows extensive stitching artefacts on the surfaces of interest, highlighting the trade-off between resolution and FoV. All systems evaluated here have a limited Z-range, either due to the working distance of the chosen objectives (OAS, OMS) or the available gauge movement (T3D), making it worthwhile assessing a surface prior to measurement to identify features that could exceed these limits. This all comes together to emphasise the requirement for appropriate measurement setup to minimize errors.

#### 4.3.3 Filter Selection

After the surface measurements were prepared according to the process described in Sections 4.2.3 and 4.2.5 the first comparison was the effect of filter nesting index for each surface and measurement system. The relative difference ( $\xi$ ) between the two nesting indices was quantified using Equation 4.2, taking Sa as an example. Where the subscripts indicate the filter nesting index used.

$$\xi = \frac{|Sa_{0.8} - Sa_{2.5}|}{Sa_{0.8} + Sa_{2.5}} \times 100 [\%] \quad \text{Equation 4.2}$$

It can be seen from Figure 4.16(A) that Ssk and Sku are most affected (higher  $\xi$ ) by the choice of nesting index (average of 16.9% and 16.4%), while Sz and Sp are the least affected (average 3.4% and 3.9%). As both the Skewness (Ssk) and Kurtosis (Sku) of a surface can be thought of as describing the shapes of features (or more accurately, the shape of the height distribution of points) it makes

sense for these to be strongly influenced by the choice of nesting index. Most parameters are affected similarly by the nesting index irrespective of which measurement system was used, with the exception of Sv and S10z which had a range of 8.3% and 9.3% respectively. There is no clear consensus for how nesting index affects measurements from the three systems relative to each other.

Meanwhile, Figure 4.16(B) clearly shows the top surfaces are much more significantly affected by the choice of nesting index than the side surfaces (average of 16.2% and 5.3% respectively). This highlights the different filtration requirements of surfaces built vertically (side) and horizontally (top). From this, it is evident different filtration strategies may be required for surfaces depending on build orientations.

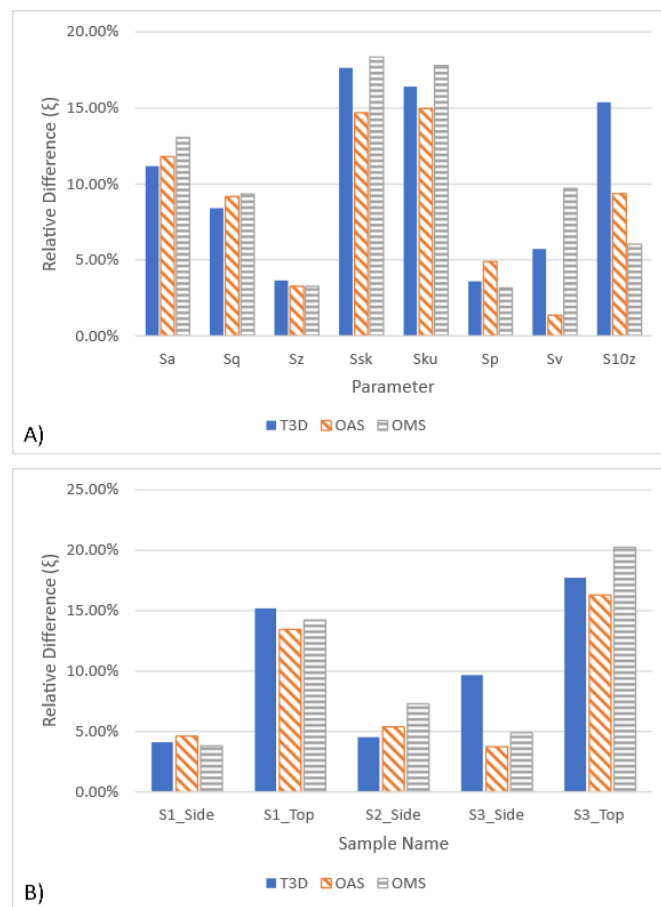


Figure 4.16: Effect of changing nesting index (0.8 mm and 2.5 mm) on (A) calculated roughness parameters, and (B) overall effect on each examined surface.

Repeating once more the observation from Lou et al. that “It is not clear what roughness and waviness mean to AM” [89] it is clear that this fundamental question should be a research priority in order for meaningful roughness values to be produced. There is a growing school of thought within AM metrology to forego “roughness” and “waviness” and instead evaluate parameters from the primary profile (or S-F surface) [2] to circumvent this issue.

It may remain beneficial to filter the surface measurements in specific circumstances, such as the influence of surface texture on mechanical properties (fatigue, tribology) or investigating specific manufacturing or post-processing features (e.g., weld ripples). However, even in this case there is the prerequisite to understand the purpose of a surface measurement, in terms of some surface function or property, to maximize the knowledge gained [90]. In this instance, as these results show,

it is ill-advised to prescribe a single nesting index for use on all AM surfaces, or even all L-PBF surfaces. The main message across the literature is to ensure details about how the measurement was taken, and data processed are included alongside any roughness parameters chosen [75].

#### 4.3.4 Roughness Values

This section will discuss only the comparisons between computed values for various surface roughness parameters depending on the measurement system used. Leach et al. have previously suggested that currently established surface roughness parameters may not be appropriate for AM [2]. Therefore, no comment is provided as to the appropriate choice of roughness parameter, or their effectiveness at characterising AM surfaces. It has been widely suggested that the choice of roughness parameters used to characterise a surface should be related to the part's intended function [27].

##### 4.3.4.1 Arithmetic Mean and RMS Heights

The arithmetic mean deviation ( $R_a$ ,  $S_a$ ) and root mean squared (RMS;  $R_q$ ,  $S_q$ ) parameters are two of the most common roughness parameters reported in the literature [90], favoured due to their simplicity and ability to provide a broad description of a surface. The results for Arithmetic Mean are shown in Figure 4.17, and those for RMS roughness in Figure 4.18.

Looking first at Figure 4.17(A), the areal measurement systems all report similarly for every surface when using the 0.8 mm filter. The average variation was found to be between 2.9% on  $S1\_Top$  and 7.2% on  $S2\_Side$ . Figure 4.17(B) shows a slightly increased variance between measurement system (5.1% to 8.8%) when using the 2.5 mm nesting index. Overall,  $S_a$  is robust to changes of measurement system when focusing on shorter spatial wavelength components, but with a slight increased sensitivity when analysing longer wavelength components. This is likely due to  $S_a$  being an averaged parameter over the entire surface, and therefore only weakly influenced by singularities and outliers. The same cannot be said of the  $R_a$  values.

While it is well known that areal and profile results should not be directly compared due to the differences in computation, it is useful to assess if the same trends are present for both. It is plain to see the T2D results were about half that of the areal systems for  $S1\_Top$  (0.8 mm nesting index), and over 50% greater on  $S1\_Side$  and  $S2\_Side$  (2.5 mm nesting index). This highlights one of the main pitfalls of profile measurements, by design they only capture a “*Vanishingly small fraction of the surface area*” (Vorburger and Raja [52]) and therefore miss a significant proportion of the complexities of AM surfaces<sup>12</sup>. Compounding this, as the  $R_a$  values presented are the maximum calculated from each surface, the statistical robustness of this method is limited. The  $R_a$  values fell within the same range as the  $S_a$  results for the remaining surfaces, however the uncertainty in these is much greater due to the aforementioned issues.

---

<sup>12</sup> One way to improve reliability/accuracy of profile measurements would be to increase the number of profiles measured. This, however, would quickly result in effectively taking a very low Y-Resolution areal measurement (the consequence of which is discussed in Section 4.3.6)

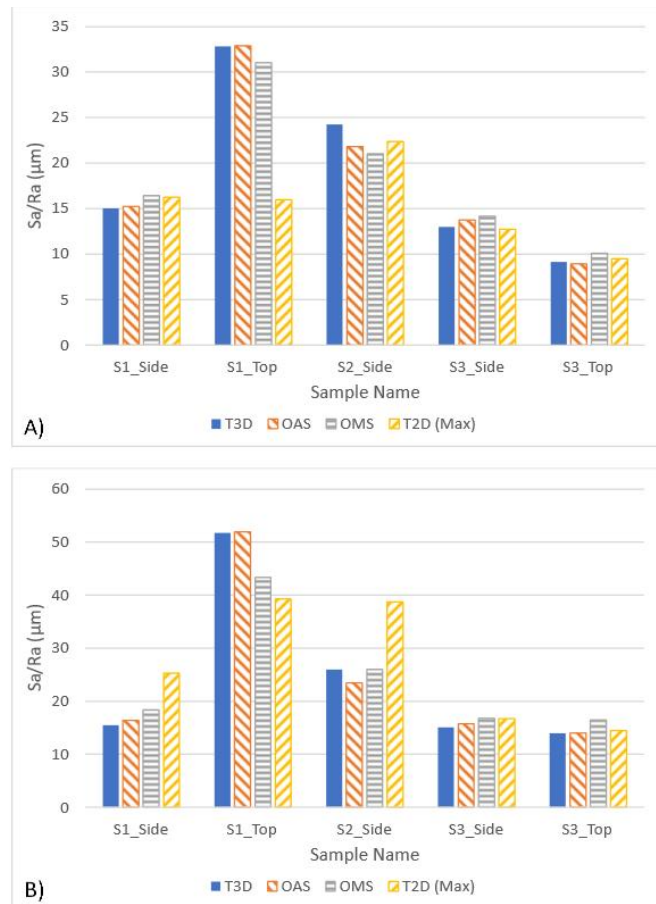


Figure 4.17: Arithmetic Mean Roughness values calculated from different measurement systems, after filtering with a (A) 0.8 mm nesting index, and (B) 2.5 mm nesting index.

The story painted by the RMS results ( $S_q$ ,  $R_q$  – Figure 4.18) are similar, with the areal results are in general agreement for all surfaces after filtering with a 0.8 mm nesting index (differences between 0.5% and 6.4%). There is increased variation when then 2.5 mm nesting index is used – an average of 7.2%, approximately double that using 0.8 mm nesting index. The greater sensitivity to the measurement system when analysing longer spatial wavelength components is more pronounced for the  $S_q$  results than  $S_a$ .

The profile results (T2D,  $R_q$ ) are lower than the areal results when using the 0.8 mm filter, and by significant margins (13% on S3\_Side, to 64% on S1\_Top). The 2.5 mm nesting index results are mixed, with those from S3 being within the range of the areal results, S1\_Top being lower by about 17%, and the remaining two surfaces returning  $R_q$  results higher than the  $S_q$  values. This indicates that while  $S_q$  is also robust to changing measurement system, it is not possible to compare the profile and areal results, even to assess trends between surfaces. If RMS roughness is of interest, areal measurement systems are essential to promote confidence in the results.

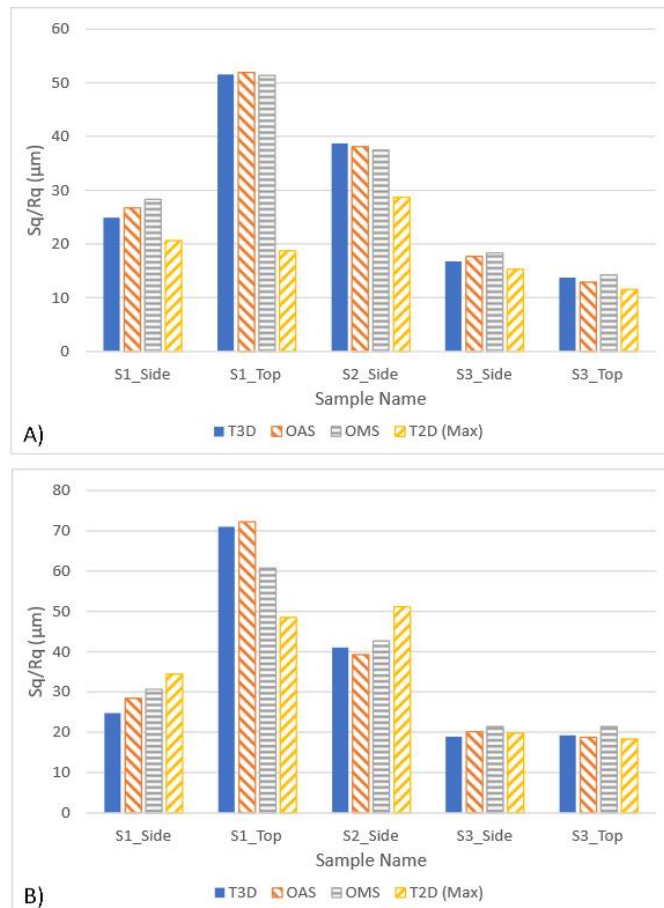


Figure 4.18: RMS Roughness values calculated from different measurement systems, after filtering with a (A) 0.8 mm nesting index, and (B) 2.5 mm nesting index.

#### 4.3.4.2 Skewness, Kurtosis, and 10-point Height

It was expected for the Skewness and Kurtosis values to be more sensitive to measurement system as they represent the shape of the height distribution of a surface, and the 10-point height to also be more variable as it is determined based solely on the extremes of a measurement.

Looking first at Skewness ( $S_{sk}$ ,  $R_{sk}$  – Figure 4.19), on the whole, the areal results are in good agreement – 6 measurements under 10% variation, and S2\_Side at 10.9% (0.8 mm filter), while the remaining three surfaces (S3\_Top, and S3\_Side with 2.5 mm filter) are in significant disagreement (>20%). It is likely these high variabilities are the result of measurement outliers and, in the case of OMS, stitching artefacts. While the measurements were processed with a low-pass 2.5  $\mu\text{m}$  filter to minimize the effects of measurement noise and the different spatial sampling of the systems, it is not inconceivable that there is still some noise present in the measurements affecting the skewness results.

In a similar way to the previous results, when using a 0.8 mm nesting index filter, the profile results cannot be relied upon to give an accurate comparison of the skewness of different surfaces. The effect is reduced when using a 2.5 mm nesting index (Figure 4.19(B)), but the average discrepancy to the areal results is 25% and still does not reflect the same trends as the  $S_{sk}$  values. This is unfortunate as there has been much interest into the skewness of surfaces as a differentiator between build orientations [88], [94], [96], with these results indicating the necessity to use areal measurements for this type of work, increasing the time requirements for those investigations.

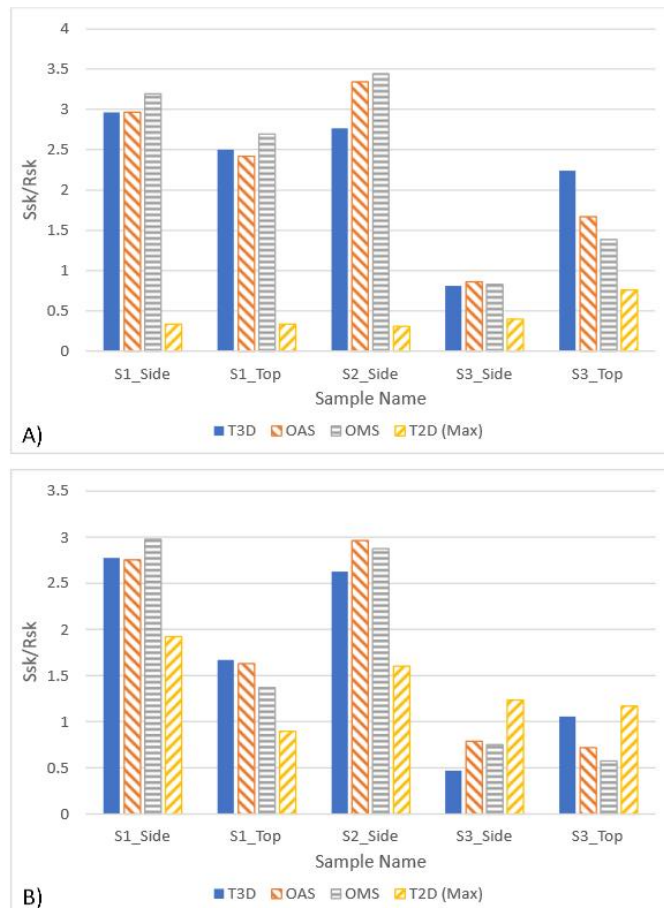


Figure 4.19: Skewness values calculated from different measurement systems, after filtering with a (A) 0.8 mm nesting index, and (B) 2.5 mm nesting index.

The Kurtosis (Sku) values are more variable again than Ssk, averaging about 15% across all surfaces and both nesting indices used (Figure 4.20). S1\_Side had the greatest variability at 23% with the 0.8 mm filter and 26% with the 2.5 mm filter, with S3\_Top also performing poorly at 24% with the 2.5 mm filter. The Rku values show poor correlation to the Sku values irrespective of the nesting index used. It is therefore not advisable to rely upon profile measurements to evaluate the kurtosis of a L-PBF AM surface.

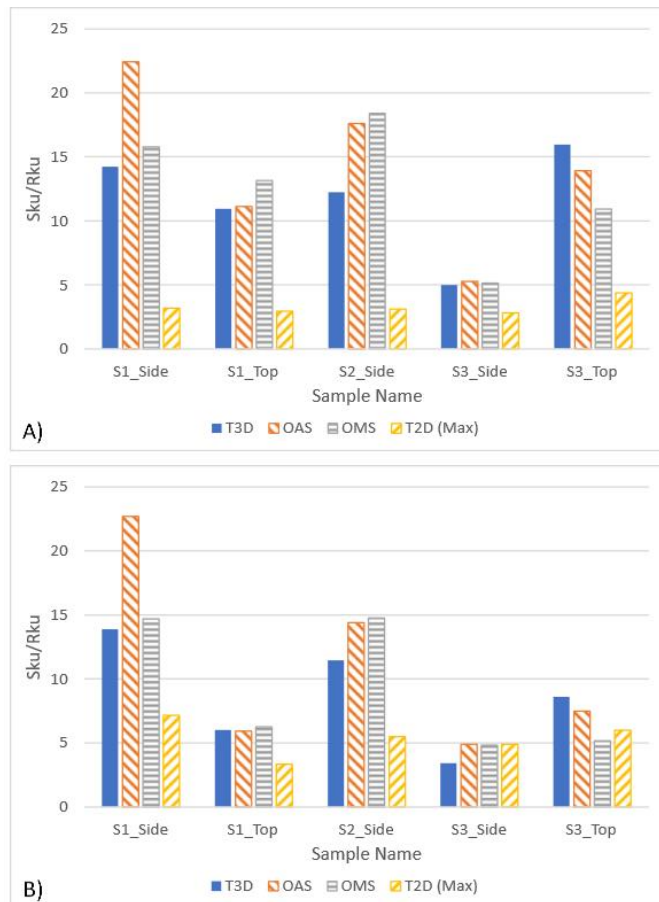


Figure 4.20: Kurtosis values calculated from different measurement systems, after filtering with a (A) 0.8 mm nesting index, and (B) 2.5 mm nesting index.

Finally, looking at the S10z values (Figure 4.21) it is clear that the different measurement systems report very differently. S1 is especially problematic, with OAS reporting values approximately 45% higher than the other two systems. As the same software was used to process all measurements, differences in data processing was not the source of this discrepancy. Referring back to Figure 4.12, it can be seen that the top surface of S1 had a series of very pronounced peaks on the surface. Furthermore, as seen in Figure 4.15 very tall peaks are liable to be measured incorrectly due to the reflectivity, giving a likely explanation for the very large errors observed here.

The remaining surfaces have average discrepancies of 13% and 20% (0.8 mm and 2.5 mm nesting indices respectively). While better, this disagreement is significant and therefore the choice of measurement system is an important factor, further emphasising the requirement to provide full details of all aspects of a measurement system and data processing when presenting roughness results.

The latest revision of ISO 4287 does not include a 10-point height parameter, and therefore profile results are not included for comparison here.

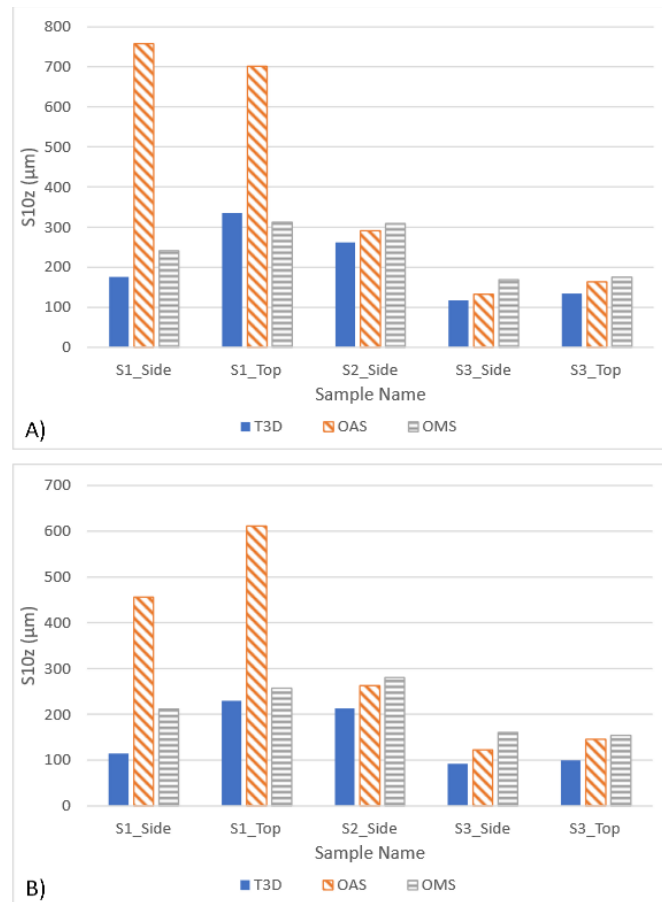


Figure 4.21: 10-point height ( $S_{10z}$ ) values calculated from different measurement systems, after filtering with a (A) 0.8 mm nesting index, and (B) 2.5 mm nesting index.

#### 4.3.5 Analysis of Surface Lay and Isotropy

The calculated isotropy values are shown in Figure 4.22, as can be seen, the results follow a similar trend for all measurement systems. The exception is OMS for S2 and S3 where the values are much lower than the average calculated from the other systems (29, 34, and 26 percentage points each). This reduced isotropy (and therefore greater lay) on these surfaces is likely due to the stitching artefacts discussed previously in Section 4.3.2. The average isotropy for the surfaces (excluding OMS on S2 and S3) were all in excess of 70%, indicating the effect of lay on these surfaces is minimal. Furthermore, there is no significant difference between the isotropy of surfaces built in different orientations in this sample set. Therefore, it can be assumed that if there is an influence of the layer height it is insignificant when compared to other roughness factors, on the primary profile / S-F surface.

The practical implication of this is that profile measurements should be somewhat agnostic towards trace direction across a surface and can be positioned to maximize the profile length in areas where space is limited. These results also show the proposed method of evaluating lay is effective and comparable to other methods. If lay is suspected, a series of line profiles can be taken at various orientations across the surface (ideally in line with and perpendicular to the assumed lay). The PSm parameter is then calculated and compared based on trace direction. Greater differences between the different orientations indicate a stronger lay.

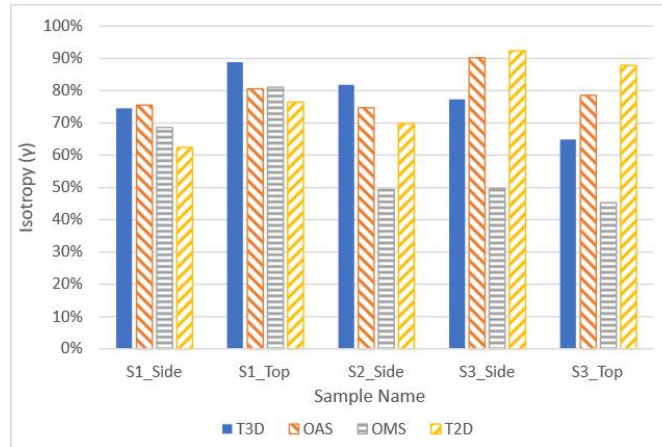


Figure 4.22: Isotropy values ( $\gamma$ ) calculated by MountainsMap (areal measurements) and using PSm (profile measurements).

### 4.3.6 Resolution

#### 4.3.6.1 Tactile Y-Spacing

Looking at Figure 4.23, different trends can be seen for different parameters. Once again, the “averaging” parameters ( $S_a$ ,  $S_q$ ,  $S_{sk}$ ,  $S_{ku}$ ) are less strongly affected than the “extreme” parameters ( $S_p$ ,  $S_v$ ,  $S_z$ ,  $S_{10z}$ ), shown in Figure 4.23. Of the former, in most cases the difference was under 0.4%, with  $S_{sk}$  and  $S_{ku}$  exceeding this when using the 2.5 mm filter (Figure 4.23(C)). Of the extreme parameters,  $S_{10z}$  is the most strongly affected with over 1.5% deviation at all Y-spacings, with  $S_v$  also strongly affected when processed with a 0.8 mm nesting index (>1% at all resolutions).  $S_p$  was weakly influenced by resolution, averaging 0.15% except for with the 2.5 mm nesting index at 100  $\mu\text{m}$  spacing where the difference was nearly 3%.

Finally, it can be seen in Figure 4.23 (D) there is a marked increase in  $\xi$  for  $S_p$ ,  $S_v$ ,  $S_z$ , and  $S_{10z}$  at 100  $\mu\text{m}$  spacing, with  $S_{10z}$  having the highest  $\xi$  at all resolutions. Overall, most parameters respond similarly to changes in resolution irrespective of the filter applied,  $S_{sk}$ ,  $S_{ku}$ , and  $S_{10z}$  are much more strongly affected with the 2.5 mm nesting index than when using 0.8 mm.

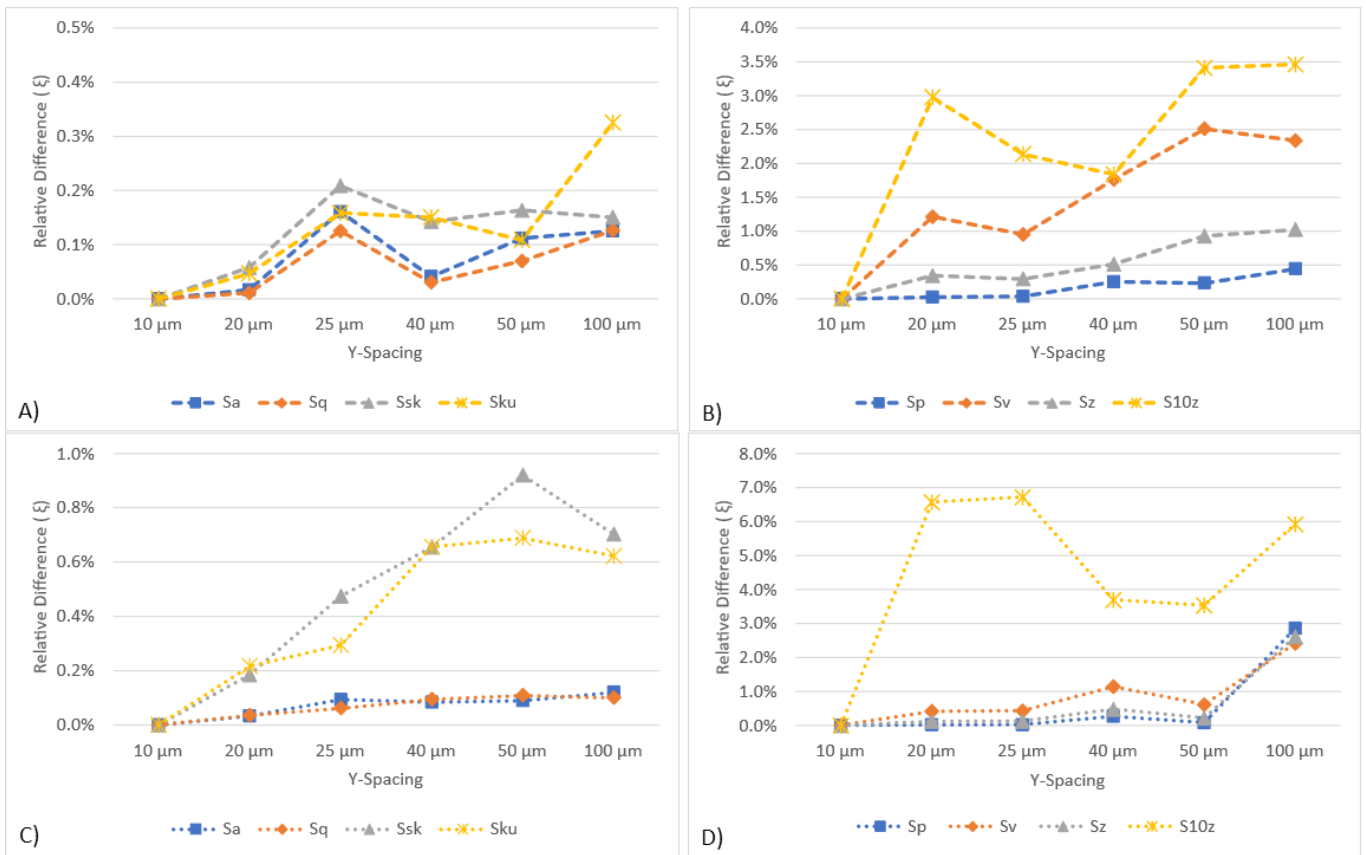


Figure 4.23: Effect of Y-spacing on different roughness parameters (A, C) Sa, Sq, Ssk, Sku, and (B, D) Sp, Sv, Sz, and S10z, when processed with different nesting indices (A, B) 0.8 mm, and (C, D) 2.5 mm.

This again shows the dependence on measurement purpose on setup – if parameters such as Sv and S10z are of interest the Y-spacing has a strong effect and higher-fidelity measurements should be conducted. Conversely; Sa, Sq, Ssk, and Sku appear agnostic towards Y-spacing due to them being calculated from an average deviation over the full surface (see Table 2.2). Therefore, lower resolutions can be used in order to reduce measurement time. Finally, Sp and Sz were not strongly influenced by reduced Y-resolution at spacings  $\leq 50 \mu\text{m}$ .

#### 4.3.6.2 Optical Magnification

Performing the same comparisons for the OMS results after down-sampling gives the plots shown in Figure 4.24. There is again a sharp distinction between the “averaging” parameters (Figure 4.24(A)) and the “extreme” parameters (Figure 4.24(B)), with the former showing very small deviations ( $<0.04\%$ ) after reducing the X-Y resolution. The extreme parameters are more strongly influenced, but to a much lesser extent than the T3D results, with the maximum difference being 3.06% compared to the full resolution results. Only the Sz, Sv, and S10z results changed by more than 1%, and even then, only when emulating the  $2.5 \times$  objective. These differences are very low, and unlikely to impact measurement quality – especially for the averaging parameters where the differences are of a similar magnitude to those caused by noise.

This shows that, for these AM surfaces, lower magnification objectives may be desirable as the measurement quality is retained while enabling much larger regions to be measured in a time-efficient manner. Using an objective with half the magnification yields a  $4 \times$  time reduction in data acquisition for a given total FoV, with additional benefits in the time required for data processing, especially image stitching.

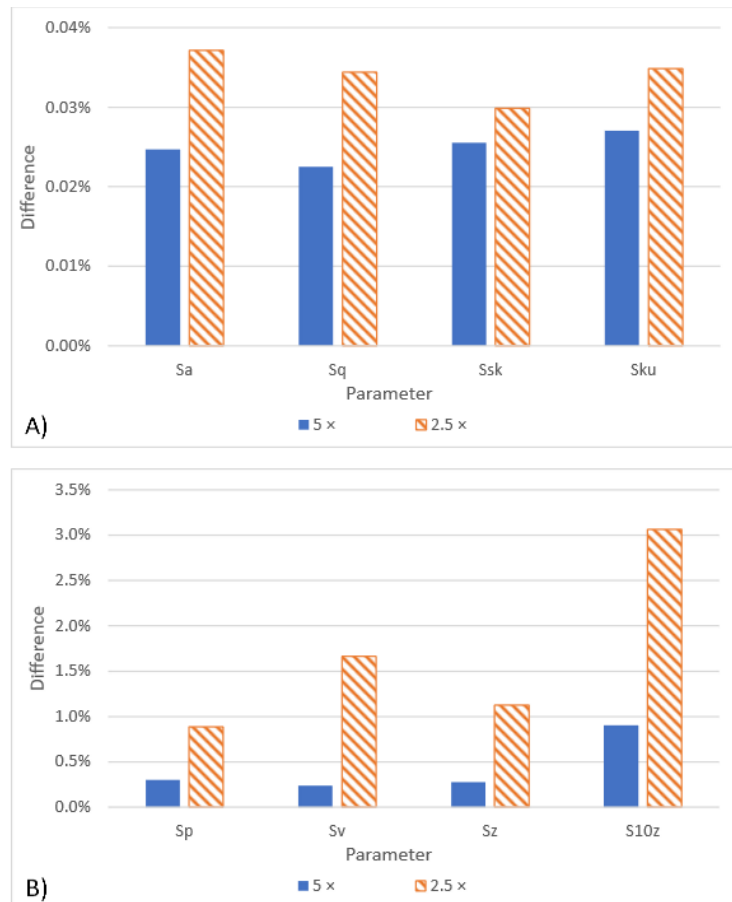


Figure 4.24: Effect of optical magnification on different roughness parameters (A) Sa, Sq, Ssk, Sku, and (B) Sp, Sv, Sz, and S10z.

### 4.3.7 Uncertainty

An uncertainty analysis was conducted using the Sensofar Smart profilometer, to assess the influence of some key measurement conditions and post processing operations. These included a quantification of the measurement noise, the use of positioning jigs, applying the localisation operator, and finally image stitching.

#### 4.3.7.1 Measurement Analysis

##### A. Measurement Noise

The maximum absolute deviation of any point to the average value was found to be 102  $\mu\text{m}$ , with an average absolute deviation of 0.33  $\mu\text{m}$  and a standard deviation of 0.72  $\mu\text{m}$  (i.e., 95% of values are within  $\pm 1.44 \mu\text{m}$  of the mean value). The distribution of errors is evenly distributed above and below the mean surface, without any skew, as shown in Figure 4.25. This even distribution implies there are not systematic sources of error biasing the results one way or the other, however, the averaging process may be masking some effects.

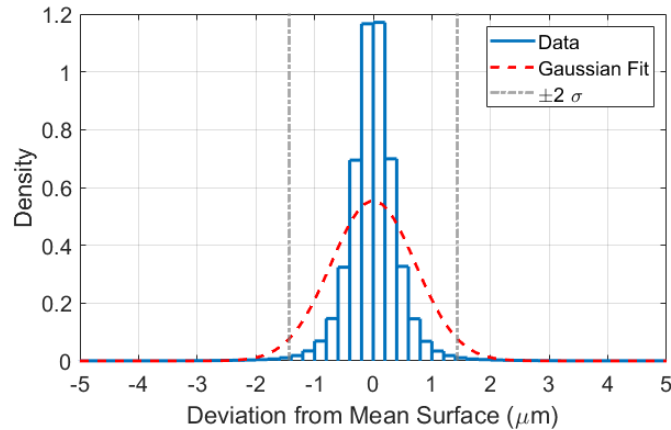


Figure 4.25: Probability density function of calculation deviations from mean surface of measurements taken without moving sample between measurements.

By investigating the average height map (mean surface, Figure 4.26(A)) in conjunction with the maximum deviation across the surface (Figure 4.26(B)), it can be seen that the height deviations are spread somewhat uniformly across the surface, and not concentrated around specific features such as tall peaks or deep valleys. This indicates the deviations noticed are likely due to measurement noise (random variations) and not from some intrinsic measurement effect.

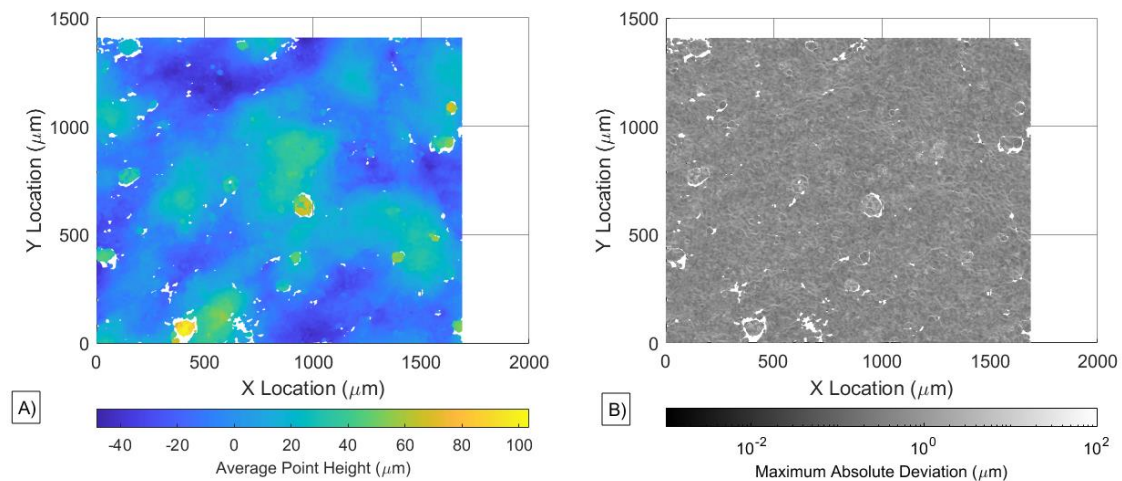


Figure 4.26: (A) Average heights of measured points (the mean surface) from an examined surface, (B) maximum absolute deviation of measured points from mean surface. Note, colour scale for (B) is logarithmic.

However, both the proportion of “non-measured points” – pixels where the height could not be computed – and the measurement variability was greatly influenced by the illumination settings used. For example, altering the axial illumination between each measurement approximately doubled the standard deviation to  $1.55 \mu\text{m}$ . This clearly shows the importance of appropriate setup when using optical solutions to measure a surface.

### B. Positioning Repeatability

When locating the sample using a jig, visual inspection of height maps showed some small misalignment between images. This was quantified by an automated MATLAB script (provided in Appendix I) that found the average translation and rotations between each surface and a reference image. For this purpose, the reference was selected to be the first measurement collected from each location. From this, it was found the average translation error was  $83 \mu\text{m}$  and a rotational error of

2.75°, while the maximum errors were 199 μm and 9.3°. This is shown in Figure 4.27, where the three different marker types represent the three different surfaces evaluated.

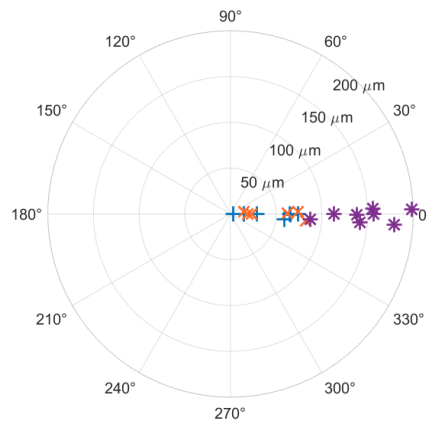


Figure 4.27: Polar plot of positioning error of measurements when using an alignment jig. The radial distance shows the translational error while the angle shows the rotational difference (both compared to an arbitrary baseline measurement).

Both the translation and rotational discrepancies can be explained by the compliance in the system. The X-Y stage is not meant to transmit horizontal loads and therefore the force applied when locating the sample into the jig may be enough to cause a slight shift. Compounding this, the jigs used were manufactured by FDM, and therefore not as stiff as if they were cut from sheet material. Another factor is the uneven surfaces of both the samples and jigs making precise positioning even more difficult.

With respect to the total measurement size, this misalignment equates to about 5% of the measurement range. When measuring larger areas (by stitching multiple FoVs together) this relative misalignment will be significantly decreased. Furthermore, as measurements later in this thesis are not evaluated through point-heights this positioning error is not impactful in a practical manner.

In terms of Z-heights, the misalignment resulted in average height errors of 4.56 μm with a standard deviation of 9.8 μm. This is clearly much higher than the measurements taken without moving the sample, however, can be easily explained by the very large deviations around large asperities (and deep valleys) where the measurements do not exactly align.

### C. Localisation

While great care was taken during the localisation procedure to achieve the closest alignment possible it was not possible to obtain perfect results. Figure 4.28(A) shows a height map of the average Z-values for each point (the mean surface), while Figure 4.28(B) shows the maximum absolute deviation of points to the mean surface. As can be seen, the largest errors are in surface depressions/valleys (blues in Figure 4.28(A)), this is likely due to these areas being insufficiently illuminated (occluded by nearby tall features) reducing the accuracy of the height calculations. This leads to an average height deviation of 0.82 μm with a standard deviation of 1.62 μm, higher than that of the measurement repeatability by 2.5 and 2.25 times respectively.

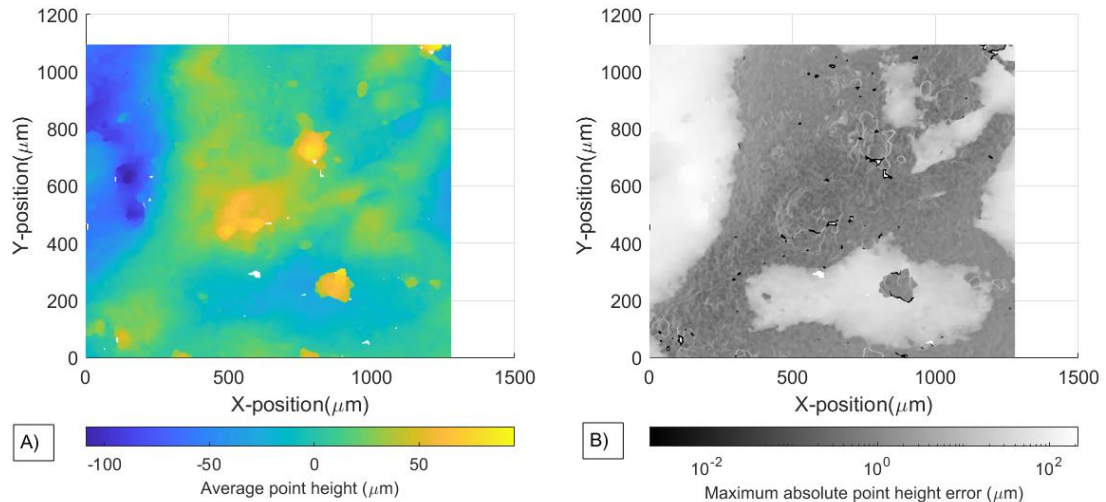


Figure 4.28: (A) Average heights of measured points (the mean surface) from an example surface, (B) maximum absolute deviation of measured points from mean surface. Note, colour scale for (B) is logarithmic.

#### D. Measurement Stitching

The average height errors for the stitched images were found to be 3.52 μm with a standard deviation of 4.61 μm, increases of 4.3 and 2.8 times compared to the localisation results (10.7 and 6.4 times compared to measurement repeatability)

Figure 4.29(A) shows the average height differences between the measured surfaces and the matching stitched surface, viewed along the Y direction. The average height at each X location is shown by the red line. From this it can clearly be seen that there is a step in the centre (750 μm ≤ X ≤ 1000 μm), corresponding to where the two stitched images overlap. This indicates the stitching process is prone to errors along these joint regions. Looking at Figure 4.29(B), showing the absolute height deviation between the stitched and native measurement, it can be seen the errors are somewhat uniformly distributed across the surface. It can be seen that the darker regions are concentrated in the bottom right of each measurement (n.b., the join is nearly vertical through the centre), indicating these are regions where the stitched measurement more closely matches the direct measurement.

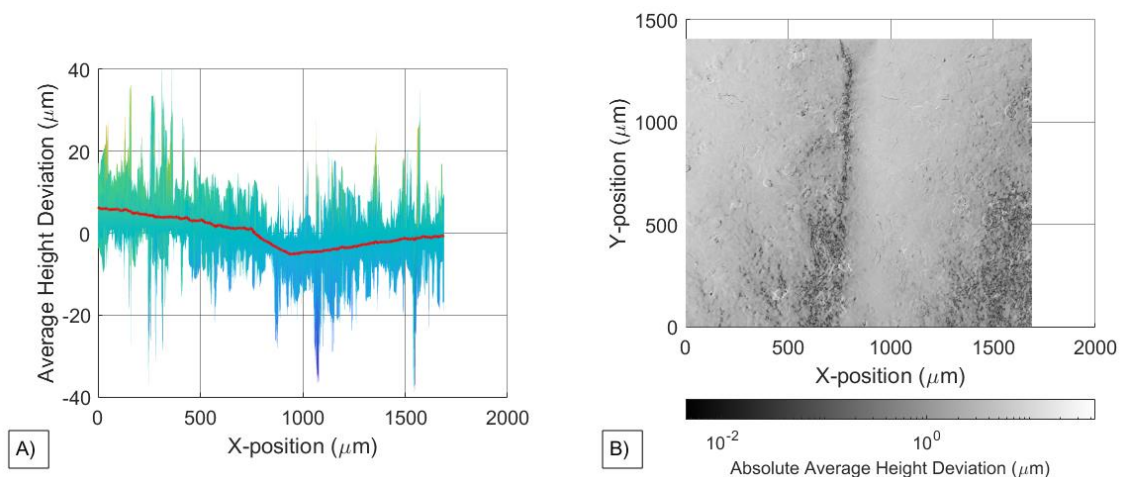


Figure 4.29: Average errors calculated comparing direct measurements with matching stitched measurements.

#### 4.3.7.2 Overall Contributions

Figure 4.30 shows the distribution of errors arising from the different evaluated sources. As can be seen, the measurement noise has a nearly vertical slope, showing the majority of points are near to

the calculated average height. Interestingly, localisation has the effect of decreasing the 95% uncertainty from 2.17  $\mu\text{m}$  to 1.44  $\mu\text{m}$ . The use of the alignment jig increased the uncertainty to 20.3  $\mu\text{m}$ , shown by an overall flattening of the curve, however the central portion ( $\pm 20\%$  of the mean) is within 1.5  $\mu\text{m}$ . This indicates that the jig accentuates the large-magnitude errors more than the low-magnitude errors.

Finally, the stitching operation further flattens the slope in the central region ( $\pm 3 \mu\text{m}$ ), showing errors are distributed over a wider range than those arising from other sources, but a reduced 95% uncertainty interval of 7.90  $\mu\text{m}$ . It can also be seen from the figure that the stitching errors are concentrated below the reference surface, likely a function of the step feature seen in Figure 4.29.

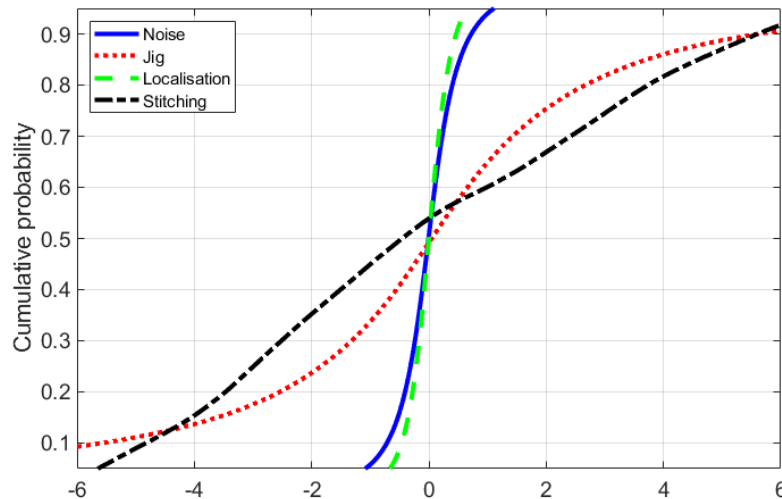


Figure 4.30: Cumulative probability curves for height errors resulting from different sources.

Overall, this shows that the amount of data processing should be kept to a minimum where practical to limit the induced uncertainties. This also highlights a potential challenge in comparing data measured in different conditions (e.g., illumination intensity) or processed differently (e.g., stitching).

#### 4.3.7.3 Effect on Roughness Parameters.

To assess how these calculated point-wise errors influence calculated roughness parameters; the  $S_a$ ,  $S_q$ ,  $S_{sk}$ , and  $S_{ku}$  were calculated for each measurement, and the variability of each set was found. These roughness parameters were chosen to avoid the influence of outliers or extreme height values that would be present when assessing parameters such as  $S_p$  and  $S_z$ . The maximum and average calculated variance for each condition is shown in Table 4.6. Similar to what was seen in Section 4.3.4,  $S_a$  and  $S_q$  were robust to additional post-processing steps with maximum variability of 2.03% and 4.87% respectively. The average change in  $S_a$  was 0.84% while for  $S_q$  it was 0.86%.

Skewness was strongly influenced (average 3.71%) however this is likely due to the very low  $S_{sk}$  values calculated on some surfaces amplifying the effect (the total range was from -0.014 to +2.9). Kurtosis was more consistent (average 1.42%) however the maximum value found (6.58%) shows care should be taken. Overall, the measurement noise (repeatability) had the greatest influence on calculated roughness parameter variability (average for all parameters, 1.3%), while the positioning jig and localisation had the greatest influence on maximum values ( $S_q$  &  $S_{ku}$  /  $S_a$  &  $S_{sk}$  respectively).

Table 4.6: Maximum variability for common roughness parameters from different data post-processing operations.

	Sa		Sq		Ssk		Sku	
	Max	Average	Max	Average	Max	Average	Max	Average
Repeatability	1.70%	1.12%	1.87%	1.13%	4.48%*	2.71%	0.79%	0.61%
Positioning Jig	1.68%	0.81%	4.87%	0.99%	4.87%	2.36%	6.58%	3.22%
Localisation†	2.03%		1.60%		17.79%		3.03%	
Stitching	0.53%	0.28%	0.67%	0.32%	3.80%	1.96%	0.88%	0.48%

\*One outlier result had a variability of over 200% due to very low Ssk values that were both positive and negative in sign.

†Only one region was analysed as part of the Localisation set.

#### 4.4 Final Methodology

Based on these evaluations the following measurement methodology is proposed, and will be subsequently followed throughout this thesis:

1. Visual inspection of surfaces to identify key features and regions that may present measurement challenges (e.g., reflectivity). Surfaces should be clean and free of debris.
2. Identify roughness parameters of interest based on surface function/properties of interest.
3. Determine the desired measurement X-Y range. In general, larger is better due to the highly variable nature of AM surfaces. A minimum area of approximately 3 mm × 3 mm should be targeted (for general roughness).
4. The measurement system used is not a primary concern, as shown by the results in Section 4.3.4. The choice is determined by availability, time commitment, and number of measurements to be taken. A skilled operator will have a greater influence on the measurement quality than specific system used (Section 4.3.7).

After data collection, it is necessary to process the results for parameter extraction. The following data-processing stream is proposed:

1. Microroughness filter (low-pass S-filter) to reduce measurement noise, this will be a function of the measurement system. For tactile measurements recommendations are available in standards (e.g., ISO 1134), meanwhile, for optical systems a nesting index three-times the pixel size on the surface is sufficient.
2. Form removal (F-operator) such as levelling.
3. Roughness filter (L-filter) to separate Roughness and Waviness components. Visually inspect results to ensure features of interest are retained. A nesting index of 0.8 mm has shown to be appropriate here, however, it is highly surface and purpose dependent.
4. Fill non-measured points (where required).
5. If comparing roughness values, as much about the measurement setup must be the same to effectively compare values, including nesting index and measurement resolutions.
6. While it is preferable to measure a surface before and after modification, in instances where this is not possible assessment of the surface variability is necessary.

Furthermore; this methodology is envisaged to be of great benefit to AM researchers and manufacturers utilising AM, through the clear and practical process enabling efficient and reliable surface roughness measurements.

#### 4.5 Surface Roughness Measurement Summary

Effective, repeatable, and reliable surface measurements are essential when working on surface modification techniques; such as smoothing, texturing, or even manufacturing of specific features. The methodology presented here has been shown to be robust to changes of measurement system

and setup in terms of calculated roughness parameters and will therefore be used throughout the following chapters.

The measurement strategy was evaluated using three different areal measurement techniques (one tactile, two optical) and one profile method, visually comparing the generated areal height maps and quantitatively comparing standard roughness parameters calculated from each. Visual inspection of height-maps showed the three areal systems all captured key features similarly, however, the optical systems encountered issues on highly reflective or especially dull regions due to incorrect illumination. For one optical system, where FoV stitching was manually performed, artefacts were induced by the stitching process, highlighting the risks associated with any additional post-processing step used. Comparing the pixel-by-pixel errors around these stitching artefacts show an average error of  $3.52\ \mu\text{m}$  compared to an unstitched measurement of the same region, approximately  $10\times$  the error estimated to be from noise. Comparing the roughness parameters calculated show these artefacts did not propagate through in a noticeable way. Furthermore, the approximate time requirement to generate measurements is reported, highlighting the benefit of “set and forget” devices that reduce the required operator effort. The most time intensive measurement system (OMS) required operator input throughout the measurement process, and to stitch the individual measurements into a range suitable for analysis.

Evaluations of the effect of changing the filter nesting-index from 0.8 mm to 2.5 mm showed a significant influence on top surfaces of around 16%, with a smaller, but still appreciable difference of about 5% on side surfaces. This shows further research is required to fully understand the applicability of different filter settings for evaluating the roughness of L-PBF Aluminium surfaces, and the likely requirement for different strategies for surfaces built in different orientations. From the results presented here, a 0.8 mm nesting index was deemed suitable based on the maximum feature size on the surfaces, and a reduction in the required measurement range compared to a 2.5 mm nesting index.

Throughout the results presented here a poor correlation was found between the profile and areal results with the exception of  $R_a$  and  $R_q$  when using the 2.5 mm filter cut-off. It is therefore suggested, wherever practical, to use areal techniques to evaluate the roughness of L-PBF surfaces. One use of profile methods identified was for the evaluation of surface lay. A technique is presented here for assessing surface directionality based on differences in the  $PS_m$  parameter, measured in different orientations across the surface. This showed close agreement to the values calculated by MountainsMap from areal data directly.

Finally, the point-wise errors induced by the processing stream (positioning using a jig, software localisation, manual stitching) were computed. The base measurement noise was estimated at  $0.33\ \mu\text{m}$  ( $\pm 1.44\ \mu\text{m}$  at 95% confidence) increasing by approximately  $2.5\times$  due to localisation and  $10\times$  from the stitching operation. The positioning jig was found to have a repeatability of  $83\ \mu\text{m}$  translation (X-Y plane) and  $2.75^\circ$  rotation (about the optical axis). The practical implication of these induced errors is a negligible effect on computed roughness parameters (average 1.3% difference across all examined surfaces –  $S_a$ ,  $S_q$ ,  $S_{sk}$ ,  $S_{ku}$ ).

## 5 Development and Evaluation of a LP Strategy for AM Aluminium Parts

*The final LP strategy developed in this section has previously been discussed at the 2022 Sustainable Design and Manufacture conference<sup>13</sup>, and published in the corresponding proceedings [63]. This section further details about how the strategy was developed, along with additional insight into the material responses to the proposed LP strategy.*

### 5.1 Introduction

For all its many benefits, AM suffers greatly from sub-standard surface quality compared to conventionally manufactured materials. For many applications this necessitates remedial work to make parts useable [73]. There are many options for post-processing of AM components, some of which were discussed in chapter 2.2.3. However, these either sacrifice the geometric freedom possible with AM processes or have undesirable environmental impacts. Due to this there is significant interest in using lasers to post-process AM surfaces previously discussed in chapters 2.4 and 2.6.2.

Furthermore, laser processing is highly adaptable, having been used for many years for micromachining operations [38], surface cleaning [8], and welding [176], among others. This opens the possibility to combine processes (e.g., polishing and machining) with a single machine, enhancing production efficiency (reduced number of setup operations) and facilitating hybrid manufacture.

### 5.2 Purpose

A series of trials were carried out to develop an LP strategy that is capable of smoothing AM aluminium surfaces. As discussed in Section 2.4.2, this is a non-trivial task due to a range of factors including the high reflectivity and thermal conductivity of aluminium, and the low melting temperature leading to a relatively narrow processing window for effective laser processing.

This chapter discusses the development of a novel LP strategy for AM AlSi10Mg surfaces where surface roughness is the primary concern. Following this the material response to the strategy is investigated, including microstructure, microhardness, and near-surface porosity. The repeatability of the developed strategy (in terms of surface roughness and roughness reduction) is also examined. Following this, in Chapters 6 and 7, the influence of the developed LP strategy on the Tensile and Fatigue performance is investigated.

### 5.3 Test Plan

#### 5.3.1 Samples

A series of test parts were manufactured using a *Renishaw AM250* using gas atomised AlSi10Mg powder supplied by Renishaw Plc. [69], the nominal composition is presented in Table 3.1 in Section 3.1. Samples measured 40 mm × 50 mm × 3 mm (h × w × d) and were manufactured using the recommended settings as discussed in Section 3.1. The samples were built with the 40 mm × 50 mm surfaces vertical and perpendicular to the recoater direction (X-Z plane). A total of 4 test samples were manufactured for this work. The samples were mechanically removed from the build plate. No further post-processing was applied other than cleaning the surfaces with compressed air prior to surface roughness measurement.

---

<sup>13</sup>9th International Conference on Sustainable Design and Manufacturing, 14-16<sup>th</sup> September 2022, Split, Croatia: <http://sdm-22.kesinternational.org/>

### 5.3.2 Strategy

#### 5.3.2.1 Strategy Development

The base laser parameters for the ablation and smoothing steps in isolation came from the previous work discussed above. A slight modification was made (based on unreported preliminary tests) for the smoothing parameters, decreasing the pulse overlaps and implementing a focus offset to improve the processing rate. The main focus of this work was to combine the previously determined ablation and smoothing steps into a cohesive strategy, resulting in superior smoothing than either step alone. Therefore, the main challenge was to optimise the number of passes for each step to work effectively within the overall strategy.

To achieve this an ablation step was followed by a smoothing step on 4 mm × 4 mm regions. The number of passes for each step was iterated to account for interactions between them. This was then followed by adding a further ablation and smoothing step and repeating the process. Throughout the process the roughness was measured before any processing, and then after each processing step to monitor the effect of each step.

#### 5.3.2.2 Hatch Angle

Eight regions were processed with four different hatch strategies: 0/90°, ±45°, 0/45/90/135°, and “random”. The random strategy is an option within the *Lasertec 40* control software, where each layer is orientated at an arbitrary angle compared to the previous. The other strategies are depicted in Figure 5.1.

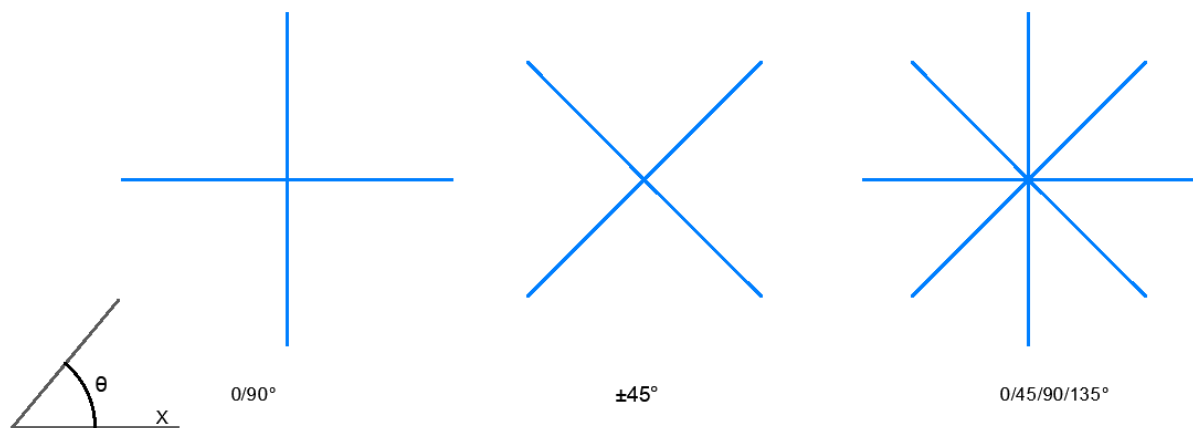


Figure 5.1: Schematic of different hatch strategies used.

#### 5.3.2.3 Optimisation

One requirement for LP to be industrially adopted is to maximize the processing rate (minimize the time taken to process a given area). To achieve this the laser power was increased to 100% ( $P_{Av} = 20$  W) and a defocus applied to maintain the same fluence as before (14 J/cm<sup>2</sup> and 12 J/cm<sup>2</sup>). The larger spot size enabled the scan speed and hatch spacing to be increased to maintain the overlap factors. In conjunction with this, further rate tests were conducted with overlaps in the range of 90% to 95%, to identify if an appropriate balance between smoothing and processing rate was met. Finally, to achieve further rate improvements, the number of passes was changed from 20 to 10 in steps of 2. A summary of the various parameters and levels is given in Table 5.1.

Table 5.1: Parameter ranges used for processing rate optimisation trials.

Parameter	Unit	Ablation Steps	Smoothing Steps
Focal offset	mm	0 – 0.38	1 – 1.34
Spot diameter	µm	32 – 35.8	53.1 – 65.1
Scan speed	mm/s	550 – 925	265 – 530
Overlap X	%	94.0 – 90.0	95.0 – 90.0
Hatch spacing	µm	3 – 3.3	3 – 5
Overlap Y	%	90.6 – 90.8	94.4 – 90.6

To evaluate the changes, small areas (4 mm × 4 mm) were processed with the process changes identified in turn. The smoothing effect, in terms of % roughness reduction, was compared to those measured in section 5.3.2.1. The alternative parameters were considered appropriate if the effectiveness (comparing reduction in roughness to initial roughness) was not equal to, or greater than, the base strategy.

#### 5.3.2.4 Comparison Between Laser Polishing of Conventionally and Additively Manufactured Surfaces.

To assess the minimum achievable surface roughness using the proposed strategy, areas of conventionally manufactured aluminium alloy surfaces were also processed, specifically, AA6062-T6 rolled bar and investment cast A357.0. In both cases the surfaces were mechanically polished using P220 SiC paper prior to LP processing to provide a uniform surface free of defects. An additional cast surface was also LP processed in the as-manufactured condition. Finally, some AM samples were mechanically polished (P220 SiC paper,  $S_a \approx 1.75 \mu\text{m}$ ) prior to LP to isolate the influence of initial roughness.

#### 3.4.6.3 Reproducibility

Once the final LP strategy was determined a series of larger areas (approximately 7 mm × 25 mm) were processed using these settings. 14 samples were manufactured and polished (as part of tensile testing, Chapter 6), giving 28 surfaces built vertically and perpendicular to the recoater direction. The samples were processed using a  $\pm 45^\circ$  hatch pattern, based on results of section 5.4.2.3, and to equalise the average length of individual laser paths. They were used to evaluate the repeatability of the process with a wider range of initial conditions, while also giving a more precise processing rate.

### 5.3.3 Surface and Material Characterisation

#### 5.3.3.1 Surface Roughness

Surfaces were measured according to the process detailed in Chapter 4 and shown in Figure 5.2. To expedite the measurement process, single FoV measurements were used. The measurements had a FoV of 1.7 mm × 1.4 mm, with a 0.8 mm L-filter applied with end effects managed (MountainsMap uses a propriety algorithm to achieve this). Measurements were taken before any processing and after each processing step on the same surface regions (X-Y positional error between successive measurements was  $\approx 83 \mu\text{m}$ , see Chapter 4.4.7).

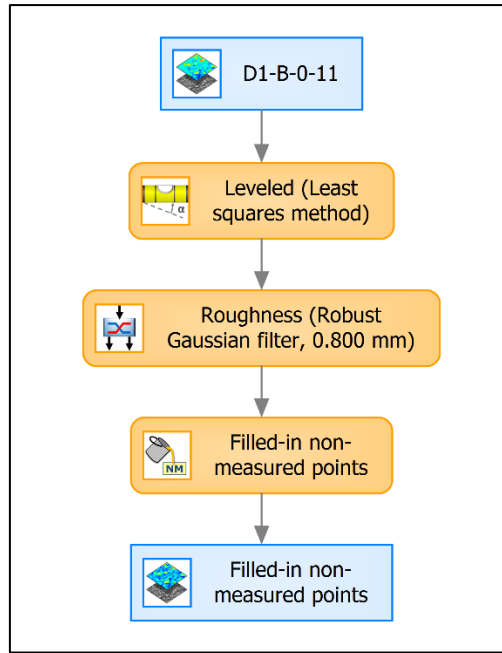


Figure 5.2: Surface measurement data post-processing flow used.

The surface roughness parameters  $S_a$ ,  $S_p$ ,  $S_v$ , and  $S_{10z}$  were used to evaluate the effectiveness of the given strategies. Both the absolute and percentage changes (Equation 5.1) were calculated for each processing step with respect to the initial AM surface, and the result of the previous processing step (where applicable).

$$Reduction = \frac{Initial - Processed}{Initial} \quad \text{Equation 5.1}$$

The larger areas (25 mm × 7 mm) were measured over a larger area by stitching arrays of 5 × 3 FoVs, resulting in a measured area of approximately 7.5 mm × 4 mm. The data processing operation was the same as with initial trials, however only initial and final conditions were measured.

### 5.3.3.2 Porosity

Voids within a material, also known as porosity, can act as crack nucleation sites, and therefore it is important to evaluate the influence of LP on the porosity in the HAZ. The process described in Section 3.4.4.2 was used to estimate the porosity of samples near the surface, and in the bulk, to evaluate the effect of LP on porosity near the surface.

### 5.3.3.3 Sub-Surface Microhardness

Samples were processed according to the final strategy, one sample with only the first step, a second with the first two steps, and so on. These were sectioned, mounted, and mechanically polished in stages, culminating with polishing using a 0.06 μm silica suspension (described in Section 3.4.1). Vickers microhardness was then conducted according to the process given in Section 3.4.2, using a Mitutoyo HM-220B. Indentations were performed in approximately 10 μm steps below the LP surface, (as shown in Figure 5.3), at multiple points within the LP-affected region. To ensure indent centre distances were maintained at least 2.5 times the average diameter (according to ASTM E-92) indents were also moved laterally by approximately 50 μm.

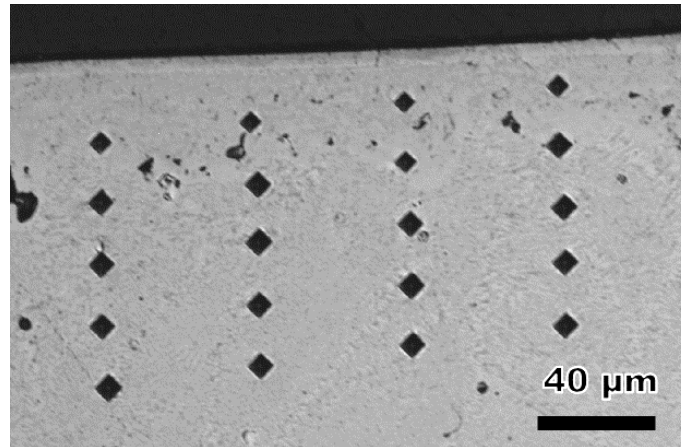


Figure 5.3: Indentation layout used to evaluate the sub surface hardness profiles.

#### 5.3.3.4 Microstructure

Microstructure was evaluated on separate samples following the process given in Section 3.4.3.

### 5.4 Results and Discussion

#### 5.4.1 Determined LP Settings.

The laser source and hatching settings determined from preliminary trials are shown in Table 5.2. It can be seen that the ablation step has nearly 15% higher fluence than the smoothing step, this greater energy intensity leads to ablation of the surface material, preferentially removing asperities as found by Petkov et al. [115]. This step also operates at a much higher frequency, and shorter exposure times, that does not permit the surface to flow into a new shape. This is borne out by the surface topography after ablation being primarily composed of small, regularly spaced dimples left by the individual laser pulses (as shown in Figure 5.4). In contrast, the smoothing step utilises a lower fluence with longer exposures and a greater total energy input, to promote melting and reflowing of the material. To increase the processing rate, the overlap factors were reduced to 94% for the smoothing step when compared to those employed by Bhaduri et al. [71] (97% in both X and Y directions). With 97% overlap, the scan speed would have been 160 mm/s, and the hatch spacing 1.6 μm (40% and 46% lower respectively), considerably reducing the processing rate.

Table 5.2: Initial laser parameters for the ablation and smoothing processes.

Parameter	Symbol	Unit	Ablation step	Smoothing step
Average Power	$P$	W	16	13.2
Scan speed	$v$	mm/s	550	265
Hatch distance	$h$	$\mu\text{m}$	3	3
Pulse Width	$T_e$	ns	15	220
Pulse Frequency	$f$	kHz	290	100
Focal Offset	$z$	mm	0	-1
Pulse Energy*	$E_p$	$\mu\text{J}$	55.2	132
Peak Power*	$P_p$	kW	3.5	0.6
Fluence †	$F$	$\text{J}/\text{cm}^2$	13.72	11.94
Pulse Overlap (X) †	$O_X$	%	94	91
Pulse Overlap (Y) †	$O_Y$	%	95	94

\* Pulse Energy and Peak power were calculated using Equations 2.4 and 2.5 respectively.

† Fluence and pulse overlaps calculated using Equations 2.9- 2.11 in turn.

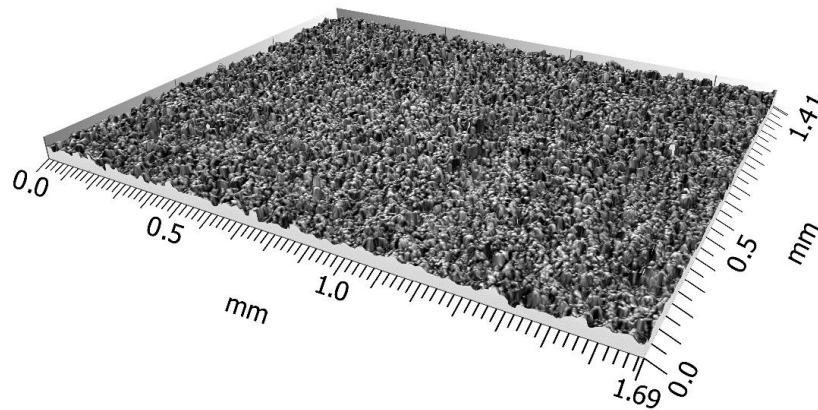


Figure 5.4: 3D view of surface roughness measurement (normalised axes) rendered with greyscale optical image showing characteristic laser ablated surface texture.

#### 5.4.2 Initial Trials

Using the above settings, initial trials iterated the number of passes for each processing step. The effectiveness of each strategy was assessed based on the change in surface roughness (Equation 5.1). Initially 2 ablation passes were used, followed by 4, 8, 16, 24, or 32 smoothing passes. These levels were chosen to have an equal number of passes in each direction when using a 90° crosshatch scan pattern. This yielded peak reductions of 59% Sa, 61% Sp, 54% Sv, and 55% S10z from the combination of 2 ablation passes followed by 16 smoothing passes (2/16 passes will be the subsequent notation). Following this, the same process was repeated for changing the number of ablation passes (2, 4, 6, 8, or 10) followed by 16 smoothing passes.

Table 5.3 summarises the process, along with maximum roughness reductions and corresponding roughness values achieved during each iteration. The full test matrix is provided in Tables A.1 and A.2, Appendix II. Optical micrographs are provided in Figure 5.5, with (A) being from the first round of trials (2/16 passes) and (B) from the third round (8/8 passes). Considering the visual appearance of the surfaces, the third round of trials appears to be significantly worse than the initial round, however it is clear when assessing the numerical surface parameter values (Table 5.3), that the surface has lower Sa, Sp, and S10z, and therefore is empirically “smoother”.

The fourth iteration (final row in Table 5.3) investigated adding a third step, also smoothing, yielding modest improvements, however, subsequent trials showed the improvement was due to

re-establishing the Z-height of the surface. The improvement was later achieved by specifying a more accurate “layer thickness” in machine control – analogous to the depth of cut for conventional machining operations.

Table 5.3: Iterations for number of polishing passes used for two-step trials, showing % reduction and surface parameter values achieved with determined number of passes (shown in **bold**).

Levels (Ablation / Smoothing)	Sa	Sp	Sv	S10z
<b>2</b> / [4,8, <b>16</b> ,24,32]	59%	9.2 μm	61%	99 μm
[2,4,6, <b>8</b> ,10] / <b>16</b>	59%	6.5 μm	70%	62 μm
<b>8</b> / [ <b>8</b> ,12,16,20,24]	35%	7.0 μm	49%	58 μm
<b>4</b> / [ <b>8</b> ,16] / [ <b>8</b> /16] †	51%	6.0 μm	53%	50 μm

\* Negative values indicate the value increased.

† One ablation step, followed by two smoothing steps of either 8 or 16 passes each.

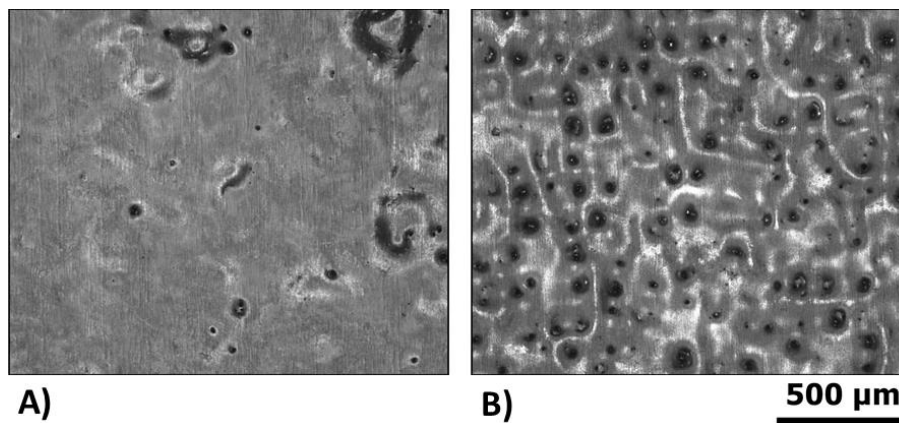


Figure 5.5: Resultant surfaces after 2-step trials (A) 2/16 passes, and (B) 8/8 passes.

These 2-step trials clearly underscored the inter-dependence of the individual strategy steps, with the optimal number of passes depending on both the preceding and following steps. From this, trials were extended to four total steps, alternating Ablation and Smoothing parameters. The levels used for the four-step strategies are presented in Table 5.4 (and the full test matrix in Table A.3, Appendix II). The ablation settings used removed approximately 6 μm of material with every pass, and therefore for the third step (2<sup>nd</sup> ablation step) four passes were chosen to balance the amount of material removed and additional smoothing achieved.

Table 5.4: Iterations for number of polishing passes used for four-step strategy trials, showing reduction and value achieved with determined number of passes (shown in **bold**) various roughness parameters.

Levels (A / S / A / S)	Sa	Sp	Sv	S10z
[4,6, <b>8</b> ] / [4,6, <b>8</b> ] / <b>4</b> / <b>16</b>	59%	4.7 μm	77%	42 μm
<b>8</b> / <b>8</b> / <b>4</b> / [ <b>8</b> ,10, <b>12</b> ,14]	71%	6.8 μm	52%	136 μm
<b>8</b> / <b>8</b> / <b>4</b> / [ <b>12</b> , <b>16</b> ]	69%	6.3 μm	64%	72 μm

Based on these initial trials, with decisions based on a combination of roughness values and roughness reductions (as presented above), along with visual assessment of the surface topographies, a strategy comprising of 8 ablation passes, 8 smoothing, 4 ablation, and a final 16 smoothing passes was found to be effective, with the lowest roughness values, and highest average reduction (see Table 5.4). Figure 5.6 shows a surface processed with this strategy, comparing it to either of the examples processed with a two-step strategy (Figure 5.5) the surface is visually

consistent and generally free of the dimples that cover the surface processed with 8 passes of both ablation and smoothing steps (Figure 5.5(B)).

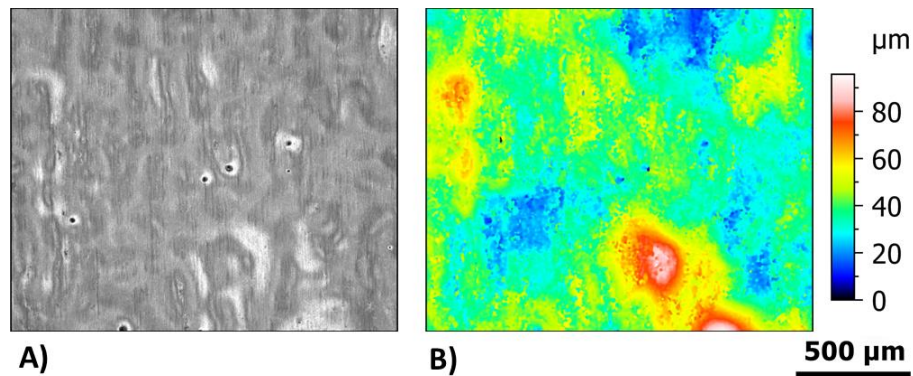


Figure 5.6: (A) optical micrograph, and (B) false-colour height map of surface processed with four step LP strategy (8/8/4/16 passes).

#### 5.4.3 Processing Rate Refinement

The determined 8/8/4/16 step LP strategy gave an area processing rate ( $R_p$ ) of approximately 60 minutes/cm<sup>2</sup>. This is significantly higher than that expected from conventional surface finishing methods ( $R_p$  between 10 and 30 minutes/cm<sup>2</sup> [177]) and therefore improvements were necessary.

To increase  $R_p$ , the maximum available average laser power was applied during each step (20 W) with an associated modification to the focal offset, scan speed, and hatch spacing to maintain the Fluence and Pulse Overlap values previously stated (Table 5.2).

The average roughness reduction for the baseline strategy was found to be 57.9% Sa, 68.0% Sp, 31.4% Sv, and 58.5% S10z. Changing the overlap factors gave similar results for Sa and Sp, but significantly worse for Sv and S10z. This implies the reduced overlaps were less able to fill in surface valleys. When maximizing the laser power (maintaining Fluence and overlap factors compared to the baseline) the effectiveness was found to increase to 87.4%, 87.4%, 67.2%, and 81.4% for the four roughness parameters in turn. This updated strategy also increased the processing rate by 30% (i.e.,  $R_p \approx 45$  min/cm<sup>2</sup>). This is substantially lower than reported by others, however none were using a multi-pass strategy. Furthermore, many authors used higher power lasers (1.7 kW, 20 cm<sup>2</sup>/min [73]) and different motion strategies. It has been shown in this chapter that an increase in laser power improves the polishing effect (requiring fewer repeat passes) and allows for larger spot diameters, reducing the processing rate. It is thus not possible to make direct comparisons.

The effect of changing the number of passes for the final smoothing step is shown in Figure 5.7. As can be seen, reducing the number of passes for the final Smoothing step from 16 to 14 slightly increased the process effectiveness, while further reductions gave reduced effectiveness and/or higher variability. The final optimized strategy is detailed in Table 5.5 and gives  $R_p \approx 40$  min/cm<sup>2</sup>.

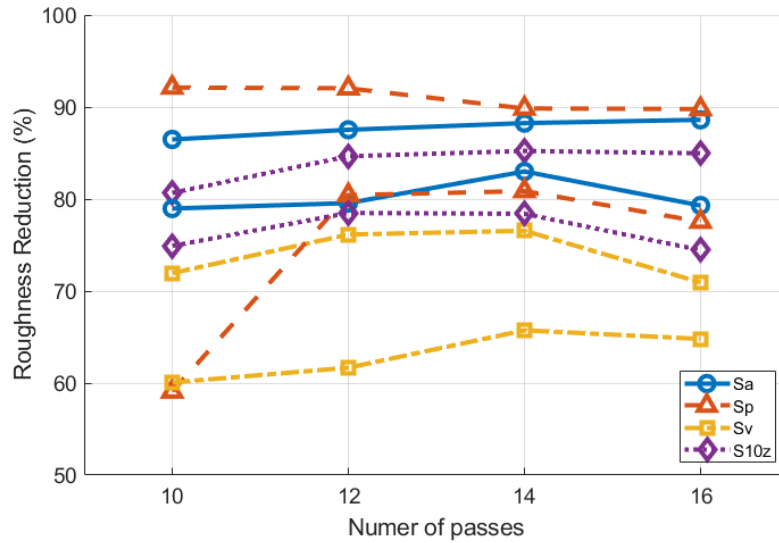


Figure 5.7: Roughness reductions ( $\pm 1$  standard deviation range) compared to number of passes for final smoothing step.

Further improvements in processing rate would necessitate a more powerful laser source capable of maintaining the required fluence levels ( $14 \text{ J/cm}^2$  and  $12 \text{ J/cm}^2$ ) with larger spot diameters. Based on the current evidence, it is possible that further increases in smoothing effect may also result from larger spot diameters.

Table 5.5: Final determined laser polishing parameters.

Parameter	Unit	Step 1	Step 2	Step 3	Step 4
		Ablation	Smoothing	Ablation	Smoothing
Scan Speed	mm/s	620	325	620	325
Hatch Distance	$\mu\text{m}$	3.3	3.7	3.3	3.7
Pulse Width	ns	15	220	15	220
Pulse Frequency	kHz	290	100	290	100
Focal offset	mm	-0.38	-1.34	-0.38	-1.34
Pulse Energy	$\mu\text{J}$	68.9	200	68.9	200
Peak Power	kW	4.3	0.9	4.3	0.9
Fluence	$\text{J/cm}^2$	13.72	11.94	13.72	11.94
Pulse Overlap (X)	%	94	95	94	95
Pulse Overlap (Y)	%	91	94	91	94
Number of passes	-	8	8	4	14

#### 5.4.4 Effects of LP Using the Final Strategy

##### 5.4.4.1 Visual Assessment of Surfaces

Visual inspection of surfaces can be a powerful tool for assessing the “quality” of a surface. The most striking feature is that the LP surface is more silver in appearance than the as built surface, which is comparatively grey, indicating the surface is free of contamination such as soot. More surface detail is revealed in micrographs, such as Figure 5.8 (n.b., the two micrographs were taken with different illumination intensities due to differences in reflectivity), where in (A) a series of asperities with very shiny peaks (white circular regions) are present across the surface. Due to their size ( $\approx 0.2 \text{ mm}$ ) and shape, it is likely these are partially melted agglomerates on the as-built surface. In contrast, the LP surface in Figure 5.8(B) is free of such features and the appearance is generally much smoother.

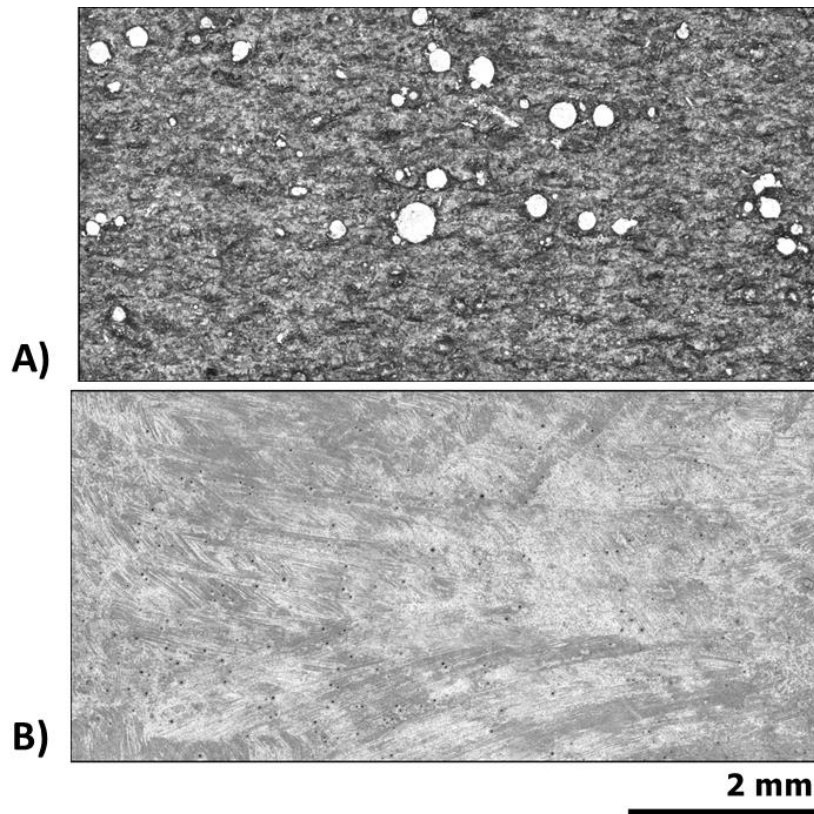


Figure 5.8: Optical micrographs of a surface (A) as built, and (B) after processing with the final LP strategy.

The last key visual inspection is of the measured surface height-maps, see Figure 5.9. The colour scales are different between the two images (range  $\approx 250 \mu\text{m}$  in (A), and  $\approx 40 \mu\text{m}$  in (B)) for clarity. Obviously, the maximum and average height of the surface is significantly reduced on the LP surface, but what can also be seen is the reduced number of asperities on the surface – corroborating the observations made on the optical images previously. An unexpected feature present on the LP surface are the very small ( $\approx 50 \mu\text{m}$ ) depressions distributed across the whole surface, shown as small blue circles in Figure 5.9(B). The source of these depressions is currently undetermined, theorised to be pores within the material breaking the surface.

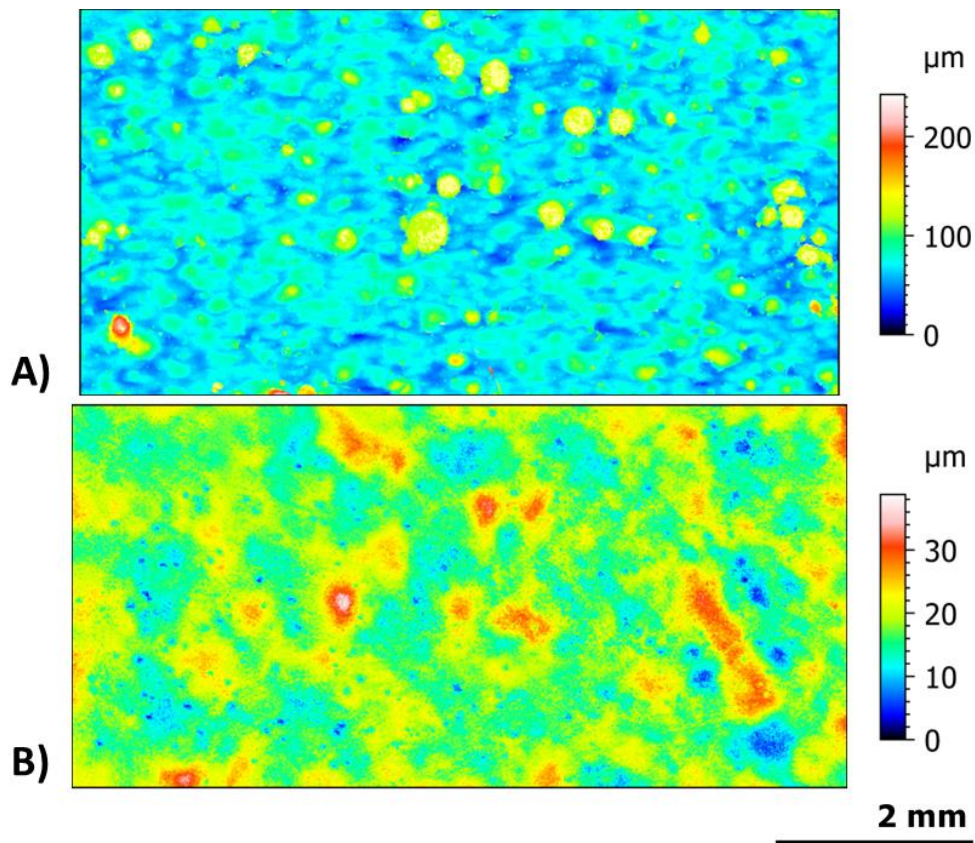


Figure 5.9: False colour height maps of a surface (A) before, and (B) after processing with the final LP strategy, note the different colour (height) scales.

#### 5.4.4.2 Smoothing

The evolution of the roughness during processing is shown in Figure 5.10 (A). It can be seen that only  $S_p$  is consistently improved at every stage of processing, with the remaining parameters being negatively affected by the third step (ablation). This clearly demonstrates the benefit of using a multi-step process, combining different processing mechanisms. It can also be seen that the final step had the greatest influence on  $S_v$ , with a 67% reduction compared to after the preceding step, while the first step had the greatest influence on  $S_a$  (65%),  $S_p$  (68%), and  $S_{10z}$  (56%).

Figure 5.10 (B) shows in detail how the  $S_a$  value changes throughout the LP process. The initial surfaces have a high variability in  $S_a$  (from  $10.5 \mu\text{m}$  to  $23.4 \mu\text{m}$ ) compared to after polishing (from  $1.95 \mu\text{m}$  to  $3.4 \mu\text{m}$ ), with the lowest variability occurring after step 4. Similar trends were observed for the other roughness parameters of interest ( $S_p$ ,  $S_v$ ,  $S_{10z}$ ) and are presented in Figure 5.11. One slight difference is for  $S_p$  where the lowest variability (38%) occurred after Step 3, an ablation step. The variability in  $S_p$  was approximately 100% (i.e., range equal to the average value) in all other conditions. The average measured roughness values are presented in Table 5.6.

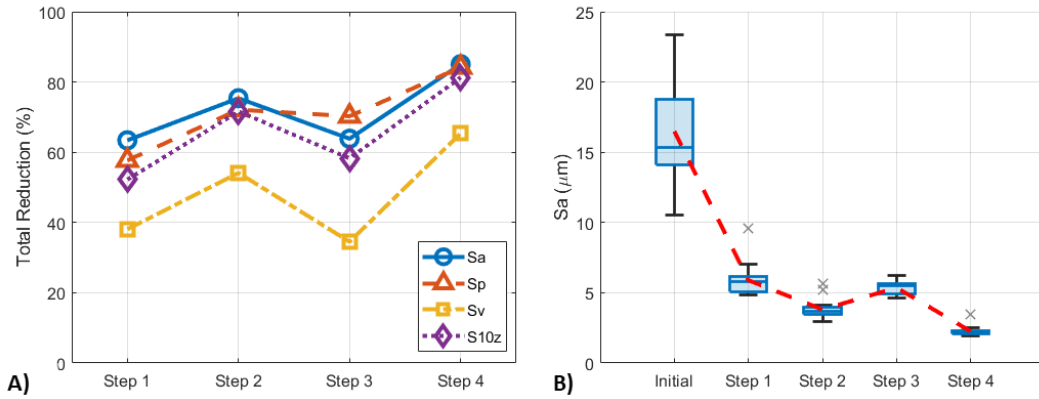


Figure 5.10: (A) Total roughness reduction after each step of final strategy, and (B) Sa values after each processing step showing range measured from different samples and areas, mean average shown by dashed line.

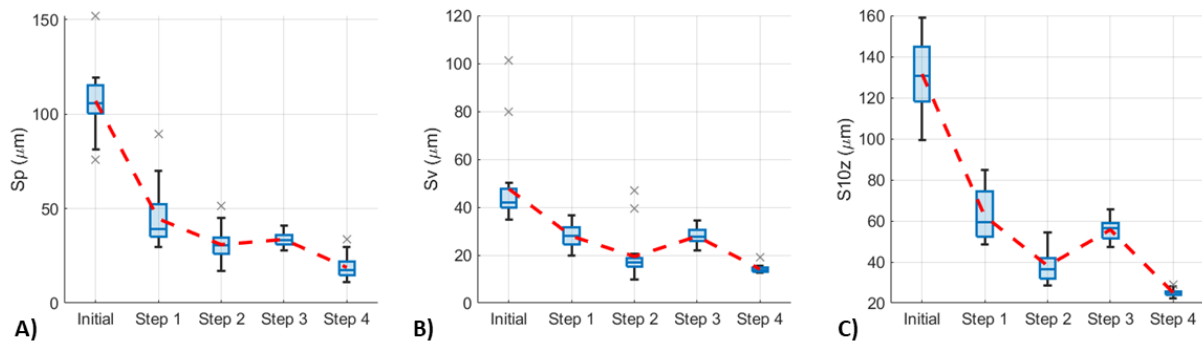


Figure 5.11: (A) Sp, (B) Sv, and (C) S10z Roughness values after each processing step, mean average shown by dashed red line.

Table 5.6: Average roughness values measured from the initial surface, and after each processing step.

Step	Sa (μm)	Sp (μm)	Sv (μm)	S10z (μm)
<b>Initial</b>	16.50	106.98	47.65	131.5
<b>1</b>	5.89	44.56	27.92	62.24
<b>2</b>	3.81	30.91	19.42	38.15
<b>3</b>	5.36	33.66	27.85	55.70
<b>4</b>	2.26	18.83	14.11	25.07

Furthermore, by looking at the surface height maps and optical micrographs (Figure 5.12) it can be seen that, in addition to the lower variation in roughness parameters, the surfaces also have a more consistent appearance. Specifically, the surfaces after the smoothing steps (2 and 4) are more uniform in appearance than after the ablation steps (1 and 3), with less variation on the height maps (Figure 5.12 top), and consistent colouring in the optical micrographs (Figure 5.12 bottom).

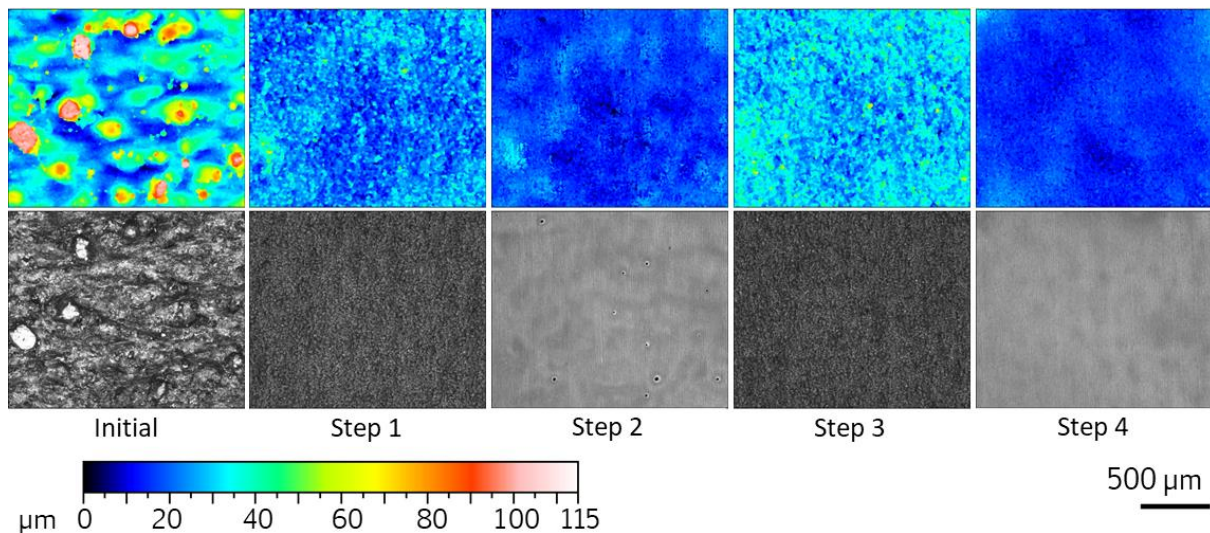


Figure 5.12: (top) Surface height maps, and (bottom) Optical Micrographs. Showing initial surface, and surface after each processing step.

It is unsurprising the first ablation step has the greatest influence on the  $S_p$  (maximum peak height) values, as it is designed to remove material and leave a more homogeneous surface for the subsequent steps to act upon. Furthermore, the smoothing steps (2 and 4) have the greatest influence on the  $S_v$  values due to the action of molten material flowing to fill depressions in the surface.

Cross-sections were taken from a representative sample to identify further changes to the surface throughout the strategy. While the micrographs were taken from different locations, the same features have been observed in all micrographs taken, across multiple different samples. Figure 5.13(A) shows a cross-section through the unpolished surface, with various multi-scale features present on the surface. Contrasting this to the surface after the ablation steps (Figure 5.13(B, D)) where the total height of the surface is reduced, but a much finer texture is present. This texture is of a very short spatial wavelength, of the order of 10 μm to 20 μm so is likely a direct result of the laser action on the surface. Conversely, Figure 5.13(C, E) show the surfaces after the smoothing steps, where the surfaces are much more uniform, with all the short wavelength features removed.

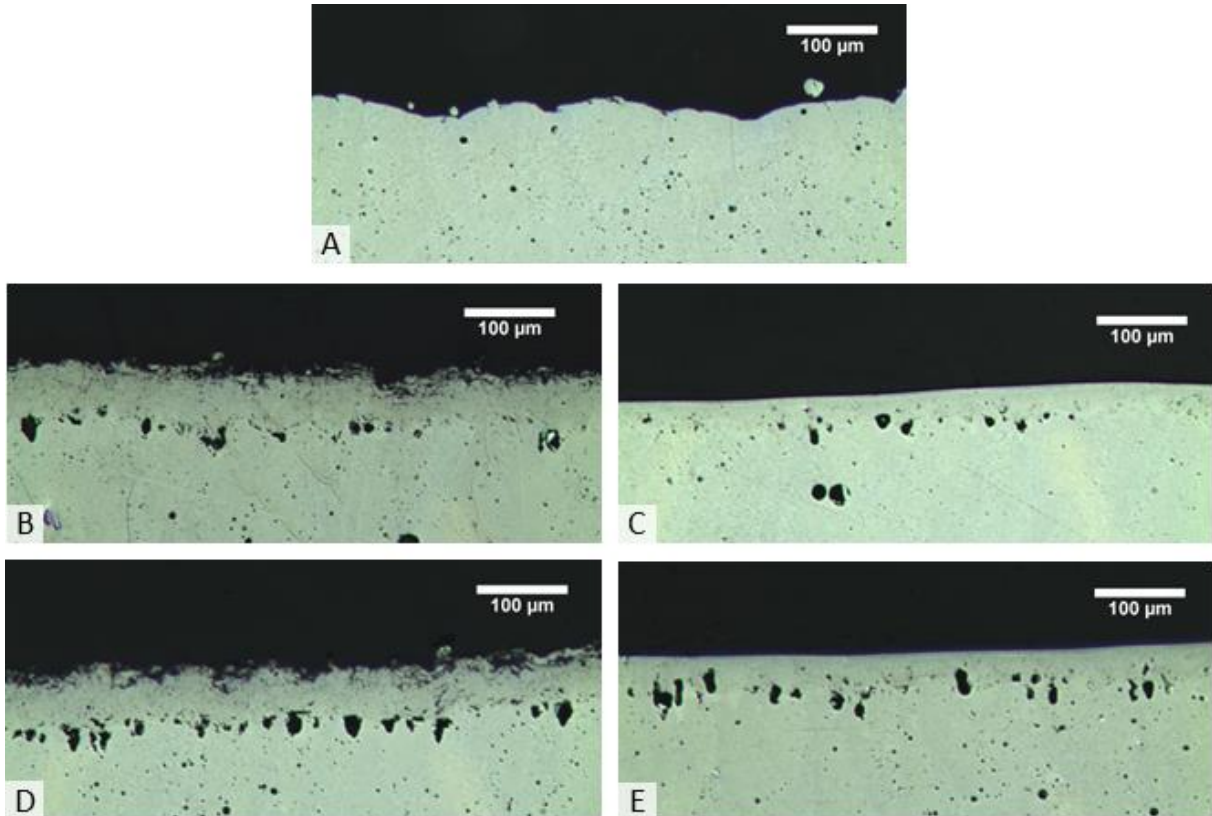


Figure 5.13: Cross-sectional micrographs of (A) the as-built surface and (B-E) after each LP processing step in turn. (B, D) ablated surfaces, (C, E) smoothed surfaces.

#### 5.4.4.3 Porosity

During processing, sub-surface porosity can be seen to have developed approximately 40  $\mu\text{m}$  to 50  $\mu\text{m}$  below the surface (see Figure 5.13). These pores have diameters around 20  $\mu\text{m}$  to 50  $\mu\text{m}$  and tend to be elongated normal to the processed surface.

The porosity was estimated for a series of samples after each LP step, both in the bulk and near the surface. This is presented in Figure 5.14, and shows that there is an increase in the average porosity in the near surface region, to between 3.8% and 5.2% from 0.9% in the bulk, and the scatter in the measurements was also found to be approximately 4.5 times higher (standard deviation from 0.4% bulk to 2% near surface). The bulk porosity was estimated for the same samples to account for any process variability, however, was found to be relatively consistent across all samples evaluated, as shown by the low standard deviation. The elevated porosity near the surface is similar to that found by Hofele et al., who reported 3.5% after PW-LP [178], implying the effect is inherent to LP and not a function of this specific strategy.

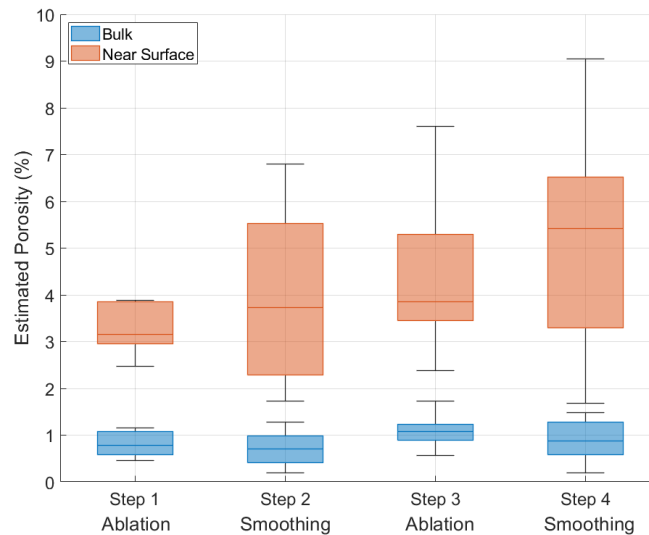


Figure 5.14: How the relative porosity in the HAZ compares to the bulk porosity throughout the LP process.

#### 5.4.4.4 Microstructural Changes

Looking at the micrographs in Figure 5.15, showing etched cross-sections of LP samples after each processing step, it can be seen that there is a marked difference between the bulk material (lower section) and the LP region (surface layer). The bulk material exhibits fish-scale patterns characteristic of the L-PBF process. Meanwhile, the LP layer has no evidence of the fish-scale patterning, and instead after ablation the surface looks more like a foam (Figure 5.15(A,C)), or wave-like patterns after the smoothing steps (Figure 5.15(B,D)).

This is due to the higher laser powers and longer exposures (200 W,  $\mu$ s PW in the case of the AM250) when compared to the LP process used in this work (20 W, ns PW). The thickness of this remelted layer is approximately 50  $\mu$ m, corresponding to the depth of the near-surface porosity discussed previously. The thickness of this layer is less than the 140  $\mu$ m found by Hofele et al. [178], however the laser source used in their studies was operating at 1.7 kW average power and thus capable of much higher energy input than the 20 W source used here.

During this LP process the thermal gradients within the molten region are much greater than those arising during L-PBF AM. This is due to the much smaller spot size and shorter pulse durations imparting less energy per pulse (0.068 mJ ablation, 0.57 mJ smoothing,  $\approx$ 30 mJ AM) but at a higher intensity (2.2 TW/m<sup>2</sup>, 390 GW/m<sup>2</sup>, and 28 GW/m<sup>2</sup> respectively). This in turn results in much smaller melt pools within the LP region when compared to those in the bulk material.

Notably, after the smoothing steps (shown in Figure 5.15 B, D) there are visible striations within the remelted zone. These striations strongly indicate the presence of material reflowing to fill depressions in the surface during successive laser passes during the smoothing steps.

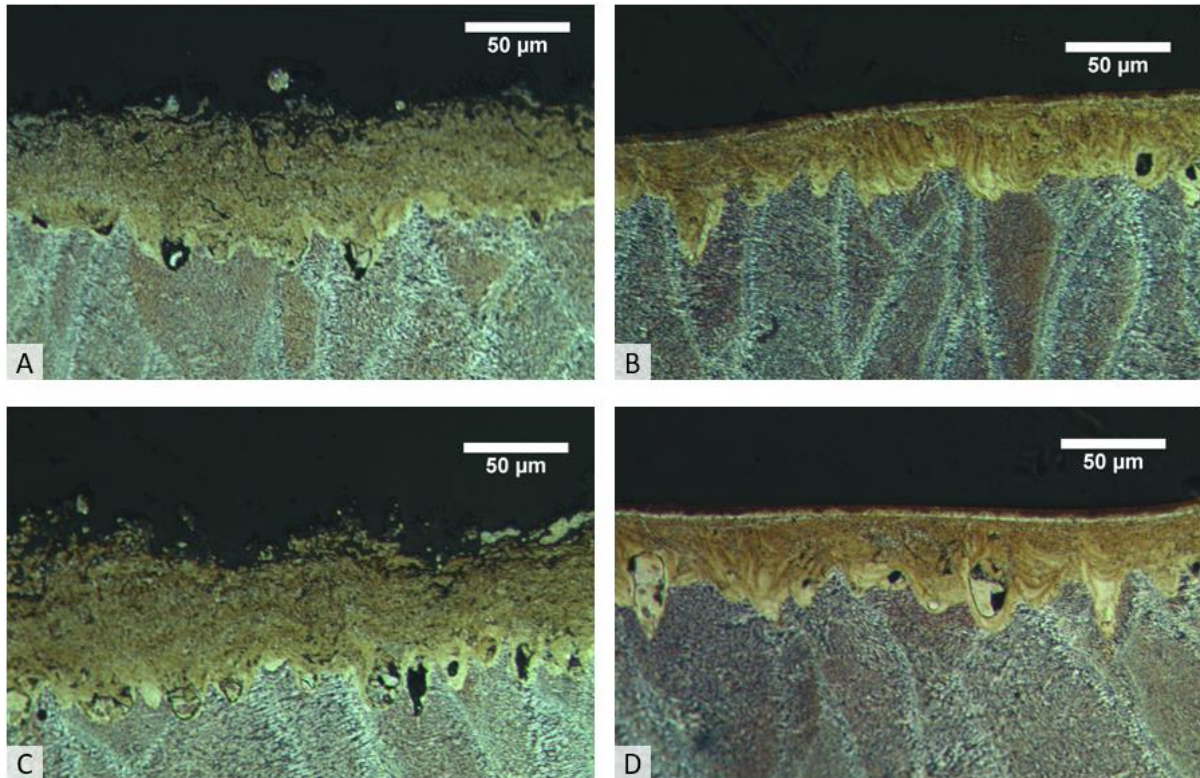


Figure 5.15: Microstructure at the processed surface after each processing step (A-D sequentially).

#### 5.4.4.5 Near Surface Microhardness

In Figure 5.16 the measured microhardness values are presented, along with a 10  $\mu\text{m}$  moving average (dashed blue line) indicating the hardness profile, and the bulk hardness estimation (grey band). The bulk hardness was estimated by averaging values taken from below 60  $\mu\text{m}$  from the LP surface, and the presented range is one standard deviation above and below that average.

Measurements were taken from near the surface progressing towards the bulk in 10  $\mu\text{m}$  increments (with a lateral offset) for 100  $\mu\text{m}$ , repeated five times per sample in different locations. An example of the indentation layout is shown in Figure 5.3. Due to tolerances within the microscope this resulted in one indent to be approximately 5  $\mu\text{m}$  from the surface, while the remainder started from 15  $\mu\text{m}$  below the surface, as seen in Figure 5.16.

Firstly, the bulk hardness estimate ( $\approx 120 \text{ Hv}_{0.005}$ ) is slightly higher than the datasheet value of  $113 \text{ Hv}_{0.5}$  [69]. This could be simply due to the different loads applied resulting in subtle differences in the reported values, and natural material variability at such small scales.

The hardness profiles clearly show an increased microhardness near the surface. The average hardness within 25  $\mu\text{m}$  of the surface after each processing step are  $176 \text{ Hv}_{0.005}$ ,  $164 \text{ Hv}_{0.005}$ ,  $178 \text{ Hv}_{0.005}$ , and  $142 \text{ Hv}_{0.005}$  respectively. This clearly shows that the smoothing steps (steps 2 and 4) give a reduced surface hardness compared to the ablation steps (steps 1 and 3). Furthermore, after ablation this harder region extends about 60  $\mu\text{m}$  from the LP surface, whereas after smoothing bulk hardness is realised from approximately 45  $\mu\text{m}$  depth. This is due to the increased cooling rates and peak temperatures during ablation resulting in higher residual stresses, while the reduced cooling rates after smoothing enable the residual stresses to relax somewhat, giving both the reduced peak hardness and hardened depth. From the results presented in the preceding two sections, it can be seen this aligns with the location of the sub-surface porosity, and the transition between the bulk material and remelted region.

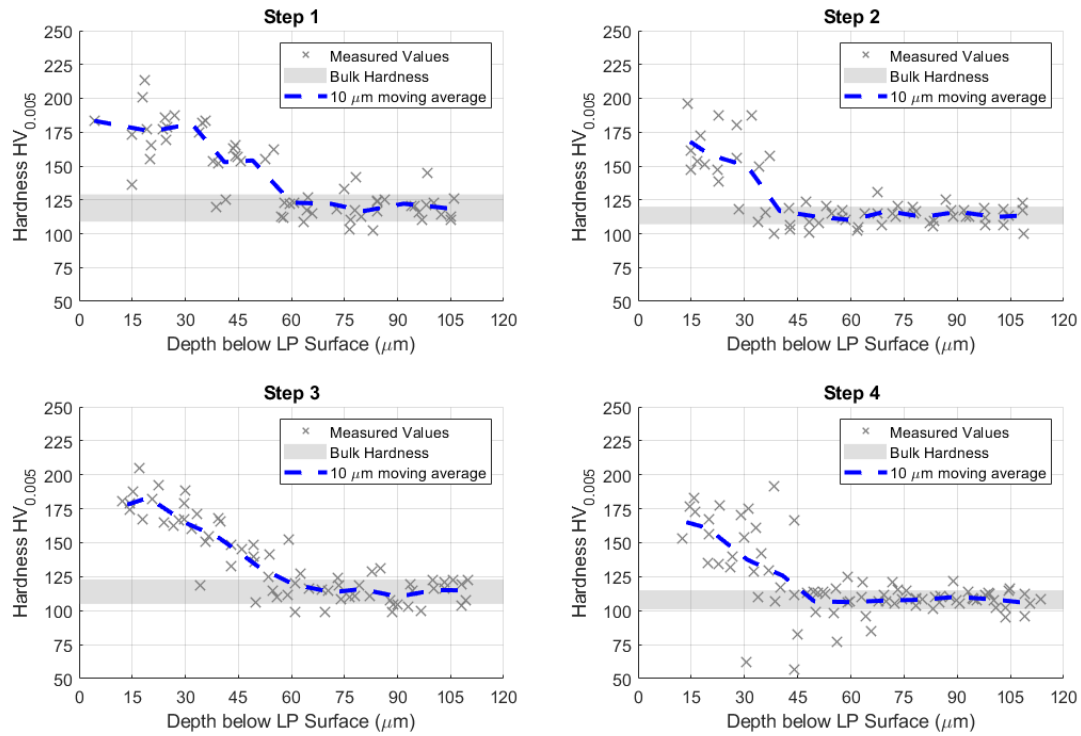


Figure 5.16: Near-surface microhardness profiles in the LP region after each processing step.

Bhaduri et al. [71] found no increase in surface hardness after LP of AM aluminium, rather a softening a short distance below the LP surface (5  $\mu\text{m}$  – 20  $\mu\text{m}$ ), attributed to silicon enrichment at around this point. Hofele et al. [178] observed more significant softening within 0.4 mm of the surface, with a minimum approximately 30% lower than the measured bulk hardness. It is possible these differences result from the very short pulse durations (15 ns, compared to 220 ns [71] and 300  $\mu\text{s}$  [178]) used in the ablation steps giving rise to residual tensile stresses, increasing the hardness.

#### 5.4.4.6 Effect of LP Scanning Hatch Angle

The hatch pattern has shown to have no significant influence on smoothing when using this strategy. However, due to the small areas trialled, few repeats, and inconsistent initial conditions, it is strongly suggested further evaluations are conducted. It is anticipated that the hatch pattern may become significant for machining operations, and therefore will be a key consideration for hybrid machining/polishing operations.

#### 5.4.4.7 Validation of the LP Strategy

The resulting surface from applying the LP process to a sample of wrought aluminium is shown in Figure 5.17 (top left), it can be seen the surface morphology is unlike those previously observed (see Figure 5.6 and Figure 5.8). While the resulting surface on AM samples was smooth and uniform, the wrought LP surface is highly irregular, and exhibits a greatly increased surface roughness ( $S_a = 15.4 \mu\text{m}$ ) compared to that measured on previous AM samples (average  $S_a \approx 2 \mu\text{m}$ ). The surface more closely resembles those found in the initial trials when excessive fluence was used and the surface was over-exposed. It is unlikely this is due to some fundamental thermal property, as the reference values for AA6062 are within the ranges expected from AlSi10Mg (see Table 5.7). This implies the wrought material has a higher absorptivity to the laser wavelength used ( $\lambda = 1064 \text{ nm}$ ) despite a higher optical reflectivity (visually shinier surface).

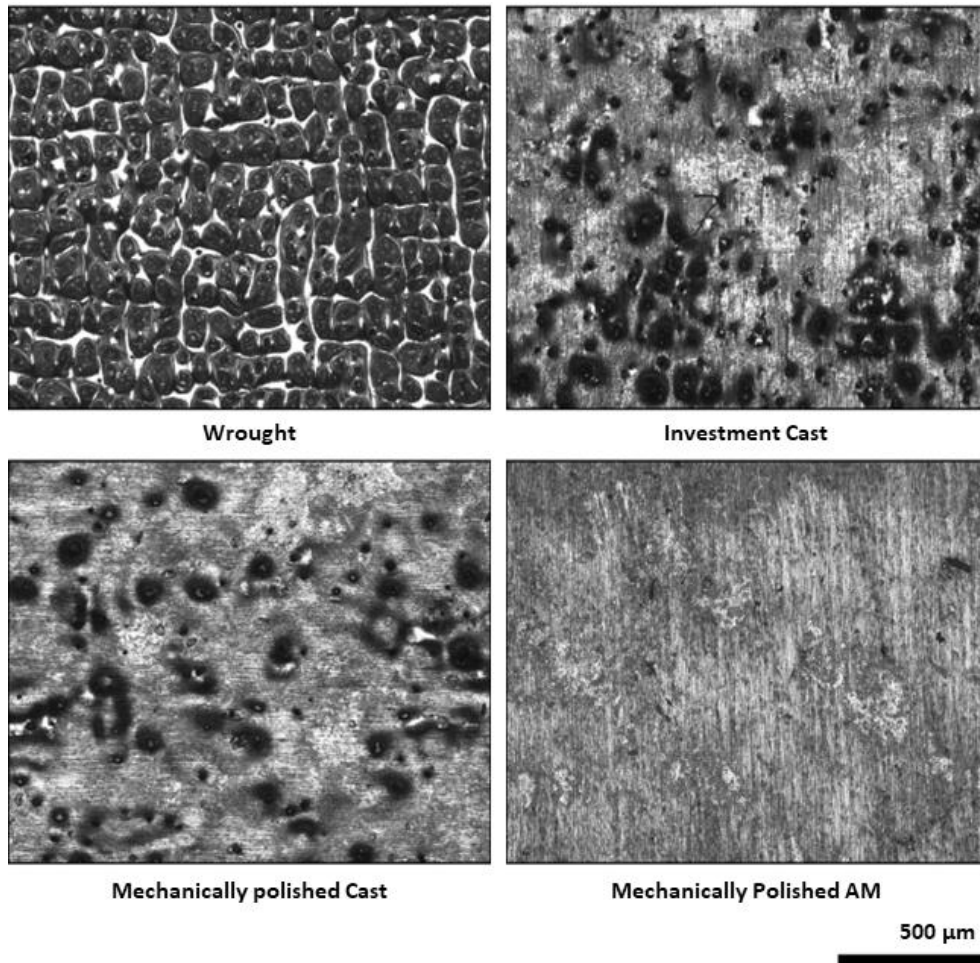


Figure 5.17: Optical micrograph of various aluminium samples after applying the final LP strategy.

It was theorised the observations could be due to the effect of surface texture. To assess this, a cast sample was prepared. The thermal properties for the BSL169 casting alloy are also presented in Table 5.7, showing a slightly increased melting temperature compared to the other two assessed alloys, and a thermal conductivity lower than that of AA6062 but within the range expected of AlSi10Mg. While the difference in conductivity would lead to differences in the temperature gradients immediately surrounding the laser spot, the processing region used (5 mm × 5 mm) resulted in the bulk temperature of the samples being raised considerably (the specimen remained noticeably hot for a prolonged period after LP) and therefore the effect of conductivity is unlikely to be a significant contributor.

Table 5.7: Thermal conductivity and melting point for AlSi10Mg and two conventionally manufactured alloys.

	<b>AlSi10Mg (AM)</b> [69]	<b>AA6062 (Wrought)</b> [179]	<b>BSL169 (Cast)</b> [180]
Thermal Conductivity	130–190 W/mK	172 W/mK	150 W/mK
Melting Point	570–590 °C	582 °C	600 °C

Cast samples were processed with both the as-manufactured surface texture and mechanically polished, to assess surface and material effects respectively. Optical micrographs are shown in Figure 5.17 (top right & bottom left), which show significant improvements compared to the wrought sample, albeit still with many visible pockmarks. The resulting Sa values were 4.17 µm and 3.33 µm respectively, this difference is within the variability of the process (as will be discussed in Section 5.4.4.8) and therefore negated the theory that surface effects are responsible for the different responses to the LP strategy.

The final confirmation that it is not the initial surface causing these effects, is the observed texture on mechanically polished AM surfaces. An example is shown in Figure 5.17 (bottom right), where the surface shows no signs of the aforementioned pockmarks and is visually homogeneous. The roughness of the example shown is 1.25  $\mu\text{m}$  Sa. The average across a series of 8 surfaces was 1.37  $\mu\text{m}$ , indicating this is the approximate lower bound for what is possible with this strategy (especially when considering two surfaces with initial roughness of 1.1  $\mu\text{m}$  and 1.2  $\mu\text{m}$  experienced an increased Sa after processing).

#### 5.4.4.8 LP Strategy Repeatability

The 20 surfaces processed with the final strategy (with  $\pm 45^\circ$  hatch rotation) showed good consistency in the reduction in Sa, with increased variability in Sp, Sv, and S10z (Figure 5.18). As Sa is an average value, it was expected to be less affected by outliers such as single large peaks or pits. Likewise, S10z is the difference between the five highest peaks, and five lowest pits, and can therefore also accommodate some extreme values. The range of reductions are given in Table 5.8, along with the minimum achieved value for each parameter (n.b., these results refer only to the 20 samples used here and thus are different from those reported in Table 5.6). While the minimum values are slightly higher than those reported by others (e.g., 0.64  $\mu\text{m}$  Sa [71], 0.164  $\mu\text{m}$  Ra [107]), direct comparisons are impossible due to the differences in how the surface roughness was evaluated.

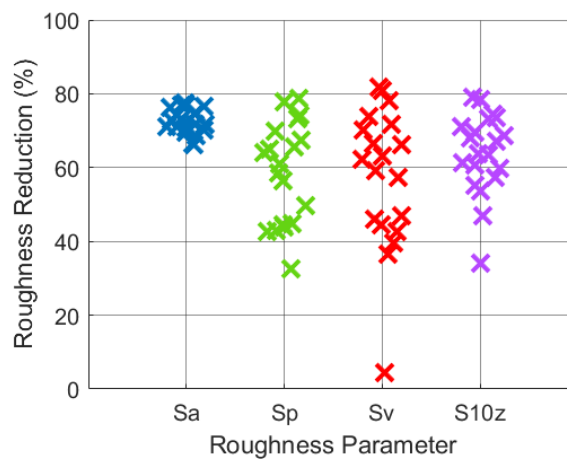


Figure 5.18: Range of reduction of different roughness parameters.

Table 5.8: Range of roughness reductions, and minimum achieved roughness.

Parameter	Minimum Reduction	Average Reduction	Maximum Reduction	Minimum Achieved Value
Sa	66.1 %	72.6 %	77.6 %	3.57 $\mu\text{m}$
Sp	32.5 %	57.9 %	78.6 %	40.3 $\mu\text{m}$
Sv	4.4 %	57.5 %	81.7 %	21.0 $\mu\text{m}$
S10z	34.1 %	63.9 %	79.0 %	60.1 $\mu\text{m}$

To establish if this gives stable results (i.e., a predictable outcome), the reduction was plotted against initial roughness, Figure 5.19. From this it can be seen that the smoothing potential (% reduction) is reduced at lower initial roughnesses. With two distinct regions presenting themselves in this data; at very high initial roughness ( $>25 \mu\text{m}$  Sa) the process appears stable, with around 80% reduction. At lower initial roughness ( $<15 \mu\text{m}$  Sa) there is a proportionality between the initial roughness and the roughness reduction. These results go against previous findings by Hofele et al. who found their LP process was agnostic to the initial surface roughness [74]. In contrast, this shows the effectiveness of the developed LP strategy has a strong dependency on the initial surface

condition and may not be appropriate for surfaces with a low initial roughness. The causes for this may be due to the higher roughness having a lower reflectivity, and therefore absorbing more of the laser energy [98], or simply rougher initial surfaces having more peaks available to be melted and fill depressions in the surface.

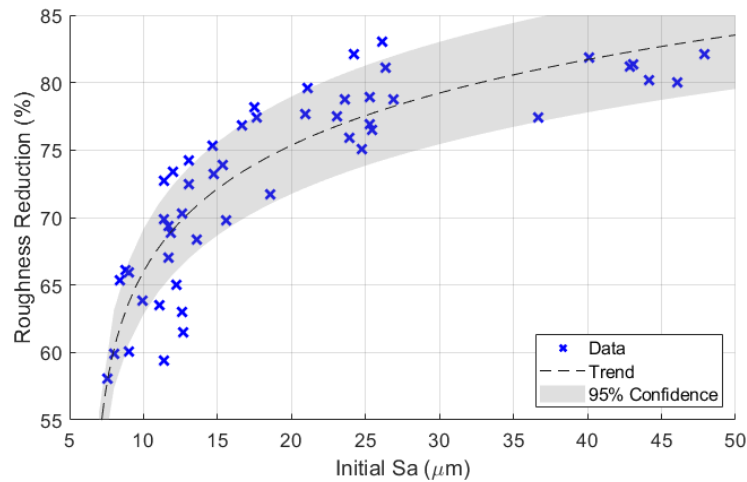


Figure 5.19: Plot of % reduction in Sa against the initial roughness value.

The other parameters ( $S_p$ ,  $S_v$ ,  $S_{10z}$ ) did not show any strong correlation between initial roughness and roughness reduction likely due to the much higher variability in roughness reduction than present with  $S_a$  (as seen in Figure 5.18) and the stronger influence of “outlier” surface features.

## 5.5 Thermal Simulations of Final LP Strategy

It is well known that different pulse durations lead to different material interaction mechanisms, but this is usually discussed over orders of magnitude – that is fs / ns /  $\mu\text{s}$  pulse durations. In this work the two pulse durations used are relatively similar, 15 ns and 220 ns, however there is still an appreciable difference in effect. To evaluate this a series of thermal simulations were undertaken to estimate the thermal fields resulting from the employed strategy.

There has been interest in using simulations to reduce the experimental burden of novel techniques (including AM and LP), allowing near-optimal settings to be determined before committing to the expense of experimental trials. For LP, much of the focus has been to relate the thermal fields to smoothing potential. For example, Ukar et al. [181] determined a melt depth equal to the  $R_z$  value to give the greatest roughness reduction for machined (ball-end mill) tool steel. Meanwhile, Shao et al. [182] focussed on the effect of laser irradiation of single asperities, finding asperities of low aspect ratio (short compared to width) can be more evenly heated, and therefore melted, compared to those with high aspect ratios. This implies with improper settings tall asperities may not fully melt and thus contribute to increased roughness after processing.

### 5.5.1 Simulation Setup

It was decided to use the commercial finite element analysis (FEA) software ANSYS (2020 R1 and 2022 R2) to model the transient thermal conditions. As Song et al. [78] noted, it is not advisable to approximate a PW source with an averaged CW input due to the higher peak intensities realised and therefore it was necessary to simulate a pulsed energy input.

To simplify the model, it was decided to simulate a single track over a length of approximately  $100\ \mu\text{m}$  as a series of discrete energy inputs (laser pulses). Other approximations included using a uniform spatial intensity distribution for the energy input, as opposed to the near-gaussian

distribution provided by the laser source used in the experimental trials (beam quality,  $M^2 \approx 1.2$ ). An example of the true spatial distribution is shown in Figure 5.20, measured using a Beam'R2 scanning slit profiler [183], where the Z-axis represents the beam intensity. The extended tails in X and Y are due to the beam travelling during measurement.

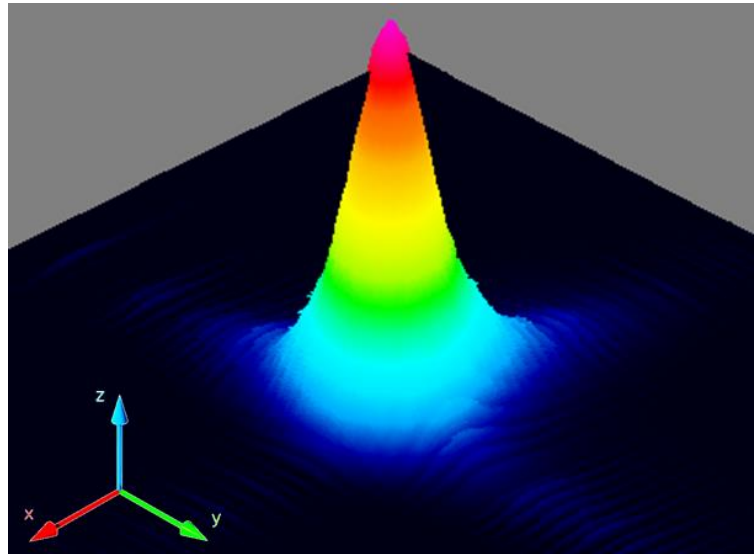


Figure 5.20: Measured beam spatial profile.

A further simplification was to assume a constant intensity over time (within a single laser-on period). This was done as the true intensity distribution in time is highly complex, shown in Figure 3.3, and therefore a non-trivial task to model accurately. This was deemed appropriate as the focus was not on the influence of individual pulses, but how the temperature field evolves over successive pulses.

The remaining simplifications included to neglect phase changes (and the energy required to melt/vaporise), assuming constant absorptivity of the surface to the laser energy, and no plasma shielding would occur.

ANSYS required a thermal energy input to be defined in units  $W/m^2$ , as opposed to the  $J/cm^2$  used in Fluence calculations previously. Therefore Equation 5.2 was used, incorporating a term ( $\alpha$ ) to account for the low absorptivity of Aluminium for IR wavelengths (taken to be 0.15 [184]).

$$Intensity = \frac{E_p/A_z}{t_p} \times \alpha \quad \text{Equation 5.2}$$

Where:  $E_p$  is Pulse energy (from eqn. 2.4),  $A_z$  is spot area at offset (using diameter at offset, eqn. 2.7), and  $t_p$  is the pulse duration (220 ns or 15 ns).

Four conditions were chosen to simulate, taking the two waveforms utilised for LP, at focus and the focus offset used in the final strategy, as summarised in Table 5.9. The waveforms are defined by the Laser source and are: WFM 0 (220 ns, 100 kHz) as used for smoothing, and WFM 5 (15 ns, 290 kHz) used to ablate the surfaces. It was anticipated the WFM 5 results to show higher maximum temperatures, with a small HAZ compared to the WFM 0 results.

Table 5.9: Simulation setup details.

Waveform	Focal Offset	Pulse Distance †	Spot Size †	Number of pulses	Track length	Applied Intensity
	mm	$\mu\text{m}$	$\mu\text{m}$		$\mu\text{m}$	$\text{GW}/\text{m}^2$
WFM 0	0	1.6	32	63	99.2	40.693
WFM 0	1.34	3.25	65.1	31	97.6	40.928
WFM 5	0	1.9	32	53	98.5	686.01
WFM 5	0.38	2.14	35.8	47	100	684.51

† Pulse Distanced and Spot Size were calculated using Equations 2.8 and 2.7 respectively.

Finally, simulations were performed on perfectly smooth geometry, measuring 0.5 mm thick (in line with energy input), 1 mm along energy travel direction, and 1 mm wide (half modelled to take advantage of symmetry). The block was meshed using linear tetrahedron elements (i.e., only vertex nodes) at a size of  $25 \mu\text{m}$ . A central region  $50 \mu\text{m} \times 200 \mu\text{m} \times 75 \mu\text{m}$  was meshed with element sizing of  $2.5 \mu\text{m}$  to increase accuracy near the energy inputs. Both regions can be seen in Figure 5.21, where the finer mesh was applied to the brown region. This gave a total element count of around 450,000. While it was noted by Gu and Li [77] that convection and radiation to the environment are insignificant compared to conduction to the underlying substrate, radiation boundary conditions were applied to all external surfaces of the simulated geometry to allow some heat loss as though the geometry was part of a much larger sample.

Temperature time histories were extracted from points at various depths below the centre of the scan track. Depths of interest were  $0 \mu\text{m}$  (i.e., at the surface),  $15 \mu\text{m}$ ,  $25 \mu\text{m}$ ,  $50 \mu\text{m}$ ,  $100 \mu\text{m}$ , and  $250 \mu\text{m}$ , shown by the axis centres in Figure 5.21.

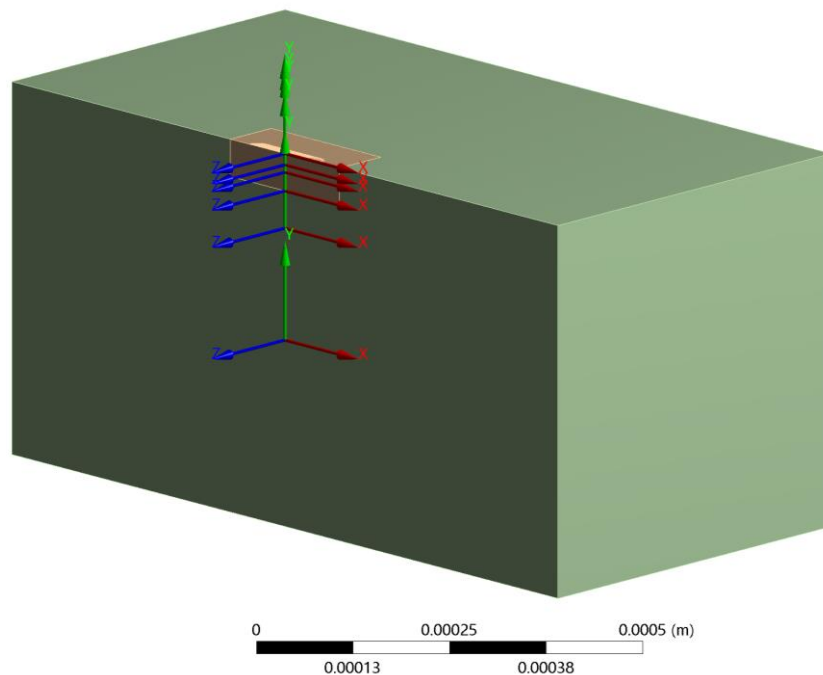


Figure 5.21: Result probe locations used in simulations (shown by axes). Also shown is full body (green) and region of refined mesh (brown).

### 5.5.2 Simulation Results and Discussion

Figure 5.22 shows the simulated temperatures in the same plane as the laser path. The geometry shown in the brown region in Figure 5.21. The timesteps shown are immediately before and at the end of the central laser pulse (top and bottom respectively) with WFM at focus. In the bottom

figure, the purple region is that simulated to be above the material melting temperature. The upper figure shows elevated temperatures behind the laser pulse compared to in front due to the accumulated heat from the preceding pulses. It also shows that in the short “laser off” time (9.78  $\mu\text{s}$ ) the maximum temperature is only slightly elevated compared to the bulk. In comparison, the lower figure shows a maximum temperature far in excess of the melting point, with a very high temperature gradient towards the bulk. This shows even with the longer pulse duration (220 ns) thermal conduction during the laser pulse is limited, minimizing the induced thermal damage. The alternative waveforms simulated showed similar characteristics and are therefore not presented here.

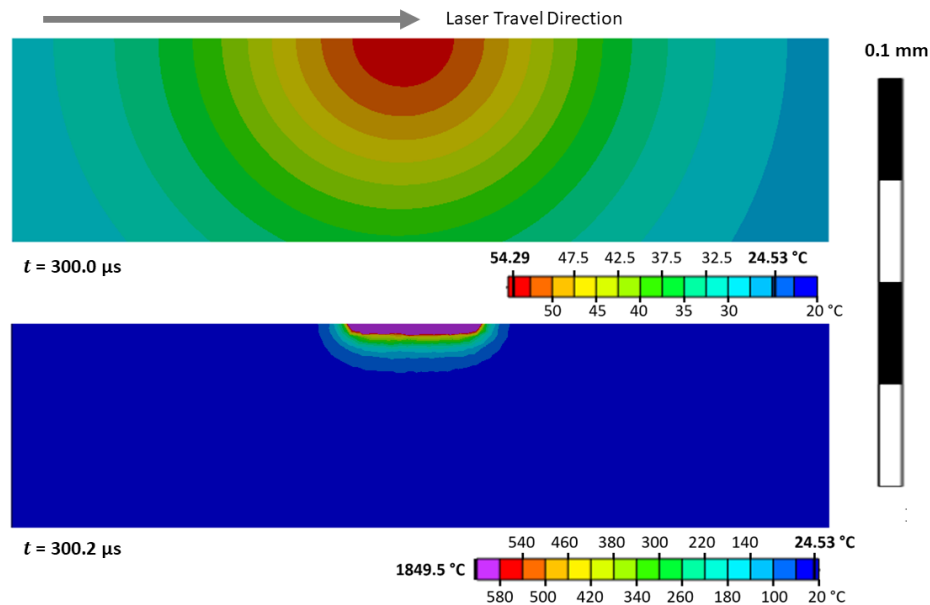


Figure 5.22: Simulated temperature fields just prior to (top) and immediately following (bottom) the mid-point pulse.

While the maximum simulated temperatures should not be regarded as accurate due to the previously discussed simplifications and extreme thermal gradients causing instabilities in the solution, they are still a valuable resource for comparing the chosen waveforms. As can be seen in Figure 5.23, the maximum simulated temperatures far exceed the melting temperature (580 °C [69]). Furthermore, when simulating WFM 5, the peak temperatures exceed the evaporation temperature of AlSi10Mg (2470 °C [185]). The existence of material above the evaporation temperature gives further credence to WFM 5 achieving ablation of the surface material. It should be noted that these extreme temperatures are likely to be significantly lower in reality due to the assumptions previously discussed. Furthermore, the figure shows a significantly higher maximum temperature for WFM 5 when working at offset compared to focus, while a much smaller effect is present for WFM 0. While there is thought to be an increase in peak temperature at offset, due to the higher total energy input per pulse and increased “melt” volume to act as a heatsink, these values are likely to be erroneous due to simulation instabilities at such high thermal gradients.

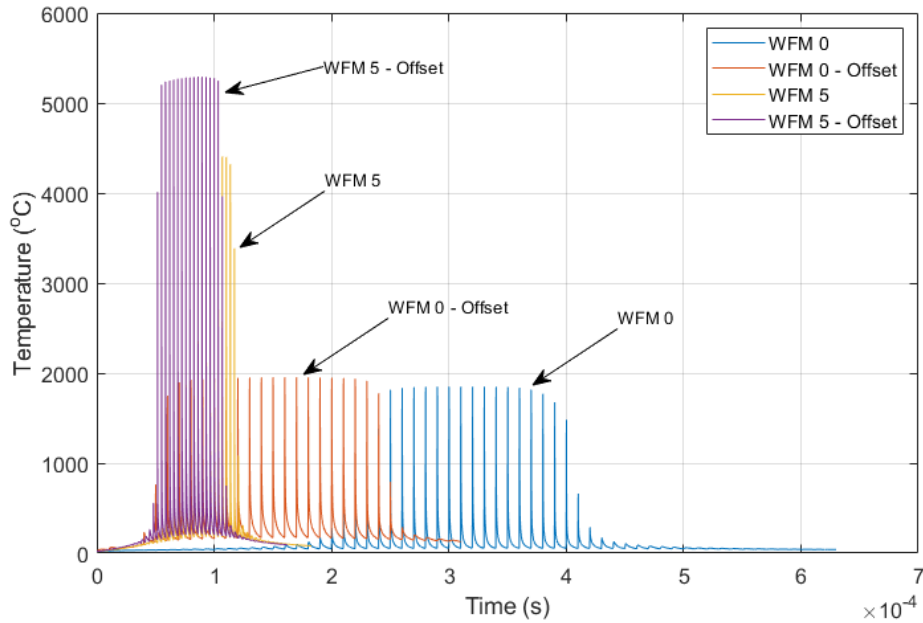


Figure 5.23: Surface temperatures simulated for different laser waveforms.

Looking instead at Figure 5.24, showing the temperature profiles at different depths below the surface, the differences are striking. While at the surface WFM 5 gives significantly higher temperatures than WFM 0, at any distance below the surface, WFM 0 with a focus offset returns the highest temperatures. This is due to the higher duty-cycle of WFM 0 (2.2%) giving proportionately less time for cooling between pulses than WFM 5 (duty cycle 0.435%). This also highlights the well-known effect of ultra-short pulses having a much-reduced HAZ compared to longer pulses.

This increased bulk temperature reduces the thermal gradients near the energy input, giving lower cooling rates and would therefore lead to larger grain-structures. The reduced cooling rate will also allow the material to remain molten for longer, giving an enhanced smoothing effect. The difference in temperature profiles for WFM 0 at focus and with a focus offset is striking. The significantly higher temperatures, both maximum and minimum, at all depths would yield a larger melt pool, that lasts longer, giving more time for surface tension etc. to pull the surface flat, and thus minimizing the part's roughness.

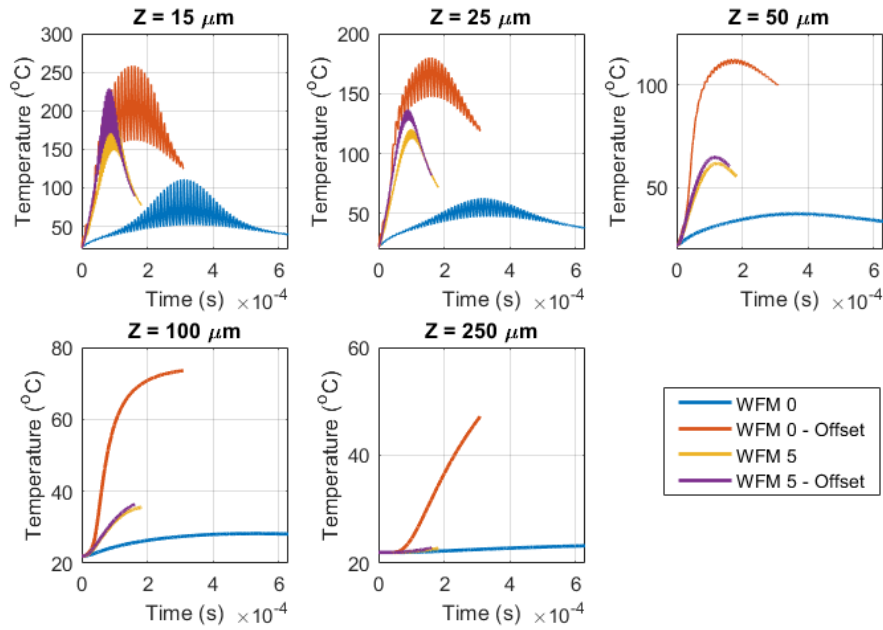


Figure 5.24: Simulated temperatures at various depths below scan track mid-point during processing with different laser waveforms. (n.b., Y-scale is different between graphs for clarity).

It is interesting that the maximum simulated temperature for WFM 0 is not greatly influenced by the change in spot size (focal offset), 1850°C at focus and 1954°C with an offset (5% higher). WFM 5, however, shows a much greater increase, from 4414°C to 5292°C (20% higher), despite the relative similarity of spot size (32 μm and 35.8 μm respectively). This is reversed when evaluating the temperatures below the surface, with WFM 5 reporting very similar results in all cases (due to the relative similarity of simulated laser settings). On the other hand, results for WFM 0 deviate significantly, with the differences increasing as the measurement location moves further below the surface. This deviation is likely a result of the same Fluence being applied over a larger area (through an increased power input) resulting in a higher total energy input.

Up to measurement depths of 50 μm, a decrease in temperature can be observed as the energy input gets further away from the measurement point, that is, after the energy input passes the track mid-point. Conversely, at 100 μm and 250 μm measurement depths the temperature continues to increase. This corresponds to the work by Gu and Li, who simulated a DED process, finding the bulk temperature did not return to ambient between layers [77]. While the temperatures simulated here are relatively modest (only the very surface exceeding the melting temperature) this implies after longer scan tracks, or during subsequent layers, peak temperatures would be higher and therefore greater volumes of molten material. This also corresponds to anecdotal evidence from the implementation of this LP strategy, where samples become far too hot to handle after processing (estimated bulk temperature >50°C) even with thick samples such as 10 mm × 10 mm × 10 mm cubes processed over one full surface. Due to limitations of the approach used here, it is not practical to simulate larger bodies or longer processing tracks to further validate this observation.

A further observation from Figure 5.24 is the persistence of individual pulses on the temperature profiles. At 15 μm and 25 μm depths all traces show ripples corresponding to the laser pulses, while at 50 μm only the WFM 0 traces show clear variations. At 50 μm depth and below the WFM 5 trace, or 100 μm for WFM 0, the temperature profiles are “smooth”, with the action of individual pulses attenuated by the preceding material. Therefore, it may be possible to simulate bulk temperature rises (greater than 0.1 mm from the surface) through the application of a CW equivalent energy

input. This would be beneficial as longer timesteps could be implemented, reducing the computation load, and enabling larger scale models to be evaluated.

## 5.6 Laser Polishing Strategy Development and Analysis Summary

A multi-step LP strategy has been developed, combining ablation and smoothing steps to give a smooth, consistent, and defect-free surface. Visual assessment of the surfaces showed the LP process yielded surfaces with greater lustre than those in the as-built condition. Roughness was evaluated using the standard Sa, Sp, Sv, and S10z roughness parameters to give a broad overview of the response throughout extensive trials optimizing the number of passes for each processing step. The maximum roughness reductions achieved were 86.3% Sa, 82.4% Sp, 81.7% Sv, and 80.9% S10z, with minimum achieved values of 2.26  $\mu\text{m}$ , 18.9  $\mu\text{m}$ , 14.1  $\mu\text{m}$ , and 25.1  $\mu\text{m}$  respectively. Through evaluation of roughness parameters after each processing step it is clear the combined ablation-smoothing strategy is significantly more effective than any single step in isolation, though the different LP mechanisms targeting different roughness features. Strong correlation was observed between initial Sa and % reduction, with the strategy effectiveness reducing considerably at initial Sa values below 15  $\mu\text{m}$ .

The sub-surface material responses were also evaluated, revealing an increase in hardness near the surface (between 150  $\text{Hv}_{0.005}$  and 175  $\text{Hv}_{0.005}$  15  $\mu\text{m}$  below the surface after the full LP strategy) that falls linearly to the bulk hardness value about 45  $\mu\text{m}$  below the surface. This correlates with a refined grain structure in this surface layer that transitions to the ubiquitous L-PBF induced fish-scale pattern at the same distance from the surface. After the smoothing steps, the remelted layer shows strong evidence of material flow, with striations following the form of the bulk material below. At the interface between the remelted layer and the bulk material an increase in porosity has been observed, with an estimated porosity of 5.5% within 100  $\mu\text{m}$  of the surface compared to less than 1% in the bulk material.

Finally, transient thermal simulations were completed to highlight the different actions of the laser settings used. These showed higher peak temperatures when using the shorter, 15 ns pulse durations, but with reduced heat penetration compared to the longer, 220 ns pulse durations. As distance below the surface increased, first the action of individual laser pulses was attenuated, followed by continuous temperature increase throughout the simulation duration despite the energy input retreating from the measurement locations.

## 6 Assessment of the Tensile Properties of AM Aluminium

### 6.1 Purpose

This chapter describes the works conducted to determine the tensile properties of AlSi10Mg coupons. Tests were undertaken to evaluate the effects of LP and different heat treatments, in isolation and in combination. The structure is as follows; a description of the test plans and testing methods (referencing Chapter 3), followed by the test results in 6.5, with discussions on these results in 6.6 including references to other sources. This chapter ends with section 6.7, a summary of findings. The background and theory of LP has been previously discussed in detail (Chapters 2.4, 3.2, and 5) and therefore not repeated in this chapter.

The aim of these tests was to evaluate the influence of LP on the ductility and strength of the AlSi10Mg material. Two tests were conducted, the first evaluating the influence of machining the outer contour ( $T_M$ ) and the second the effect of heat treatment ( $T_H$ ) on the quasi-static tensile properties. In addition, as the LP operation can only be applied to the front/rear faces of the dog-bone specimens, it was decided to evaluate the influence of the side surfaces of the samples (through thickness) by manufacturing some samples directly as net shapes using L-BPF, and machining other samples to achieve the final shape. These samples are henceforth referred to as the  $T_M$  sample set. Machining was used to realise the reduced gauge section, to ensure geometric accuracy. An additional goal was to reduce the chance of failure originating on these edges where LP could not be applied, and therefore any differences observed could be attributed to the application of LP.

Following this, a second sample set was manufactured to assess the interaction between LP and different HT processes on the mechanical properties of AM AlSi10Mg, referred to as  $T_H$  samples. The specific heat treatments applied were Stress Relief (SR) and a conventional T6 temper.

### 6.2 Test Plan

For both  $T_M$  (machining) and  $T_H$  (heat treatment) sample sets, a full factorial test matrix was implemented with 5 replications. For the  $T_M$  trial this required a total of 20 samples, as shown in Table 6.1. Two additional samples were manufactured in the net-shape condition, which were also tested, as it was envisioned that the net-shape samples would have a greater spread of data. This greater variability is thought to be due to the rough edges and the effect of removing the support structures required following manufacture.

Table 6.1: Post processing applied to  $T_M$  (machining trial) tensile samples.

Sample Set	Profile	Surface	Number of Samples
$T_{M1}$	Net-Shape	As Built	6
$T_{M2}$	Net-Shape	LP	6
$T_{M3}$	Machined	As Built	5
$T_{M4}$	Machined	LP	5

The  $T_H$  trials included 28 samples split between six conditions. Based on the  $T_M$  results, all had the profile machined after manufacture but before any other post processing. To improve testing efficiency, four of each as-built (i.e., without any heat treatment) sample type were prepared. The results from these were compared to the machining trial results for consistency and augmented by those machining trial results if appropriate. SR was not a primary concern and therefore only three of each were prepared, with the results referenced against datasheet values for process monitoring. Finally, five of each fully heat treated (SR and Tempered) sample type were prepared. The full test matrix is shown in Table 6.2.

Table 6.2: Post processing applied to  $T_H$  tensile samples (HT trial).

Sample Set	Heat Treatment	Surface	Number of Samples
$T_{HA}$	None	As Built	4
$T_{HB}$	SR	As Built	3
$T_{HC}$	SR+T6	As Built	5
$T_{HD}$	None	LP	4
$T_{HE}$	SR	LP	3
$T_{HF}$	SR+T6	LP	5

Tensile tests were performed using a *Zwick-Roell Z50* load machine in conjunction with a VG system from *Imetrum* (both as described in Chapter 3.4.5).

## 6.3 Methods

### 6.3.1 Sample Manufacture

Samples were manufactured from gas atomized AlSi10Mg powder from *Renishaw plc.*, using a *Renishaw AM250* L-PBF machine (see Chapter 3.1 for further details). At the time of manufacture, the AM250 was configured with the RBV installed, and therefore this was used to build the  $T_M$  samples. The space available using the RBV is 78 mm × 78 mm × 55 mm. Sample geometry was based on that specified in ASTM E8-E8M [186], modified slightly to fit within the build envelope available using the RBV. The samples were built in a horizontal orientation (H specimen, Figure 2.20), chosen due to the reportedly similar tensile properties to wrought, and enhanced compared to alternative build orientations. The  $T_M$  sample profile is shown in Figure 6.1, the thickness was 3 mm. Samples were mechanically removed from the build plates and cleaned of loose powder before any other processing.

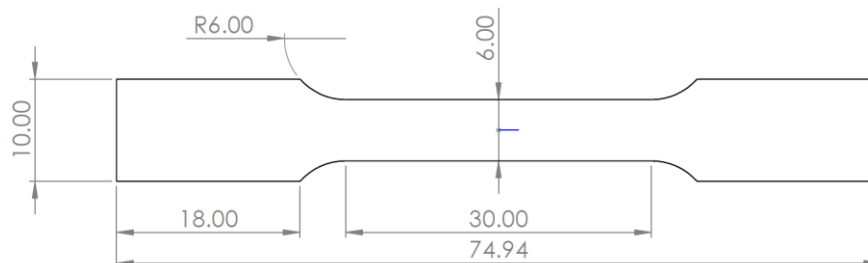


Figure 6.1:  $T_M$  trial tensile test specimen, based on ASTM E8-E8M. All dimensions in mm.

For manufacture of the  $T_H$  samples the full build volume became available for use (build volume 250 mm × 250 mm × 300 mm), enabling all samples required to be manufactured in a single build, and with build plate heating of 150°C. Zhang et al. found that miniaturized tensile sample geometries, for various steel alloys, gave comparable results to the standard geometry, except for Young's Modulus which had higher scatter with non-standard sample geometry [187]. In the interest of time, and following findings by Zhang et al. a miniaturized geometry was chosen for the  $T_H$  samples. To address the increased scatter found in [187], four additional samples were manufactured in the original geometry and added to sample sets D and F. The test results from these functioned as a comparison point between the two different coupon geometries.

Miniaturization was achieved by reducing the gauge length to 15 mm and changing the aspect ratio of the grips to 15 mm × 12 mm (length × width), maintaining the same area as in the first design. The thickness was maintained at 3 mm, and therefore the cross-sectional area in the gauge length was also the same at 18 mm<sup>2</sup>. These changes had the twin benefits of reducing the overall length of the samples to 55.3 mm, increasing the number that could be manufactured at a time, and reducing the

LP area allowing more samples to be processed in a given time. The miniaturized geometry is shown in Figure 6.2.

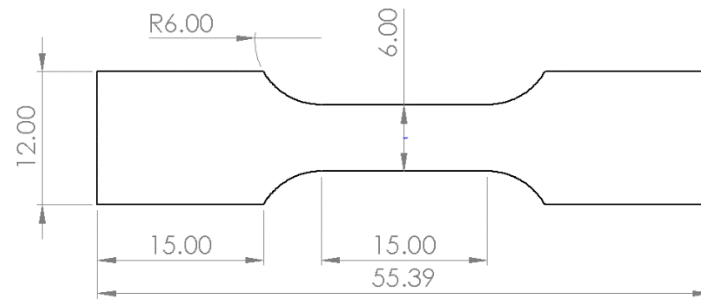


Figure 6.2: Miniaturised tensile sample.

### 6.3.2 Heat Treatment

Samples were heated using an electric-resistance furnace (manufactured by Carbolite [188]) in air at the temperatures and times given in Table 2.4. All samples were processed at once, and cooling was achieved either in ambient air overnight or immersing in cold water until fully cooled. The quenching water did not appreciably change temperature during the process. The various heating steps were conducted on sequential days to minimize effect of natural aging between the SHT and AA processes.

### 6.3.3 Sample Polishing

LP was applied to the test coupons using the equipment described in Chapter 3.2. Samples used for the initial trials were polished using the unoptimized LP strategy as described in Table 5.1 – not using 100% laser power and 16 passes for the final smoothing step.

Between preparation of the samples for the  $T_M$  and  $T_H$  tensile trials, the LP strategy was further optimized (refer to Chapter 5.4.3) to improve the processing rate. The final strategy (Table 5.4) was therefore selected to reduce the time required to manufacture the  $T_H$  samples. To evaluate the influence of the updated strategy on mechanical properties, an additional set of 18 tensile samples were manufactured, built vertically (long axis normal to build plate) and net-shape. Six samples of each condition were prepared (as built, initial LP, final LP). In this way, any different effects on the mechanical properties due to the different LP strategies would be apparent, and therefore ensure correlations between the  $T_M$  and  $T_H$  trials could be made.

For all polished samples, the LP region covered the entire gauge length, and extended a short distance towards the grip sections, as shown by Figure 6.3. Polishing the full sample surface was not considered as the time required to achieve that was nearly double that of the reduced area as selected.

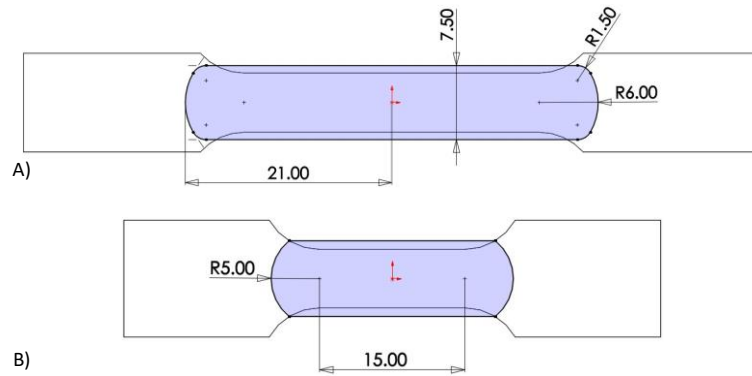


Figure 6.3: Dimensions of the polished region (shaded) overlaid on the sample outline. Geometry of (A) Initial, and (B) Miniaturised specimen. Dimensions in mm.

#### 6.3.4 FEA Validation of Miniaturisation and LP Geometry

First, a structural FEA model was used to compare the stress distribution within the original and miniaturized sample geometries. A 50% model (sectioned vertically through the centre as presented in the above figures) was used to take advantage of symmetry and an equivalent load of 1 kN applied to the gripped regions, as shown by red area in Figure 6.4, with a frictionless support on the sectioned face (blue region in the figure). The miniaturized geometry did not induce any undesirable stress fields within the gauge length (see Figure 6.5), with the maximum stress occurring at the sample shoulders in both instances. As is also shown in the figure, the magnitude of maximum stress only differs by 0.1%, likely due to subtle differences in the applied mesh. Based on this, the miniaturized geometry was deemed suitable for further testing.

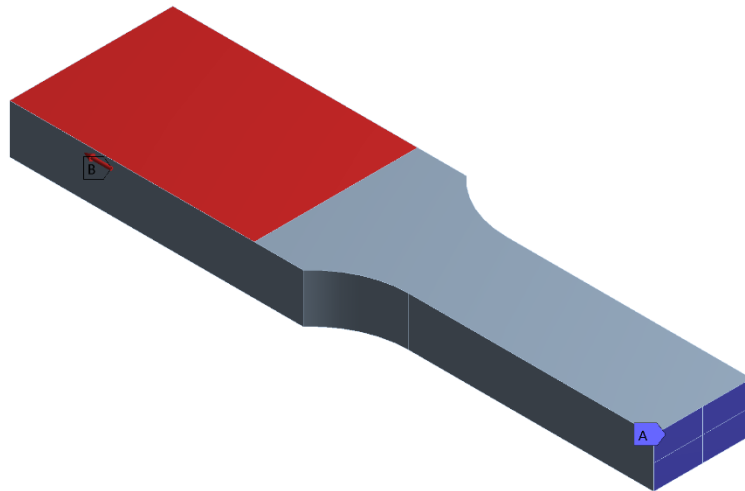


Figure 6.4: Image of the FEA model used (initial trial sample), showing the areas where the frictionless support (A – Blue) and load (B – Red) were applied.

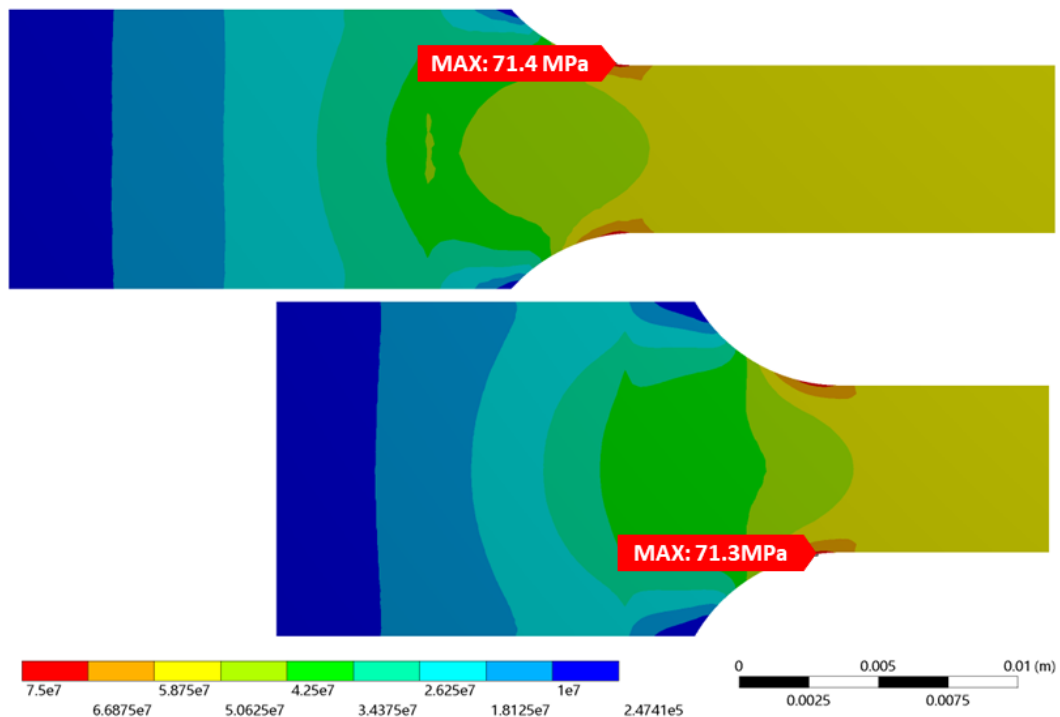


Figure 6.5: Structural FEA model of (top) initial, and (bottom) miniaturized sample geometries, showing von-mises stress.

To check for stress concentrations at the transition from the base surface to the polished region, due to the reduced thickness (ablated material) another basic FEA model was used, following the same setup as described previously (see Figure 6.4). The total depth of ablation was measured on a series of test areas, found to be 0.14 mm from each side. The results from the model were visually checked for stress concentrations away from the gauge length, especially at the edge of the polished region.

In both cases the maximum stress occurred at the shoulder of the gauge length, as shown in Figure 6.6. The maximum stress was found to differ by approximately 3% between the two polishing strategies (also accounting for sample geometry difference). The reduced material thickness due to LP resulted in maximum stress values 10% and 12% higher for the initial and miniaturized geometries respectively.

While there was increased stress at the periphery of the polished region (also shown in the figure), the magnitudes were approximately half the maximum. The average stress at the step was also lower than that in the gauge length – the gauge length is coloured in yellow, while the step is green and blue. Based on this, the polishing geometry was therefore deemed suitable.

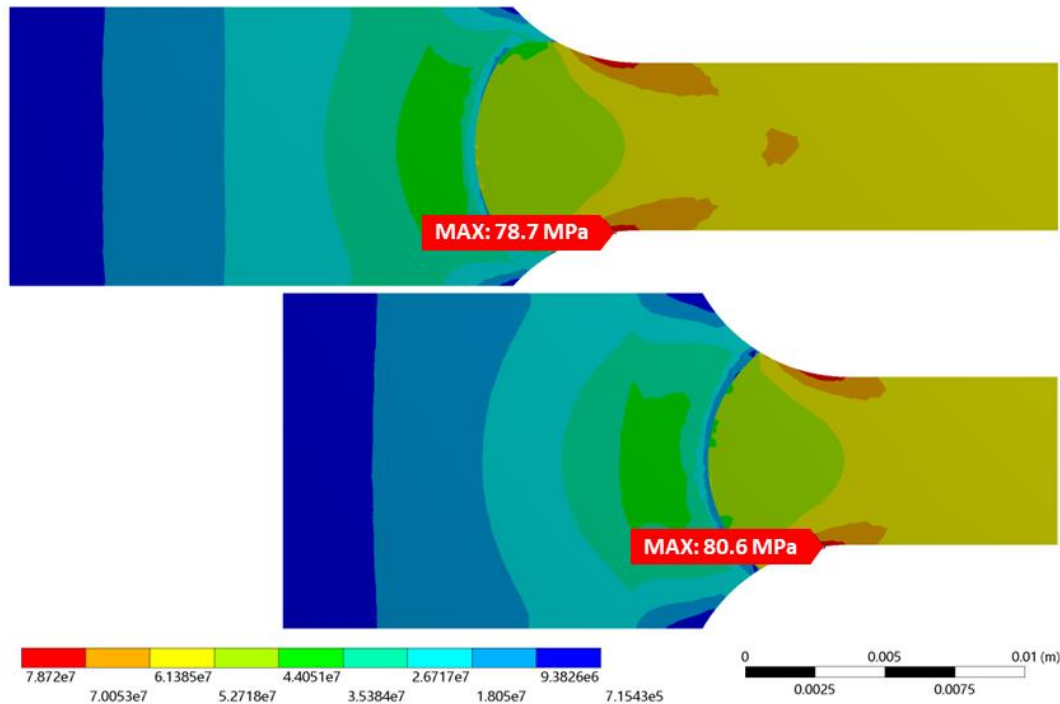


Figure 6.6: Structural FEA model of (top) initial, and (bottom) miniaturized sample geometries with ablated volume removed, showing von-mises stress.

### 3.4.7 Sample Preparation

After manufacture, samples were removed from the build platform and cleaned of loose powder. As required, samples were then CNC milled to final shape, followed by heat treatment and LP. Finally, surface roughness was measured immediately prior to testing.

### 6.3.5 Surface Roughness Measurement

Surface roughness measurements were taken in the as-tested condition (with or without LP, as appropriate). Measurements were taken using a *Sensofar Smart* optical profiler as described in Chapter 3.3, following the procedure developed in Chapter 4. Arrays of 3 x 8 measurements were used to give a total FoV of approximately 4 mm x 10 mm. The full array of surface roughness parameters described in Table 2.2 were computed and assessed for correlations with mechanical performance.

### 6.3.6 Material Properties

The cross section of each sample was measured after testing, near the fracture surface, to calculate the engineering stress ( $\sigma$ ) within the samples. Strain ( $\epsilon$ ) was directly obtained from the VG data. As the samples showed relatively brittle failure (no load reduction immediately before fracture, the UTS and Failure Strain ( $\epsilon_{Fail}$ ) were taken from the point of maximum load, as the material showed no load reduction prior to rupture.  $E$  was found using the MATLAB *fit linear regression model* “FitLM” function (documentation for which is available at [189]). For the purpose of this test, the yield point was defined as the point where the local Young’s Modulus ( $dE$ ), calculated over a period of 5 consecutive data points (see Equation 3.2) dropped to 50% the value calculated for Young’s modulus up to that point ( $dE \leq E/2$ ). From this point, the Yield Stress ( $\sigma_{Yield}$ ) and Yield Strain ( $\epsilon_{Yield}$ ) were found. The elastic region was taken to be from 0.025% Strain (to account for settling and initial measurement noise) up to the yield point. An example stress-strain curve is shown in Figure 6.7, with the various calculated properties highlighted. The MATLAB script used to find this elastic region is provided in Appendix III.

$$dE \cong \frac{\sigma_{i+5} - \sigma_i}{\varepsilon_{i+5} - \varepsilon_i}$$

Equation 6.1

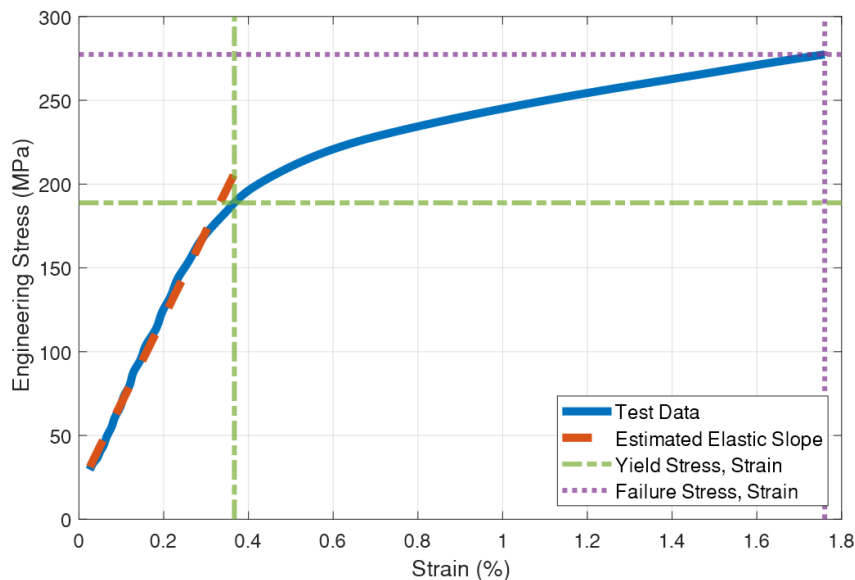


Figure 6.7: Example stress strain curve (solid line) showing the estimated elastic region (dashed line), along with yield (dot-dash line) and failure (dotted line) stress and strains.

Bulk hardness was measured on samples after testing, using the Mitutoyo HM-220B (described in Chapter 3.4.2). Indents were performed on the grip sections that were mechanically polished with P220 SiC paper, up to a load of 0.5 kg. The load was chosen to match the values given in the material datasheets from Renishaw. A series of ten indents were performed on each sample (5 on each end) with 1 mm between indents to avoid interactions in line with standards [190]. Diameters were measured automatically by the HM-220B, with values checked visually and manually remeasured if required. The average hardness for each sample was used to monitor process stability and to ensure any changes in mechanical properties were due to the applied post-processing and not manufacturing variations.

## 6.4 Results

### 6.4.1 $T_M$ (Machining) Trial

Figure 6.8 shows the results (blue cross) and average value (red bar) for each sample type for each of  $E$ , UTS,  $\varepsilon_{Fail}$ ,  $\sigma_{Yield}$ , and  $\varepsilon_{Yield}$  in turn. Also shown in the figure are the reference values (black dashed line) and the expected range (shaded area). Reference values were taken from the Renishaw material datasheet [69], no reference value is available for Yield Strain. All reference values are for fully machined samples and therefore some discrepancy is expected.

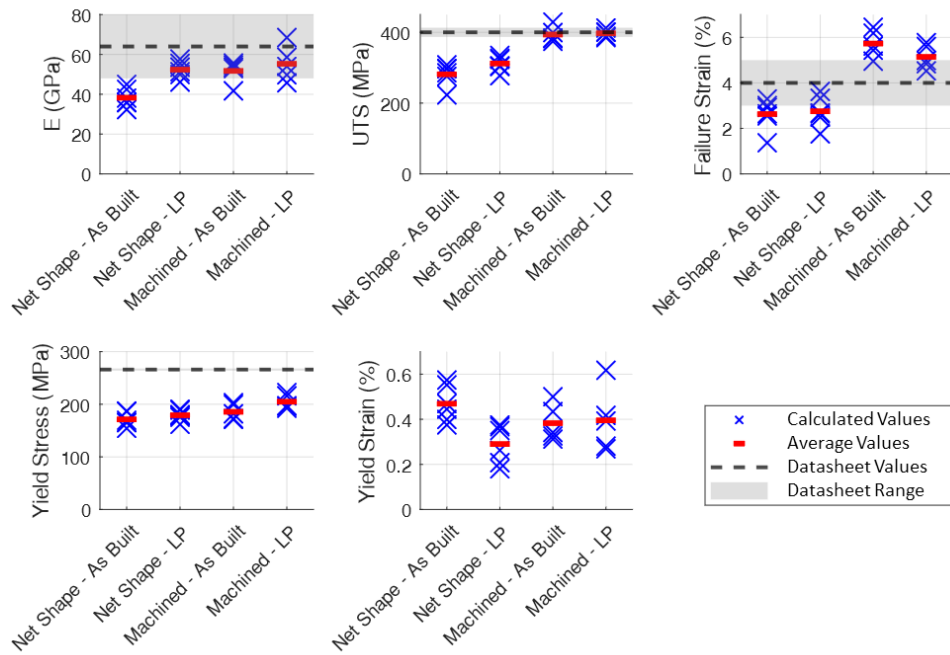


Figure 6.8: Mechanical property results from  $T_M$  tests.

The average values for each sample type are provided in Table 6.3, along with the % change compared to the  $T_{M1}$  (as-built) samples, where positive values indicate an increase and negative values a reduction. Looking at the UTS and  $\epsilon_{Fail}$  it can be seen that the machined samples have much higher values than the net-shape manufactured samples, with a smaller increase for  $E$  and  $\sigma_{Yield}$ . Furthermore, the datasheet value for UTS is  $400 \pm 13$  MPa [69], and the average values for the machined samples are within this range (397.4 MPa and 393.8 MPa with and without LP respectively).

The failure strain is less clear, while the datasheet value is 4% ( $\pm 1\%$ ) [69], the machined samples were in the range of 4.5% - 6.4%, and therefore have much higher ductility than the net-shape samples (1.4% - 3.6%). This is likely due to the smoother side surfaces not promoting crack initiation. A similar picture comes from looking at the range of Young's Modulus values for each sample type. In this case it appears LP and machining both increase average  $E$  values by about 35% to 52.4 GPa and 51.7 GPa respectively, while applying both machining and LP to samples gave further increases to 55.3 GPa.

As expected, the as-built samples (Net-shape without LP) had the greatest variance in UTS (15.1%),  $\epsilon_{Fail}$  (36.6%), and  $\sigma_{Yield}$  (9.58%), while the machined and LP samples had the lowest variability in those parameters (3.41%, 12.1%, and 7.29% respectively). Interestingly, the machined and LP samples had the greatest variability for  $E$  and  $\epsilon_{Yield}$  at 20.5% and 44.1% each, approximately double the lowest variability found with net-shaped LP ( $E$ , 11.1%) and net-shaped non-LP ( $\epsilon_{Yield}$ , 21.2%).

It is hypothesised that this is due to the increased near-surface porosity induced by the LP strategies used. While the application of LP leads to a more consistent surface roughness (across samples), these pores are comparatively inconsistent in terms of shape, size, and relative density (the large ranges shown in Figure 5.14). This porosity acts as crack initiation locations of different severity, leading to the greater variability in the yield properties (and therefore  $E$ ).

Table 6.3: Average value for range of outputs for each  $T_M$  sample type. Change with respect to the “Net Shape – As Built” condition given in brackets, where positive values indicate an increase, while negative indicate a reduction.

Sample Type	Young’s Modulus (GPa)	UTS (MPa)	Failure Strain (%)	Yield Stress (MPa)	Yield Strain (%)
<b>T<sub>M1</sub></b> Net-Shape As-Built	38.24	281.2	2.628	171.3	0.4691
<b>T<sub>M2</sub></b> Net-Shape LP	52.36 (36.9%)	311.9 (10.9%)	2.753 (4.7%)	179.1 (4.6%)	0.2903 (-38.1%)
<b>T<sub>M3</sub></b> Machined As-Built	51.73 (35.3%)	393.8 (40.0%)	5.727 (117.9%)	185.6 (8.4%)	0.3827 (-18.4%)
<b>T<sub>M4</sub></b> Machined LP	55.31 (44.6%)	397.4 (41.3%)	5.143 (95.7%)	204.8 (19.6%)	0.3954 (-15.7%)

To quantify the effects of the Machining and LP operations, a correlation analysis was carried out in MATLAB using the “corrcoef” function. The MATLAB function uses the Pearson correlation coefficient and also returns the significance of the calculated correlation coefficients [191]. It was clear from investigation of the scatter plots (Figure 6.8) that the controlled variables (Machining and LP) were not independent. Therefore, four separate analyses were required first looking at the effect of machining on as-built and polished samples (see Figure 6.9), and then the effect of LP on samples with and without machining (see Figure 6.10). In both cases, correlation coefficients ( $r$ ) are presented only when the associated probability value ( $p$ ) was  $< 0.05$  (95% confidence in line with standard practice [192]).

Looking at Figure 6.9, the only similarities are the increased UTS and  $\epsilon_{Fail}$  by machining the profile. The magnitudes of the correlation coefficients are also very similar, ranging between 0.90 and 0.94. In the laser polished condition, there is also an increase in  $\sigma_{Yield}$  after machining. It is notable that in the as-built condition there is a strong negative correlation ( $r \approx -0.88$ ) between  $S_v$  and  $E$ , UTS, and  $\epsilon_{Fail}$ , which is not observed after LP. This shows LP can reduce the sensitivity to surface conditions for AM AlSi10Mg parts.

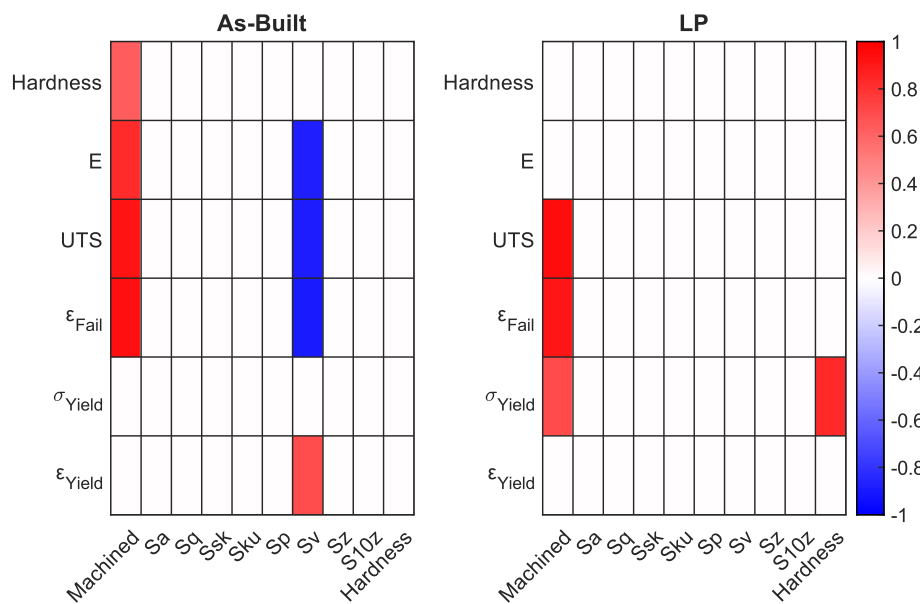


Figure 6.9: Correlation coefficients for the influence of the machining operation, Sample bulk hardness, and surface roughness on mechanical tensile properties. Only coefficients with significance  $< 0.05$  are shown.

Following a similar method, from Figure 6.10 it can be seen that machined samples are desensitised to all the various inputs evaluated, with the exception of  $S_v$  which negatively correlates with  $E$  ( $r = -0.69$ ). Net-shape samples showed  $\epsilon_{Yield}$  positively correlating to most surface roughness parameters (except  $S_{sk}$  and  $S_{ku}$ ), while being negatively influenced by LP.  $E$  and UTS both negatively correlate to surface roughness, with  $E$  positively correlating with the application of LP.

While it is tempting to conclude that when manufactured net-shape the samples are highly sensitive to surface roughness, it is clear that the application of LP is the driving factor. For  $E$  the correlation coefficient with LP is 0.88, while the average to the roughness parameters is -0.79 (only accounting for combinations with  $p < 0.05$ ). This is suspiciously close to equal and opposite. Therefore, it can be said that the significant reduction in surface roughness due to LP (Chapter 5.5) causes the spurious correlations observed here to present themselves. This is further confirmed by the lack of such widespread correlations in any of the other analyses presented.

To properly assess the influence of surface roughness on tensile properties, a much more varied sample set would be required (in terms of surface roughness), resulting from different manufacturing methods (sanding, blasting, etching etc.).

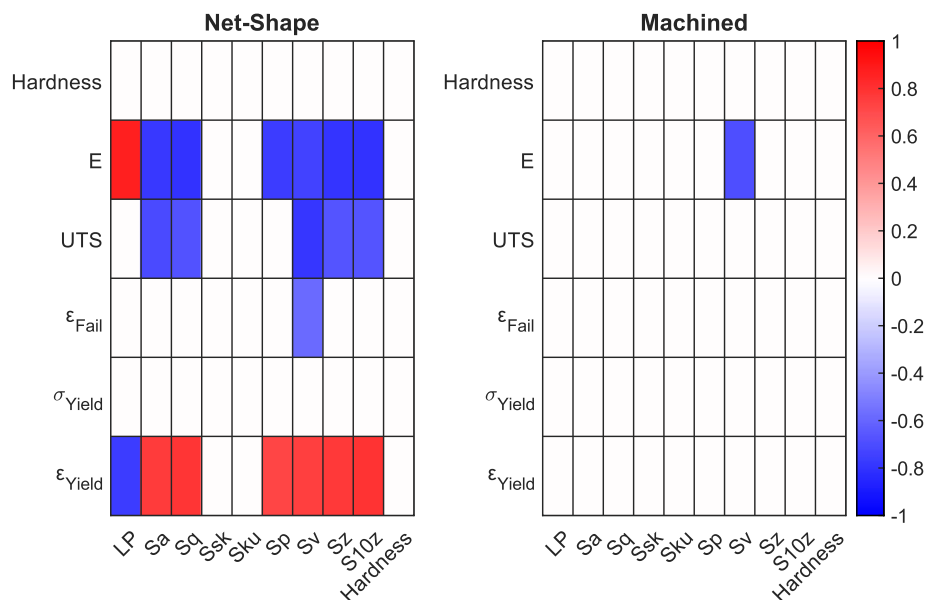


Figure 6.10: Correlation coefficients for the influence of Laser Polishing, Sample bulk hardness, and surface roughness on mechanical tensile properties. Only coefficients with significance  $< 0.05$  are shown.

Overall, it is clear that both machining and LP are highly influential in the mechanical properties calculated from these samples, with the effects dependent on the status of both. It is interesting that both processing options reduce the correlations between the various inputs and outputs investigated here. Similar to what has been observed by others [125], [193], there is no strong link observed between surface roughness and the mechanical properties, other than those also associated with the application of LP.

## 6.4.2 $T_H$ (Heat Treatment) Trial

### 6.4.2.1 Differences Between LP strategies.

During testing, only one of the “initial LP” samples failed within the gauge length, the remainder failed at the periphery of the polished region. All samples from the other two conditions failed within the gauge length. An example is provided in Figure 6.11.



Figure 6.11: Example of sample failure (top) within the gauge length, and (bottom) failure at edge of polished region.

It is notable that all the samples that failed at the edge of the polished region, did so at the end furthest from the build plate during manufacture (higher layer number). It is therefore possible that the samples were manufactured with a slight weakness in this region due to the lower cooling rates<sup>14</sup>, leading to these failures. It is also possible that as the samples were manufactured net-shape with support structures between the sample shoulders, the presence of these supports may have influenced the failure mode.

Figure 6.12 shows the results for samples in either the As-Built condition, processed with the initial LP strategy, or with the final optimized LP strategy. Also highlighted, by the pink circles, are the results for the “Initial LP” sample that failed within the gauge length. As these samples were built vertically the results are not directly comparable to other results presented in this chapter.

Firstly, it is clear that the results scatter is greatly improved by LP for  $E$ ,  $\epsilon_{Fail}$ , and  $\sigma_{Yield}$ , with the two LP strategies performing similarly. The only potentially significant difference between the LP strategies is for  $\epsilon_{Fail}$ , however, due to the previously discussed sample failures it is not possible to conclusively state if there is an effect.

Overall, the results follow a similar pattern to the machined samples from the  $T_M$  trials, with a modest reduction in  $\epsilon_{Fail}$ , a slight increase in  $\sigma_{Yield}$ , and no change in the remaining parameters. However, remembering that none of those effects were found to be significant in the initial trials (see Figure 6.10) and therefore these inferences are not conclusive in any way.

<sup>14</sup> Due to the larger part cross section compared to the preceding layers.

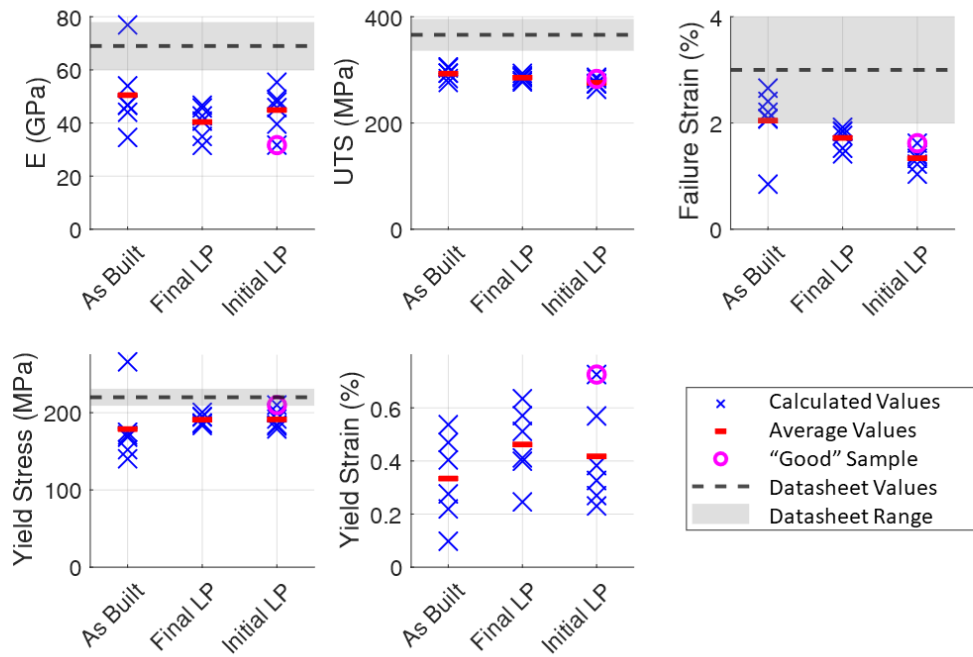


Figure 6.12: Scatter plot of results comparing initial and final, optimized LP process.

Based on this, it is assumed results for the different LP strategies are comparable, and not likely to be influencing the presented results.

#### 6.4.2.2 Effect of Miniaturised Geometry

Throughout the test, there were various sample conditions that were tested on the two different sample geometries. Within the machining trial, laser polished samples in the non-HT and T6 conditions were available, with an additional comparison possible for non-HT samples between the  $T_M$  and  $T_H$  sample sets. In all three cases, samples were machined to achieve the desired sample profile. These results are presented in Figure 6.13.

It can be seen that for the  $T_H$  samples (blue cross and red circle), the calculated UTS,  $\epsilon_{Fail}$ , and  $\sigma_{Yield}$  are not significantly affected by sample geometry in the T6 temper. On the other hand, in the LP condition, all calculated properties are slightly reduced for the miniaturized geometry. The results for  $E$  and  $\epsilon_{Yield}$  showed higher scatter for the miniaturised geometry (in the T6 + LP condition), similar to what was found by Zhang et al. [187].

When also looking at results from the  $T_M$  trial (pink diamond), for the As Built and LP samples the ranges for  $E$ ,  $\sigma_{Yield}$ , and  $\epsilon_{Yield}$  overlap and are therefore unlikely to be excessively influenced by the sample geometry. For UTS and  $\epsilon_{Fail}$  the ranges do not overlap, with the miniaturized samples reporting lower values, and therefore may be dependent on sample geometry.

Overall, as the largest differences appear to be for  $E$  and  $\epsilon_{Yield}$ , which are both calculated from test data rather than directly extracted, or when comparing across different AM builds. This shows that the miniaturized geometry does not unduly affect the tensile properties, especially when considering the inherent material and process variability.

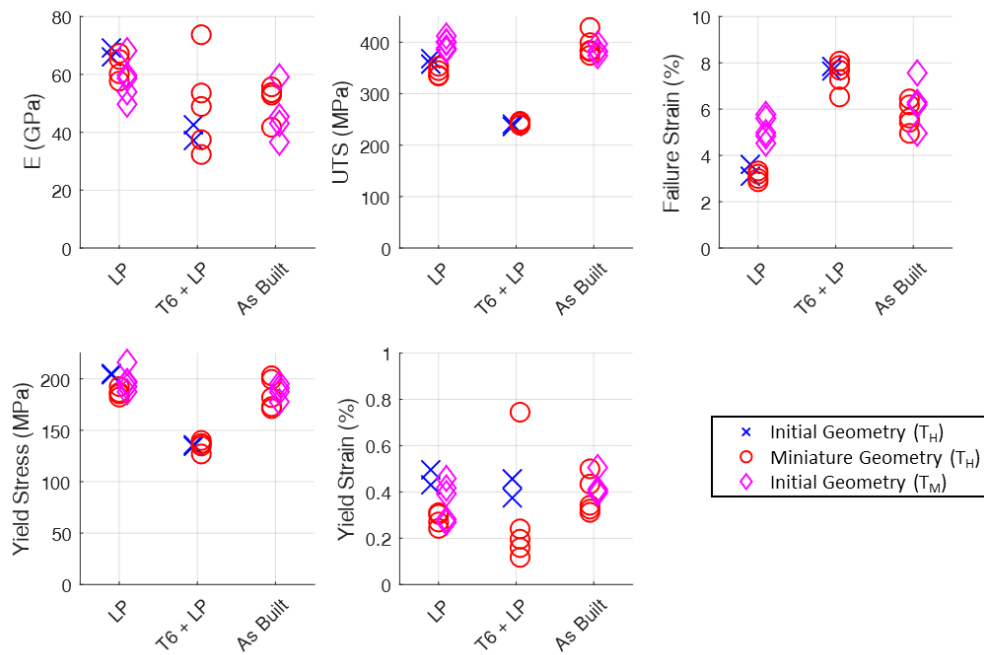


Figure 6.13: Scatter plot of results comparing initial and miniaturized geometry.

#### 6.4.2.3 Effect of Heat Treatment.

Figure 6.14 shows the calculated mechanical properties from the T<sub>H</sub> trial samples. The reference values are for un-heat-treated samples, and therefore not representative of what should be expected from SR or SHT samples.

The observed scatter in Young's Modulus and Yield Strain results is significantly increased compared to the machining trials, despite the HT trial samples all being manufactured in a single build, and the properties calculated in the same way. Taking each sample type in turn (e.g., T6 without LP) and checking for correlations between bulk hardness and mechanical properties yielded no results of significance. Therefore, it is clear the scatter in the tensile properties seen are likely due to the inherent material variability and process instability arising from AM.

From Figure 6.14, LP only has a significant effect on  $E$  for un-heat-treated samples, with the variability in results for heat treated samples greater than the difference arising due to LP. A similar story is present for  $\epsilon_{Yield}$ , but with LP causing a reduction in the un-heat-treated condition.  $\sigma_{Yield}$  is only affected by LP for samples in the T6 condition (but still with averages falling within the range of the other condition). The last two properties, UTS and  $\epsilon_{Fail}$ , appear to be affected by LP in all conditions, with  $\epsilon_{Fail}$  decreasing after LP in each instance. The UTS decreases after LP in the un-heat-treated and SR conditions, and then increases slightly for samples in the T6 condition.

While the effect of heat treatment on samples was only of minor interest in this work, it can be seen to result in progressive reductions in UTS and  $\sigma_{Yield}$ , and increases in  $\epsilon_{Fail}$ . Due to the scatter in  $E$  and  $\epsilon_{Yield}$ , it is not possible to clearly identify trends from the presented data.

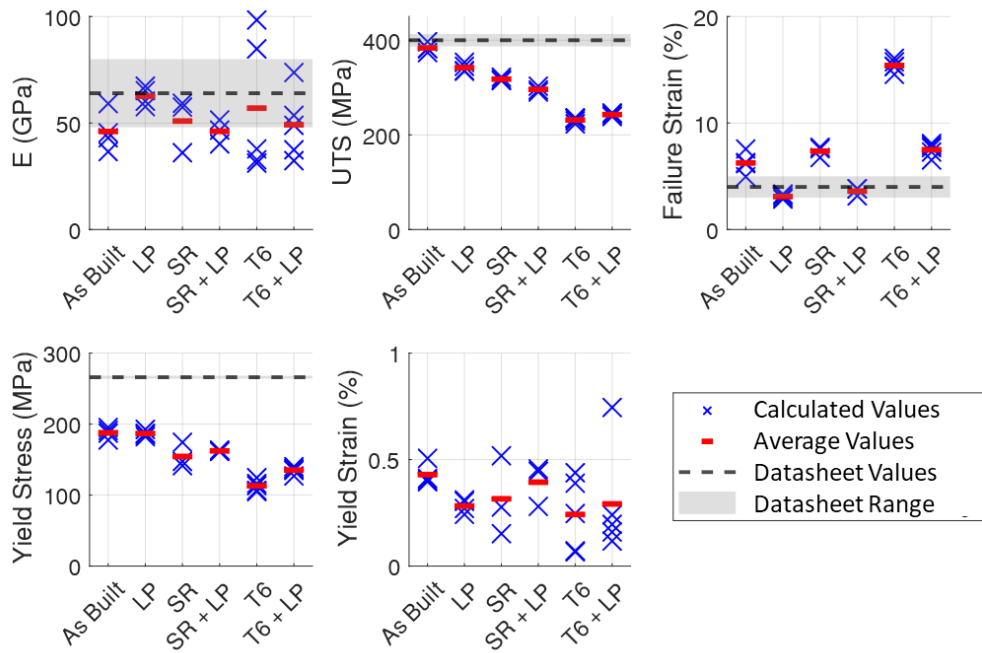


Figure 6.14: Scatter plots of test data (blue cross) and average values (red bar) for calculated tensile properties for samples showing effect of LP and heat treatment.

These observations are confirmed by analysis of the correlation coefficients, evaluated in a similar way to before, Figure 6.15. Surface roughness values are not included due to them being a result of LP rather than an input, as found in the machining trials (Figure 6.10). It can be seen that there are strong negative correlations ( $r \approx -0.97$ ) between the application of LP and the sample  $\epsilon_{Fail}$  in all states of heat treatment.  $E$  and  $\sigma_{Yield}$  are increased after LP, but only in the as-built and T6 conditions respectively. UTS increases with LP in the T6 condition, decreasing otherwise. Yield strain is not significantly affected by LP according to this data.

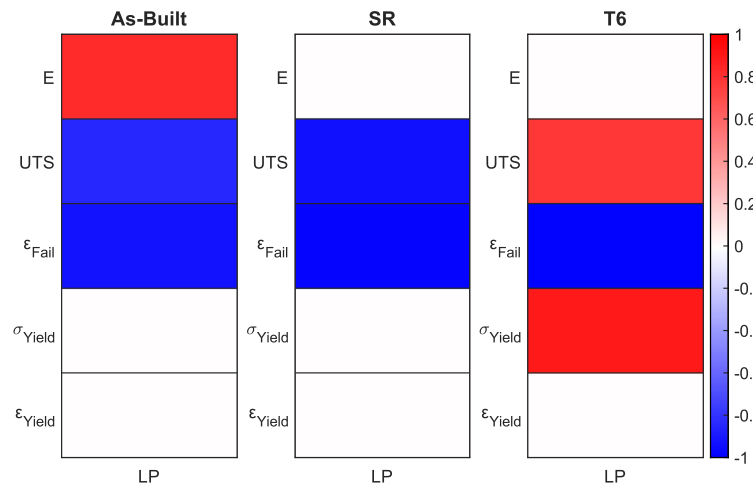


Figure 6.15: Correlation coefficients for the effect of LP on samples in various states of heat treatment.

Looking instead at Figure 6.16 and the correlation coefficients for the application of HT (coded values where 0 = no HT, 0.5 = SR, and 1 = T6 condition) shows even stronger links to the mechanical properties (magnitude of  $r > 0.9$ ). With each successive HT option, the sample hardness decreases, with an associated reduction in UTS and  $\sigma_{Yield}$ , and increased  $\epsilon_{Fail}$ .

These observed mechanical property differences are due to the increased material ductility, especially in the T6 condition, and the effect is present in both the as-built and LP conditions. It is clear from the similarity in responses for as-built and LP samples to HT, heat treatment is far more influential on the tensile properties than the application of LP, however the influence of LP is not negligible. Furthermore, it is clear from the scatter plots that there is a significant inter-dependence between the choice of HT and the effect of LP on a sample's mechanical properties.

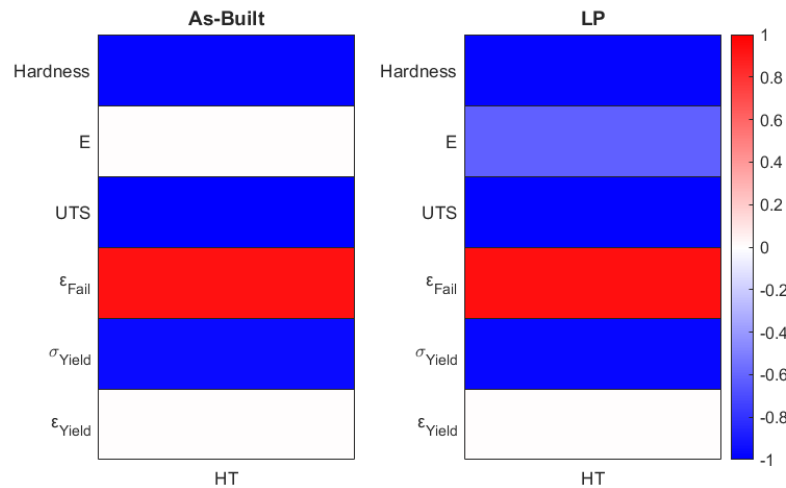


Figure 6.16: Correlation coefficients for the effect of SR/T6 heat treatment on samples with and without LP.

### 6.4.3 Comparisons Between Sample Sets.

Considering the challenges for comparing AM samples from different builds and machines (see Chapter 2.5), the results from the  $T_M$  and  $T_H$  trials were compared for matching sample conditions (machined, with and without LP), as shown in Figure 6.17. It can be seen that in the majority of cases, the average for one trial falls within the range for the other. The exceptions are UTS and  $\epsilon_{Fail}$  for LP samples, where the machining trial reported higher values than the  $T_H$  trial.

This could be related to the sample size, as discussed in section 6.4.2.2, or resulting from the use of build plate heating for the  $T_H$  trial samples. However, both of these would be expected to also influence the results for other properties and for samples in other conditions. Alternative explanations relate to the UTS and  $\epsilon_{Fail}$  properties individually. For the reduction in  $\epsilon_{Fail}$  is the reduced gauge length impacting the accuracy of the VG strain measurement system, as will be discussed further in Chapter 6.5.4, however this would be expected to present for all strain properties and the non-LP samples similarly. Meanwhile, the UTS reduction is likely related to the sub-surface porosity discussed in Chapter 5.3.3.2. It is possible (however not quantified) different LP strategies used result in differing levels of porosity. The increased relative porosity reduces the true cross-sectional area available to sustain the applied loads, and therefore the calculated engineering stresses will be lower.

As both UTS and  $\epsilon_{Fail}$  relate to sample rupture, the differences are likely to be less concerning for a design engineer than the yield properties (or a value substantially lower than yield once safety factors are applied).

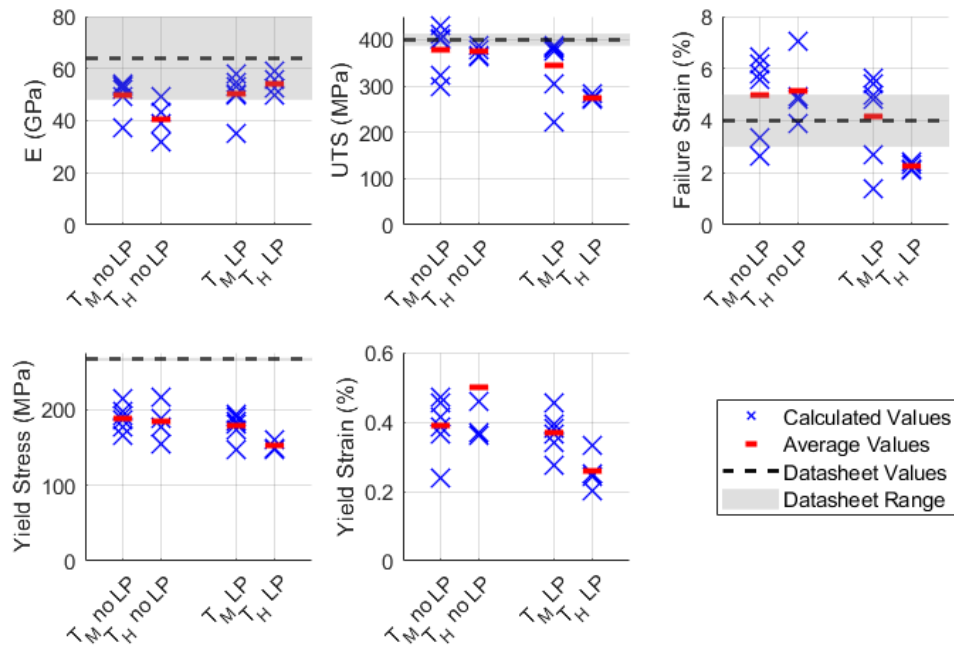


Figure 6.17: Scatter plot of results from matching samples manufactured as part of the  $T_M$  and  $T_H$  trials.

#### 6.4.4 Bulk Hardness

The bulk hardness measured for the samples averaged 123.5  $Hv_{0.5}$  in the as built condition, with a 95% confidence interval of 8.4  $Hv_{0.5}$ . This is higher than the datasheet values of 113  $Hv_{0.5}$  ( $\pm 3 H_{v_{0.5}}$ ) [69], and similar to those reported by Uzan et al. of 122  $Hv_{0.1}$  ( $\pm 4 H_{v_{0.1}}$ ) [194]. Stress relieved samples returned hardness values of 101.9  $Hv_{0.5}$  ( $\pm 10.7 H_{v_{0.5}}$ ), higher than the 95  $Hv_{0.1}$  ( $\pm 3 H_{v_{0.1}}$ ) from Uzan et al. [194] or 50 HRB ( $\approx 95 Hv$ ) from Mertens et al. [136], while also being lower than the datasheet value of 112  $Hv_{0.5}$  ( $\pm 2 H_{v_{0.5}}$ ) [69]. A summary of the hardness values measured here, given in the Renishaw datasheets, and some published literature is shown in Figure 6.18, highlighting the inconsistencies found by researchers.

Finally, the T6 prepared samples were measured at 69.4 ( $\pm 6.9$ )  $Hv_{0.5}$ , lower than other comparable literature. The range of hardness reported in the literature, for AlSi10Mg in the T6 condition ranges between 107  $Hv_{0.1}$  [194], and 72 Hv (unspecified load) [126]. This broad range in reported values underscores the difficulty in properly optimizing the process, with the time and temperature for both the SHT and AA stages being of great importance. As discussed in [117], the AA process is especially sensitive to changes when targeting a T6 temper (see Figure 27 in the same reference). It is possible that the reduced hardness found here compared to that reported in the literature is due to either under- or over-ageing in the current work.

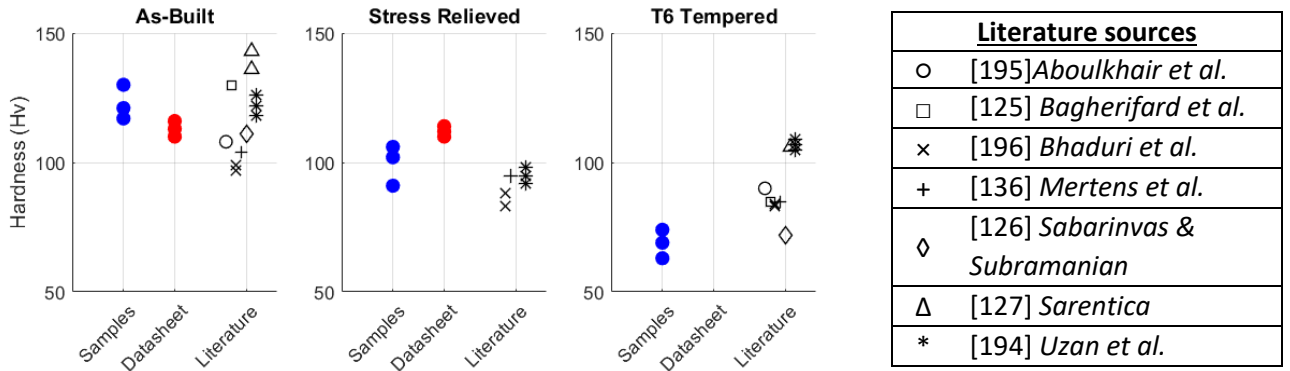


Figure 6.18: Plot of maximum, minimum, and average bulk hardness from measurements, datasheets, and reported literature.

## 6.5 Discussion

### 6.5.1 Comparisons to Datasheet Values

The net-shape manufactured samples all had significantly lower UTS than expected, while the machined samples had averages within the nominal range given in the datasheet, albeit with greater variability than expected. Net-shape and unpolished samples gave inferior  $E$  values compared to the datasheet range, with all other sample conditions averaging lower than the datasheet values, but within the nominal range. The variability in calculated  $E$  were similar to the datasheet range ( $\pm 16$  GPa [69]). All yield stress values were far below expected, and with increased variation, but getting closer with the applied post-processing. Finally, it is interesting that the failure strains for net-shape samples was below nominal, and above for machined samples.

Finally, it is worth noting that the datasheet values are for fully machined components and therefore not fully representative of the components tested here. The differences in sample preparation make direct comparisons challenging, but still provide a useful benchmark against which to identify trends.

### 6.5.2 Comparisons to Literature Values

It is difficult to fully assess how the presented tensile properties relate to values published in the literature. Absolute values cannot easily be compared, due to the expected high variability in material properties, the sensitivity to changes in the HT process, and unknown methods used to evaluate the Yield point, and therefore Young's Modulus. However, it is possible to compare trends between the different HT states.

The most commonly reported values in previous studies are UTS and  $\epsilon_{Fail}$ , with many authors finding gradual reductions in UTS, and increasing  $\epsilon_{Fail}$  after the samples underwent SR and T6 heat treatments (compared to the as-built condition). Notably, Bagherifard et al. [125] found a very similar decrease in UTS after T6 treatment (from 393 MPa to 265 MPa) to the results presented in this chapter (389 MPa to 231 MPa). Uzan et al. [194] and Hofele et al. [178] found a substantial reduction in UTS after SR (131 MPa and 104 MPa respectively), meanwhile, Zyguła et al. [197] found an increase after a T6 treatment (160 MPa to 192 MPa). A similar pattern appears when looking at  $\epsilon_{Fail}$ , with some finding substantial increases in this value in both the SR [178], [194] and T6 conditions [124], [125], while others found much smaller effects [128], [139]. These reported values are presented in Table 6.4, emphasising the difficulty in finding widely accepted trends.

Table 6.4: Values for UTS,  $\epsilon_{Fail}$ ,  $\sigma_{Yield}$ , and  $E$ , from various literature. Heat treatment conditions reported from each of the following conditions: AB – As Built, SR – Stress Relief, T6 – T6 Temper.

UTS (MPa)			Failure Strain (%)			Yield Stress (MPa)			E (GPa)			Ref.
AB	SR	T6	AB	SR	T6	AB	SR	T6	AB	SR	T6	
393		265	2.5		13	273		201	72		73	[125]
333		292	1.4		3.9	268		239	77		73	[139]
160		192	1.59		1.77	159		171	32		64	[197]
318	310	275	4	7	13	175	150	230				[136]
346	242		3.9	12.6		192	125					[178]
384	253		6	18		241	205					[194]
247		305	4.5		6.0	187		240				[128]
434		192	5.3		21.4							[124]
456		193-300*	5.2		4.2-8.2*							[127]

\* Value depends on time and temperature used to achieve the T6 temper.

Of those that reported UTS and  $\epsilon_{Fail}$  results, two compared both SR and T6 tempering to the as-built condition, and their trends are of great interest here. Sarentica [127] found a decrease in both UTS and  $\epsilon_{Fail}$  after SR, with a slight recovery of UTS (and enhanced  $\epsilon_{Fail}$ ) in the T6 condition. The overall effect on UTS of their T6 treatment was similar to the present work - approximately 160 MPa reduction compared to as-built. For  $\epsilon_{Fail}$ , the trends found by Mertens et al. [136] closely resemble those found here, as summarised in Table 6.5

Table 6.5: Comparing Failure Strain results in various states of heat treatment found in this work and by Mertens et al. [136].

	As Built	Stress Relived	T6 Temper
Present work	5.96%	7.36%	15.4%
Mertens et al. [136]	4%	7%	13%

Yield stress is the next most often reported tensile property, and for this, Bagherifard et al. [125] (As-Built and T6 condition) and Uzan et al. [194] (As-Built and Stress Relived) both found very similar reductions, but with values approximately 85 MPa and 50 MPa higher than reported in this chapter respectively. Mertens et al. [136] reported very similar values (175 MPa and 150 MPa), to those reported here (187 MPa, 155 MPa) for the as-built and SR conditions however they found a substantial increase in the T6 condition to 230 MPa.

Very few studies have reported the effect of different heat treatments on Young's Modulus of AM AlSi10Mg, and those that do have focussed on comparing T6 tempered samples with those in the as-built condition. This lack of information is likely due to the ambiguity of determining the Yield point from test data. Of the reported literature, there is no consensus on what to expect, with Aboulkhair [139] reporting a modest reduction (77 GPa to 73 GPa), and Zyguła et al. [197] reporting a substantial increase (32 GPa to 64 GPa). Finally, Bagherifard et al. [125] found no substantial change in  $E$  from the application of a T6 temper ( $72 \pm 1.5$  GPa to  $73 \pm 1$  GPa).

### 6.5.3 Effect of Laser Polishing on Tensile Properties

There are scant published results for the effect of LP on the tensile properties of AM AlSi10Mg, with one such study from Hofele et al. [178]. From four samples in each condition, they prepared samples with and without LP (both CW and PW, only PW is discussed here) and in the as-built and stress relieved conditions. The study found a substantial decrease in  $\sigma_{Yield}$  after LP without stress relief, and no change with SR. In the present work, no change in  $\sigma_{Yield}$  was found due to LP in either HT state. UTS followed a similar trend for Hofele et al. as found here, with LP causing a reduction in UTS

without SR and no significant change with SR. Finally, looking at  $\epsilon_{Fail}$ , it is interesting that the other study found a reversed trend for the as built samples (3.4% to 6.8% after LP) compared to this work (5.0% to 2.9% after LP), while also finding LP to have a similar effect on SR parts but with much higher ductility than found here (11.5% to 8.7%, 6.8% to 3.2%).

It is thought that the application of LP can increase the failure strain by reducing the surface roughness, and therefore minimizing crack initiation locations [178]. However, this has not been observed here (or in [178] for SR samples), with  $\epsilon_{Fail}$  consistently reducing with the application of LP (except for the net-shape manufactured in the initial trial where there was no change). Therefore, alternative influences must be at play causing this reduction in  $\epsilon_{Fail}$ . It has been previously found that LP leads to changes in the near-surface microhardness. Softening in the case of Hofele et al. [178], without associated compositional changes. Alternatively, Bhaduri et al. [71] reported hardening at the surface, with a softer layer a short distance below, corresponding to silicon and aluminium enrichment respectively.

From the work presented in Chapter 5, increased hardness without any appreciable softening, it is unclear what the specific mechanisms are. Further evaluations of the composition and residual stresses are suggested for future work. It is thought the hardened surface layer acts similarly to case hardening, reducing the deformation of the parts during testing.

Compared to results found for other materials, Wei et al. [198] looked at the Ti6Al4V alloy, while Chen et al. [4] focussed on 316L Stainless Steel. Both found that  $\epsilon_{Fail}$  was increased by LP, from 7.6% to a maximum of 8.9% after three passes on Ti64, and from 58.3% to a maximum of 63.3% for 316L also after three polishing passes. Chen et al. [4] also found LP increased the UTS from 621 MPa to 669 MPa (7.7%) after LP while Wei et al. [198] found no significant change to either UTS or  $\sigma_{Yield}$  after LP. The findings by Wei et al. mirror those in this work, also finding no difference in UTS and  $\sigma_{Yield}$ , while the main trials here found reduced  $\epsilon_{Fail}$  in all HT conditions.

#### 6.5.4 Yield Strain Variability

The calculated Yield Strains showed the highest spread of the tensile properties found, especially for the samples comparing the LP strategies (Figure 6.12). For those tests, the average values were approximately 0.4%, with test data varying by about  $\pm 0.2\%$ . As described in Chapter 3.4, the strain was measured using a Video Gauge from Imentrum. Assessing the uncertainty of such systems is non-trivial, and highly dependent on the test setup (lens characteristics, distance from camera to sample, alignment of camera and sample, etc.) [160]. Therefore, to assess the measurement noise, the standard deviation of strain data from before the application of any load was found for all tests, and the average deviation was found.

This gave an overall value of  $\pm 0.33\%$  for the initial sample geometry, and  $\pm 0.55\%$  for the miniaturized geometry, closely mirroring the variation in calculated  $\epsilon_{Yield}$ . This variability could be due to noise coming from the load machine or a limitation of the measurement system. However, as the landmarks used to measure strain were placed approximately 30 mm or 15 mm apart for the initial and miniaturized sample geometries respectively, this noise equates to a displacement error of  $\pm 0.2$  mm (at 95% confidence). Mower and Long used a similar device during their testing and deduced the induced error in  $E$  calculations was between 1% and 3% [25], much lower than the scatter observed in the results found here (minimum 10 %).

## 6.6 Tensile Testing Summary

The results presented in this chapter show laser polishing has a mixed influence on the tensile properties of AM AlSi10Mg coupons, summarised in Table 6.6. Specifically, increases were seen in

Young's modulus in the absence of heat treatments, and to a much lesser extent Yield stress for heat treated parts. UTS was reduced by LP in all conditions, with a stronger effect seen for failure strain, however for both UTS and  $\epsilon_{Fail}$ , the application of heat treatments (stress relief or T6 tempering) was much more influential. Finally, no significant effect was seen for yield strain in any state, Young's modulus after heat treatment, or yield stress unless in the T6 condition.

Table 6.6: Summary of the influence of LP on Tensile properties.

Property	LP Influence
$E$	↑ Increased without HT
	↓ Reduced scatter (with HT)
	→ No change with machining and/or HT
$UTS$	→ No change
$\epsilon_{Fail}$	↓ Reduced with HT
	↓ Reduced scatter without HT
$\sigma_{Yield}$	↑ Increase after T6 tempering
	→ No change in other conditions
$\epsilon_{Yield}$	↑ Increased scatter
	↓ Reduced without machining or HT

The values found here do not conform to the nominal datasheet values, likely due to differences in sample preparation (as-built surfaces here, fully machined for the datasheet values) and manufacturing variability. For non-HT sample sets, the average  $E$  values often fell within the reference range, however many of the calculated values were lower than the nominal range. Similar disagreements have been found when comparing to other published research, equally reporting higher, lower, or similar values. However, tensile properties reported in the literature often showed similar trends for the effect of different heat treatments. This highlights the process sensitivity of AM parts and the care required during design when selecting reference strengths.

The influence of LP on the tensile properties of AlSi10Mg is not widely reported, and it is well known the LP process is highly dependent on the laser system used. The results presented here follow similar trends for Yield stress, UTS, and Failure Strain after stress relief, and also for UTS without stress relief, to a recently published work.

Overall, the LP strategy developed in Chapter 5 has been shown to influence the mechanical tensile properties of AlSi10Mg samples in a repeatable way, or to have no significant change. This shows the LP strategy could be combined with surface texturing, or functionalisation, to achieve hybrid additive/subtractive manufacturing of AlSi10Mg parts without requiring significant design changes compared with those used for as-built equivalents.

## 7 Assessment of the Fatigue Strength of AM Aluminium

### 7.1 Introduction

The fatigue performance of materials is of paramount importance for engineers. In nearly every application, structures will be subjected to some degree of cyclic loading. It is therefore imperative to understand to what degree a material can be fatigued before failure.

Fatigue can be broadly described as either high-cycle or low-cycle, depending on the number of cycles expected. LCF is generally described as that where the number of cycles to failure is less than  $10^5$ , while HCF covers longer durations ( $10^7$  cycles is not uncommon). LCF is typically dominated by crack propagation, while HCF performance more closely relates to crack initiation [5]. Therefore, both are of keen interest to engineers, with each being more relevant in different applications (e.g., LCF for airframes, and HCF for engine components [83]).

### 7.2 Purpose

As discussed in Chapter 2.5.2, fatigue is often the limiting factor for how long a component can be used safely. It is clear, therefore, that the current lack of knowledge surrounding the fatigue performance of AM AlSi10Mg is a significant inhibitor to the widespread adoption of the material. To this end, following assessment of the static tensile properties in Chapter 6, it was felt necessary to test the effect of LP on the fatigue performance of AlSi10Mg parts.

Many authors report the presence of “killer notches” in failed AM fatigue specimen (for example [103]). It is therefore envisioned the LP process developed in Chapter 5 may work to extend the fatigue life of components thanks to the vastly reduced surface roughness ( $S_a$  2.26  $\mu\text{m}$ ,  $S_v$  14.11  $\mu\text{m}$  after LP (Table 5.6)). However, there are conflicting influences; the ablated material removing approximately 0.14 mm from each surface, and the increased near-surface porosity (average 4.5%) likely adversely affecting the fatigue properties. With this in mind, it was necessary to identify how these competing factors combined in both LCF and HCF conditions.

### 7.3 Test Plan

Two identical sets of fatigue specimens were manufactured during the same AM build in a horizontal orientation. The geometry was according to ASTM E466 [199], shown in Figure 7.1 (the thickness was 3 mm). The reduced section (between the radii) is a critical feature so was realised using mechanical milling to ensure geometric accuracy. An additional benefit of milling the radii was the consistent surface roughness of the side, isolating the influence of LP on the fatigue endurance of the samples. Details of the manufacturing parameters are provided in Chapter 3.1. One set of samples was used for LCF testing at Cardiff University, while the other was used for HCF testing. The condition for each sample is given in Table 7.1. Laser Polishing was carried out to the specification detailed in Chapter 5. The HT parts (F3, F4) were stress relieved followed by a T6 temper, details of which are given in Chapter 6. Two replicates were conducted, for a total of 16 samples. While more replicates and sample conditions are desirable, a relatively small test plan was selected to limit the test durations and provide guidance for future, more in-depth studies.

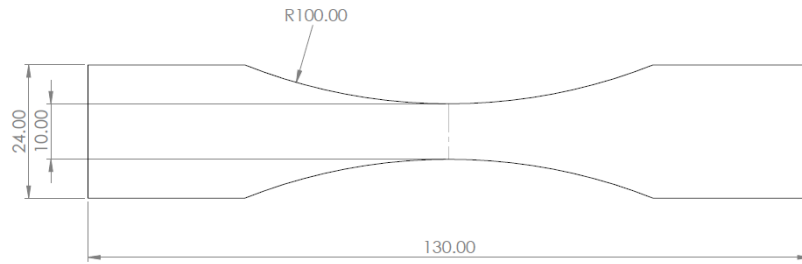


Figure 7.1: Fatigue sample geometry, from ASTM E466 (all dimensions in mm).

Table 7.1: Fatigue sample conditions.

Series	Surface Condition	Heat Treatment
F1	As Built	None
F2	LP	None
F3	As Built	SR and T6 temper
F4	LP	SR and T6 temper

A target  $N_{Life}$  for the LCF testing was set at 10,000 cycles. From a review of published S-N curves [5], [6], [135] for  $R_\sigma=0.1$  axial fatigue testing of AM AlSi10Mg stress levels targeting approximately 75% of the UTS were selected. It was initially hypothesised that the reduced surface roughness and increased hardness would offset the thickness reduction and porosity resulting from LP. Therefore, for sample series F1 and F2 the same maximum load (10 kN) was used. Due to the reduction in thickness from LP, applying the same load resulted in the F2 LCF samples being stressed slightly above the average (349.0 MPa) and approximately equal to the maximum (368.1 MPa) UTS found in Chapter 6. The applied maximum stress, load, and stress as a percentage of UTS are presented in Table 7.2.

Table 7.2: Test conditions for LCF samples.

Series	Maximum Stress (MPa)	% UTS	Maximum load (kN)
F1	297.5	77.5	10
F2	369.5	<b>105.87</b>	10
F3	181.5	78.39	6.1
F4	181.1	74.95	4.9

Initially, HCF testing was to be performed at constant maximum stress to failure, with a stress of 100 MPa selected based upon S-N curves published in the literature for comparable test setups, namely [5], [6], [135]. However, upon testing, the first sample endured  $3 \times 10^7$  cycles without failing (Series F1).

It was therefore decided to proceed with a stepped-load method described by [129]. Block sizes (target fatigue life,  $N_{Life}$ ) were set at  $10^6$  cycles and  $\Delta\sigma$  to 17 MPa (representing 0.5 kN load). While this  $\Delta\sigma$  is higher than the 7% recommended by [129], it was deemed appropriate as this work is intended to be an exploratory study for future investigations. Subsequent tests were also commenced at 117 MPa rather than 100 MPa to expedite results. Discussion of the applied stresses, and how they relate to the mechanical properties, will follow in Section 7.5.

#### 7.4 Sample Preparation

After the samples were removed from the build plate and machined to the final profile half were heat treated as described in Chapter 6. All HT samples were treated simultaneously to eliminate the possibility for process variability. Following HT LP was applied to the relevant samples.

It is known from previous chapters that there is a reduction in thickness due to LP, and this change in thickness was liable to result in significant stress concentrations if not managed appropriately. The change in surface height after each processing step was measured and the results are presented in Table 7.3.

Table 7.3: Material removal per LP step.

Step	Layers	Total height change	Height change per layer
1 (Ablation)	8	64 $\mu\text{m}$	8 $\mu\text{m}$
2 (Smoothing)	8	24 $\mu\text{m}$	3 $\mu\text{m}$
3 (Ablation)	4	16 $\mu\text{m}$	4 $\mu\text{m}$
4 (Smoothing)	14	28 $\mu\text{m}$	2 $\mu\text{m}$

Using this information, an FEA model was produced, initially with all LP steps covering an identical area as was done in Chapter 6 (i.e., 132  $\mu\text{m}$  material removed per side), and compared with the unpolished geometry. The simulation setup was similar to that used in Chapter 6, using a half-model due to symmetry, constraining the section plane, and applying a representative 1 kN load to the grip section. The von Mises stress results from this are shown in Figure 7.2. It is clear that this unrefined approach leads to significantly elevated stress levels at the periphery of the LP region. Failure is likely to occur near the location of maximum stress, and therefore this condition is to be avoided. Such stress raisers were not observed for the tensile samples, likely due to the relative difference between the gauge width and the maximum polished width being much greater than for the fatigue samples.

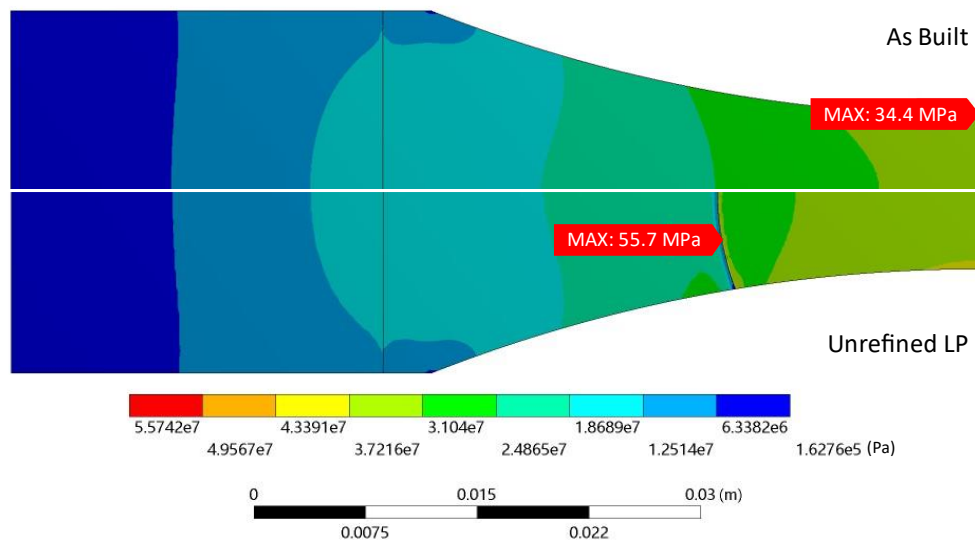


Figure 7.2: Von Mises stress plot of fatigue sample, showing location and magnitude of maximum stress.

Therefore, to ensure samples failed in the central section, terraced polishing regions were pursued, with each successive LP step covering a slightly smaller area than the last. This is shown schematically in Figure 7.3, where  $R$  is the radius of the first LP step, and  $dR$  is the radius change for each successive LP step. Furthermore, owing to the Lasertec 40 being capable of 3D machining operations, chamfers were applied to each thickness change to smooth the transition as much as possible.

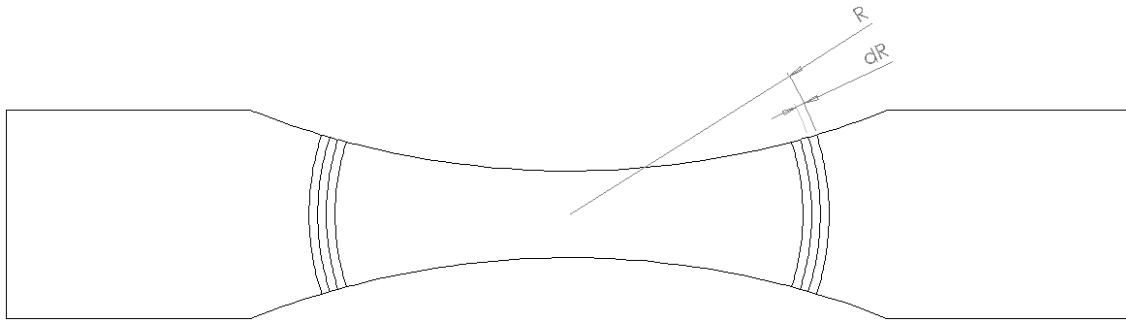


Figure 7.3: Terraced LP geometry used for fatigue samples.

The different iterations are described in Table 7.4, where “T1” is the unrefined geometry (simulation results in Figure 7.2) without changing the LP region for each processing step. Also presented in the table is the maximum part von Mises stress as a percentage of the unpolished geometry. In addition, the stress at the base of each thickness change was compared to the maximum part stress, which is also presented. The goal was to have the part stress similar to that for unpolished geometry, accounting for the reduction in minimum cross section, and for the maximum stress to not occur at any change in thickness. The von Mises stress plot for the finalised polishing geometry is shown in Figure 7.4, where it can be clearly seen the maximum stress is in the centre of the sample, far away from the thickness changes, and the stress field shows no sign of discontinuities around the thickness changes. It was therefore deemed to be suitable for use on the fatigue samples.

Table 7.4: Variations in  $R$ ,  $dR$ , and chamfer geometry trialled for terraced LP geometries, along with maximum part stress as a percentage of maximum stress in unpolished geometry (scaled to minimum cross section), and maximum root stress as percentage of maximum part stress.

	$R$	$dR$	Chamfer geometry	Maximum Stress	Root Stress (% of maximum)
T1	18.5 mm	<i>n/a</i>	<i>n/a</i>	117%	100%
T2	20 mm	0.5 mm	<i>n/a</i>	118%	100%
T3	22.5 mm	0.5 mm	<i>n/a</i>	108%	100%
T4	22.5 mm	1 mm	<i>n/a</i>	117%	100%
T5	20 mm	1 mm	<i>n/a</i>	116%	100%
T6	25 mm	1 mm	<i>n/a</i>	102%	100%
T7	25 mm	0.5 mm	<i>n/a</i>	101%	100%
C1	22.5 mm	0.5 mm	45°	129%	100%
C2	22.5 mm	0.5 mm	0.25 mm *	101%	100%
C3	25 mm	1 mm	0.5 mm *	101%	79.4%
C4	30 mm	1 mm	0.5 mm *	101%	68.0%

\* Where chamfer geometry is given by a distance, that is the distance it extends along the base of the terrace. In all cases the “top” of the incline coincides with the “bottom” of the next highest terrace.

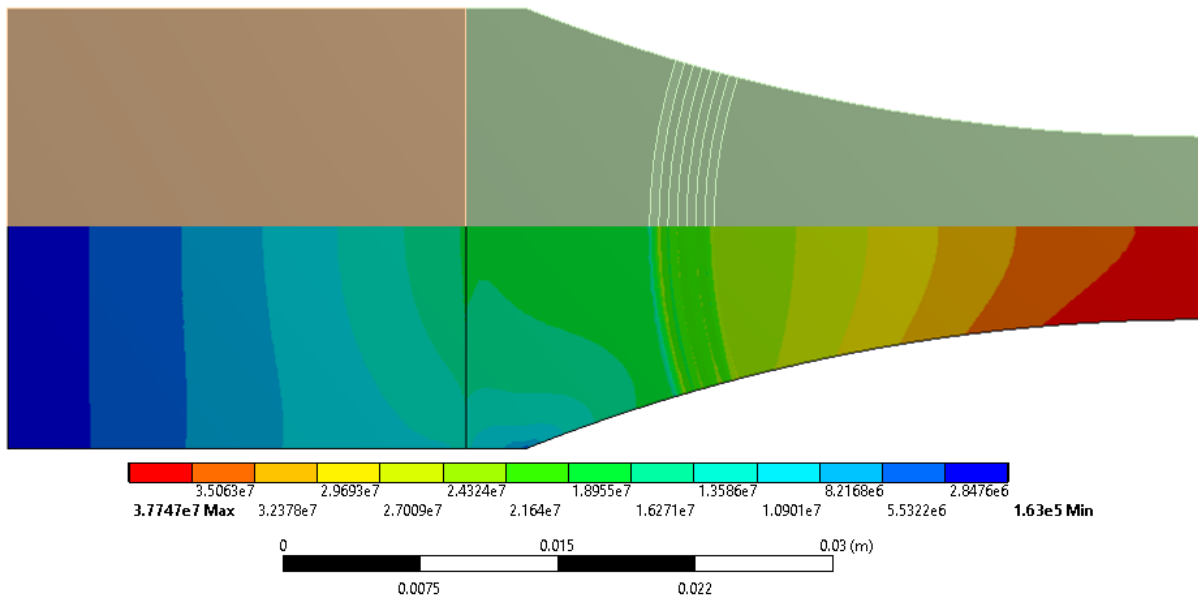


Figure 7.4: top) FEA model geometry (section plane on right end), and bottom) von Mises stress plot of finalised LP fatigue geometry (C4:  $R = 30$  mm,  $dR = 1$  mm, 0.5 mm chamfer).

To confirm the effectiveness of the micro-machining process, the transition area between fully polished and unpolished areas was measured using the Talysurf tactile profilometer. An example raw (i.e., unfiltered) measurement is shown in Figure 7.5, with different regions identified. As can be seen, there are no step-features present. Smooth transitions in height are shown, especially in region (B) corresponding to an ablation step. It is clear from the figure that the applied LP process is not contributing to increased stress concentrations, and therefore samples are expected to fail in the gauge length. It is interesting to note that in region (D) there is an increase in height at the border with region (C), this shows material is boiling rather than ablating due to insufficient energy input.

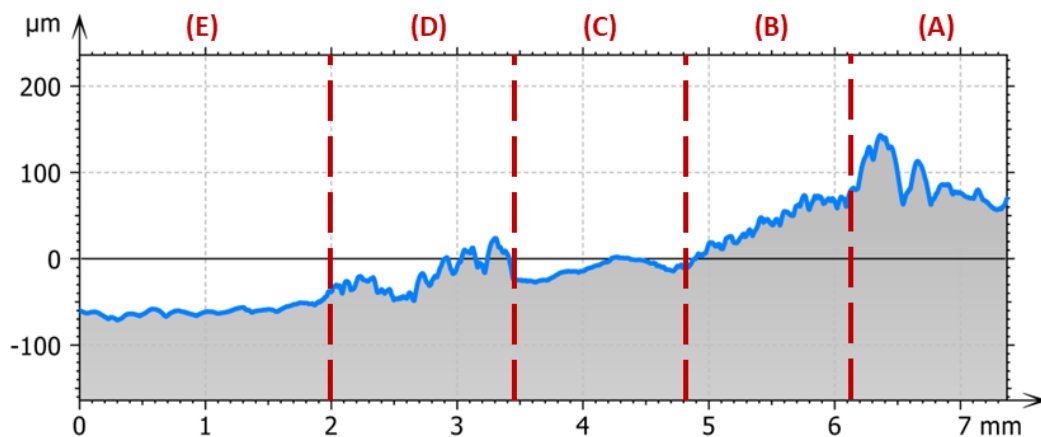


Figure 7.5: Example profile measurement from LP fatigue sample transition region, where (A) is the unpolished region and (B-E) after each LP step in turn. (E) is the fully polished region.

## 7.5 Results and Discussion

### 7.5.1 Low Cycle Fatigue Tests

Looking first at the LCF results, Figure 7.6, it can be seen that the results follow the usual S-N plot format, with an approximately linear relationship when presented on log-normal axes. This implies that all four sample types are performing similarly, irrespective of HT or LP state. As discussed in the

literature review, applying a T6 temper to AM materials generally improves the fatigue life, but the same cannot be said of these results, possibly due to the much lower UTS found in Chapter 6.

LP, on the other hand, is clearly having no significant effect, especially for the tempered samples. This can be seen in the plot by the yellow squares and purple triangles. The T6 + LP samples had a higher variability (63k to 89k cycles, 17.3%) than the T6 samples (77k to 80k cycles, 1.9%). The LP samples also had an exceptionally low variability (1008 to 1135 cycles, 5.9%) however this is likely due to the load being too close to the static limit. The as built samples had the highest variability (4k to 10k cycles, 41.4%), however still within the expected variance of fatigue results, reported to be as high as “9 to 1” [83].

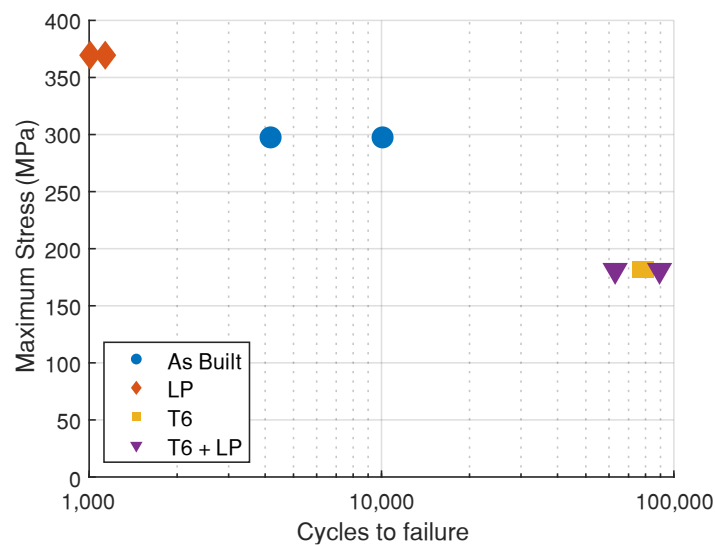


Figure 7.6: LCF results showing cycles to failure against maximum tensile stress.  $R = 0.1$ , tension-tension.

Comparing the cycles to failure with maximum stress as a proportion of UTS shows the tempered samples have vastly increased life (as built, T6, and T6 + LP samples all tested at  $\approx 75\%$  UTS). This is due to the reduced static properties of the tempered material.

Combined with the increased ductility, it may therefore be advantageous for a designer to specify lower part stress (more material use) and apply a T6 temper to parts, for low cycle or high stress fatigue environments.

SEM was used to observe the fracture surfaces<sup>15</sup>, with Figure 7.7 showing the identified initiation sites. Also shown is the extent of the crack propagation region by the dashed line. Propagation is characterised by the relatively smooth fracture surface, compared to the rough appearance of the final rupture surface. It is interesting that the unpolished samples (Figure 7.7 (A) and (C)) showed crack initiation originating at the base of adhered particles. The T6 + LP Sample has the largest propagation region (approximately 300  $\mu\text{m}$  radius) compared to either of the unpolished samples (150  $\mu\text{m}$  to 200  $\mu\text{m}$  in Figure 7.7). On the examined fracture surface, for the LP sample (without HT), no clear initiation site could be identified. This is likely due to the high stress level used (105% UTS) meaning there was a very small propagation stage before final rupture.

<sup>15</sup> Tescan MAIA3 FEG-SEM operating at 5kV using both secondary and backscattered electron imaging. Samples were mounted on 12.5 mm aluminium stubs with adhesive copper tape and ultrasonically cleaned with Isopropyl Alcohol (IPA) prior to analysis.

Based on these SEM images, it could be inferred that while LP effectively removes adhered particles on the surface, and therefore likely inhibits crack initiation, the addition of sub-surface porosity (see Chapter 5.5.4) counteracts this and results in the observed LCF fatigue life not being significantly altered.

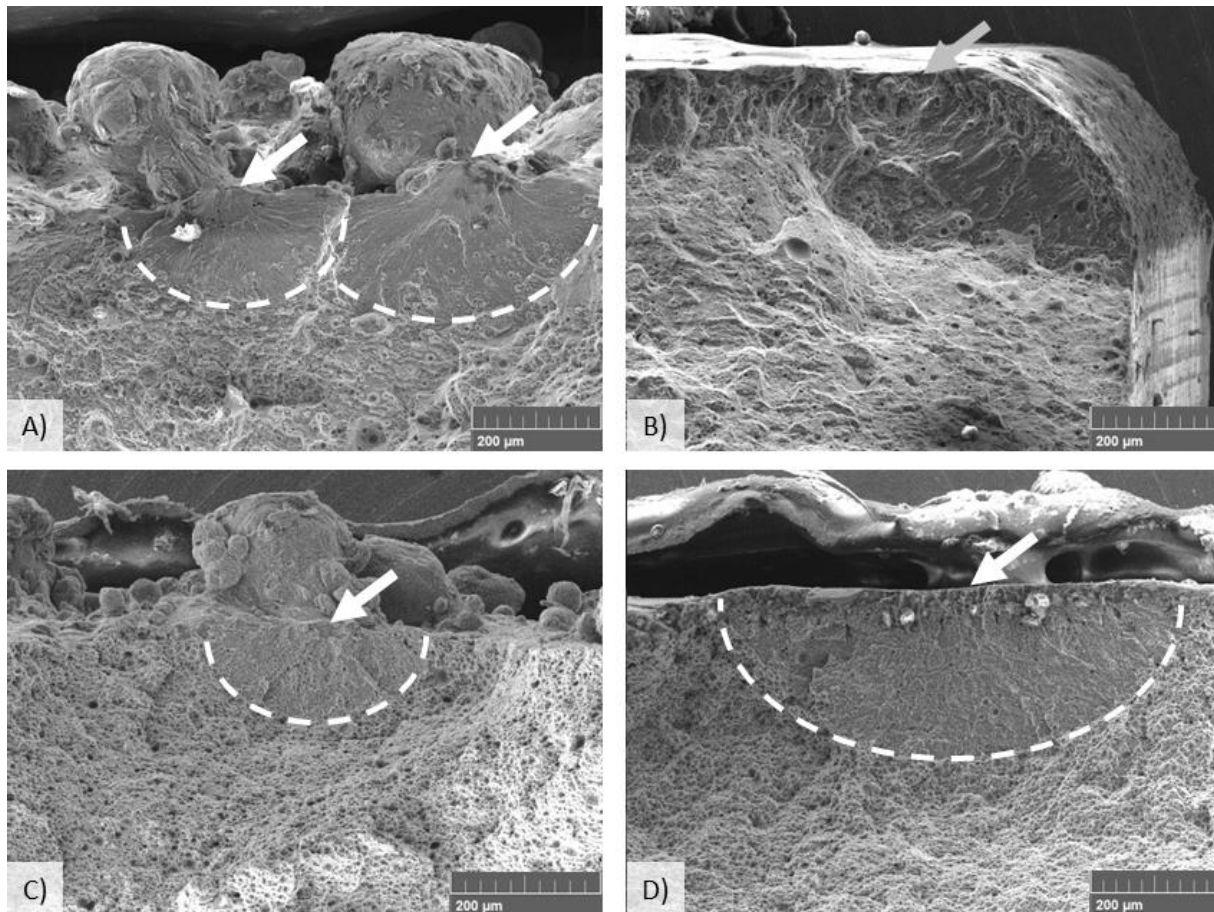


Figure 7.7: Examples of LCF crack initiation sites (arrows), where the dashed lines show the extent of the propagation regions. Sample conditions are: (A) As Built, (B) LP, (C) T6, and (D) T6 + LP.

Electron Dispersive X-ray (EDX) maps were also generated for several samples<sup>16</sup> to assess if contamination was present near the crack initiation sites. One such map, for the F1 condition sample, is presented in Figure 7.8. As can be seen, there is no obvious concentration of contaminating elements near the initiation site. The presence of carbon is indicative of post-failure contamination, such as from cleaning solvents (IPA).

<sup>16</sup> Analysis was conducted using Oxford Instruments XMAX 80 and processed using Oxford's Aztec software.



Figure 7.8: EDX composition map from As Built condition LCF sample.

### 7.5.2 High Cycle Fatigue Tests

The peak stress, required load, and cycle count for each sample subjected to HCF testing are provided in Table 7.5. As can be seen, the majority of samples survived one load step and failed upon application of a second. Sample F4-A (T6 + LP) failed during the first load step, while samples F3-B (T6) and both as built samples endured two full load steps and failed during a third.

Table 7.5: Peak stress, Peak Force, and cycle count for each HCF sample at each load-step used.

Sample	Peak Stress (MPa)	Peak Force (N)	Cycles
F1-A	100	3002	30,000,000
	117	3513	1,000,000
	133	3993	385,900
F1-B	117	3574	1,000,000
	133	4062	1,000,000
	164	5009	211,100
F2-A	117	3096	1,000,000
	133	3519	455,900
F2-B	117	3070	1,000,000
	133	3490	310,400
F3-A	117	3564	1,000,000
	133	4051	169,000
F3-B	117	3563	1,000,000
	133	4051	1,000,000
	150	4568	8,600
F4-A	117	3100	640,800
F4-B	117	3101	1,000,000
	133	3525	206,700

Therefore, the  $10^6$  cycle endurance limit could be calculated according to Equation 2.15 for all samples except F4-A. For the purpose of calculating the endurance strengths, it was assumed sample F4-A would have survived a prior load step without failing, and still endured the same number of cycles at 117 MPa peak stress (i.e.,  $\sigma_0 = 100 \text{ MPa}$ ). The calculated endurance limits are presented in Figure 7.9. It can be seen that all sample types yield very similar endurance limits, with averages of 131 MPa, 123 MPa, 126 MPa, and 116 MPa for as built, LP, T6, and T6 + LP sample types respectively. The range for each is also very consistent (16 MPa, 2 MPa, 13 MPa, and 9 MPa in turn) implying no significant change in endurance limit arising from the application of LP or a T6 temper.

The as-built  $10^6$  endurance limit of these samples (131 MPa, 123 MPa with LP) is higher than comparable results from Aboulkhair et al. (80 MPa) [5] and Brandl et al. (110 MPa) [135]. The endurance limit for T6 tempered samples (126 MPa T6, 116 MPa T6 + LP) is substantially lower than that reported by Brandl et al. (165 MPa) [135], however is slightly elevated to that from Maskery et al. (115 MPa) [6], and comparable to Aboulkhair et al. (126 MPa) [5]. It should be noted that of those three references, only Brandl et al. manufactured samples horizontally (as done here), while Aboulkhair et al. and Maskery et al. both tested vertically built samples.

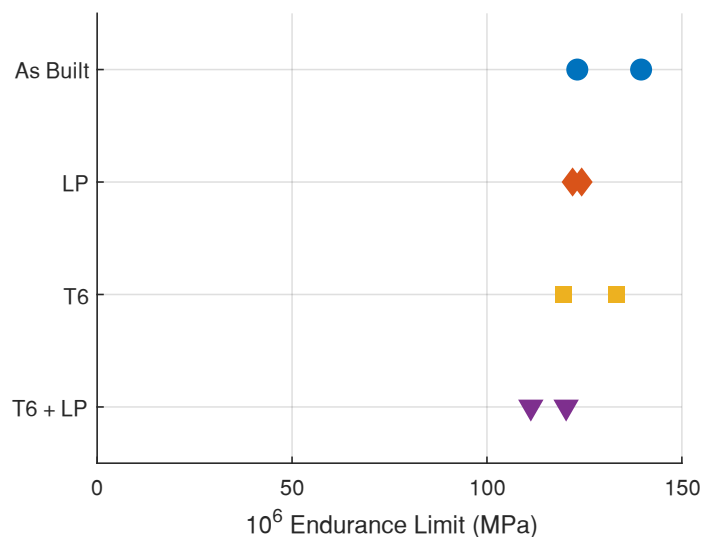


Figure 7.9: Endurance limit of HCF samples as calculated using Equation 3.1.

SEM examination of the HCF fracture surfaces did not reveal any definitive signs of crack initiation or propagation for the T6 tempered samples, and therefore only shed light on the crack initiation for the As Built and LP samples (i.e., those without T6 temper). Figure 7.10 shows the initiation site for an As Built sample. Much like for the LCF samples, crack initiation occurred near the base of an adhered particle, shown in Figure 7.10 by the white arrow. As expected, the propagation region is much larger than from LCF testing, due to the much lower loads applied. In this case, the propagation region is over 1 mm radius.

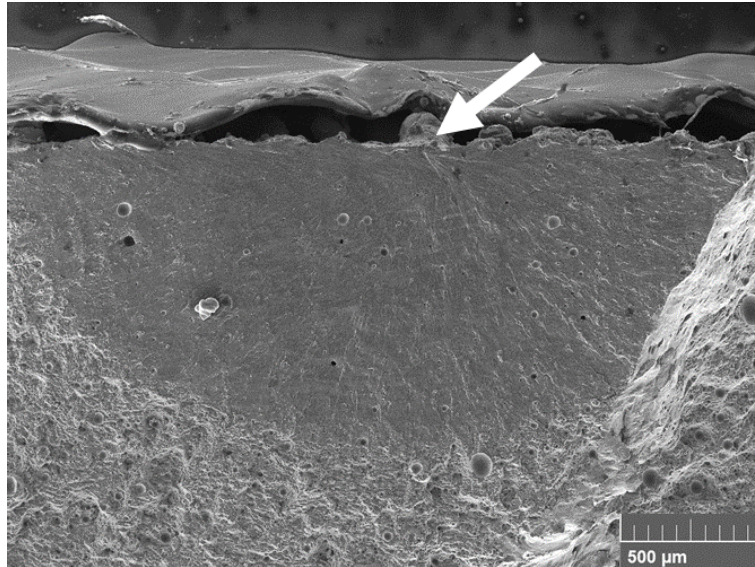


Figure 7.10: HCF crack propagation region for As Built sample. Initiation shown by the white arrow.

For the LP sample, the propagation region extends approximately twice as far ( $\approx 2$  mm), as shown in Figure 7.11. Much like in other studies, the initiation site in this case is clearly from a surface defect, or “killer notch” [103]. Similar defects were observed in other locations on the fracture surface, without the associated crack propagation. These surface defects are likely the result of near-surface porosity, breaking through the surface during LP. The morphology of these defects, relatively deep and narrow depressions, clearly act as strong stress concentrations encouraging fatigue cracking. Furthermore, as can be seen in the image, the defect extends further into the bulk material than most of the other porosity (approximately 100 μm compared to 60 μm observed in Chapter 5.5.4) and therefore, locally bypassing the harder surface layer.

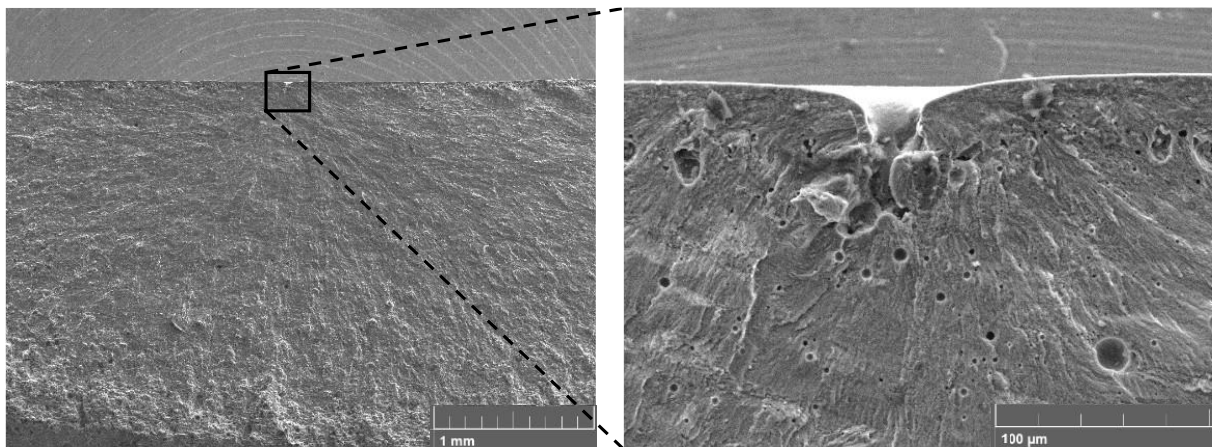


Figure 7.11: HCF Crack propagation region for LP sample, with detail of the killer notch at initiation site.

While most of the EDX surveys for the HCF samples showed no abnormalities, the surface defects (such as in Figure 7.11) had elevated concentrations of oxygen and carbon. One such map is shown in Figure 7.12. It is clear from the figure, that the excess oxygen and carbon are mainly on the sample exterior, and not on the fracture surface. This in turn indicates that oxygen and carbon were introduced during the LP process, due to being conducted in ambient air, and likely related to the defect formation. This is unlike the findings by Hofele et al. [178] who found no evidence of compositional changes following LP (applied in an inert atmosphere).

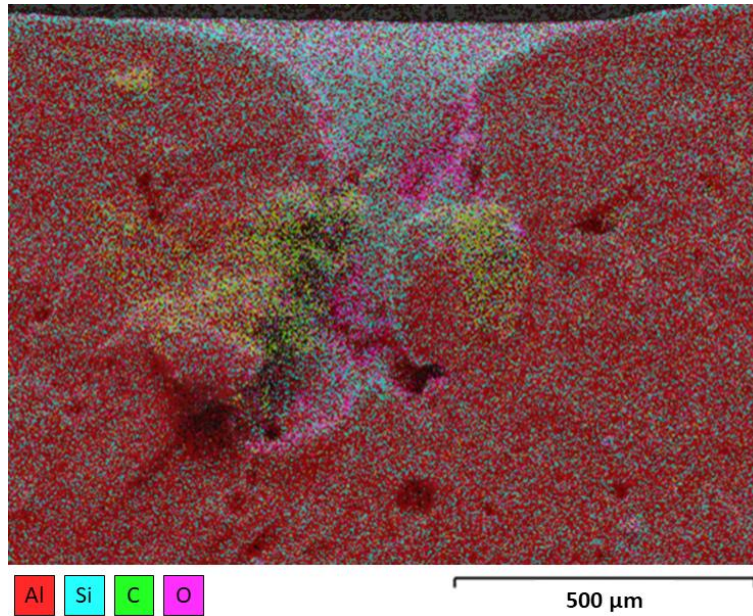


Figure 7.12: EDX composition layered image from LP HCF sample.

A section of material from fatigue samples in each condition were mounted, mechanically polished, and etched in the usual manner (see Chapter 3.4) to observe the microstructural details. The As Built and LP sections showed the same features identified in Chapter 5, specifically a fish-scale pattern in the bulk resulting from the L-PBF manufacturing process, and a surface layer showing remelt and flow resulting from the action of LP. In contrast, the T6 samples were much less clear. In the bulk there is no sign of microstructural features, while the T6 + LP sample (Figure 7.13) still exhibits the surface remelt structures. This aligns with findings by others that noted the grain structure is totally eliminated by heat treatment.

There is, however, evidence of precipitates in the structure - the black speckles in Figure 7.13. As explained in [117] and Chapter 6.3, the final stage of T6 tempering is precipitation hardening, where super-saturated compounds form distinct agglomerates within the bulk material. In this case it is likely to be compounds of Magnesium and Silicon (e.g.,  $Mg_2Si$ ) [117], that give the T6 parts their modified static properties compared to As-Built.

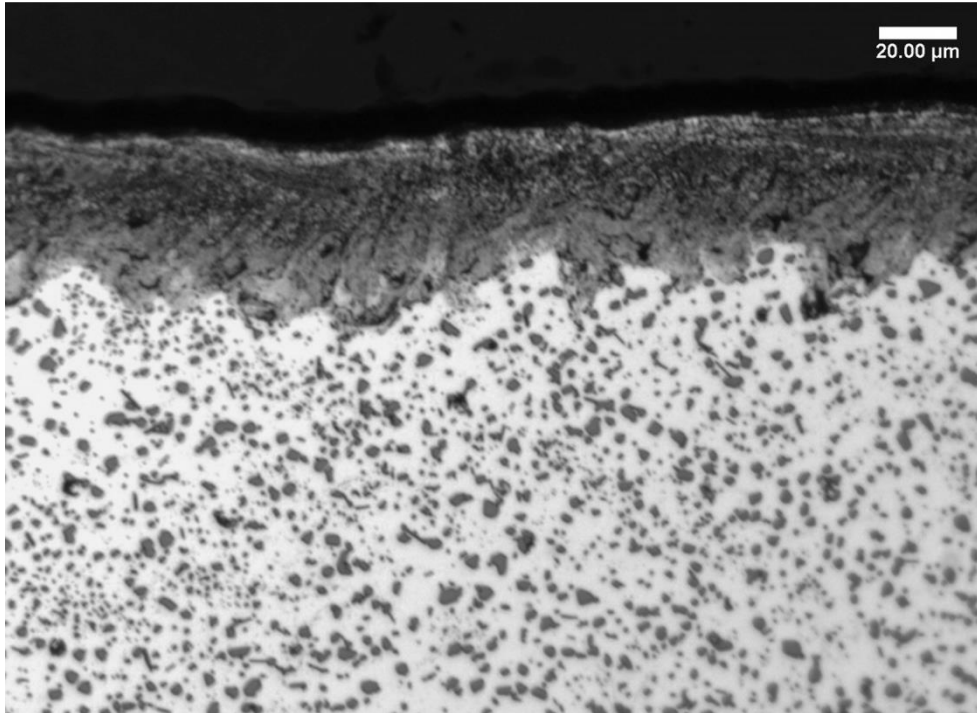


Figure 7.13: Optical micrograph showing etched cross section of T6 + LP sample.

These results show that, in contrast to the findings of others, the applied temper has not resulted in a significant change in the fatigue performance of this AlSi10Mg alloy [5], [6], [135]. This gives further support to the conclusion made in Chapter 6, that the applied temper did not achieve the T6 state, despite following the same (or similar) process as employed by others.

Much like the tensile results, the fatigue tests show that the LP operation used does not affect the performance of the material. Therefore, so long as the reduction in thickness resulting from the LP process is accounted for (i.e., enlarging the manufactured part), this process would facilitate surface modification (smoothing and/or texturing) without sacrificing the fatigue life of components.

## 7.6 Fatigue Testing Summary

A series of samples were manufactured and prepared with and without LP and a T6 temper (four conditions) for fatigue testing. Fatigue tests were conducted in both HCF and LCF regimes to identify any potential effects.

Overall, the presented LP strategy has shown to be ineffective with respect to the fatigue performance of this AM AlSi10Mg material. While it was expected the smoother surface resulting from LP would increase the fatigue strength of samples, by eliminating the so-called killer notches, it is apparent that the induced sub-surface porosity negates this effect. Furthermore, in some samples it was observed that new killer notches were present, arising from the LP process, as shown in Figure 7.11.

Furthermore, the applied T6 temper has also been shown to not have an effect on the fatigue performance of this alloy, contrasting with what is reported in the literature. The reasons for this remain unclear but are likely due to differences in the SHT and precipitation hardening processes, leading to different microstructures than would ordinarily be expected for T6 aluminium.

## 8 Overarching Conclusions and Future Work.

### 8.1 Conclusions

A method has been developed for the repeatable, reliable, and practical assessment of the surface roughness of AM PBF parts. The methodology has been shown to be robust to changes of measurement system, and while the uncertainty induced by different data post-processing has been quantified the influence on standard roughness parameters is insignificant compared to the scale of roughness observed. The selection of filter nesting index (or cut-off for profile measurements) has a large influence on computed parameters, it is suggested here that a 0.8 mm nesting index is appropriate for L-PBF Aluminium, based on the maximum feature size on the surface, however further investigations are encouraged to aid in filter selection in future. While the measurement methodology was evaluated using L-PBF Aluminium parts, the concepts contained within it are transferrable to other powder-based AM technologies.

A novel, multi-step LP strategy has been developed through a comprehensive evaluation of different process parameters, including laser power, scan speed, hatch spacing, focal offset, and number of passes during each step. The effectiveness was evaluated based on measured surface roughness (according to the method in Chapter 4) using the standard parameters Sa, Sp, Sv, and S10z. It was found that the overall strategy resulted in a much smoother final surface (and greater % reduction) than any single step in isolation, clearly emphasising the benefits of this approach. Maximum roughness reductions of approximately 80% were achieved for each parameter, however the smoothing effect for Sa was found to be highly dependent on initial surface roughness, with reduced effectivity at lower initial roughness. Thermal simulations were employed to add insight into the surface heating effects of the two different pulse durations and frequencies utilised. It was found that the shorter pulse durations (used to ablate the surface) gave much higher peak temperatures than the longer pulses (used for smoothing), but the heat penetrated less far into the bulk material.

The near surface effects of the LP strategy were investigated revealing an increase in microhardness within the remelted region, with different hardness profiles resulting from the ablation and smoothing steps. The final result was microhardness at the surface approximately 75% higher than the bulk hardness, falling steadily to the bulk value after 45  $\mu\text{m}$ . This coincided with the extent of the remelted region, and a layer of increased porosity (about 5.5% compared to 1% in the bulk). The remelted region was clearly identifiable in micrographs that also show evidence of material redistribution, proving the strategy is truly polishing the surface and not just machining away the roughness.

Tensile testing of samples gave insight into the effect of LP on the mechanical properties of the aluminium alloy used, and how those effects changed with the application of different conventional heat treatments. It was found that without heat treatment LP increased the Young's modulus, while after heat treatment yield stress was slightly increased by LP. On the other hand, LP reduced the UTS in all instances. While the effects are relatively consistent (the range of results is similar in all tested conditions), the differing effects on different properties, and the compounding effect of heat treatment, make firm conclusions difficult to make based on this data. Further understanding is required before the LP strategy presented can be recommended based on the quasi-static tensile properties alone.

Finally, the fatigue testing results showed a negligible influence of the LP strategy on fatigue strength, under both low and high cycle conditions. This showed that while the reduction in surface roughness may impede crack initiation, and the harder surface layer may also slow crack

propagation, the increase in near surface porosity provided additional initiation sites, negating the effect. This shows that while there are no mechanical benefit of the applied LP strategy, there is also no detrimental effects and thus, it is a viable post-processing technique if the aesthetic properties are desired.

A challenging result from this data is there is no apparent influence of T6 tempering on the fatigue life of this alloy. While this goes against previously published research by others, it is an invaluable insight into the challenges facing engineers with determining the properties of AM aluminium, and how different post-processing may affect these properties. It is imperative that the knowledge of this is further bolstered to enable industrial uptake of this alloy in structural applications.

Overall, while the LP strategy presented has been shown to have significant effects on the surface roughness, near surface microhardness, and near surface porosity, there is no clear influence on either the static or fatigue tensile properties.

## 8.2 Contributions

The novelty in this work has been demonstrated by:

- A practical method of assessing the surface roughness of AM parts has been developed, including guidance on the appropriate data post-processing. This is unique with the majority of existing literature focussing instead on novel data processing options (extracting specific features from a measurement) or the development of new roughness metrics (quantifying the number and distribution of features).
- A unique laser processing strategy has been developed, incorporating multiple processing steps to alternately ablate and smooth the surface peaks giving a smoother result than either in isolation. The strategy has comparable effectiveness to single-step processes proposed by others using more powerful laser sources. A previously unidentified link between initial roughness and smoothing effect has also been identified.
- The tensile properties of AM Aluminium have been determined. This represents a more complete understanding of the mechanical properties than has been previously reported due to the wider range of calculated values (Young's modulus, ultimate tensile stress, failure strain, yield stress, and yield strain). Furthermore, the inclusion of as built, stress relieved, and peak hardened samples, with and without laser polishing, is a much broader selection of sample conditions than is reported elsewhere. This work, therefore, strongly contributes to the wider knowledge regarding the mechanical properties of this material.
- Tension-tension fatigue tests have been conducted on AM Aluminium samples. The interactions between heat treatment and laser polishing on fatigue strength of AM Aluminium have not been previously reported. Therefore, this is a unique insight into the fatigue strength of this material and is an invaluable resource for the further industrialisation of AM Aluminium.

## 3.5 Novelty Statement

This thesis covers three main themes: The measurement of rough AM surfaces; Laser polishing of AM Aluminium surfaces; and determination of the effect of laser polishing on the mechanical properties of AM Aluminium. The fundamental contributions of this work can thus be summarised as such:

- Contribution of key knowledge through the development of a reliable, repeatable, and practical methodology for the surface roughness measurement of AM PBF surfaces.

- Development of new understanding regarding laser polishing of AM Aluminium through a novel multi-step strategy, reducing the as-built roughness by over 80%.
- Improved understanding of the tensile properties of AM Aluminium. The tensile response to different standard heat treatment processes and the developed laser polishing strategy has been quantified.
- Improved understanding of the fatigue strength of AM Aluminium in the as built condition and after application of a T6 temper. New understanding has been developed regarding the influence of laser polishing on the fatigue strength.

### 8.3 Future Work

While there has been significant progress made here on laser polishing of AM Aluminium, and its influence on mechanical properties, there are many avenues still to be investigated. Some suggested future investigations are as follows:

Laser Polishing of AM Aluminium using different laser architectures.

- The laser system used in this work operates in the nanosecond range of pulse durations (15 ns – 220 ns), however many industrial systems are using longer pulses (ms durations) or continuous wave sources. Developing an understanding of these systems has the potential to enhance the industrialisation of the process through reduced barriers to entry and increased productivity (kW range average powers are not uncommon). Furthermore, most L-PBF machines utilise these types of lasers, and therefore enhanced understanding here would facilitate in-situ, hybrid manufacture of AM parts.
- Likewise, assessing the possibility of laser ablation using ultra-short pulse durations (picosecond/femtosecond) opens up new avenues for reducing the thermal effects on the material while maintaining the surface roughness reductions. However, these laser sources are typically more expensive and have reduced productivity due to lower average powers.
- Finally, the laser wavelength used here was 1064 nm. While near IR is common in industrial machines, it has very low absorptivity on aluminium. Therefore, alternative wavelengths such as green, blue, or UV are likely to improve the process effectiveness thanks to greater absorption by the material.

More in-depth mechanical testing of AM Aluminium, with and without laser polishing.

- In this work, the mechanical properties were only assessed for quasi-static tension and tension-tension fatigue. There are many other loading conditions of interest to design engineers, such as compression, bending, and impact, that should be evaluated to support more widespread adoption of the material.
- It is well known that different fatigue loading regimes can vastly affect the material life, and in operation, loading is rarely as simple as tested here. Therefore, further fatigue testing is essential for the industrialisation of AM Aluminium.

Finally, it would be interesting to benchmark the AlSi10Mg alloy manufactured by L-PBF and casting.

- Many studies reference the AlSi10Mg properties to various conventionally manufactured alloys, however, they have subtle compositional differences making comparisons imprecise.
- It would be trivial for samples to be cast from either virgin powder, recycled powder, and/or recycled AM parts in an inert-atmosphere furnace. These cast samples can then be tested alongside AM samples to judge to what extent the AM process affects the mechanical

properties. This would also give a different perspective on the influence of powder recycling on manufacture.

## References

- [1] 'RR1195: Exposure to Metal Powders in Additive Manufacturing'. Accessed: Mar. 15, 2024. [Online]. Available: <https://www.hse.gov.uk/Research/rrhtm/rr1195.htm>
- [2] R. K. Leach, D. Bourell, S. Carmignato, A. Donmez, N. Senin, and W. Dewulf, 'Geometrical metrology for metal additive manufacturing', *CIRP Annals*, vol. 68, no. 2, pp. 677–700, 2019, doi: 10.1016/j.cirp.2019.05.004.
- [3] C. J. Luis Pérez, J. Vivancos Calvet, and M. A. Sebastián Pérez, 'Geometric roughness analysis in solid free-form manufacturing processes', *J Mater Process Technol*, vol. 119, no. 1–3, pp. 52–57, 2001, doi: 10.1016/S0924-0136(01)00897-4.
- [4] L. Chen, B. Richter, X. Zhang, K. B. Bertsch, D. J. Thoma, and F. E. Pfefferkorn, 'Effect of laser polishing on the microstructure and mechanical properties of stainless steel 316L fabricated by laser powder bed fusion', *Materials Science and Engineering A*, vol. 802, no. November 2020, p. 140579, 2021, doi: 10.1016/j.msea.2020.140579.
- [5] N. T. Aboulkhair, I. Maskery, C. Tuck, I. Ashcroft, and N. M. Everitt, 'Improving the fatigue behaviour of a selectively laser melted aluminium alloy: Influence of heat treatment and surface quality', *Metallurgical and Materials Transactions A*, vol. 64A, pp. 3337–3342, 2015, doi: 10.1016/j.matdes.2016.05.041.
- [6] I. Maskery *et al.*, 'Fatigue performance enhancement of selectively laser melted aluminium alloy by heat treatment', *Solid Freeform Fabrication Symposium*, no. February 2016, pp. 1017–1025, 2015.
- [7] M. Agarwala, D. Bourell, J. Beaman, H. Marcus, and J. Barlow, 'Post-processing of selective laser sintered metal parts', *Rapid Prototyp J*, vol. 1, no. 2, pp. 36–44, 1995, doi: 10.1108/13552549510086853.
- [8] M. Hofele, J. Schanz, B. Burzic, S. Lutz, M. Merkel, and H. Riegel, 'Laser based post processing of additive manufactured metal parts', in *Lasers in Manufacturing Conference*, Munich, Germany, 2017, pp. 1–12.
- [9] MTC, 'Industry Leading Laser Technology'. Accessed: Oct. 29, 2023. [Online]. Available: <https://www.the-mtc.org/what-we-do/technologies/industry-leading-laser-technology/>
- [10] TWI Ltd., 'Laser Processing - TWI'. Accessed: Oct. 29, 2023. [Online]. Available: <https://www.twi-global.com/what-we-do/research-and-technology/technologies/welding-joining-and-cutting/lasers>
- [11] Automobili Lamborghini S.p.A., 'Customization | Lamborghini.com'. Accessed: Oct. 29, 2023. [Online]. Available: <https://www.lamborghini.com/en-en/customization>
- [12] Michał Kuliś, 'Just-In-Time Production and TPS Supported by 3D Printing', Zortrax Blog. Accessed: Oct. 29, 2023. [Online]. Available: <https://zortrax.com/blog/just-time-production-tps-3d-printing/>
- [13] Ralf Carlström, 'Additive manufacturing can reduce industry's environmental impact'. Accessed: Oct. 29, 2023. [Online]. Available: <https://www.theengineer.co.uk/content/opinion/additive-manufacturing-can-reduce-industry-s-environmental-impact>

- [14] T. Wholers and T. Gornet, 'History of Additive Manufacturing', 2016. doi: 10.4018/978-1-5225-2289-8.ch001.
- [15] H. Kodama, 'Automatic method for fabricating a three-dimensional plastic model with photo-hardening polymer', *Review of Scientific Instruments*, vol. 52, no. 11, pp. 1770–1773, Nov. 1981, doi: 10.1063/1.1136492.
- [16] M. Leinster, *Things Pass By*. 1945. [Online]. Available: <https://archive.org/details/ThrillingWonderStoriesV27N021945Su/page/n9/mode/2up>
- [17] R. F. Jones, 'Tools of the Trade', *Astounding Science Fiction*, pp. 48–67, Nov. 1950.
- [18] University of Maine, 'UMaine Composites Center receives three Guinness World Records related to largest 3D printer'. Accessed: Sep. 29, 2022. [Online]. Available: <https://composites.umaine.edu/2019/10/11/umaine-composites-center-receives-three-guinness-world-records-related-to-largest-3d-printer/>
- [19] I. Gibson, D. Rosen, and B. Stucker, *Additive Manufacturing Technologies 3D Printing, Rapid Prototyping, and Direct Digital Manufacturing*, 2nd ed. 20. New York, N.Y.: Springer, 2015.
- [20] J. J. Beaman, 'Historical background', in *Fundamentals of Laser Powder Bed Fusion of Metals*, Elsevier Inc., 2021, pp. 1–14. doi: 10.1016/B978-0-12-824090-8.00002-0.
- [21] Nikon Corporation, 'Overview | Additive manufacturing'. Accessed: Aug. 11, 2023. [Online]. Available: <https://ngpd.nikon.com/en/additive-manufacturing/overview.html>
- [22] P. O'Regan, P. Prickett, R. Setchi, G. Hankins, and N. Jones, 'Metal Based Additive Layer Manufacturing: Variations, Correlations and Process Control', *Procedia Comput Sci*, vol. 96, pp. 216–224, 2016, doi: 10.1016/j.procs.2016.08.134.
- [23] S. Siddique, M. Imran, E. Wycisk, C. Emmelmann, and F. Walther, 'Influence of process-induced microstructure and imperfections on mechanical properties of AlSi12 processed by selective laser melting', *J Mater Process Technol*, vol. 221, pp. 205–213, 2015, doi: 10.1016/j.jmatprotec.2015.02.023.
- [24] T. B. Sercombe and X. Li, 'Selective laser melting of aluminium metal matrix composites', *Materials Technology: Advanced Performance Materials*, vol. 31, no. 2, pp. 77–85, 2016, doi: 10.1179/1753555715Y.0000000078.
- [25] T. M. Mower and M. J. Long, 'Mechanical behavior of additive manufactured, powder-bed laser-fused materials', *Materials Science and Engineering A*, vol. 651, pp. 198–213, 2016, doi: 10.1016/j.msea.2015.10.068.
- [26] C. S. Montross, T. Wei, L. Ye, G. Clark, and Y.-W. Mai, 'Laser shock processing and its effects on microstructure and properties of metal alloys: a review', 2002. [Online]. Available: [www.elsevier.com/locate/ijfatigue](http://www.elsevier.com/locate/ijfatigue)
- [27] D. J. Whitehouse, *Surfaces and their measurement*. in Kogan Page Science paper edition. London: Kogan Page Science, 2004.
- [28] BSI, '8785: Geometrical Product Specification (GPS) - Surface imperfections', vol. 3, pp. 1–20, 1998.

- [29] F. Calignano, D. Manfredi, E. P. Ambrosio, L. Iuliano, and P. Fino, 'Influence of process parameters on surface roughness of aluminum parts produced by DMLS', *International Journal of Advanced Manufacturing Technology*, vol. 67, no. 9–12, pp. 2743–2751, 2013, doi: 10.1007/s00170-012-4688-9.
- [30] P. Delfs, M. Trows, and H. J. Schmid, 'Optimized build orientation of additive manufactured parts for improved surface quality and build time', *Addit Manuf*, vol. 12, pp. 314–320, 2016, doi: 10.1016/j.addma.2016.06.003.
- [31] Airblast Limited, 'What is Shot Blasting? - Airblast Eurospray'. Accessed: Mar. 08, 2024. [Online]. Available: <https://airblast.co.uk/resource-hub/what-is-shot-blasting/>
- [32] L. Denti and A. Sola, 'On the effectiveness of different surface finishing techniques on A357.0 parts produced by laser-based powder bed fusion: Surface roughness and fatigue strength', *Metals (Basel)*, vol. 9, no. 12, Dec. 2019, doi: 10.3390/MET9121284.
- [33] Ervin Germany GmbH, 'The Ultimate Guide to Shot Blasting & Material Preparation', 2023. Accessed: Aug. 18, 2023. [Online]. Available: <https://www.ervin.eu/shot-blasting-guide/>
- [34] A. Merlo, D. Ricciardi, E. Salvi, D. Fantinati, and E. Iorio, 'Novel Adaptive Fixturing for Thin Walled Aerospace Parts', *IOP Conf Ser Mater Sci Eng*, vol. 26, p. 012020, Dec. 2011, doi: 10.1088/1757-899X/26/1/012020.
- [35] AT Machining, 'Surface Finish Chart: A Guide to Understanding Surface Finishing Chart'. Accessed: Mar. 08, 2024. [Online]. Available: <https://at-machining.com/surface-finish-chart/>
- [36] TWI Ltd., 'What is Laser Polishing and How Does it Work? – TWI - TWI'. Accessed: Mar. 08, 2024. [Online]. Available: <https://www.twi-global.com/technical-knowledge/faqs/what-is-laser-polishing-and-how-does-it-work#HowDoesLaserPolishingWork>
- [37] A. Krishnan and F. Fang, 'Review on mechanism and process of surface polishing using lasers', *Frontiers of Mechanical Engineering*, vol. 14, no. 3, pp. 299–319, Sep. 2019, doi: 10.1007/S11465-019-0535-0/METRICS.
- [38] H. Wyatt, M. Elliott, P. Revill, and A. Clarke, 'The effect of engineered surface topography on the tribology of CFR-PEEK for novel hip implant materials', *Biotribology*, vol. 7, pp. 22–30, 2016, doi: 10.1016/j.biotri.2016.08.001.
- [39] P. S. Sibanda, P. Carr, M. Ryan, and S. Bigot, 'State of the Art in Surface Finish of Metal Additive Manufactured Parts', in *Advances in Transdisciplinary Engineering*, 2020, pp. 221–225. doi: 10.3233/ATDE190039.
- [40] H. Dagnall, *Exploring surface texture*, 7th Ed. Leicester: Taylor Hobson Ltd., 2011. [Online]. Available: [https://books.google.fr/books/about/Exploring\\_Surface\\_Texture.html?id=eANStwAACAAJ&redir\\_esc=y](https://books.google.fr/books/about/Exploring_Surface_Texture.html?id=eANStwAACAAJ&redir_esc=y)
- [41] Q. Zeng, Y. Qin, W. Chang, and X. Luo, 'Correlating and evaluating the functionality-related properties with surface texture parameters and specific characteristics of machined components', *Int J Mech Sci*, vol. 149, no. July, pp. 62–72, 2018, doi: 10.1016/j.ijmecsci.2018.09.044.
- [42] BSI, '1134: Assessment of Surface Texture - Guidance and General Information', *BSI Standards Publication*, vol. BS, p. 1134:2010, 2010.

- [43] F. Blateyron, 'Good practices for the use of areal filters', *3rd Seminar on Surface Metrology of the Americas (SSMA)*, no. August, pp. 1–12, 2014, doi: 10.13140/2.1.1007.9361.
- [44] BSI, '16610-28: Geometrical product specifications (GPS) — Filtration Part 28: Linear profile filters: Gaussian filters', 2012.
- [45] BSI, '4287-1998: Geometrical product specification (GPS) - Surface texture: Profile method - Terms, definitions and surface texture parameters', 2009.
- [46] BSI, '25178-2: Geometrical product specifications (GPS) — Surface texture: Areal Part 2: Terms, definitions and surface', 2012.
- [47] Keyence Corp., 'Surface Roughness Parameters : Skewness'. Accessed: Aug. 19, 2021. [Online]. Available: <https://www.keyence.com/ss/products/microscope/roughness/line/skewness.jsp>
- [48] Keyence Corp., 'Surface Roughness Parameters : Kurtosis'. Accessed: Aug. 19, 2021. [Online]. Available: <https://www.keyence.com/ss/products/microscope/roughness/line/kurtosis.jsp>
- [49] PCBway, 'How To Distinguish CNC machining Surface Roughness Between 6.3 And 0.8?'. Accessed: Aug. 18, 2023. [Online]. Available: [https://www.pcbway.com/blog/CNC\\_Machining/Can\\_you\\_distinguish\\_roughness\\_between\\_6\\_3\\_and\\_0\\_8\\_with\\_naked\\_eyes\\_\\_It\\_s\\_much\\_mor.html](https://www.pcbway.com/blog/CNC_Machining/Can_you_distinguish_roughness_between_6_3_and_0_8_with_naked_eyes__It_s_much_mor.html)
- [50] Taylor Hobson, 'Form Talysurf® i-Series PRO Range'. Accessed: Nov. 14, 2022. [Online]. Available: <https://www.taylor-hobson.com/products/surface-profilers/i-series-pro-range/talysurf-pro>
- [51] Sensofar, 'S mart & S onix: In-line 3D Surface Sensors'. Accessed: Jan. 15, 2020. [Online]. Available: <https://www.sensofar.com/metrology/products/sensors/specifications/>
- [52] T. V. Vorburger and J. Raja, *Surface Finish Metrology Tutorial*. Gaithersburg, MD: National Institute of Standards and Technology, 1988. [Online]. Available: <https://www.google.com/url?sa=t&rct=j&q=&esrc=s&source=web&cd=&cad=rja&uact=8&ved=2ahUKEwj5upXzspL9AhUNSMaKHx2AAngQFnoECBoQAQ&url=https%3A%2F%2Fwww.nist.gov%2Fsystem%2Ffiles%2Fdocuments%2Fcalibrations%2F89-4088.pdf&usq=AOvVaw3A7vxB030HVmfEXeKZTG4c>
- [53] R. Danzl, F. Helml, and S. Scherer, 'Focus variation - A robust technology for high resolution optical 3D surface metrology', *Strojniski Vestnik/Journal of Mechanical Engineering*, vol. 57, no. 3, pp. 245–256, 2011, doi: 10.5545/sv-jme.2010.175.
- [54] L. Newton *et al.*, 'Areal topography measurement of metal additive surfaces using focus variation microscopy', *Addit Manuf*, vol. 25, no. August 2018, pp. 365–389, 2019, doi: 10.1016/j.addma.2018.11.013.
- [55] K. Stout and L. Blunt, *Three-dimensional surface topography*, 2nd ed. London: Penton, 2000.
- [56] Lasertec Corp., 'Principle of confocal microscope'. Accessed: Jun. 06, 2023. [Online]. Available: [https://www.lasertec.co.jp/en/products/microscope/optelics\\_hybrid/principle/microscope.html](https://www.lasertec.co.jp/en/products/microscope/optelics_hybrid/principle/microscope.html)

- [57] LIGO Lab; Caltech, 'LIGO Technology'. Accessed: Aug. 11, 2023. [Online]. Available: <https://www.ligo.caltech.edu/page/ligo-technology>
- [58] Wikipedia contributors and User: Cmglee, 'LIGO', Wikipedia, The Free Encyclopedia.
- [59] M. von Allmen and A. Blatter, 'Heating by Laser Light', Springer, Berlin, Heidelberg, 1995, pp. 41–67. doi: 10.1007/978-3-642-57813-7\_3.
- [60] TRUMPF Ltd., 'CO2 lasers | TRUMPF'. Accessed: Sep. 29, 2023. [Online]. Available: [https://www.trumpf.com/en\\_GB/products/lasers/co2-lasers/](https://www.trumpf.com/en_GB/products/lasers/co2-lasers/)
- [61] Rüdiger Paschotta, 'Ultraviolet lasers'. Accessed: Sep. 16, 2023. [Online]. Available: [https://www.rp-photonics.com/ultraviolet\\_lasers.html](https://www.rp-photonics.com/ultraviolet_lasers.html)
- [62] J. F. Seely, 'Quantum Theory of Inverse Bremsstrahlung Absorption and Pair Production', *Laser Interaction and Related Plasma Phenomena*, pp. 835–847, 1974, doi: 10.1007/978-1-4684-8416-8\_20.
- [63] B. Mason, M. Ryan, R. Setchi, A. Kundu, W. N. Ayre, and D. Bhaduri, 'Development of a Novel Laser Polishing Strategy for Additively Manufactured AlSi10Mg Alloy Parts', in *Sustainable Design and Manufacturing*, S. G. Scholz, R. J. Howlett, and R. Setchi, Eds., Singapore: Springer Nature Singapore, 2023, pp. 272–282. doi: 10.1007/978-981-19-9205-6\_26.
- [64] E. V. Bordatchev, A. M. K. Hafiz, and O. R. Tutunea-Fatan, 'Performance of laser polishing in finishing of metallic surfaces', *International Journal of Advanced Manufacturing Technology*, vol. 73, no. 1–4, pp. 35–52, 2014, doi: 10.1007/s00170-014-5761-3.
- [65] K. G. Watkins, M. A. McMahon, and W. M. Steen, 'Microstructure and corrosion properties of laser surface processed aluminium alloys: A review', *Materials Science and Engineering A*, vol. 231, no. 1–2, pp. 55–61, 1997, doi: 10.1016/s0921-5093(97)00034-8.
- [66] Fraunhofer ILT, 'Laser Polishing of Metals - Brochure'. Accessed: Aug. 18, 2023. [Online]. Available: <https://www.ilt.fraunhofer.de/en/media-center/brochures/b-laser-polishing-of-metals.html>
- [67] The Laser Institute, 'Laser Safety Information'. Accessed: Mar. 08, 2024. [Online]. Available: <https://www.lia.org/laser-safety-information>
- [68] Materion Microelectronics & Services, 'Reflectance in Thin Films', 2007. [Online]. Available: [https://materion.com/~media/Files/PDFs/Advanced Materials Group/ME/TechnicalPapers/Reflectance In thin Films\\_All.pdf](https://materion.com/~media/Files/PDFs/Advanced Materials Group/ME/TechnicalPapers/Reflectance In thin Films_All.pdf)
- [69] Renishaw plc., 'AlSi10Mg-0403 powder for additive manufacturing'. 2015. [Online]. Available: [www.renishaw.com/additive](http://www.renishaw.com/additive)
- [70] D. Zhang *et al.*, 'Investigation of laser polishing of four selective laser melting alloy samples', *Applied Sciences (Switzerland)*, vol. 10, no. 3, 2020, doi: 10.3390/app10030760.
- [71] D. Bhaduri *et al.*, 'Pulsed laser polishing of selective laser melted aluminium alloy parts', *Appl Surf Sci*, vol. 558, no. April, p. 149887, 2021, doi: 10.1016/j.apsusc.2021.149887.
- [72] R. Avilés, J. Albizuri, A. Lamikiz, E. Ukar, and A. Avilés, 'Influence of laser polishing on the high cycle fatigue strength of medium carbon AISI 1045 steel', *Int J Fatigue*, vol. 33, no. 11, pp. 1477–1489, 2011, doi: 10.1016/j.ijfatigue.2011.06.004.

- [73] M. Hofele, J. Schanz, A. Roth, D. K. Harrison, A. K. M. De Silva, and H. Riegel, 'Process parameter dependencies of continuous and pulsed laser modes on surface polishing of additive manufactured aluminium AlSi10Mg parts', *Materwiss Werksttech*, vol. 52, no. 4, pp. 409–432, 2021, doi: 10.1002/mawe.202000335.
- [74] M. Hofele, A. Roth, J. Schanz, D. K. Harrison, A. K. M. De Silva, and H. Riegel, 'Laser Polishing of Laser Powder Bed Fusion AlSi10Mg Parts—Influence of Initial Surface Roughness on Achievable Surface Quality', *Materials Sciences and Applications*, vol. 12, no. 01, pp. 15–41, 2021, doi: 10.4236/msa.2021.121002.
- [75] A. Diaz, *Surface texture characterization and optimization of metal additive manufacturing-produced components for aerospace applications*. Elsevier Inc., 2019. doi: 10.1016/b978-0-12-814062-8.00018-2.
- [76] J. Zhou *et al.*, 'In-situ Laser Polishing Additive Manufactured AlSi10Mg: Effect of Laser Polishing Strategy on Surface Morphology, Roughness and Microhardness', *Materials*, vol. 14, no. 2, pp. 1–19, 2021, doi: 10.3390/ma14020393.
- [77] H. Gu and L. Li, 'Computational fluid dynamic simulation of gravity and pressure effects in laser metal deposition for potential additive manufacturing in space', *Int J Heat Mass Transf*, vol. 140, no. June 2019, pp. 51–65, 2019, doi: 10.1016/j.ijheatmasstransfer.2019.05.081.
- [78] J. Song, Q. Tang, R. Setchi, and M. Ryan, *A Comparative Study of Pulse Wave and Continuous Wave Laser Patterns During Laser Powder Bed Fusion*, vol. 338 SIST. Springer Nature Singapore, 2023. doi: 10.1007/978-981-19-9205-6\_27.
- [79] P. R. Gradl, A. Park, and D. C. Tinker, 'Metal Additive Manufacturing Process Selection and Development for Propulsion Components', in *1st International Conference on Advanced Manufacturing for Air, Space and Land Transportation*, Virtual, 2022. [Online]. Available: <https://ntrs.nasa.gov/citations/20220004028>
- [80] Digital Micrometers Ltd., '7 Types Of Hardness Testers! The Best Method, Scale, And Test For Your Application'. Accessed: Aug. 18, 2023. [Online]. Available: <https://digitalmicrometers.co.uk/types-of-hardness-testers>
- [81] H. Lim and S. W. Hoag, 'Plasticizer Effects on Physical–Mechanical Properties of Solvent Cast Soluplus® Films', *AAPS PharmSciTech*, vol. 14, no. 3, pp. 903–910, Sep. 2013, doi: 10.1208/s12249-013-9971-z.
- [82] F. Braithwaite, 'On the fatigue and consequent fracture of metals', *Institute of Civil Engineers, Minutes of Proceedings*, vol. 13, pp. 463–474, 1854.
- [83] J. A. Boyd-Carpenter, 'Civil Aircraft Accident Report of the Court of Inquiry into the Accidents to Comet G-ALYP on 10th January, 1954 and Comet G-ALYY on 8th April, 1954', London, 1954. [Online]. Available: <https://www.baaa-acro.com/crash/crash-de-havilland-dh106-comet-1-elbe-island-35-killed>
- [84] J. Baker, 'An Investigation into the Handlebar Failure that Occurred in the Australian Men's Team Pursuit race at the Tokyo 2020 Olympics', Feb. 2022. Accessed: Oct. 27, 2023. [Online]. Available: [https://assets.auscycling.org.au/s3fs-public/2022-02/handlebar-9\\_21-ev-3\\_5-combined-inc-annexes-appendicies.pdf](https://assets.auscycling.org.au/s3fs-public/2022-02/handlebar-9_21-ev-3_5-combined-inc-annexes-appendicies.pdf)

- [85] DfAM, 'This is Not a 3D Print Fail'. Accessed: Oct. 07, 2022. [Online]. Available: <https://www.designforam.com/p/this-is-not-a-3d-print-fail?triedSigningIn=true&fbclid=IwAR2TRKN-UFDZN0cnuUmCH4i-KY2CCqb4yF07Zi55RDnyjy4XfcWQqTmi4E>
- [86] L. Newton, N. Senin, E. Chatzivagiannis, B. Smith, and R. Leach, 'Feature-based characterisation of Ti6Al4V electron beam powder bed fusion surfaces fabricated at different surface orientations', *Addit Manuf*, vol. 35, no. April, 2020, doi: 10.1016/j.addma.2020.101273.
- [87] M.-A. A. de Pastre *et al.*, 'Polymer powder bed fusion surface texture measurement', *Meas Sci Technol*, vol. 31, no. December, 2019, doi: 10.1088/1361-6501/ab63b1.
- [88] A. Triantaphyllou *et al.*, 'Surface texture measurement for additive manufacturing', *Surf Topogr*, vol. 3, no. 2, 2015, doi: 10.1088/2051-672X/3/2/024002.
- [89] S. Lou, X. Jiang, W. Sun, W. Zeng, L. Pagani, and P. J. Scott, 'Characterisation methods for powder bed fusion processed surface topography', *Precis Eng*, vol. 57, no. January 2018, pp. 1–15, 2019, doi: 10.1016/j.precisioneng.2018.09.007.
- [90] A. Townsend, N. Senin, L. Blunt, R. K. Leach, and J. S. Taylor, 'Surface texture metrology for metal additive manufacturing: a review', *Precis Eng*, vol. 46, pp. 34–47, 2016, doi: 10.1016/j.precisioneng.2016.06.001.
- [91] L. Newton, N. Senin, B. Smith, E. Chatzivagiannis, and R. Leach, 'Comparison and validation of surface topography segmentation methods for feature-based characterisation of metal powder bed fusion surfaces Comparison and validation of surface topography segmentation methods for feature-based characterisation of metal po', *Surf Topogr*, 2019.
- [92] N. Senin, A. Thompson, and R. K. Leach, 'Characterisation of the topography of metal additive surface features with different measurement technologies', *Meas Sci Technol*, vol. 28, no. 9, 2017, doi: 10.1088/1361-6501/aa7ce2.
- [93] W. Sun *et al.*, 'Establishment of X-ray computed tomography traceability for additively manufactured surface texture evaluation', *Addit Manuf*, vol. 50, no. September 2021, p. 102558, 2022, doi: 10.1016/j.addma.2021.102558.
- [94] J. Li, J. Hu, Y. Zhu, X. Yu, M. Yu, and H. Yang, 'Surface roughness control of root analogue dental implants fabricated using selective laser melting', *Addit Manuf*, vol. 34, no. February, p. 101283, 2020, doi: 10.1016/j.addma.2020.101283.
- [95] S. Pal *et al.*, 'As-fabricated surface morphologies of Ti-6Al-4V samples fabricated by different laser processing parameters in selective laser melting', *Addit Manuf*, vol. 33, no. January, p. 101147, 2020, doi: 10.1016/j.addma.2020.101147.
- [96] Z. Chen, X. Wu, D. Tomus, and C. H. J. Davies, 'Surface roughness of Selective Laser Melted Ti-6Al-4V alloy components', *Addit Manuf*, vol. 21, no. February, pp. 91–103, 2018, doi: 10.1016/j.addma.2018.02.009.
- [97] S. Bagehorn, J. Wehr, and H. J. Maier, 'Application of mechanical surface finishing processes for roughness reduction and fatigue improvement of additively manufactured Ti-6Al-4V parts', *Int J Fatigue*, vol. 102, pp. 135–142, 2017, doi: 10.1016/j.ijfatigue.2017.05.008.

- [98] V. Alfieri, P. Argenio, F. Caiazzo, and V. Sergi, 'Reduction of surface roughness by means of laser processing over additive manufacturing metal parts', *Materials*, vol. 10, no. 1, 2017, doi: 10.3390/ma10010030.
- [99] G. Strano, L. Hao, R. M. Everson, and K. E. Evans, 'Multi-objective optimization of selective laser sintering processes for surface quality and energy saving', *Proc Inst Mech Eng B J Eng Manuf*, vol. 225, no. 9, pp. 1673–1682, 2011, doi: 10.1177/0954405411402925.
- [100] F. Calignano, 'Investigation of the accuracy and roughness in the laser powder bed fusion process', *Virtual Phys Prototyp*, vol. 13, no. 2, pp. 97–104, 2018, doi: 10.1080/17452759.2018.1426368.
- [101] K. Mumtaz and N. Hopkinson, 'Top surface and side roughness of Inconel 625 parts processed using selective laser melting', *Rapid Prototyp J*, vol. 15, no. 2, pp. 96–103, 2009, doi: 10.1108/13552540910943397.
- [102] A. D. Brandão, J. Gumpinger, M. Gschweidl, C. Seyfert, P. Hofbauer, and T. Ghidini, 'Fatigue Properties of Additively Manufactured AlSi10Mg-Surface Treatment Effect', *Procedia Structural Integrity*, vol. 7, pp. 58–66, 2017, doi: 10.1016/j.prostr.2017.11.061.
- [103] A. du Plessis and S. Beretta, 'Killer notches: The effect of as-built surface roughness on fatigue failure in AlSi10Mg produced by laser powder bed fusion', *Addit Manuf*, vol. 35, no. March, p. 101424, 2020, doi: 10.1016/j.addma.2020.101424.
- [104] A. El Hassanin, M. A. Obeidi, F. Scherillo, and D. Brabazon, 'CO2 laser polishing of laser-powder bed fusion produced AlSi10Mg parts', *Surf Coat Technol*, vol. 419, no. May, p. 127291, 2021, doi: 10.1016/j.surfcoat.2021.127291.
- [105] A. Lamikiz, J. A. Sánchez, L. N. López de Lacalle, and J. L. Arana, 'Laser polishing of parts built up by selective laser sintering', *Int J Mach Tools Manuf*, vol. 47, no. 12–13, pp. 2040–2050, 2007, doi: 10.1016/j.ijmactools.2007.01.013.
- [106] S. Marimuthu, A. Triantaphyllou, M. Antar, D. Wimpenny, H. Morton, and M. Beard, 'Laser polishing of selective laser melted components', *Int J Mach Tools Manuf*, vol. 95, pp. 97–104, 2015, doi: 10.1016/j.ijmactools.2015.05.002.
- [107] J. Schanz *et al.*, 'Metallurgical investigations of laser remelted additively manufactured AlSi10Mg parts', *Materwiss Werksttech*, vol. 48, no. 5, pp. 463–476, 2017, doi: 10.1002/mawe.201700039.
- [108] I. Mingareev *et al.*, 'Femtosecond Laser Post-Processing of Metal Parts Produced by Laser Additive Manufacturing', *J Laser Appl*, vol. 25, no. 5, p. 052009, 2013, doi: 10.2351/1.4824146.
- [109] N. Worts, J. Jones, and J. Squier, 'Surface structure modification of additively manufactured titanium components via femtosecond laser micromachining', *Opt Commun*, vol. 430, no. August 2018, pp. 352–357, 2019, doi: 10.1016/j.optcom.2018.08.055.
- [110] Thorlabs Inc., 'Pulsed Lasers Introduction to Power and Energy Calculations Serving the Intellectually Curious Pulsed laser or CW laser , does it make a difference ?', 2022. [Online]. Available: [https://www.thorlabs.com/newgrouppage9.cfm?objectgroup\\_id=10823#ad-image-0](https://www.thorlabs.com/newgrouppage9.cfm?objectgroup_id=10823#ad-image-0)

- [111] C. Nüsser, I. Wehrmann, and E. Willenborg, 'Influence of intensity distribution and pulse duration on laser micro polishing', *Phys Procedia*, vol. 12, no. PART 1, pp. 462–471, 2011, doi: 10.1016/j.phpro.2011.03.057.
- [112] F. Zhihao, L. Libin, C. Longfei, and G. Yingchun, 'Laser Polishing of Additive Manufactured Superalloy', *Procedia CIRP*, vol. 71, pp. 150–154, 2018, doi: 10.1016/j.procir.2018.05.088.
- [113] C. Liang *et al.*, 'Laser polishing of Ti6Al4V fabricated by selective laser melting', *Metals (Basel)*, vol. 10, no. 2, pp. 1–13, 2020, doi: 10.3390/met10020191.
- [114] W. L. Xu, T. M. Yue, H. C. Man, and C. P. Chan, 'Laser surface melting of aluminium alloy 6013 for improving pitting corrosion fatigue resistance', *Surf Coat Technol*, vol. 200, no. 16–17, pp. 5077–5086, 2006, doi: 10.1016/j.surfcoat.2005.05.034.
- [115] P. V Petkov, P. Penchev, F. Lacan, and S. Bigot, 'Finishing of Titanium ALM parts by Laser Ablation', in *WCMNM 2018 World Congress on Micro and Nano Manufacturing*, Singapore: Research Publishing Services, 2018, pp. 111–114. doi: 10.3850/978-981-11-2728-1\_85.
- [116] Thorlabs Inc., 'Pulsed Lasers Introduction to Power and Energy Calculations Serving the Intellectually Curious Pulsed laser or CW laser , does it make a difference ?', 2022.
- [117] ASM International, 'Heat Treating of Aluminum Alloys.', in *ASM Handbook*, vol. 4: Heat Tr, 1991, pp. 841–874. doi: 10.1361/asmhba0001205.
- [118] MatWeb LLC, 'Aluminium Alloy Heat Treatment Temper Designations'. Accessed: May 11, 2023. [Online]. Available: <https://www.matweb.com/reference/aluminumtemper.aspx>
- [119] EOS GmbH, 'EOS Aluminium AlSi10Mg Material Data Sheet', 2022.
- [120] M. S. Younger and K. H. Eckelmeyer, 'SANDIA REPORT Overcoming Residual Stresses and Machining Distortion in the Production of Aluminum Alloy Satellite Boxes', 2007. doi: <https://doi.org/10.2172/922073>.
- [121] A. M. A. Mohamed and F. H. Samuel, 'A Review on the Heat Treatment of Al-Si-Cu/Mg Casting Alloys', in *Heat Treatment - Conventional and Novel Applications*, F. Czerwinski, Ed., IntechOpen, 2012, pp. 55–72. doi: 10.5772/50282.
- [122] I. Rosenthal, A. Stern, and N. Frage, 'Microstructure and Mechanical Properties of AlSi10Mg Parts Produced by the Laser Beam Additive Manufacturing (AM) Technology', *Metallography, Microstructure, and Analysis*, vol. 3, no. 6, pp. 448–453, 2014, doi: 10.1007/s13632-014-0168-y.
- [123] J. Suryawanshi, K. G. Prashanth, S. Scudino, J. Eckert, O. Prakash, and U. Ramamurty, 'Simultaneous enhancements of strength and toughness in an Al-12Si alloy synthesized using selective laser melting', *Acta Mater*, vol. 115, pp. 285–294, 2016, doi: 10.1016/j.actamat.2016.06.009.
- [124] W. Li *et al.*, 'Effect of heat treatment on AlSi10Mg alloy fabricated by selective laser melting: Microstructure evolution, mechanical properties and fracture mechanism', *Materials Science and Engineering A*, vol. 663, pp. 116–125, 2016, doi: 10.1016/j.msea.2016.03.088.
- [125] S. Bagherifard, N. Beretta, S. Monti, M. Riccio, M. Bandini, and M. Guagliano, 'On the fatigue strength enhancement of additive manufactured AlSi10Mg parts by mechanical and thermal post-processing', *Mater Des*, vol. 145, pp. 28–41, 2018, doi: 10.1016/j.matdes.2018.02.055.

- [126] A. Sabarinivas and R. Subramanian, 'Comparative study of Al6061 and AlSi10Mg produced by Selective Laser Melting Process', *IOP Conf Ser Mater Sci Eng*, vol. 1059, no. 1, 2021, doi: 10.1088/1757-899X/1059/1/012052.
- [127] Atilla Sarentica, 'Conventional heat treatment of additively manufactured AlSi10Mg', 2019.
- [128] F. Sajadi, J. M. Tiemann, N. Bandari, A. C. Darabi, J. Mola, and S. Schmauder, 'Fatigue improvement of AlSi10Mg fabricated by laser-based powder bed fusion through heat treatment', *Metals (Basel)*, vol. 11, no. 5, pp. 1–17, 2021, doi: 10.3390/met11050683.
- [129] D. C. Maxwell and T. Nicholas, 'Rapid method for generation of a Haigh diagram for high cycle fatigue', *ASTM Special Technical Publication*, no. 1332, pp. 626–641, 1999, doi: 10.1520/stp14974s.
- [130] T. Nicholas, 'Step loading for very high cycle fatigue', *Fatigue Fract Eng Mater Struct*, vol. 25, no. 8–9, pp. 861–869, 2002, doi: 10.1046/j.1460-2695.2002.00555.x.
- [131] G. M. Sinclair, 'An investigation of the coaxing effect in fatigue of metals', *ASTM Proceedings*, pp. 743–758, 1952.
- [132] T. Thompson, J. Liu, and C. Hu, 'A comparative analysis of step loading and staircase testing for fatigue strength estimation of an engine component', *Fatigue Fract Eng Mater Struct*, vol. 46, no. 2, pp. 667–681, 2022, doi: 10.1111/ffe.13898.
- [133] B. A. Lerch, S. L. Draper, and J. M. Pereira, 'Conducting high-cycle fatigue strength step tests on gamma TiAl', *Metallurgical and Materials Transactions A*, vol. 33, no. 12, pp. 3871–3874, Dec. 2002, doi: 10.1007/s11661-002-0259-2.
- [134] S. Beretta, M. Gargourimotlagh, S. Foletti, A. du Plessis, and M. Riccio, 'Fatigue strength assessment of "as built" AlSi10Mg manufactured by SLM with different build orientations', *Int J Fatigue*, vol. 139, no. February, p. 105737, 2020, doi: 10.1016/j.ijfatigue.2020.105737.
- [135] E. Brandl, U. Heckenberger, V. Holzinger, and D. Buchbinder, 'Additive manufactured AlSi10Mg samples using Selective Laser Melting (SLM): Microstructure, high cycle fatigue, and fracture behavior', *Mater Des*, vol. 34, pp. 159–169, 2012, doi: 10.1016/j.matdes.2011.07.067.
- [136] A. Mertens, O. Dedry, D. Reuter, O. Rigo, and J. Lecomte-Beckers, 'Thermal treatments of AlSi10Mg processed by laser beam melting', in *Proceedings - 26th Annual International Solid Freeform Fabrication Symposium - An Additive Manufacturing Conference, SFF 2015*, Austin, TX, USA, 2020, pp. 1007–1016.
- [137] N. E. Uzan, S. Ramati, R. Shneck, N. Frage, and O. Yeheskel, 'On the effect of shot-peening on fatigue resistance of AlSi10Mg specimens fabricated by additive manufacturing using selective laser melting (AM-SLM)', *Addit Manuf*, vol. 21, no. September 2017, pp. 458–464, 2018, doi: 10.1016/j.addma.2018.03.030.
- [138] A. B. Spierings, T. L. Starr, and K. Wegener, 'Fatigue performance of additive manufactured metallic parts', *Rapid Prototyp J*, vol. 19, no. 2, pp. 88–94, 2013, doi: 10.1108/13552541311302932.
- [139] N. T. Aboulkhair, 'Additive Manufacture of an Aluminium Alloy: Processing, Microstructure, and Mechanical Properties', PhD Thesis, University of Nottingham, 2016.

- [140] W. W. Wits, E. Scolaro, E. Amsterdam, and A. T. Clare, 'The role of scan strategies in fatigue performance for laser powder bed fusion', *CIRP Annals*, vol. 71, no. 1, pp. 185–188, 2022, doi: 10.1016/j.cirp.2022.03.006.
- [141] A. Ghiotti, R. Bertolini, M. Sorgato, A. Campagnolo, E. Savio, and S. Bruschi, 'Ti6Al4V titanium alloy fatigue strength after AM- and machining-based process chains', *CIRP Annals*, vol. 71, no. 1, pp. 461–464, 2022, doi: 10.1016/j.cirp.2022.04.021.
- [142] B. Gillham, A. Yankin, F. McNamara, C. Tomonto, D. Taylor, and R. Lupoi, 'Application of the Theory of Critical Distances to predict the effect of induced and process inherent defects for SLM Ti-6Al-4V in high cycle fatigue', *CIRP Annals*, vol. 70, no. 1, pp. 171–174, 2021, doi: 10.1016/j.cirp.2021.03.004.
- [143] T. Buchenau *et al.*, *Fatigue and Surface Texture of Post-Processed Metal Additive Ti-6Al-4V*, no. April. Toulouse, France, 2023.
- [144] L. Hackel, J. R. Rankin, A. Rubenchik, W. E. King, and M. Matthews, 'Laser peening: A tool for additive manufacturing post-processing', *Addit Manuf*, vol. 24, no. September, pp. 67–75, 2018, doi: 10.1016/j.addma.2018.09.013.
- [145] E. Maleki, S. Bagherifard, and M. Guagliano, 'Correlation of residual stress, hardness and surface roughness with crack initiation and fatigue strength of surface treated additive manufactured AlSi10Mg: Experimental and machine learning approaches', *Journal of Materials Research and Technology*, vol. 24, no. April, pp. 3265–3283, 2023, doi: 10.1016/j.jmrt.2023.03.193.
- [146] M. Hamidi Nasab *et al.*, 'An investigation on the fatigue behavior of additively manufactured laser shock peened AlSi7Mg alloy surfaces', *Mater Charact*, vol. 200, no. November 2022, 2023, doi: 10.1016/j.matchar.2023.112907.
- [147] M. Kahlin *et al.*, 'Improved fatigue strength of additively manufactured Ti6Al4V by surface post processing', *Int J Fatigue*, vol. 134, no. January, 2020, doi: 10.1016/j.ijfatigue.2020.105497.
- [148] S. Lee, Z. Ahmadi, J. W. Pegues, M. Mahjouri-Samani, and N. Shamsaei, 'Laser polishing for improving fatigue performance of additive manufactured Ti-6Al-4V parts', *Opt Laser Technol*, vol. 134, no. June 2020, 2021, doi: 10.1016/j.optlastec.2020.106639.
- [149] D. Ordnung, J. Metelkova, A. Cutolo, and B. Van Hooreweder, 'Improving fatigue performance of metal parts with up-facing inclined surfaces produced by laser powder bed fusion and in-situ laser remelting', *Additive Manufacturing Letters*, vol. 3, no. April, p. 100049, 2022, doi: 10.1016/j.addlet.2022.100049.
- [150] R. Avilés, J. Albizuri, E. Ukar, A. Lamikiz, and A. Avilés, 'Influence of laser polishing in an inert atmosphere on the high cycle fatigue strength of AISI 1045 steel', *Int J Fatigue*, vol. 68, pp. 67–79, 2014, doi: 10.1016/j.ijfatigue.2014.06.004.
- [151] Renishaw plc., 'Resource centre - RBV'. Accessed: Aug. 18, 2023. [Online]. Available: <https://www.renishaw.com/resourcecentre/en/details/RBV--90680?lang=gen>
- [152] Renishaw plc., 'QuantAM V5.3 build preparation software', no. January 2016. 2020.
- [153] SPI Lasers UK Ltd., 'G3.1 SM Series Pulsed Fibre Lasers: Installation Guide and User Manual', 2010.

- [154] Alicona Imaging GmbH, 'InfiniteFocusG5 plus'. Accessed: May 13, 2020. [Online]. Available: <https://www.alicon.com/en/products/infinitefocus/>
- [155] Easy Composites, 'IN2 EPOXY INFUSION RESIN-Technical Datasheet'. Accessed: Sep. 27, 2022. [Online]. Available: <https://www.easycomposites.co.uk/in2-epoxy-infusion-resin>
- [156] Buehler Ltd., 'EcoMet 30 Single Semi-Automatic'. Accessed: Aug. 18, 2023. [Online]. Available: <https://shop.buehler.com/ecomet-30-single-semi-automatic>
- [157] Mitutoyo, 'Mitutoyo, Product: Micro-Vickers hardness testing machine'. Accessed: Aug. 18, 2023. [Online]. Available: [https://shop.mitutoyo.eu/web/mitutoyo/en/mitutoyo/AT-400/Micro-Vickers hardness testing machine/\\$catalogue/mitutoyoData/PR/810-409D-BSET2/index.xhtml](https://shop.mitutoyo.eu/web/mitutoyo/en/mitutoyo/AT-400/Micro-Vickers%20hardness%20testing%20machine/$catalogue/mitutoyoData/PR/810-409D-BSET2/index.xhtml)
- [158] C. Arvieu, C. Galy, E. Le Guen, and E. Lacoste, 'Relative Density of SLM-Produced Aluminum Alloy Parts: Interpretation of Results', *Journal of Manufacturing and Materials Processing*, vol. 4, no. 3, p. 83, Aug. 2020, doi: 10.3390/jmmp4030083.
- [159] W. W. Wits, S. Carmignato, F. Zanini, and T. H. J. Vaneker, 'Porosity testing methods for the quality assessment of selective laser melted parts', *CIRP Ann Manuf Technol*, vol. 65, no. 1, pp. 201–204, 2016, doi: 10.1016/j.cirp.2016.04.054.
- [160] C. Liu, Y. Yuan, and M. Zhang, 'Uncertainty analysis of displacement measurement with Imetrum Video Gauge', *ISA Trans*, vol. 65, pp. 547–555, 2016, doi: 10.1016/j.isatra.2016.08.020.
- [161] MTS Systems, 'Bionix® Tabletop Test Systems'. Accessed: Nov. 02, 2022. [Online]. Available: <https://www.mts.com/en/products/biomedical/biomaterial-test-systems/bionix-tabletop>
- [162] ZwickRoell, 'Product Information: ZwickRoell Vibrophore 250'. 2022.
- [163] William Thompson, 'Electrical Units of Measurement (1883 Lecture)', in *Popular Lectures and Addresses, Volume 1*, London: Richard Clay and Sons Ltd., 1889, pp. 73–136. [Online]. Available: <https://archive.org/details/popularlecturesa01kelvuoft/page/n9/mode/2up>
- [164] A. Yarden Escudero-Ornelas, D. Bhaduri, H. Martinez-Zavala, A. Valera-Medina, and S. Bigot, 'On the Performance Evaluation of Microtextured Surfaces Using Computational Fluid Dynamics: A Comparative Study WCMNM 2022', in *World Congress on Micro and Nano Manufacturing*, Leuven, Belgium, 2022.
- [165] J. C. Fox, S. P. Moylan, and B. M. Lane, 'Effect of Process Parameters on the Surface Roughness of Overhanging Structures in Laser Powder Bed Fusion Additive Manufacturing', *Procedia CIRP*, vol. 45, pp. 131–134, 2016, doi: 10.1016/j.procir.2016.02.347.
- [166] R. Leach, 'Metrology for Additive Manufacturing', *Measurement and Control (United Kingdom)*, vol. 49, no. 4, pp. 132–135, 2016, doi: 10.1177/0020294016644479.
- [167] E. Yasa, J. Deckers, T. Craeghs, M. Badrossamay, and J. P. Kruth, 'Investigation on occurrence of elevated edges in selective laser melting', in *International Solid Freeform Fabrication Symposium*, Austin, TX, USA, 2009, pp. 180–192.
- [168] L. De Chiffre *et al.*, 'Quantitative Characterisation of Surface Texture', *CIRP Annals*, vol. 49, no. 2, pp. 635–652, 2000, doi: 10.1016/S0007-8506(07)63458-1.

- [169] Mitutoyo, 'Quick guide to surface roughness measurement', *Mitutoyo America Corporation*, p. 8, 2016, doi: 10.3886/ICPSR31521.v1.
- [170] Digital Surf, 'What's inside MountainsMap®'. Accessed: Jul. 17, 2020. [Online]. Available: <https://www.digitalsurf.com/software-solutions/profilometry/>
- [171] BSI, '13565-1: Geometric Product Specifications (GPS) — Surface texture: Profile method — Surfaces having stratified functional properties — Part 1: Filtering and general measurement conditions', no. 1, 1998.
- [172] Digital Surf, '3D Advanced Surface Texture Module for MountainsMap'. Accessed: Apr. 01, 2020. [Online]. Available: <https://www.digitalsurf.com/uploads/2018/06/3D-Advanced-Surface-Texture-Mountains-7-Optional-Module.pdf>
- [173] C. W. Jones, W. Sun, H. Boulter, and S. Brown, '3D roughness standard for performance verification of topography instruments for additively-manufactured surface inspection', *Meas Sci Technol*, vol. 33, no. 8, 2022, doi: 10.1088/1361-6501/ac6397.
- [174] A. Thompson, N. Senin, and R. K. Leach, 'Towards an additive surface atlas', *Proceedings - ASPE/euspen 2016 Summer Topical Meeting: Dimensional Accuracy and Surface Finish in Additive Manufacturing*, pp. 156–161, 2016.
- [175] A. Thompson, N. Senin, C. Giusca, and R. Leach, 'Topography of selectively laser melted surfaces: A comparison of different measurement methods', *CIRP Ann Manuf Technol*, vol. 66, no. 1, pp. 543–546, 2017, doi: 10.1016/j.cirp.2017.04.075.
- [176] TWI Ltd., 'What is Laser Welding and How Does it Work'. Accessed: Apr. 14, 2023. [Online]. Available: <https://www.twi-global.com/technical-knowledge/faqs/faq-how-does-laser-welding-work>
- [177] M. T. C. Chow, A. M. K. Hafiz, O. R. Tutunea-Fatan, G. K. Knopf, and E. V. Bordatchev, 'Experimental statistical analysis of laser micropolishing process', *2010 International Symposium on Optomechatronic Technologies, ISOT 2010*, 2010, doi: 10.1109/ISOT.2010.5687316.
- [178] M. Hofele *et al.*, 'Influence of Laser Polishing on the Material Properties of Aluminium L-PBF Components', *Metals (Basel)*, vol. 12, no. 5, p. 750, Apr. 2022, doi: 10.3390/met12050750.
- [179] Aalco Metals Limited, 'Aluminium Alloy - Commercial Alloy - 6063 - T6 Extrusions'. Accessed: Apr. 12, 2023. [Online]. Available: [https://www.aalco.co.uk/datasheets/Aluminium-Alloy-6063-T6-Extrusions\\_158.ashx](https://www.aalco.co.uk/datasheets/Aluminium-Alloy-6063-T6-Extrusions_158.ashx)
- [180] MakeltFrom.com, 'EN AC-42200-T6 Cast Aluminum'. Accessed: Apr. 13, 2023. [Online]. Available: <https://www.makeitfrom.com/material-properties/EN-AC-42200-T6-Cast-Aluminum>
- [181] E. Ukar, A. Lamikiz, L. N. López de Lacalle, D. del Pozo, and J. L. Arana, 'Laser polishing of tool steel with CO2 laser and high-power diode laser', *Int J Mach Tools Manuf*, vol. 50, no. 1, pp. 115–125, 2010, doi: 10.1016/j.ijmachtools.2009.09.003.
- [182] T. M. Shao, M. Hua, H. Y. Tam, and E. H. M. Cheung, 'An approach to modelling of laser polishing of metals', *Surf Coat Technol*, vol. 197, no. 1, pp. 77–84, 2005, doi: 10.1016/j.surfcoat.2005.01.010.

- [183] DataRay Inc., 'Beam'R2 - XY Scanning Slit Beam Profiler | DataRay Inc.' Accessed: Jun. 21, 2023. [Online]. Available: <https://dataray.com/collections/scanning-slit-beam-profilers/products/beamr2-xy-scanning-slit-beam-profiler-system>
- [184] Materion Microelectronics & Services, 'Reflectance in Thin Films', 2007.
- [185] D. Dai and D. Gu, 'Tailoring surface quality through mass and momentum transfer modeling using a volume of fluid method in selective laser melting of TiC/AlSi10Mg powder', *Int J Mach Tools Manuf*, vol. 88, pp. 95–107, 2015, doi: 10.1016/j.ijmachtools.2014.09.010.
- [186] ASTM International, 'E8/E8M-21: Standard test methods for tension testing of metallic materials', *Annual Book of ASTM Standards 4*, no. C, pp. 1–27, 2010, doi: 10.1520/E0008.
- [187] L. Zhang, W. Harrison, M. A. Yar, S. G. R. Brown, and N. P. Lavery, 'The development of miniature tensile specimens with non-standard aspect and slimmness ratios for rapid alloy prototyping processes', *Journal of Materials Research and Technology*, vol. 15, no. September, pp. 1830–1843, 2021, doi: 10.1016/j.jmrt.2021.09.029.
- [188] Carbolite Gero Ltd., 'Muffle furnace solutions from Carbolite Gero'. Accessed: Sep. 16, 2023. [Online]. Available: <https://www.carbolite-gero.com/products/muffle-furnace/>
- [189] Mathworks, 'Fit linear regression model - MATLAB fitlm'. 2020. Accessed: Jun. 15, 2023. [Online]. Available: <https://uk.mathworks.com/help/stats/fitlm.html>
- [190] ASTM International, 'E92 - 17: Standard Test Methods for Vickers Hardness and Knoop Hardness of Metallic Materials'. doi: 10.1520/E0092-17.2.
- [191] 'Correlation coefficients - MATLAB corrcoef - MathWorks United Kingdom'. Accessed: Feb. 16, 2024. [Online]. Available: <https://uk.mathworks.com/help/matlab/ref/corrcoef.html#f80-999628-P>
- [192] National Institute of Standards and Technology, 'Engineering Significance', Engineering Statistics Handbook. Accessed: May 04, 2023. [Online]. Available: <https://www.itl.nist.gov/div898/handbook/pri/section5/pri5972.htm>
- [193] E. Yasa, J. Deckers, J. P. Kruth, M. Rombouts, and J. Luyten, 'Experimental investigation of charpy impact tests on metallic SLM parts', *Innovative Developments in Design and Manufacturing - Advanced Research in Virtual and Rapid Prototyping*, pp. 207–214, 2010, doi: 10.1201/9780203859476-38.
- [194] N. E. Uzan, R. Shneck, O. Yeheskel, and N. Frage, 'Fatigue of AlSi10Mg specimens fabricated by additive manufacturing selective laser melting (AM-SLM)', *Materials Science and Engineering A*, vol. 704, no. February, pp. 229–237, 2017, doi: 10.1016/j.msea.2017.08.027.
- [195] N. T. Aboulkhair, C. Tuck, I. Ashcroft, I. Maskery, and N. M. Everitt, 'On the Precipitation Hardening of Selective Laser Melted AlSi10Mg', *Metall Mater Trans A Phys Metall Mater Sci*, vol. 46, no. 8, pp. 3337–3341, 2015, doi: 10.1007/s11661-015-2980-7.
- [196] D. Bhaduri *et al.*, 'On the surface integrity of additive manufactured and post-processed AlSi10Mg parts', *Procedia CIRP*, vol. 87, pp. 339–344, 2020, doi: 10.1016/j.procir.2020.02.093.
- [197] K. Zyguła, B. Nosek, H. Pasiowiec, and N. Szysiak, 'Mechanical properties and microstructure of AlSi10Mg alloy obtained by casting and SLM technique', vol. 104, no. July, pp. 462–472, 2018.

- [198] K. Wei *et al.*, 'Effect of laser remelting on deposition quality, residual stress, microstructure, and mechanical property of selective laser melting processed Ti-5Al-2.5Sn alloy', *Mater Charact*, vol. 150, no. October 2018, pp. 67–77, 2019, doi: 10.1016/j.matchar.2019.02.010.
- [199] ASTM International, 'E466 - 21: Standard Practice for Conducting Force Controlled Constant Amplitude Axial Fatigue Tests of Metallic Materials 1', doi: 10.1520/E0466-21.
- [200] Nagwa, 'Lesson Explainer: Radiation Pressure on Perfectly Reflective Surfaces'. Accessed: May 18, 2023. [Online]. Available: <https://www.nagwa.com/en/explainers/930186872308/>
- [201] Pulsar Photonics, 'Ultra-short pulse laser technology'. Accessed: Aug. 11, 2023. [Online]. Available: <https://www.pulsar-photonics.de/en/about-us/ultra-short-pulse-laser-technology/>
- [202] National Transportation Safety Board, 'National Transportation Safety Board Reports', USA.gov. [Online]. Available: <https://www.nts.gov/Pages/search.aspx#Default=%7B%22k%22%3A%22fatigue%22%2C%22r%22%3A%5B%7B%22n%22%3A%22Mode%22%2C%22t%22%3A%5B%22%5C%22%20%22%3A%22and%22%2C%22k%22%3A%22false%22%2C%22m%22%3A%22null%22%7D%5D%7D>
- [203] Air Accidents Investigation Branch, 'Air Accidents Investigation Branch Reports', GOV.UK. Accessed: Jun. 06, 2023. [Online]. Available: <https://www.gov.uk/aaib-reports?keywords=fatigue>

## I. Appendix – MATLAB Localisation script

```
fig1orig = imread('Picture1.png'); %open first image
fig2orig = imread('Picture2.png'); %open second image

figure(1)
imshowpair(fig1orig,fig2orig,'montage') %shows images together

%% crop image (manually set the limits)
cropTLC = [40 30];
cropBRC = [30 40];
wid = size(fig1orig,1)-cropTLC(1)-cropBRC(1);
ht = size(fig1orig,2)-cropTLC(2)-cropBRC(2);
fig1 = imcrop(fig1orig,[cropTLC(1) cropTLC(2) wid ht]);
wid = size(fig2orig,1)-cropTLC(1)-cropBRC(1);
ht = size(fig2orig,2)-cropTLC(2)-cropBRC(2);
fig2 = imcrop(fig2orig,[cropTLC(1) cropTLC(2) wid ht]);

fig1gray = rgb2gray(fig1); %make images gray scale
fig2gray = rgb2gray(fig2);

figure(2)
imshowpair(fig1gray,fig2gray,'montage') %show gray scale images together

figure(3)
imshow(rgb2gray(fig1))

outputView = imref2d(size(fig1gray));
tform = affine2d(eye(3));
fig2gray = imwarp(fig2gray,tform,'OutputView',outputView);

figure(4)
imshowpair(fig1gray,fig2gray,'montage')

%% autodetecting picture features
%{
detectSURFFeatures, detectBRISKFeatures, and detectMSERFeatures all tried,
Maximally Stable Extremal Regions (MSER) was found to be the most reliable
and accurate for this application
%}
ptsfig1 = detectMSERFeatures(fig1gray);
ptsfig2 = detectMSERFeatures(fig2gray);

[featuresfig1, validPtsfig1] = extractFeatures(fig1gray, ptsfig1);
[featuresfig2, validPtsfig2] = extractFeatures(fig2gray, ptsfig2);

% plot of the identified features
figure(5)
subplot(1,2,1)
imshow(fig1gray); hold on;
scatter(ptsfig1.Location(:,1),ptsfig1.Location(:,2),'*')
hold off;
subplot(1,2,2)
imshow(fig2gray); hold on;
scatter(ptsfig2.Location(:,1),ptsfig2.Location(:,2),'*')
hold off;
```

```

% labelling the identified feature
figure(6)
subplot(1,2,1)
    imshow(fig1gray); hold on;
    scatter(ptsfig1.Location(:,1),ptsfig1.Location(:,2),'ro')
    for ii = 1:ptsfig1.Count
        Labels = sprintf('%d', ii);
        Xloc = double(ptsfig1.Location(ii,1))+rand(1)*2-1)*1e1;
        Yloc = double(ptsfig1.Location(ii,2))+rand(1)*2-1)*1e1;
        text(Xloc, Yloc, Labels, 'HorizontalAlignment', 'center', 'rotation',0);
    hold on;
    end
    hold off
subplot(1,2,2)
    imshow(fig2gray); hold on;
    scatter(ptsfig2.Location(:,1),ptsfig2.Location(:,2),'ro')
    for ii = 1:ptsfig2.Count
        Labels = sprintf('%d', ii);
        Xloc = double(ptsfig2.Location(ii,1))+rand(1)*2-1)*1e1;
        Yloc = double(ptsfig2.Location(ii,2))+rand(1)*2-1)*1e1;
        text(Xloc, Yloc, Labels, 'HorizontalAlignment', 'center', 'rotation',0);
    hold on;
    end
    hold off

%% manual identification of matched features
matchind = [ 92  1  61  105  31  70
            215 213 202 172 142 279 ];

% use this figure to track the matched indices w.r.t. fig1
figure(7)
imshow(fig1gray); hold on;
scatter(ptsfig1.Location(matchind(1,:),1),ptsfig1.Location(matchind(1,:),2),'ro')
scatter(ptsfig2.Location(matchind(2,:),1),ptsfig2.Location(matchind(2,:),2),'b*')
for ii=1:size(matchind,2)
    X=[ptsfig1.Location(matchind(1,ii),1) ptsfig2.Location(matchind(2,ii),1)];
    Y=[ptsfig1.Location(matchind(1,ii),2) ptsfig2.Location(matchind(2,ii),2)];
    plot(X,Y,'-k','LineWidth',2)
    Labels = sprintf('%d', matchind(1,ii));
    Xloc = double(X(1))+rand(1)*2-1)*1e1;
    Yloc = double(Y(1))+rand(1)*2-1)*1e1;
    text(Xloc, Yloc, Labels, 'HorizontalAlignment', 'center', 'rotation',0); hold
on;
    Labels = sprintf('%d', matchind(2,ii));
    Xloc = double(X(2))+rand(1)*2-1)*1e1;
    Yloc = double(Y(2))+rand(1)*2-1)*1e1;
    text(Xloc, Yloc, Labels, 'HorizontalAlignment', 'center', 'rotation',0); hold
on;
end
hold off

matchedfig1 = ptsfig1(matchind(1,:));
matchedfig2 = ptsfig2(matchind(2,:));

figure(8)
showMatchedFeatures(fig1gray,fig2gray,matchedfig1,matchedfig2);
title('Putatively matched points (including outliers)');

```

```

figure(9)
subplot(1,2,1)
    imshow(fig1gray); hold on;
    scatter(matchedfig1.Location(:,1),matchedfig1.Location(:,2),'ro')
    for ii = 1:matchedfig1.Count
        Labels = sprintf('%d', ii);
        Xloc = double(matchedfig1.Location(ii,1))+rand(1)*2-1)*1e1;
        Yloc = double(matchedfig1.Location(ii,2))+rand(1)*2-1)*1e1;
        text(Xloc, Yloc, Labels, 'HorizontalAlignment', 'center','rotation',0);
    hold on;
    end
    hold off
subplot(1,2,2)
    imshow(fig2gray); hold on;
    scatter(matchedfig2.Location(:,1),matchedfig2.Location(:,2),'ro')
    for ii = 1:matchedfig2.Count
        Labels = sprintf('%d', ii);
        Xloc = double(matchedfig2.Location(ii,1))+rand(1)*2-1)*1e1;
        Yloc = double(matchedfig2.Location(ii,2))+rand(1)*2-1)*1e1;
        text(Xloc, Yloc, Labels, 'HorizontalAlignment', 'center','rotation',0);
    hold on;
    end
    hold off

```

```

figure(10)
imshow(fig1); hold on;
scatter(ptsfig1.Location(:,1),ptsfig1.Location(:,2),'r*')
scatter(matchedfig1.Location(:,1),matchedfig1.Location(:,2),'bo')
hold off;

```

```

%% Transform fig2 to match fig1
%%finding transform matrix

```

```

[tform, inlierDistorted, inlierOriginal] = estimateGeometricTransform(...
    matchedfig2, matchedfig1, 'affine');

```

```

figure(11)
showMatchedFeatures(fig1gray,fig2gray,inlierOriginal,inlierDistorted);
title('Matching points (inliers only)');
legend('ptsOriginal','ptsDistorted');

```

```

Tinv = tform.invert.T;

```

```

ss = Tinv(2,1);
sc = Tinv(1,1);
scaleRecovered = sqrt(ss*ss + sc*sc);
thetaRecovered = atan2(ss,sc)*180/pi;

```

```

outputView = imref2d(size(fig1gray));
fig2grayR = imwarp(fig2gray,tform,'OutputView',outputView);
fig2CR = imwarp(fig2,tform,'OutputView',outputView);

```

```

figure, imshowpair(fig1gray,fig2grayR,'montage')

```

```

figure(12)
subplot(1,2,1)
    imshow(fig1gray); hold on;
    scatter(ptsfig1.Location(:,1),ptsfig1.Location(:,2),'*')
    hold off;
subplot(1,2,2)
    imshow(fig2grayR); hold on;
    scatter(ptsfig1.Location(:,1),ptsfig1.Location(:,2),'*')
    hold off;

figure(13)
imshow(fig2grayR);
title('Recovered image');

% crop images (manually set the limits)
cropTLC = [50 0]; wid = 397 - cropTLC(1); ht = 457 - cropTLC(2);
fig1F = imcrop(fig1gray,[cropTLC(1) cropTLC(2) wid ht]);
fig2F = imcrop(fig2grayR,[cropTLC(1) cropTLC(2) wid ht]);

figure, imshowpair(fig1F,fig2F,'montage')

fig1CF = imcrop(fig1,[cropTLC(1) cropTLC(2) wid ht]);
fig2CF = imcrop(fig2CR,[cropTLC(1) cropTLC(2) wid ht]);

figure(14)
subplot(2,2,1)
    imshow(fig1);
    title('Original Fig1')
subplot(2,2,2)
    imshow(fig2);
    title('Original Fig2')
subplot(2,2,3)
    imshow(fig1CF);
    title('Transformed Fig1')
subplot(2,2,4)
    imshow(fig2CF);
    title('Transformed Fig2')
savefig('./ImageTransformFig1_3.fig') % saved as Matlab figure
print -dpng ./ImageTransformFig1_3.png; % saved as png

```

## II. Appendix – LP initial development test matrix

Table A. 1: 2-step LP strategy development test matrix.

Sample Reference	Passes		Sa ( $\mu\text{m}$ )		Reduction			
	Step 1	Step 2	Initial	Final	Sa	Sp	Sv	S10z
S1a_05	2	4	26.44	14.99	43.31%	14.01%	-68.75%	12.42%
S1a_06	2	8	14.11	8.56	39.34%	-8.78%	-134.47%	-43.10%
S1a_07	2	16	22.28	9.18	58.78%	60.94%	45.31%	55.35%
S1a_08	2	24	22.53	12.54	44.32%	12.12%	-29.73%	15.86%
S1a_09	2	32	16.85	9.84	41.62%	22.03%	-124.14%	-5.21%
S1a_10	2	16	11.05	6.87	37.87%	57.39%	36.86%	42.15%
S1a_11	4	16	11.16	6.21	44.35%	31.60%	20.78%	51.43%
S1a_12	6	16	11.48	6.30	45.13%	55.75%	1.12%	42.98%
S1a_13	8	16	15.92	6.52	59.03%	69.70%	-27.27%	51.50%
S1a_14	10	16	12.51	5.27	57.89%	67.32%	53.95%	62.45%
S1a_15	8	8	10.81	7.01	35.17%	49.27%	-115.58%	8.15%
S1a_16	8	12	18.06	8.37	53.64%	35.70%	-241.10%	-1.98%
S1a_17	8	16	20.31	9.38	53.84%	28.82%	-88.19%	18.33%
S1a_18	8	20	11.50	6.65	42.14%	28.86%	-177.37%	-2.91%
S1a_19	8	24	17.57	7.95	54.74%	1.98%	-6.45%	32.06%

Table A. 2: 3-step LP strategy development test matrix.

Sample Reference	Passes			Sa ( $\mu\text{m}$ )		Reduction			
	Step 1	Step 2	Step 3	Initial	Final	Sa	Sp	Sv	S10z
S1a_26	4	8	8	12.33	6.07	50.81%	53.06%	-32.36%	35.66%
S1a_27	4	16	8	14.87	7.98	46.32%	31.43%	-0.72%	33.29%
S1a_28	4	16	16	14.40	6.35	55.90%	19.21%	77.54%	69.85%
S1a_29	8	16	16	13.78	6.42	53.42%	66.11%	-43.69%	30.31%
S1a_30	4	8	16	15.91	7.23	54.55%	32.65%	-78.57%	50.08%

Table A. 3: 4-step LP strategy development test matrix.

Sample Reference	Passes				Sa ( $\mu\text{m}$ )		Reduction			
	Step 1	Step 2	Step 3	Step 4	Initial	Final	Sa	Sp	Sv	S10z
S1a_23	4	8	4	16	13.11	6.35	51.58%	38.40%	-0.32%	34.19%
S1a_24	4	8	4	16	13.75	7.16	47.95%	16.41%	25.19%	26.05%
S1a_25	4	8	4	16	25.32	8.74	65.48%	-22.58%	-120.69%	-10.11%
S1a_31	4	8	4	8	19.31	9.08	52.96%	59.31%	-56.33%	51.10%
S1a_32	8	8	4	8	21.73	6.53	69.95%	76.36%	12.91%	61.69%
S1a_33	4	16	4	8	12.48	6.05	51.52%	70.62%	-396.42%	40.04%
S1a_34	8	16	4	8	11.40	5.74	49.65%	68.22%	-136.58%	32.67%
S1a_35	8	8	4	8	13.48	5.38	60.09%	80.64%	-75.04%	44.75%
S1a_37	8	8	4	16	14.73	5.91	59.87%	68.72%	-44.90%	38.98%
S1a_40	4	4	4	16	10.97	5.95	45.70%	64.25%	-59.02%	33.01%
S1a_44	4	4	4	4	18.92	8.10	57.21%	59.49%	-19.98%	63.05%
S1a_L01	4	4	4	8	10.76	5.56	48.36%	43.40%	-3.54%	44.94%
S1a_L03	8	8	4	16	11.42	4.73	58.61%	77.09%	39.72%	61.16%
S1a_L04	2	2	2	4	14.41	7.65	46.88%	27.82%	14.57%	30.34%
S2b_L13	4	8	4	16	13.56	6.06	55.35%	17.57%	-37.70%	16.91%
S2b_L14	8	4	4	16	16.02	5.66	64.67%	67.37%	-19.25%	38.21%
S2b_L15	4	4	4	16	15.25	6.00	60.64%	20.00%	-26.19%	43.62%
S2b_L16	8	6	4	16	22.48	7.42	66.97%	-13.74%	-21.36%	12.54%
S2b_L17	6	8	4	16	17.26	6.26	63.73%	34.38%	-83.51%	37.14%
S2b_L18	6	4	4	16	16.83	6.31	62.53%	45.45%	-245.85%	27.99%
S2b_L19	6	6	4	16	12.08	5.63	53.43%	57.93%	-42.66%	44.54%
S2b_L20	8	8	4	12	23.29	6.83	70.66%	52.22%	58.43%	51.89%
S2b_L21	8	8	4	8	14.40	6.03	58.09%	70.13%	0.30%	47.15%
S2b_L22	8	8	4	10	16.26	6.08	62.58%	54.15%	6.24%	46.24%
S2b_L23	8	8	4	14	19.44	6.89	64.53%	35.64%	2.85%	44.22%

### III. Appendix – MATLAB script for determining elastic region and calculating mechanical properties.

%input arrays contain: Displacement, Load, Strain, and Time from throughout the test (@5Hz) and measured Width and Depth of the sample

```
Res=zeros(length(Sample),5);

for a=1:length(Sample)
    load(append(Sample(a),".mat"));

    T=Time; %Time input
    D=smoothdata(Displacement,'gaussian',15); %Displacement
    F=smoothdata(Load,'gaussian',15); %Load
    F=-F; %Load recorded as negative values on some tests
    e=smoothdata(Strain1,'gaussian',15); %Smoothed Strain
    e=e/100; %strain input to decimal

    %Rate of change in Force
    dF=zeros(length(F)-10,1);
    for t=11:length(F)
        dF(t)=F(t)-F(t-10);
    end
    %Rate of change in Strain
    de=zeros(length(e)-10,1);
    for t=11:length(F)
        de(t)=e(t)-e(t-10);
    end

    %Start of test, when force application starts (based on strain)
    st=round(length(de)/2); %Start search at test mid-point, working backwards
    while de(st)>0 %find point where strain rate is positive (initial settling
        period)
        st=st-1;
    end

    %End of test, when sample ruptures
    ed=st;
    while dF(ed)>-1000 %Finding rapid load reduction
        ed=ed+1;
    end
    ed=ed-5; %Take point 1 second earlier to avoid transience

    %Cropped test data
    Tt=T(st:ed);
    Dt=D(st:ed);
    Ft=F(st:ed);
    et=e(st:ed)-e(st);
    St=Ft/(w*d); %Stress Calculation

    %% Initial guess for Elastic region based on strainrate
    %Rate of change of Strain
    de=zeros(length(et)-10,1);
    for t=11:length(et)
        de(t)=et(t)-et(t-10);
    end
end
```

```

%Yield point by when strain rate increases (initial guess)
yld=50;
while de(yld)<0.0025
    yld=yld+1;
end

EFit=fitlm(et(1:yld),St(1:yld));
E=EFit.Coefficients.Estimate(2);

%Saving Results
Res(a,1)=E*10^-9;          %Young's Modulus (GPa)
Res(a,2)=max(St)*10^-6;   %UTS (MPa)
Res(a,3)=max(et)*100;     %Failure Strain (%)
Res(a,4)=St(yld)*10^-6;   %Yield Stress (MPa)
Res(a,5)=et(yld)*100;     %Yield Strain

%% Calculating elastic region based on local Young's Modulus
L=5; %local E calc. window
dE=zeros(length(et)-1,1);

%Calculating local E for every timestep
for i=L:length(et)-(L+1)
    EFit=fitlm(et(i:i+L),St(i:i+L));
    dE(i)=EFit.Coefficients.Estimate(2);
end

ERes(a,1)=E; %initial estimate for E
SRes(a,1)=St(t);
eRes(a,1)=et(t);

%% iterative loop to find linear elastic region, 10 iterations found to give good
results
for z=2:10
    %When does local E reach 50% the E up to that point? (Yield point)
    Yld=length(dE);
    while dE(Yld) < 0.5 * ERes(a,z-1)
        Yld=Yld-1;
    end
    %When does local E reach 75% the E up to that point? (Initial settling)
    s=1;
    while dE(s)<0.75*ERes(a,z-1)
        s=s+1;
    end

    %Calculating E between initial settling and yield points identified
    est=fitlm(et(s:Yld),St(s:Yld));

    ERes(a,z)=est.Coefficients.Estimate(2);
    SRes(a,z)=St(Yld);
    eRes(a,z)=et(Yld);
end

et=et*100; St=St*10^-6;          %Unit conversion
est=fitlm(et(s:Yld),St(s:Yld));
E=est.Coefficients.Estimate(2); %Final value of E

```